THE UNIVERSITY *of* EDINBURGH

Modelling microcircuits of grid cells and theta-nested gamma oscillations in the medial entorhinal cortex

Lukas Solanka

Doctor of Philosophy

Institute for Adaptive and Neural Computation
School of Informatics
University of Edinburgh

2015

Abstract

The relationship between structure, dynamics, and function of neural networks in nervous systems is still an open question in the neuroscience community. Nevertheless, for certain areas of the mammalian nervous system we do have sufficient data to impose constraints on the organisation of the network structure. One of these areas is the medial entorhinal cortex which contains cells with hexagonally repeating spatial receptive fields, called grid cells. Another intriguing property of entorhinal cortex and other cortical regions is a population oscillatory activity, with frequency in the theta (4-10 Hz) and gamma (30-100 Hz) range. This leads to a question, whether these oscillations are a common circuit mechanism that is functionally relevant and how the oscillatory activity interacts with the computation performed by grid cells.

This thesis deals with applying the continuous attractor network theory to modelling of the microcircuit of layer II in the medial entorhinal cortex. Based on recent experimental evidence on connectivity between stellate cells, and fast spiking interneurons, I first develop a two-population spiking attractor network model that is capable of reproducing the activity of a population of grid cells in layer II. The network was implemented with exponential integrate and fire neurons that allowed me to address both the attractor states and the oscillatory activity in this region. Subsequently, I show that the network can produce theta-nested gamma oscillations with properties that are similar to the cross-frequency coupling observed *in vivo* and *in vitro* in entorhinal cortex, and that these theta-nested gamma oscillations can co-exist with grid-like receptive fields generated by the network. I also show that the connectivity inspired by anatomical evidence produces a number of directly testable predictions about the firing fields of interneurons in layer II of the medial entorhinal cortex.

The excitatory-inhibitory attractor network, together with the theta-nested gamma oscillations, allowed me to explore potential relationships between nested gamma oscillations and grid field computations. I show, by varying the overall level of excitatory and inhibitory synaptic strengths, and levels of noise, in the network, that this relationship is complex, and not easily predictable. Specifically, I show that noise promotes generation of grid firing fields and theta-nested gamma oscillations by the model. I subsequently demonstrate that theta-nested gamma oscillations are dissociable from the grid field computations performed by the network. By changing the relative strengths of interactions between excitatory and inhibitory neurons in the network, the power and frequency of the gamma oscillations changes without disrupting the rate-coded grid field computations. Since grid cells have been suggested to be a part of the spatial cognitive circuit in the brain, these results have potential implications for several cognitive disorders, including autism and schizophrenia, as well as theories that propose a cognitive role for gamma oscillations.

Acknowledgements

I would like to thank my supervisors Matthew Nolan and Mark van Rossum for their invaluable guidance during the project. I would also like to thank Ellen Barber, Helen Ramsden, Sang Soo-Seo and Lukas Fischer for useful and relevant comments during the revision of this manuscript.

Declaration

I declare that this thesis was composed by myself, that the work contained herein is my own except where explicitly stated otherwise in the text, and that this work has not been submitted for any other degree or professional qualification except as specified.

(*Lukas Solanka*)

Table of Contents

Chapter 1

Introduction

Determining the relationship between the structure and input-output dynamics of neural networks in nervous systems is challenging. One of the likely reasons for this is the problem of experimental identification and analysis of connections in neural microcircuits, which results in a huge parameter space to explore in models of neural networks. Nevertheless, there are areas in nervous systems of mammals in which parameters for neuronal connectivity and activity can be reasonably well constrained. One of these areas is the medial entorhinal cortex (MEC) of mammals which contains cells with regularly repeating spatial receptive fields, called grid cells (Hafting et al., 2005). These cells are of great interest as they provide a possible neural substrate for encoding spatial representations (Moser et al., 2014).

Extensive experimental and modelling work has provided insight into how these spatial maps of the environment are created. There is evidence, particularly from rodents, that the receptive fields of grid cells are a result of integration of both external cues in the environment and self-motion cues (Hafting et al., 2005; Sargolini et al., 2006). This has resulted in different influential models of how input from self-motion cues, as well as inputs from external landmarks, can be transformed into cell discharges that depend on the position of an animal in the environment (Welinder et al., 2008; Zilli, 2012; Barry and Burgess, 2014).

Another intriguing property of the entorhinal cortex, which is shared by other cortical areas, is a population oscillatory activity, observable from local field potentials and single cell activity (Buzsáki and Draguhn, 2004). Neural dynamics in the entorhinal cortex include both theta and gamma oscillations (Chrobak and Buzsaki, 1998; Quilichini et al., 2010). This leads to the question of why this activity is common and whether it serves any functional role. One possibility is that neural oscillations are

only a by-product of neural dynamics. In this case, oscillations should not impose a specific relationship between the dynamics of neural networks and cognitive performance. However, experimental evidence shows that abnormal gamma oscillations are correlated with cognitive deficits in various psychological disorders (Traub and Whittington, 2010; Uhlhaas and Singer, 2012), suggesting that they might be important for neural computation.

Putting together both grid-like receptive fields and theta-nested gamma oscillatory activity with the recent experimental evidence that principal cells in the MEC contact each other exclusively through feedback inhibition (Dhillon and Jones, 2000; Pastoll et al., 2013; Couey et al., 2013), it is natural to ask what the common mechanism that underlies all the above mentioned properties is. The answer to this question would provide a better insight into how entorhinal cortex performs computation.

In this thesis, I will outline the application of the continuous attractor network theory (Zhang, 1996; Samsonovich and McNaughton, 1997; Conklin and Eliasmith, 2005; Song and Wang, 2005) to generate a model of the microcircuit of layer II in the MEC that reproduces both the grid-like responses and oscillatory activity. In the next sections, I will describe the major findings of the field that are important for this work, including the experimental characterisation of cellular and network properties of grid cells, as well as attempts that have been made to model the spatial firing fields of grid cells in the MEC. This will lay foundations for defining the specific objectives of the thesis.

1.1 Grid cells in the medial entorhinal cortex

1.1.1 Properties of grid cells

Grid cells are cells that possess spatially modulated firing fields (Hafting et al., 2005). In rats, they are found primarily in layer II of the MEC (Sargolini et al., 2006), which is part of the parahippocampal region. For a large enough environment in which an animal can move, each grid cell fires only at specific locations of the animal. The structure of the firing fields is periodic and uniform, with firing fields lying at vertices of approximate equilateral triangles (Fyhn et al., 2004; Hafting et al., 2005). An example of a grid firing field is illustrated in Figure 1.1.

The presence of these grid-like firing fields in the MEC is preserved across several mammalian species. Grid cells have been found in both rats (Fyhn et al., 2004; Haft-

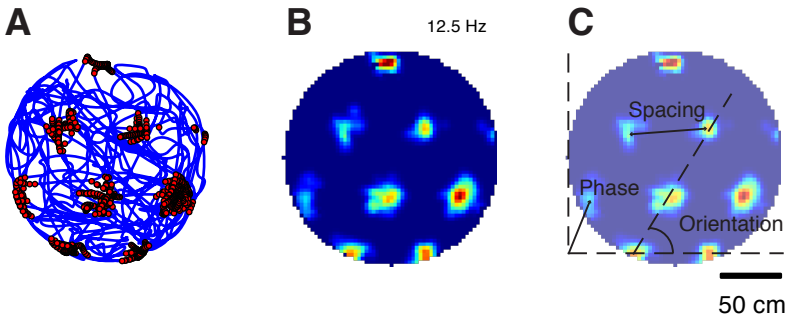

Figure 1.1: **Examples of simulated grid fields. (A)** Animal trajectory in a circular arena with a diameter of 180 cm (blue lines), together with locations of action potentials fired by a single grid cell (red dots). **(B)** Smoothed spatial firing rate map of the firing field in (A). Blue values denote zero firing, while red values stand for maximal firing rate, indicated by the number in the top-right corner. **(C)** Three basic properties of a grid field: spacing between the fields, orientation, and phase with respect to a reference point.

ing et al., 2005) and mice (Fyhn et al., 2008; Buetfering et al., 2014). In both of these species they have a strikingly regular hexagonal structure. Grid cells have also been identified in bats (Yartsev et al., 2011). Egyptian fruit bats were trained to crawl in a square enclosure, and recordings from the MEC revealed sufficient hexagonality to be classified as grid cells in 36% of the cells (Yartsev et al., 2011). In humans, there have also been attempts to determine whether the entorhinal cortex contains grid cells (Doeller et al., 2010; Jacobs et al., 2013). Doeller et al. (2010) have accomplished this indirectly using functional magnetic resonance imaging (fMRI). They exploited the fact that if the entorhinal cortex contains grid cells, the neural population dynamics, as recorded by fMRI, would depend on whether the running direction of participants is aligned or misaligned with the main axis of the grid field. This would lead to systematic differences in blood oxygenation levels during the experiment, dependent on the running direction. These differences have been found in this study (Doeller et al., 2010) and provide indirect evidence. Another study, which used invasive recordings from several brain regions in human epilepsy patients (Jacobs et al., 2013), also identified cells with grid-like spatial receptive fields. In this study, participants performed a navigational task in a virtual environment while recordings were being made. A proportion of the cells in amygdala, cingulate cortex, frontal cortex, entorhinal cortex, hippocampus and parahippocampal gyrus had a gridness score significantly higher than chance, suggesting that in humans this kind of representation could be more widespread (Ja-

cobs et al., 2013). It should be noted, however, that grid fields of these cells appeared more noisy than in rodents (Hafting et al., 2005; Jacobs et al., 2013). Finally, another study found grid-like visual receptive fields in monkeys (Killian et al., 2012), although in the task monkeys only had to fixate in a visual field and did not have to perform any spatial navigation. The evidence that cells with grid firing fields are present in a variety of mammalian species could point to an important role of grid cells in spatial computation.

A grid field can be characterised by three basic parameters (Figure 1.1C; see also Barry and Burgess, 2014). The spacing is determined by the distance between the individual firing fields. Orientation is defined as the angle of one of the three main axes of the compound firing field. The phase of the grid field is defined as the offset of the field from a reference position. The distribution of the individual firing fields can also be characterised by fitting a template structure with more than three parameters (Yoon et al., 2013). The advantage of this technique is that it captures field distortions, such as stretching. In the context of this thesis, however, spacing, orientation and phase of the grid field are sufficient parameters for the analysis of the grid firing fields.

In rodents, the phase and orientation of grid firing fields is remarkably stable when experiments are repeated over the course of several minutes, hours or even between consecutive days. In rats, the spatial phase and orientation remains stable between consecutive trials (Hafting et al., 2005; Sargolini et al., 2006). In mice, the phase and orientation are stable even in trials separated by 24 hours, in the same experimental enclosure (Fyhn et al., 2008). The study in bats (Yartsev et al., 2011) did not report on the stability of grid fields. This apparent stability across environments could point to the grid cell population forming a universal spatial map that is independent of a particular environment.

Certain properties of grid cells are not uniform across the MEC but appear to be topographically organised, a feature that may enhance spatial coding (Fiete et al., 2008; Sreenivasan and Fiete, 2011; Mathis et al., 2012). Recordings from grid cells at different distances from the dorsal border of the MEC show that the spacing of the grid increases from the dorsal to ventral region both in rats (Hafting et al., 2005; Brun et al., 2008) and mice (Fyhn et al., 2008). This progressive increase in grid spacing, combined with treating grid cell responses as multi-modal tuning curves, has been considered as a basis for a residue number system coding of animal's position (Fiete et al., 2008). Such type of coding could be exploited to code much larger animal habitats than classical population codes, while also providing a certain degree of error correc-

tion capabilities (Fiete et al., 2008; Sreenivasan and Fiete, 2011). The residue number system coding relies on the fact that grid scale is quantised, a feature that has been observed experimentally (Barry et al., 2007; Stensola et al., 2012). The quantisation and progressive increase in grid spacing could also be used to substantially increase the precision of the grid cell population code with respect to the classical, single-peak tuning curve (Mathis et al., 2012). Thus, the nervous system could utilise the output of grid cells to efficiently encode spatial locations.

It has been shown that grid cells may also be important in forming a "map-like" structure of the environment. Hafting et al. (2005) performed experiments showing that in a two dimensional maze grid cells seem to be anchored to visual cues because the receptive fields of a single cell rotated together with visual cue rotation. However, an important aspect of this relationship is that the firing was not itself determined purely by visual stimuli. Hafting et al. (2005) also demonstrated that the firing fields persist in total darkness and that consistent hexagonally organised receptive fields could be formed in total darkness even without prior exposure to the environment with lights on. In addition, the distribution of grid phases seems to cover the entire recording enclosure (Hafting et al., 2005; Yoon et al., 2013). These properties suggest that animals, and possibly humans, could use their self-motion cues in order to construct a map-like representation of space. Thus, grid cells have been very influential in constructing some of the abstract, and more biophysically detailed models of spatial representation. Modelling work will be reviewed later in Section 1.2.

There are also other functionally identified cell types in the MEC. In all layers of the MEC, there are cells sensitive to head direction, as well as grid cells with conjunctive grid and head-direction sensitivity (Sargolini et al., 2006). Some cells respond only to borders of the experimental enclosure (Solstad et al., 2008; Bjerknes et al., 2014). These cells, together with grid cells, could also participate in forming spatial representations of the environment.

The presence of cells with grid firing fields in a variety of mammalian species could point to an important role of grid cells in spatial navigation. Entorhinal cortex itself is a part of a more extensive circuitry in the hippocampal region. In fact the output of the MEC cells projects into dentate gyrus and CA3, while the MEC also receives reciprocal connections back from hippocampal CA1 into deeper layers (Witter and Amaral, 2004) and possibly from CA2 directly to layer II (Rowland et al., 2013), although this has not been confirmed by more recent studies (Hitti and Siegelbaum, 2014). Therefore taken altogether, entorhinal cortex, and especially its medial part, can be viewed as a

brain region considerably involved in spatial navigation, and thus necessary to study both experimentally and by modelling work.

1.1.2 Cell types in layer II of the MEC

In order to study computations performed by grid cells in layer II of the MEC, it is necessary to be familiar with the organisation of the local circuits in this area. Layer II comprises several types of excitatory and inhibitory cells, and extensive work has been performed in mapping the connectivity between these cells, as well as their functional identification. In this section, I will therefore describe the findings of this work.

Layer II primarily consists of two types of principal neurons: spiny stellate cells and pyramidal cells (Alonso and Klink, 1993; Klink and Alonso, 1997). Stellate cells are electrophysiologically characterised by prominent, depolarisation-induced, subthreshold membrane potential fluctuations in the theta range (Alonso and Llinás, 1989; van der Linden and Lopes da Silva, 1998; Dickson et al., 2000; Erchova et al., 2004). Upon injection of a depolarising current, these neurons exhibit membrane potential fluctuations at a frequency similar to the theta range (4-10 Hz) (Alonso and Llinás, 1989) and possess theta frequency resonance properties (Erchova et al., 2004; Nolan et al., 2007; Pastoll et al., 2012). Stellate cells are the most abundant cell type in this layer, accounting for ~66% of cell bodies (Alonso and Klink, 1993; Gatome et al., 2010). The other principal neuron type, pyramidal cells, are also present in relatively high proportions (~32–39%)(Alonso and Klink, 1993; Gatome et al., 2010). Pyramidal cells, unlike stellate cells, do not have subthreshold theta-like oscillations and lack a strong, depolarisation-induced, sag potential (Alonso and Klink, 1993; Klink and Alonso, 1997).

Recent work by Varga et al. (2010) and Kitamura et al. (2014) has provided an important insight into the organisation of layer II in the MEC. Varga et al. (2010) have identified two types of cells in layer II. One of them, a population of calbindin positive cells, projected extrahippocampally, to the contralateral MEC. However, more recent work suggests that these cells project to the CA1 region of the hippocampus (Kitamura et al., 2014). The other population, positive for reelin, projects to the dentate gyrus of the hippocampus. These two populations had distinct morphological and electrophysiological properties (Varga et al., 2010). The work of Kitamura et al. (2014) later corroborated these results and further identified that the reelin positive cells have electrophysiological characteristics of stellate cells, while pyramidal cells were identified

as those expressing calbindin. Thus, stellate cells are very likely to form the perforant path to the hippocampus, while calbindin positive cells are the pyramidal cells.

Progress has been made in functionally characterising the cell types in the superficial layers of the MEC. Zhang et al. (2013) performed recordings from freely moving rats that expressed Channelrhodopsin-2 (ChR2) selectively in hippocampus-targeting neurons in layer II and III. This allowed them to identify these neurons *in vivo*, while at the same time determining their spatial firing fields. They found that the cells that project to the hippocampus are formed by a variety of spatially selective cells: grid, border, head direction, and conjunctive grid $\times$ head-direction cells. Also a large proportion of these projection neurons had irregular spatial firing fields and no spatial selectivity (Zhang et al., 2013). Burgalossi et al. (2011) obtained evidence from juxtacellular recordings that both stellate and pyramidal cells in layer II of the MEC have repeating spatial firing fields in an O-shape arena. At the time of the recordings, the arenas were novel to the animals. However, because these recordings were of short duration and were not in an open arena, it is not clear whether the cells' firing fields were grid-like. More recently, *in vivo* whole cell recordings have also demonstrated that both stellate and pyramidal cells in layer II have multi-peaked firing fields when mice navigated in linear virtual environments (Domnisoru et al., 2013; Schmidt-Hieber and Häusser, 2013). Thus, both stellate and pyramidal cells in superficial layers of the MEC could participate in the microcircuit that forms spatially and directionally selective cells. These include grid, head-direction, border, and conjunctive grid $\times$ head-direction cells.

The functional properties of grid cells in superficial MEC depend upon their dorsoventral position. Namely, as recording location progresses from dorsal to ventral, the spacing between the firing fields increases (Brun et al., 2008). Interestingly, it has also been shown that some of the intrinsic properties of stellate cells vary along the dorso-ventral axis (Garden et al., 2008; Giocomo and Hasselmo, 2008b; Pastoll et al., 2012), suggesting a possible link between the cellular properties of stellate cells and their functional response. Earlier and more recent work has suggested that the spacings between grid fields in individual animals have a tendency to cluster (Barry et al., 2007; Stensola et al., 2012). Stensola et al. (2012) showed that the discretized progression in spacing in individual animals is part of a modular structure of grid spatial representations in the MEC, since the main properties of the firing fields, such as spacing and orientation, as well as their distortions, are clustered together. Whether there is any discreteness in the cellular properties of stellate cells is currently not known. Thus,

it is not yet clear whether this modular functional organisation reflects discrete cell populations.

In summary, superficial layers of the MEC contain cells with various spatial and directional tuning properties. The spatial tuning properties have a modular structure and in grid cells the spacing between grid fields increases along the dorso-ventral axis of the MEC. In layer II specifically, spiny stellate cells are the most abundant cell type. Grid cells are also most abundant in this layer. Thus, it is likely that stellate cells will be a major contributor to the grid cell microcircuit.

1.1.3 Cells in deeper layers of the MEC

Deeper layers of the MEC contain spatially and directionally modulated cells as well, albeit with different proportions than layer II. Grid cells are present in other layers of the MEC, not only in layer II, although they are not as abundant (Sargolini et al., 2006). This is relevant for two reasons; first, they may be encoding different information to layer II grid cells, and second they may provide input to layer II grid cells. Cells classified as pure grid cells, i.e. those that are not sensitive to head direction, are mostly present in layers II and III, while deeper layers contain grid cells intermingled with head-direction cells or cells with conjunctive properties, i.e. cells whose firing rate is sensitive to both location in space and head direction (Sargolini et al., 2006). Deeper layers of the MEC also contain border cells (Solstad et al., 2008; Bjerknes et al., 2014).

A number of anatomical (Köhler, 1986; van Haeften et al., 2003) and functional studies (Jones, 1994; Kloosterman et al., 2003) suggest that deep layers have extensive projections to the cells in superficial layers (for a review see Canto et al., 2008). Since the deep layers contain mostly head direction-modulated cells it is reasonable to assume that cells that form the grid cell microcircuit in layer II or perhaps layer III receive input from head direction cells. As we will see in the modelling section, this is consistent with some of the mechanisms of bump attractor models that utilise a form of head directional information for generating grid firing fields (see Section 1.2.3 for a review of the attractor models). The projections from border cells in deep layers to layer II could also provide spatial information to the local microcircuit in layer II.

1.1.4 Feedback inhibition between stellate cells in the MEC

Layer II is the part of the MEC where grid cells are the most prevalent (Hafting et al., 2005; Sargolini et al., 2006; Fyhn et al., 2008). As discussed previously, stellate cells in layer II have been identified as grid, head-direction, and border cells (Zhang et al., 2013) and form the perforant path to the hippocampus (Varga et al., 2010; Kitamura et al., 2014; Burgalossi et al., 2011; Burgalossi and Brecht, 2014). Thus, most of the work that has attempted to systematically determine the synaptic organisation between grid cells has focused on layer II, stellate cells, and accompanying cell types (Dhillon and Jones, 2000; Pastoll et al., 2013; Couey et al., 2013).

The first study to systematically investigate the connectivity in MEC used paired recordings in layers II, III, and V (Dhillon and Jones, 2000). Most importantly, the study revealed that stellate cells in layer II lack direct excitatory connections between each other. Another study (Kumar et al., 2007) showed, by glutamate uncaging in layer II, the presence of direct excitatory feedback connections between stellate cells. However, since glutamate uncaging is not specific to any cell type, it is possible that other excitatory cells (e.g. pyramidal cells) were stimulated in this study. A more direct method of determining the local connectivity was performed by Pastoll et al. (2013). Here, the authors were able to probe a much higher number of possible connections than possible with paired recordings. Pastoll et al. (2013) used a mouse line that allowed for the expression of Channelrhodopsin-2 (ChR2) only in stellate cells and fast spiking (FS) interneurons in layer II, but not in pyramidal cells. This allowed for controlled optical stimulation of only ChR2-expressing cells. When recording from stellate cells while at the same time driving them to spike, no excitatory responses were observed. Given that several thousand possible connections were tested, with a 95% confidence, they found that the probability that a pair of stellate cells in layer II is connected is less than 1.5×10^{-3} (Pastoll et al., 2013). The evidence from Pastoll et al. (2013) thus supports the results of Dhillon and Jones (2000).

The experiment in Pastoll et al. (2013) showed, at the same time, that when stellate cells and FS interneurons were stimulated, stellate cells received abundant inhibition. This inhibition was mediated by the FS interneurons. At the same time during the light-induced activation of the network FS interneurons received strong synaptic excitation. Thus, the study showed that stellate cells, likely to be grid cells, are immersed in an inhibitory network, and communicate with each other only via feedback inhibition.

Couey et al. (2013) focused specifically on the development of inhibitory connec-

tivity in layer II and similarly, they found that stellate cells communicate with each other only via FS interneurons. Moreover, the authors reported that the inhibitory connections undergo a process of maturation. In young mice, there were sparse excitatory synapses between stellate cells, which completely disappeared by P22. By that time, the total number of inhibitory connections increased rapidly (Couey et al., 2013). In the study, Couey et al. were also able to perform simultaneous recordings of stellate and pyramidal cells. This revealed possible monosynaptic connections from stellate cells to pyramids, but again, no connections from the direction of pyramids could be detected. This work thus collectively establishes that stellate cells in layer II of the MEC are immersed in an inhibitory network, a feature that might be important for the generation of grid firing fields (Moser et al., 2014).

The lack of direct excitatory-excitatory connections between stellate cells in layer II puts this layer in a unique position. In the other layers of MEC, there are abundant direct excitatory connections between pyramidal cells (Dhillon and Jones, 2000), and in neocortex, it is common to find direct connectivity between pyramidal cells (Deuchars et al., 1994; Feldmeyer and Sakmann, 2000; Markram et al., 1997), and also between spiny stellate cells (Feldmeyer and Sakmann, 2000). As we will see later, this lack of excitatory connections creates important constraints on the models of grid cells and as a result grid cell models that incorporate the connectivity constraints provide interesting predictions about the firing fields of interneurons in MEC layer II.

1.1.5 Oscillatory neural activity in the MEC

Oscillatory neural activity can be observed at network level, recorded either by non invasive scalp electrode recordings (EEG), or by invasive local field potential recordings (LFP). The oscillatory activity in this case reflects an averaged population activity over a localised region. Oscillatory activity is present in many brain areas, including visual cortex (Henrie and Shapley, 2005), hippocampus (Colgin and Moser, 2010; Skaggs et al., 1996), entorhinal cortex (Chrobak and Buzsaki, 1998; Cunningham et al., 2003) and others. The frequency range is wide, ranging from very slow periods (< 1 Hz), to ultra fast oscillations (200-600 Hz) (Buzsáki and Draguhn, 2004).

There is a wealth of experimental and modelling work, spanning several decades of research, and therefore providing a complete literature review of only a subset of the types of oscillations present in different cortical and subcortical regions in mammalian species is beyond the scope of this thesis. However, I will briefly mention several types

of oscillatory activity to motivate the work in this thesis. I will focus on theta (4-10 Hz) and gamma (30-100 Hz) oscillations present in entorhinal cortex, since the oscillations in these frequency ranges are central to this work.

1.1.5.1 Theta and gamma activity in the entorhinal cortex *in vivo*

In rodents the entorhinal cortex *in vivo* exhibits prominent theta (4-10 Hz) and gamma (30-100 Hz) power peaks in LFP spectrograms during exploratory behaviour and anaesthesia (Chrobak and Buzsaki, 1998; Quilichini et al., 2010). Chrobak and Buzsaki (1998) recorded LFPs from superficial layers of the entorhinal cortex. In layer II-III, they found theta oscillations with highest power in the range of 6-12 Hz. Superimposed on the theta troughs, gamma LFPs could be seen, whose amplitude was also modulated by theta. In another study, Quilichini et al. (2010) recorded in anaesthetised rats in the entorhinal cortex again, and found a similar relationship to Chrobak and Buzsaki (1998). It should be noted that simply summing two independent oscillations with different frequencies together does not produce modulation of gamma amplitude by theta phase. Rather, this interaction is known as a type of cross-frequency coupling (CFC; e.g. Jensen and Colgin, 2007), or phase-amplitude coupling (PAC), and has been suggested to play a role in cognitive functioning of the nervous system (Canolty and Knight, 2010). Figure 1.2 shows an example of PAC between an 8 Hz theta and 90 Hz gamma oscillation.

Extracellularly recorded single unit activity was also analysed in the studies of Chrobak and Buzsaki (1998) and Quilichini et al. (2010). The main result was phase-locked discharge of single neurons with respect to both theta and gamma. Principal cells (spiny stellate neurons and pyramidal cells) in layer II seem to discharge at the trough of theta. Interneurons in superficial layers also tended to be phase locked to the theta signal (Quilichini et al., 2010). Although the measurements of Quilichini et al. (2010) were noisy, the discharge of both principal cells and interneurons in all layers of entorhinal cortex tended to be phase-locked to the trough of the gamma cycle as well.

A study by Colgin et al. (2009) investigated communication between the hippocampus and MEC mediated by coherence between fast and slow gamma in these regions. The authors showed that high frequency gamma oscillations in hippocampal CA1 (~65–140 Hz, fast gamma) are coherent with fast gamma oscillations in the MEC (~90 Hz). At the same time, slow gamma oscillations in CA1 (~25–50 Hz) were coherent with slow gamma in CA3. Coherence between oscillations has been suggested

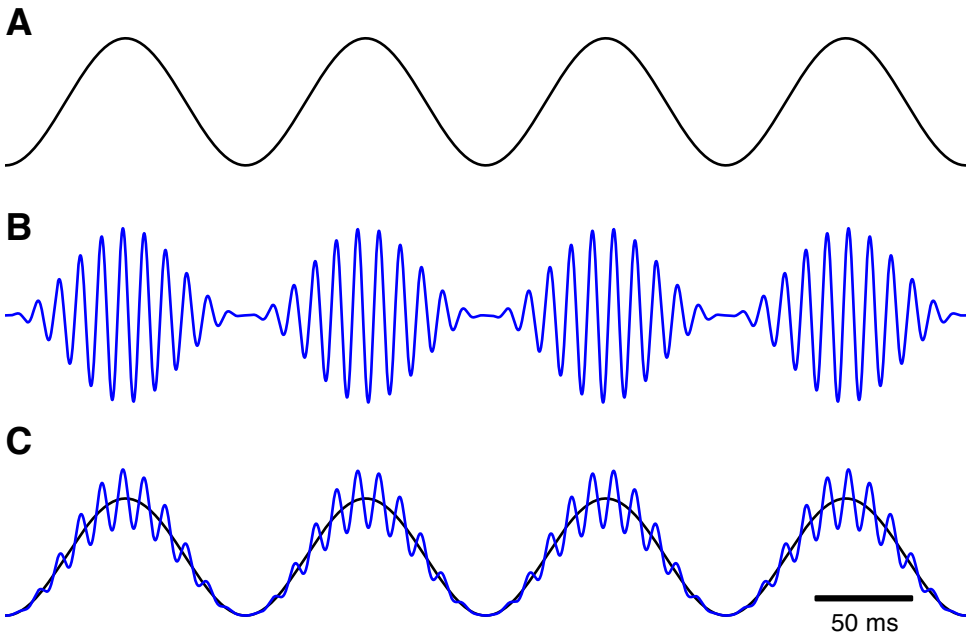

Figure 1.2: **Phase-amplitude coupling of idealised theta and gamma oscillations.** Illustration of 4 theta cycles (8 Hz) **(A)**, a gamma oscillation (90 Hz) whose amplitude is modulated by the phase of the theta signal **(B)**, and a superposition of both signals (blue) together with the theta signal (black) **(C)**. In (C) the maximal amplitudes are different from (A) and (B).

to play a role in selective information transfer between two or more brain areas (Fries, 2005, 2009; Akam and Kullmann, 2012). Thus, these experimental data suggest that the presence of PAC and associated neural dynamics, such as phase locking to theta and gamma in the MEC and hippocampus, could be relevant for communication between two or more brain areas, in that the strength of coupling between the two areas could be mediated by their mutual oscillatory coherence.

1.1.5.2 Persistent gamma in the entorhinal cortex *in vitro*

Gamma activity can also be evoked *in vitro*. Application of kainate to entorhinal cortical slices induces a long lasting oscillation in the gamma range (Cunningham et al., 2003, 2004). The oscillation remains active even for several hours, and thus this kind of activity is termed "persistent gamma oscillation". In the entorhinal cortex, antagonists of GABA and AMPA receptors, as well as gap junction blockers, decrease the power of these oscillations (Cunningham et al., 2003, 2004). Stellate cells in layer II and pyramidal cells in layer III discharge at a frequency much lower than the observed

gamma rhythm (stellate and pyramidal cells: ~0.5 and ~5 Hz, respectively, gamma: ~46 Hz in superficial layers of MEC), while interneurons discharge at the frequency of the field gamma oscillation (~45 Hz; Cunningham et al., 2003).

The frequency of persistent gamma oscillations in entorhinal cortical slices can be switched between two induced frequencies, ~40 and ~30 Hz, by the N-methyl-D-aspartate (NMDA) receptor blocker (Middleton et al., 2008). The mechanism may depend on the presence of two populations of interneuron subtypes: basket and goblet cells. Goblet cells differ from basket cells in morphology and their intrinsic properties, and are located in layer III of the MEC. Middleton et al. (2008) suggested that the basket cell-dependent oscillations are primarily mediated by NMDA receptors, while goblet cells are not, and thus, block of NMDA receptors disrupts the faster, approximately 40 Hz rhythm. The faster rhythm is replaced by a slower frequency rhythm mediated by goblet cells. The experimental results have been reproduced by a model that replicated the connectivity between stellate, pyramidal and inhibitory cells in the superficial layers (Middleton et al., 2008).

There are a number of differences between gamma activity observed *in vivo* and persistent gamma. As mentioned previously, the frequency of persistent gamma activity is lower than gamma oscillations observed in superficial layers of the MEC in behaving animals (~90 Hz; Chrobak and Buzsaki, 1998; Colgin et al., 2009). Unlike *in vivo* (Quilichini et al., 2010), no clear peak at theta frequency was observed during kainate induced gamma, although the persistent gamma power was modulated at theta frequency (Cunningham et al., 2003). The lack of a clear theta signal is consistent with evidence that the theta signal might be originating from medial septum (Green and Arduini, 1954; Petsche et al., 1962; Stumpf et al., 1962; Brandon et al., 2011; Koenig et al., 2011). Cunningham et al. (2003) instead attributed the theta modulation of persistent gamma power to subthreshold theta oscillations in stellate cells, since the subthreshold oscillations were correlated with the observed theta modulation of the field gamma activity, and the modulation was abolished when the subthreshold membrane oscillation was blocked pharmacologically (Cunningham et al., 2003).

1.1.5.3 Light-activated nested gamma oscillations in the slices of MEC

Pastoll et al. (2013) used the expression of ChR2 in stellate cells and in FS interneurons in layer II to investigate the dynamics of these two populations during light activation. When both populations were activated by theta frequency (8 Hz) optical stimulation, nested gamma frequency oscillations were observed in recordings of membrane cur-

rents from both cell types, as well as from adjacent LFP recordings in the slice. The frequency of the nested gamma activity found by Pastoll et al. (2013) was in the range of ~62–100 Hz, similar to the frequency of nested gamma oscillations observed in the MEC of behaving animals (Chrobak and Buzsaki, 1998; Colgin et al., 2009) (Figure 1.3A,B). Both stellate cells and FS interneurons fired action potentials during the activation phase of theta cycles (Figure 1.3C; see also Pastoll et al., 2013), and their phase relationship to theta and between each other was also similar to that recorded from behaving animals (Chrobak and Buzsaki, 1998; Mizuseki et al., 2009; Pastoll et al., 2013).

In addition, the experiment in Pastoll et al. (2013) established that antagonists of GABA receptors substantially reduced nested gamma oscillations in stellate cells, while antagonists of ionotropic glutamate receptors abolished theta nested gamma oscillations in both stellate cells and FS interneurons. Therefore, theta nested gamma oscillations in this experiment require participation of synaptic activity of both populations.

The involvement of stellate cells and FS interneurons in generation of theta-nested gamma oscillations was further demonstrated by cross correlation analysis of membrane currents of neurons from both populations (Pastoll et al., 2013). The analysis showed that excitation from stellate cells preceded inhibition from FS interneurons by a few milliseconds. This demonstrated that the activity is initiated by stellate cells, which triggers inhibition by the FS interneurons, which then closes the inhibitory feedback loop onto the stellate cells. The timing of the firing of action potentials by stellate cells was near the trough of the gamma cycle, shortly followed by inhibitory spikes from the FS interneurons (Pastoll et al., 2013), similarly to timing during exploratory behaviour (Chrobak and Buzsaki, 1998). These data therefore suggest that a mechanism mediated by FS interneurons could be responsible for the generation of theta-nested gamma oscillations *in vivo*.

1.1.6 Path integration

What is the computational role of the MEC? One possibility raised soon after the discovery of grid cells is that the MEC performs path integration. Path integration is a process whereby an agent is able to estimate its position solely by integrating information derived from self motion cues, without the use of landmarks. Informally, path integration can be described as successive additions of movement signals onto

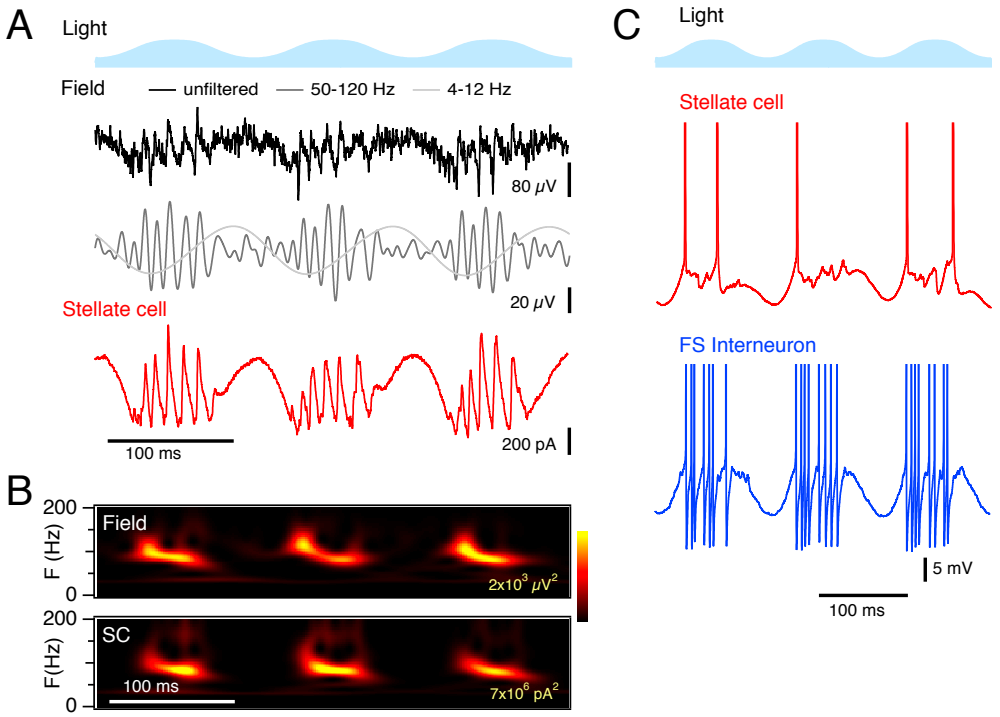

Figure 1.3: **Theta frequency stimulation enables nested gamma oscillations**. **(A)** Example of LFP activity and membrane current recorded from a stellate cell during 3 theta cycles induced by an 8 Hz optical stimulation. The LFP trace is also shown band-pass filtered to illustrate the theta and gamma signals. **(B)** Wavelet transforms of the LFP (top) and synaptic (bottom) activity corresponding to panel (A). Colour plots show power corresponding to each frequency as a function of time. The power corresponding to the maximum of the colour scale is indicated in the bottom right of the plot. **(C)** Action potentials fired by an example stellate cell and FS interneuron recorded simultaneously during the theta stimulation, illustrating that both neuron types fire action potentials on the phase of the theta cycle at which nested gamma oscillations are observed. *(The data are part of Figure 1 from Pastoll et al. (2013), with permission.)*

a continually updated representation of direction and distance from the starting point (Etienne and Jeffery, 2004). Formally, we can define the representation of position as an integral (sum) $\mathbf{p} = \int_0^T \mathbf{v}(t)\,\mathrm{d}t$, which results in the estimate of the actual position vector $\mathbf{p}$.

Currently, there is no consensus about the neuronal mechanism of path integration and experimental work on path integration in mammals is not itself conclusive, although much progress has been made (Mittelstaedt and Mittelstaedt, 1980; Etienne and

Jeffery, 2004). Lesion studies mostly support the idea that vestibular signals are necessary for correct orientation and navigation without visual landmarks (Cohen, 2000; Stackman and Herbert, 2002; Wallace et al., 2002). However, the concrete mechanisms of how vestibular signals contribute to path integration are missing.

A study on gerbils (Mittelstaedt and Mittelstaedt, 1980) devised an experiment that tests some aspects of path integration. In this experiment, a female gerbil collects its pups that have been displaced from the nest into a shallow cup in the centre of a circular arena. This arena could be rotated independently of the cup. In control conditions, the subject can return to the nest on a straight line connecting the cup and the nest, after having collected the displaced pup. However, when the mother was in the cup with its pups, in total darkness, and the rest of the arena was rotated quickly around, the mother returned to the original position where the nest had been. If the cup was rotated very slowly, under the threshold of detection by the vestibular system, the nest was missed precisely by the amount of rotation (Mittelstaedt and Mittelstaedt, 1980). The same effects were observed if the cup with the mouse on it was shifted sideways, i.e. its homing path was also displaced by the amount of the shift. These results are a direct evidence that gerbils use vestibular information to estimate their directional heading.

In another study, related to place cells, rats were trained to either walk on a circular track or pressed a lever that operated a car on this track, or experienced a pseudo-motion, in which the animal was stationary and the environment was rotated (Terrazas et al., 2005). Recordings from place cells have shown that in the case of passive and pseudo-movement, the place fields appeared wider, and the overlap between them increased. The authors attributed this to a decrease in the gain of the self-motion velocity signal, and so the animal perceived these types of "movement" as slower, moving on a track with smaller diameter (Terrazas et al., 2005). These results suggest that self-motion signals might affect spatial representations in hippocampus.

Another study related to hippocampal place cells addressed how visual and self-motion cues combine together and influence place fields in CA1 (Chen et al., 2013). In this study rats were trained to run on a linear track in a virtual environment (VE), while either the visual information was manipulated (by removing salient cues) or the animals were forced to stand still on the treadmill, while simulated motion was being played on the screen. The authors found a variety of place cells that were differently sensitive to these manipulations. Some cells maintained their place field even in the absence of salient visual cues, another set of place cells required a subset or a combination of visual cues. Also, when the gain of self-motion cues was halved (i.e the animal

had to run twice the physical distance on the treadmill to cover the original distance in the VE), a certain proportion of place cells recorded shifted their firing fields closer towards the starting point of the linear track. These results thus demonstrated that both self-motion and visual cues can influence spatial representations in the hippocampus and that these two types of information can also be combined together, although non-linearly (Chen et al., 2013).

Thus, while the available information about the presence of path integration in mammalian nervous systems is currently not conclusive, from the experimental studies so far it is evident that animals use some form of self-motion signals in order to update their representation of position in the environment, and to successfully navigate when salient landmark cues are not present.

Grid cell responses have been suggested to be consistent with the outcome of a path integration process (Moser et al., 2014), in that their firing fields can express distance from a reference position (Derdikman et al., 2009; Moser et al., 2014). Moreover, the hexagonal firing fields are stable in two dimensional environments, while their phase can only be realigned when place fields undergo global remapping (Fyhn et al., 2007), suggesting that grid cells form a universal spatial map that is independent of the environment. These properties collectively point to the MEC as a brain region that could perform path integration.

1.2 Models of grid cells

In this section, I will review the modelling work that attempted to reproduce the firing fields of grid cells in the MEC (Hafting et al., 2005; Sargolini et al., 2006; Fyhn et al., 2008; Buetfering et al., 2014). I will describe three classes of grid cell models. Two of them are the oscillatory interference models (Burgess et al., 2007) and continuous attractor network models (Fuhs and Touretzky, 2006; Burak and Fiete, 2009; see also Zilli, 2012 for a comprehensive review). The working hypothesis in these two classes is that grid cells perform path integration by integrating a velocity input that is translated into the activity of either a single cell or populations of grid cells that collectively represent the grid-like tuning curves. The third class are models that postulate that grid cells do not perform path integration (Kropff and Treves, 2008) or that the grid cell circuit integrates inputs from path integrators located upstream (Pilly and Grossberg, 2012, 2013).

1.2.1 Oscillatory interference models of grid cells

The oscillatory interference model is based on the idea that spatial firing patterns of grid cells arise from interference of at least two oscillators with frequencies controlled by the velocity of an animal. The interference between the oscillators generates a repeating spatial firing pattern.

All of the oscillatory interference models that have been proposed to date are based on the path integration principle outlined in Section 1.1.6. Originally, the interference model was based on the idea that theta-phase precession of hippocampal place cells (O'Keefe and Recce, 1993) is the mechanism of path integration. After their discovery, place cells have been suggested to constitute an animal's "cognitive map" due to the fact that their firing fields can synergistically encode the location of the animal (O'Keefe and Dostrovsky, 1971). Moreover, the rate coded place fields are complemented by a so called "phase code", by which the times of action potentials of place cells during traversals are phase-locked to the ongoing theta rhythm. In a standard experiment, a rat runs along a linear track, while place cells are being recorded from. Thus, when the animal enters the place field, the cell spikes at progressively later phases of the theta cycle, with the phase progressing as the animal runs towards the end of the field (O'Keefe and Recce, 1993). This happens independently of the firing rate of the place cell.

To account for place cell firing and phase precession, O'Keefe and Recce (1993) proposed a simple model that consisted of two theta frequency oscillators with slightly different frequencies. Let us assume that the frequency of the first oscillator is 9 Hz and that of the second one is 11 Hz (O'Keefe and Recce, 1993). When these oscillators interfere together, the resulting signal will be a combination of a 10 Hz oscillation modulated by a 1 Hz envelope. If this interference signal represents the membrane potential of a place cell, the cell will fire only on the peaks of the envelope pattern. Moreover, action potentials of the cell will precess with respect to the theta signal and thus account for phase precession.

While place cells normally have only a single firing field, the model presented in O'Keefe and Recce (1993) predicts that the firing fields are repeating. This prediction did not fit with the data on place cells. Thus, when grid cells were discovered (Fyhn et al., 2004; Hafting et al., 2005), with their strikingly regular firing fields, the repeating firing fields of the oscillatory interference model received new attention. Since grid cells in the MEC also show phase precession (Hafting et al., 2008), the attention turned

to building a model that postulates that phase precession is the underlying mechanism of path integration and grid firing.

The original version of the interference model on a linear track (O'Keefe and Recce, 1993) was subsequently generalised to two dimensions (Burgess et al., 2007). In general, the interference model can be stated as a firing rate of the cell being a product of n velocity controlled oscillators (Burgess et al., 2007):

$$f(t) = \Theta(\prod_{i=1}^{n}(\cos\{[w_s + \beta s\cos(\phi - \phi_i)]t + \varphi_i\} + \cos w_s t)) \tag{1.1}$$

$$\Theta(x) = \begin{cases} x & x > 0 \\ 0 & \text{otherwise} \end{cases}$$

Here, w_s is theta frequency, s is running speed, ϕ is running direction, ϕ_i is the preferred direction, φ_i is the phase offset of the i^{th} dendritic input, β is a positive constant, and Θ is the Heaviside function. When there are at least 2 velocity controlled oscillators with preferred directions 60° apart, the spatial interference will produce grid-like firing fields.

An earlier work that demonstrated subthreshold membrane potential oscillations of stellate cells in layer II of the MEC (Alonso and Llinás, 1989; van der Linden and Lopes da Silva, 1998; Dickson et al., 2000; Erchova et al., 2004) provided correlative evidence in support of the interference mechanism. This is consistent with the main hypothesis of the oscillatory interference model, which states that that velocity-dependent dendritic oscillators interfere with a basal, somatic oscillator beating at theta frequency (Burgess et al., 2007).

The oscillatory interference model provides a number of interesting predictions that are directly testable experimentally. Firstly, the model predicts that the EEG theta frequency scales linearly with running speed (Jeewajee et al., 2008). Indeed, Jeewajee et al. (2008) showed that theta frequency is an increasing function of running speed. However, the relationship in the experiments was not exactly linear. The frequency deviated from linear when the animal's speed was below 5 cm/s, while at high speed it saturated (Jeewajee et al., 2008). The model also qualitatively predicts that the firing rates of grid cells increase with running speed and this has also been confirmed (Jeewajee et al., 2008). The data also show that the theta frequency and firing rates of cells scale down with increasing spacing between grid firing fields, which is another prediction of the model.

Another line of evidence supporting the interference mechanism comes from recordings of the membrane potential fluctuations from stellate cells in MEC layer II (Gio-

como et al., 2007; Pastoll et al., 2012). These experiments have shown that theta frequency of subthreshold fluctuations decreases with the distance from the dorsal border. Since the grid spacing increases as a function of this distance (Brun et al., 2008), the theta frequency thus decreases as a function of grid spacing. Similar observations have been found for the resonant frequency in stellate cells, which is the frequency where membrane potential impedance is maximal when a sinusoidal current with smoothly increasing frequency is injected (Giocomo et al., 2007; Pastoll et al., 2012). This is consistent with the prediction of the interference model (Burgess, 2008). However, later work has shown that the subthreshold fluctuations of stellate cells are not rhythmic, but rather a result of stochastic fluctuations (Erchova et al., 2004; Dodson et al., 2011).

While the above evidence supports the plausibility of the oscillatory interference mechanism, it has been shown that the mechanism by which several dendritic, velocity-coupled oscillators interfere with each other to produce the grid fields is implausible. Firstly, Remme et al. (2010) showed, by simulating a detailed model of a stellate cell, that there is a strong dendritic coupling that results in phase locking of the dendritic oscillators. As a result, the activity of the simulated grid cell could not produce stable grid fields in a time scale of 5 minutes. Another study (Giocomo and Hasselmo, 2008a) investigated the effect of frequency noise on the stability of grid firing fields in the interference model, showing that the presence of even a very small amount of frequency noise disrupts grid firing fields completely (Giocomo and Hasselmo, 2008a). Moreover, it is now clear that the subthreshold membrane potential fluctuations in stellate cells are rather the result of stochastic fluctuations and thus are unsuitable for an implementation of a stable theta frequency oscillator (Dodson et al., 2011). Thus, the oscillatory interference model, under the hypothesis of long term velocity integration, is in its basic form implausible. On the other hand, the dendritic "democracy-independence" principle, as stated by (Remme et al., 2010) is relevant to only oscillators in different dendrites and efforts have been made to make the velocity coupled oscillators more independent. This can be achieved by synaptically coupling several independent velocity controlled oscillators together and feeding their spiking output into the putative grid cell or a network of thereof (Burgess et al., 2007; Burgess, 2008; Zilli and Hasselmo, 2010). Such velocity controlled oscillators have been found by Welday et al. (2011). Another attempt to ameliorate the divergence of phases of the velocity controlled oscillators was to entrain the baseline frequency of the oscillators to their mean frequency (Burgess and Burgess, 2014). This was implemented in a spiking attrac-

tor network model using the neural engineering framework (Eliasmith and Anderson, 2004). This amendment provided for error correction in the divergence of the oscillator phases. Another way how to correct for the phase divergence is to correct for the path integrator drift by place cell input, as suggested by O'Keefe and Burgess (2005) and Burgess et al. (2007). In addition, recent *in vivo* recordings of cells in bat medial entorhinal cortex have demonstrated the presence of grid-like firing fields in the absence of theta oscillations in this region, suggesting that the oscillatory interference model might be limited to rodent species. Finally, *in vivo* intracellular recordings from grid cells in mice suggest that the drive to spike when the animal is traversing through the grid field is generated by slow ramp and not by changes in the amplitude of the theta oscillation, as would be predicted by the interference model (Domnisoru et al., 2013).

1.2.2 Non-path integration and hybrid grid cell models

The oscillatory interference model explains the mechanisms of path integration and theta phase precession. Here I describe two models of grid cells which do not adopt the hypothesis that the grid cell circuit performs path integration. The first one, based on adaptation, was proposed by Kropff and Treves (2008). The model comprises a set of grid cells with firing rate adaptation. Grid cells receive input from place cells. The model, through Hebbian learning, learns synapse strengths from place cells to grid cells, by employing firing rate adaptation and competition between grid cells. The resulting firing fields have a range of gridness scores and orientations (Kropff and Treves, 2008). Interestingly, the networks in this model can achieve a relatively acceptable distribution of gridness scores even when clean, Gaussian-like place cell inputs are replaced with more general spatially modulated fields. Therefore, even despite the fact that there are a few unresolved issues with this model, such as (i) the need for adaptation and (ii) a relatively hidden competition between the cells, the model by Kropff and Treves (2008) emphasises the role of non-path integration mechanisms in the formation of grid firing fields.

The second type of model (Pilly and Grossberg, 2012, 2013), hypothesises that grid cells integrate spatial information from the so called "stripe cells". Stripe cells have band-like firing fields, in which the orientation and spacing between the bands of activity can vary. They can be interpreted as a one dimensional realisation of velocity integration in 2D space along a single direction. The grid cell model is a complex cooperation of angular and linear velocity integration, in which grid cells in the superficial

layers of the MEC self-organise using a variant of a competitive Hebbian learning rule (Grossberg, 1976; Grossberg and Seitz, 2003; Pilly and Grossberg, 2012). Interestingly, this model predicts gradients in the synaptic integration properties of grid cells along the dorso-ventral axis found in Garden et al. (2008). Namely, dorsal cells prefer co-activation of inputs that reoccur, on average, at a smaller temporal interval, while ventral cells prefer the opposite (Pilly and Grossberg, 2013). These predictions are consistent with the observed gradients in synaptic integration found by Garden et al. (2008). Recently, experimental evidence has suggested that stripe cells are present in the MEC (Krupic et al., 2012, referred to as band cells). This provides evidence in favour of the model of Pilly and Grossberg (2012). Thus, the model presents an alternative mechanism to the all-in-one path integration idea of the 2-dimensional attractor model presented here and elsewhere.

1.2.3 Continuous attractor models of grid cells

Grid cells have been suggested to compute their repeating firing fields by the means of a continuous attractor network. In the simplest case, a continuous attractor network encodes a one-dimensional continuous variable, such as a position on a linear track. Each neuron in the network is assigned a preferred value of the encoded variable. The connectivity between neurons is assigned so that neurons that encode close-by values mutually excite each other, while neurons with dissimilar values inhibit each other. The connectivity is arranged so that the synaptic strength between two neurons depends only on the difference between the preferentially encoded values of the neurons. In this way, the network can exhibit a continuum of stable states, each of them shifted by a small amount. The activity of the neurons resembles a “bump”, and the population as a whole encodes the one-dimensional variable (Amari, 1977; McNaughton et al., 2006).

All of the current attractor network models of grid cells are at a conceptual level closely related to earlier work either on orientation tuning curves in visual cortex (Ben-Yishai et al., 1995; Somers et al., 1995), work on persistent activity during working memory tasks (Amit and Brunel, 1997; Camperi and Wang, 1998; Wang, 1999; Compte et al., 2000) or from the modelling work on angular integration in the head direction system or on path integration of place cells (Taube et al., 1990a; Zhang, 1996; Xie et al., 2002; Song and Wang, 2005; Boucheny et al., 2005). These models are extensions of the firing rate models first introduced by Amari (1977), the first models

to predict spatially localised neural firing patters such as bump attractors.

In the context of neural representations of space, continuous attractors were extended to two dimensions and first applied to model the firing fields of place cells (Samsonovich and McNaughton, 1997) and path integration (Conklin and Eliasmith, 2005; Eliasmith, 2005). The modellers, however, faced a significant issue, in that the continuous attractor model predicted that the firing fields of neurons repeat in space. While this is not an issue for the models of orientation tuning and head-direction cells, place cells only have a single firing field, at least over distances of only a few meters (O'Keefe, 1976; Leutgeb et al., 2005).

After the grid cell discovery (Hafting et al., 2005; Fyhn et al., 2004) the attractor network theories of path integration radically shifted from place cells to grid cells. Thus, all of the attractor models of grid cells are based on a premise that the attractor network performs the path integration mechanism, hence translating estimates of animal's velocity into a substrate that codes for spatial position, i.e. a grid field.

Perhaps the first work that intentionally reproduced the hexagonally repeating firing fields of grid cells was a model by Fuhs and Touretzky (2006). The authors built an attractor network with local excitatory-inhibitory interactions that comprised two parts: the symmetric part was used to establish the attractor state, while the asymmetric part of the connectivity function enabled bump movement on the neural sheet. The symmetric connections were composed of local excitatory and longer range inhibitory interactions that were translationally invariant. For the asymmetric part, it was assumed that neurons in the network population were preferentially excited by head direction cells with different preferred directions. The outgoing synaptic connections of the neurons were thus shifted, with the direction of the shift corresponding to the preferred direction of the head direction cell connected to each neuron. This allowed for a velocity-dependent movement of the bump attractor in the network. Using a simplified simulated movement of an animal, the authors demonstrated that these networks are capable of path integration.

However, the model in Fuhs and Touretzky (2006) has certain limitations. It has been shown that the network does not produce grid firing fields when the velocity integration occurs over longer, realistic animal trajectories ($\approx$200 m), which is a usual distance travelled by rats in experimental settings (Burak and Fiete, 2006; Hafting et al., 2005). By performing additional analysis on the model by Fuhs and Touretzky (2006), Burak and Fiete (2006) demonstrated that the loss of grid firing fields was due

to rotations of the hexagonal pattern of bumps[1] and due to the non-linear response of bump movement as a function of animal velocity. This limited the accuracy of path integration in Fuhs and Touretzky (2006). In their subsequent work, Burak and Fiete (2009) presented a similar model, that was able to accurately integrate velocity inputs for realistic trajectories and behavioural time ranges (Hafting et al., 2005). This was performed by showing that attractor networks with multiple bumps and periodic boundary conditions, i.e. torus, are stable with respect to rotations. In order to enable the velocity-dependent movement of the activity bump the authors used synaptic profile shifts in four different directions. The outgoing synaptic profile of a neuron in the middle of the torus used in Burak and Fiete (2009), together with synaptic shifts, is illustrated in Figure 1.4A. Burak and Fiete (2009) also showed that networks with aperiodic boundary conditions, and neurons that are silenced at the boundaries, can also produce stable grid firing fields, but are less accurate than toroidal networks.

In general, attractor networks are an orthogonal mechanism with respect to oscillatory interference model and thus, they do not explain the phase precession of spike times in place (O'Keefe and Recce, 1993; Skaggs et al., 1996) and grid cells (Hafting et al., 2008). One recent model, however, tried to explain how phase precession could arise in an attractor network model composed of spiking neurons (Navratilova et al., 2012). This study used two ring models: one pure grid cell attractor, and an accompanying ring of neurons that modelled conjunctive grid-by-head-direction cells. This attractor model was then augmented with realistic after-spike dynamics on a single-neuron level, that enabled the bump attractor to "look-ahead" of the current simulated position. This mechanism thus resulted in action potentials precessing in phase relative to theta rhythm when the animal traversed through the one-dimensional firing field. Other than this, no other model of grid cells actually incorporates a mechanism of phase precession intrinsic to the attractor network itself, although hybrid models exist as well (Schmidt-Hieber and Häusser, 2013; Bush and Burgess, 2014).

More recently, there has been progress in dissecting the neural circuitry in layer II of the MEC, which is important to constrain the features of models. Namely, optogenetic methods have allowed several groups to track connectivity between principal cells in layer II. The results show that stellate cells, which are believed to constitute the majority of grid cells in this layer are connected indirectly through feedback inhibition mediated by fast spiking interneurons (Pastoll et al., 2013; Couey et al., 2013). This spawned simulations in Couey et al. (2013), which investigated path integration in a

[1]Note that this is not the grid-like firing field but population activity.

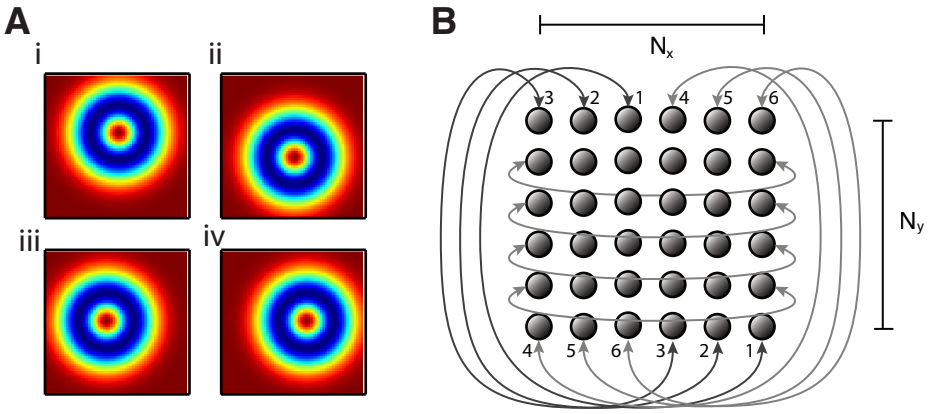

Figure 1.4: **Examples of connectivity profiles from Burak and Fiete (2009) and boundary conditions of a twisted torus (Guanella et al., 2007) (A)** Colour plots show outgoing synaptic weights of a neuron in the centre of a square lattice with size 30×30 neurons (red: maximum, blue:minimum). The weights have been derived from Eqs. (2-3) in Burak and Fiete (2009). The parameters were: $\lambda_{\text{net}} = 20$, $a = 1$, $\beta = 3/\lambda_{\text{net}}^2$, $\gamma = 1.05 \times \beta$, $l = 5$. The profiles are shifted up (i), down (ii), left (iii), and right (iv). All weights with these parameter values are inhibitory. **(B)** Illustration of a twisted torus with size 6×6 neurons (Guanella et al., 2007).

model with pure inhibition, and the two-population attractor model elaborated on in Chapter 3 in this thesis, and published in Pastoll et al. (2013).

In general, continuous attractor models arrange the neurons either on torus topology (Samsonovich and McNaughton, 1997; Burak and Fiete, 2009) or provide an envelope "inhibitory" input that prevents runaway excitation at the edges of the neural sheet (Burak and Fiete, 2009). These models exhibit population activity with hexagonal structure, that is then translated in accordance with the simulated movement of an animal to produce the hexagonal grid firing fields. However, an interesting alternative is to use a twisted torus topology that contains a single, 2D attractor bump (Guanella et al., 2007). When the bump moves through the horizontal edges it re-appears on the other side, but horizontally shifted half the size of the horizontal extent of the torus (Figure 1.4B). This way the resulting spatial firing field is hexagonal, in the same way as it is in the multiple-bump attractor models.

Due to the necessary network interactions between cells in the attractor models, they are inevitably more complicated than the original version of the oscillatory interference model (Burgess et al., 2007). This is likely to be the reason why the interference model has been tested and amended more extensively than the attractor network

idea (Remme et al., 2010; Zilli and Hasselmo, 2010; Bush and Burgess, 2014). Let us briefly mention two important experimental results that are related to test the viability of the attractor model mechanism. Firstly, since there is strong interaction between neurons that participate in a continuous attractor together, firing fields of neurons (grid cells) from this attractor must differ only along two dimensions. This has been shown to be true when firing fields of simultaneously recorded grid cells were analysed from experiments performed in several independent laboratories (Yoon et al., 2013). Secondly, a study by Bonnevie et al. (2013) showed that inactivation of the hippocampus by applying muscimol abolished grid firing fields. This was accompanied by a decrease in the firing rate of grid cells and a subsequent recovery after the drug washout. The loss of grid firing fields was consistent with a decrease of excitatory input into an attractor model implemented in the same study, and a subsequent break down of the attractor state necessary for the generation of stable grid fields. Thus, the current experimental evidence largely supports the idea that grid cells are part of a low-dimensional attractor network.

To complete the review of attractor models, I will discuss a recent study that provides another piece of evidence that supports the attractor network idea. Attractor networks have been widely criticised for their complicated nature and the fact that no known developmental mechanism has been proposed to account for the precise tuning of connections necessary for bump formation. A recent modelling study by Widloski and Fiete (2014), however, showed that spike timing-dependent plasticity (STDP; Bi and Poo, 1998) and spatial inputs, e.g. originating from hippocampal place cells, are sufficient for formation of a continuous attractor capable of path integration. Thus, the attractor model, based on the current evidence, is perhaps the most plausible idea of grid field computation.

1.3 Discussion

In this chapter I have reviewed the experimental and modelling work related to the medial entorhinal cortex. This brings up several interesting questions.

Firstly, the studies on gerbils (Mittelstaedt and Mittelstaedt, 1980), manipulation of self-motion signal gain in rats (Terrazas et al., 2005; McNaughton et al., 2006; Chen et al., 2013), and many other experimental studies (Etienne and Jeffery, 2004), collectively point to the participation of self-motion signals in establishing the spatial representation map in hippocampus and surrounding areas. Thus the synergistic view

to date is that the neural substrates of path integration could lie in hippocampus or areas upstream (Etienne and Jeffery, 2004). The discovery of grid cells, with their hexagonal firing fields (Hafting et al., 2005), and the subsequent modelling (Fuhs and Touretzky, 2006; Burak and Fiete, 2009; Burgess et al., 2007; Remme et al., 2010), supports the current view that the MEC forms the path integrator itself. In this work, I take this view and treat the formation of grid cells as a process whereby an animal integrates self-motion signals by means of translating the bump of activity in concert with a velocity signal, thus essentially computing the grid-like spatial firing field.

Secondly, the anatomical evidence shows that stellate cells in layer II are connected via feedback inhibition only (Dhillon and Jones, 2000; Pastoll et al., 2013; Couey et al., 2013). This idea seems to be at odds with most of the attractor models that assume the presence of excitatory connectivity, and as pointed out in McNaughton et al. (2006), it might be that the path integrator is located in some other areas. In this work, I challenge this idea and implement a two-population attractor network model that does not contain any recurrent excitation. Chapters 2 and 3 deals with this implementation.

Thirdly, LFP recordings from the MEC show a prominent cross-frequency coupling of slow theta rhythm with fast gamma (Chrobak and Buzsaki, 1998; Quilichini et al., 2010) and recent *in vitro* studies of the dynamics of light-activated stellate cells and fast spiking interneurons suggest that the theta-gamma oscillations could be generated by the local circuit in layer II (Pastoll et al., 2013), the layer where grid cells are the most abundant (Sargolini et al., 2006). These results thus beg the question: if the oscillatory activity is generated by the local grid cell circuit, is it possible that the aforementioned attractor model co-exists with the theta-nested gamma oscillations? Again, in Chapter 3 I take the attractor model further, and show that attractor networks that generate grid-like firing fields can co-exist with theta-nested gamma oscillations that are very similar to those observed both *in vivo* and *in vitro*. The solution to the problem of the co-existence of attractor states and theta nested gamma oscillations is not a trivial one, since attractor states cannot be sustained during periods of low activity (Roudi and Latham, 2007; see also Bonnevie et al., 2013). In Chapters 2 and 3 I demonstrate that this can be achieved by including a slow, NMDA-like component in the network. The dual rate- and spike-timing based coding can be important for information transmission and filtering (Akam and Kullmann, 2010), or perhaps even for more sophisticated means of working memory implementations in the nervous system (Jensen and Lisman, 1996). I will defer the detailed discussion to the final section of Chapter 3.

The relationship between synaptic structure, network dynamics, and computations performed by attractor networks is so far unclear. To investigate this relationship in more detail, Chapter 4 goes beyond the implementation of attractor networks that co-exist with theta-nested gamma oscillations. In this chapter, I investigate the dynamics of computation of grid fields and gamma oscillations in the two population attractor network given three parameters: global strengths of excitatory and inhibitory connections between the two populations, and levels of intrinsic noise in the network. I show, unexpectedly, that moderate noise promotes both the pattern formation and computations underlying grid field formation, as well as the presence of theta-nested gamma oscillations in the network. This is unexpected, since the classical theory of signal transmission tells us that noise generally impairs signal transmission (Shannon, 1956), even though some studies suggest positive effects of noise in neural networks (Benzi et al., 1999; Longtin et al., 1991; Shu et al., 2003). As part of the chapter, I try to dissect possible mechanisms of this unexpected benefit of noise.

In Chapter 4, I extend this further, and contemplate the relationship between grid field computation and the presence and power of theta-nested gamma oscillations in the attractor model. My motivation stems from the evidence from several studies that there is a correlation between incidence of some of the neurological disorders, such as autism and schizophrenia, and the intricate balance between excitation and inhibition (Rubenstein and Merzenich, 2003; Lewis et al., 2012). Since grid cells are believed to be part of an extensive cognitive system, I use the model to correlate the power of nested gamma oscillations with the capabilities of the networks I have developed to generate grid firing fields. I show that the power of gamma oscillations is largely independent of gridness score, the metric used to assess the quality of grid firing fields. In fact, as I show, with moderate noise, one can effectively fine tune the power and frequency of nested gamma oscillations while retaining a relatively constant gridness score generated by the cells in the network. My results are thus rather consistent with the "routing" proposal, in which oscillations participate in a selection process that binds information flow to specific brain regions (Fries, 2005, 2009; Akam and Kullmann, 2010; Akam et al., 2012). In our case, the grid cell network in the medial entorhinal cortex, and some other region, such as the hippocampus.

In the following chapters I will discuss the specific implementations and results arising from the network model that I have developed. The results from Chapters 2 and 3 have been published in Pastoll et al. (2013), and the results from Chapter 4 are in preparation for publication.

Chapter 2

Single-bump spiking continuous attractor network

2.1 Introduction

In this chapter, I will present the details of the developed attractor model. The chapter recapitulates experimental evidence used to constrain the model, which also serves as motivation for why I developed it into the current form. In order to model the theta oscillations, the network receives external inputs with amplitude modulated by an 8 Hz cosine function. A crucial challenge for an attractor network that generates stable attractor states with theta frequency inputs is the maintenance of the bump of activity across periods of low activity. This was accomplished by using NMDA synaptic currents between the E and I populations in the network. NMDA receptors have a long time constant and this fact allowed the network to retain the information about which cells should preferentially fire from one theta cycle to the next once the attractor has settled down into the so-called "bump state".

Section 2.2.1 outlines the general network architecture, i.e. mainly the topographical organisation of neurons on the twisted torus, while also presenting a schematic of various inputs external to the attractor network itself. Section 2.2.2 outlines single neuron properties, while Sections 2.2.3 and 2.2.4 provide a detailed description of how the neurons are connected. Sections 2.2.5–2.2.7 provide information about the various external inputs to the network, namely theta frequency inputs, velocity inputs, and inputs from place cells. Finally, Section 2.2.8 provides a description of the gridness score estimation procedure used throughout the thesis.

The description of the network is in a mathematical form, and is independent of a

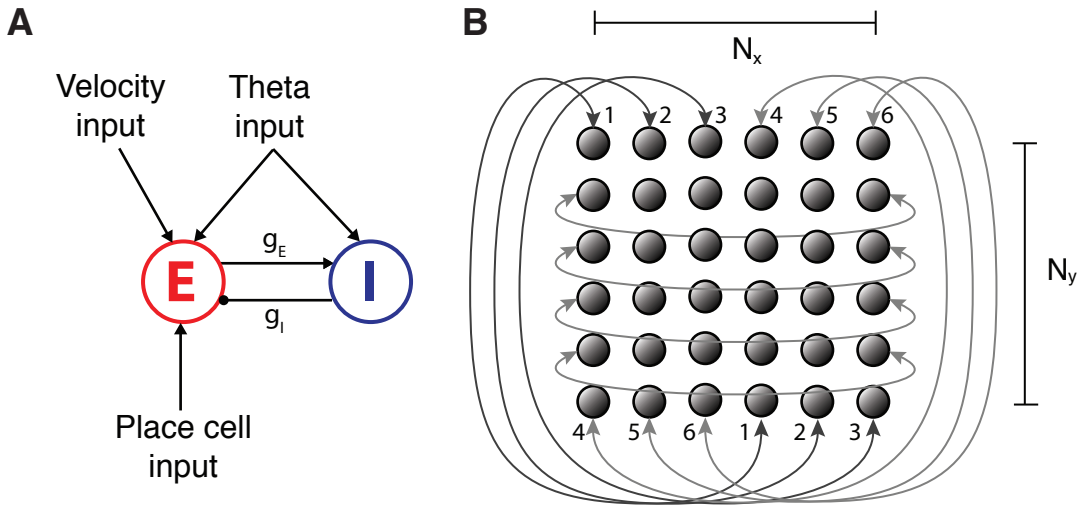

Figure 2.1: **Two population continuous attractor network model. (A)** Model schematic describing the two populations of excitatory stellate cells (E), fast spiking interneurons (I) and inputs to the network (velocity, theta and place input). **(B)** An illustration of a neural sheet containing 6×6 neurons. The arrows show the continuation of boundaries on the twisted torus.

specific simulator used for numerical simulation. The simulations in Chapter 3 were performed using the Brian simulator (Goodman and Brette, 2008). Due to technical limitations of Brian simulator, and for speed-up improvements, the model in Chapter 4 was re-implemented using the NEST simulator (Gewaltig and Diesmann, 2007). This chapter contains a general methods description that is valid for all the following chapters, if not mentioned otherwise.

2.2 Network architecture and methods

2.2.1 General network architecture

We have seen in Section 1.1.2 that MEC layer II stellate cells are likely to be grid cells, as well as border cells and head direction cells (Varga et al., 2010; Burgalossi et al., 2011; Zhang et al., 2013; Kitamura et al., 2014), although pyramidal cells also have repeating firing fields when animals move in real-world linear tracks (Burgalossi et al., 2011) and in virtual arenas (Domnisoru et al., 2013; Schmidt-Hieber and Häusser, 2013). Stellate cells communicate with each other only via FS interneurons (Pastoll et al., 2013; Couey et al., 2013), and this provides important constraints on connectivity in the attractor network developed in this thesis.

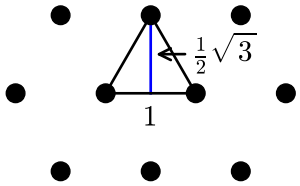

Figure 2.2: **Ratio of sizes of the twisted torus necessary to generate hexagonal firing fields.** The approximate ratio should be $1 : \frac{\sqrt{3}}{2}$, as indicated by the height of the equilateral triangle.

The model consists of two populations of neurons (Figure 2.1A): excitatory (E) cells (red; stellate cells) and inhibitory (I) cells (blue; fast spiking interneurons, FS). The only connections are between the two populations. Excitatory cells synapse solely on interneurons, while interneurons connect only to excitatory cells (Figure 2.1A; g_E and g_I). Both populations are laid-out on a twisted torus. Figure 2.1B illustrates, on an example of the torus with 6×6 neurons, how boundaries of the torus are connected with each other. One can imagine the boundaries, illustrated with arrows, as if a person was walking on the torus. If the person walks in a horizontal direction, when she reaches the left or right edge of the torus, she will immediately re-appear on the right or left edge, respectively. This is consistent with the standard topography of a torus. However, when the person travels in a vertical direction, the situation changes. If the person stands in the top-left edge, and steps up, she will re-appear in the centre of the torus, thus being shifted half the torus size in the horizontal direction, as shown by vertical arrows in Figure 2.1B. The same holds, but with a shift in an opposite direction, when the person stands in the right hand side of the torus. A twisted torus is therefore a structure in which its boundaries in one of the directions are shifted and subsequently connected, while the other direction wraps in a standard, toroidal manner.

It has been previously shown in simplified models, that a bump attractor on a twisted torus can produce grid fields when the ratio of horizontal and vertical sizes of the torus are selected in accordance with the ratios of lengths of the side and height of an equilateral triangle (Guanella et al., 2007). Figure 2.2 illustrates that this ratio is always $1 : \frac{\sqrt{3}}{2}$. The model presented here approximates this ratio, up to the resolution of a discrete population of neurons.

It is not necessary to use twisted torus topology to create two-dimensional bump attractors. Earlier modelling has shown that multiple bumps of activity that form a hexagonal lattice can arise from the Mexican hat connectivity (Burak and Fiete, 2009) or connectivity similar to a Mexican hat (Fuhs and Touretzky, 2006). Burak and Fiete

(2009) have moreover shown that attractor networks without wrap-around boundaries can also function as accurate path integrators, although these types of networks are less stable than attractors implemented on the torus.

The precise connectivity profiles necessary to distinguish between these different variants of topology and bump attractor structures are not available yet. The implementation of a single-bump attractor on twisted torus is arguably the simplest and in principle it might require less neurons than multiple-bump attractors. Thus, for this thesis, I have chosen to implement the attractor network on a twisted torus.

In Chapter 3 I have simulated the network with E cells distributed on the torus of size 68×58 and I cells distributed on a torus of size 34×30 neurons, according to Figure 2.2. This gives a total of 4080 E cells and 1020 I cells. In Chapter 4 the size of the E population was decreased to 34×30 neurons, solely for the purpose of computational efficiency. Since the ratio of stellate cells to FS interneurons has not been determined yet (although see Gatome et al. (2010) for estimations of numbers of some of the cell types in the MEC), the number of cells in each population were chosen arbitrarily. These numbers are consistent with some of the previous spiking attractor models in other brain areas (Song and Wang, 2005; Compte et al., 2000).

2.2.2 Neuron membrane and synaptic dynamics

Each neuron's membrane potential (V_m) is governed by the passive membrane equation:

$$C_\mathrm{m}\dot{V}_\mathrm{m} = I_\mathrm{m} + I_\mathrm{syn} + I_\mathrm{ext}, \tag{2.1}$$

in which the total membrane current is a sum of three separate components: the trans-membrane current (I_m), the total synaptic current (I_syn), and the current injected externally from other brain regions (I_ext).

For stellate cells, the trans-membrane current

$$I_\mathrm{m} = g_\mathrm{L}(E_\mathrm{L} - V_\mathrm{m}) + g_\mathrm{AHP}(t)(E_\mathrm{AHP} - V_\mathrm{m}) + g_\mathrm{L}\Delta_\mathrm{T}\exp\left(\frac{V_\mathrm{m} - V_\mathrm{T}}{\Delta_\mathrm{T}}\right) \tag{2.2}$$

contains the leak conductances ("L" subscript), after-spike hyperpolarisation conductance ("AHP" subscript) and an exponential part that initiates a spike when the membrane potential gets close to the threshold (V_T). After each spike, there is a reset of membrane potential and the AHP conductance:

$$\begin{aligned} V_\mathrm{m} &\rightarrow V_\mathrm{r} \\ g_\mathrm{AHP} &\rightarrow g_{\mathrm{AHP}_\mathrm{max}}. \end{aligned} \tag{2.3}$$

The FS interneurons do not possess AHP, but instead contain a simple adaptation term. The trans-membrane current has the following form:

$$I_{\mathrm{m}} = (g_{\mathrm{L}} + g_{\mathrm{ad}}(t))(E_{\mathrm{L}} - V_{\mathrm{m}}) + g_{\mathrm{L}}\Delta_{\mathrm{T}} \exp\left(\frac{V_{\mathrm{m}} - V_{\mathrm{T}}}{\Delta_{\mathrm{T}}}\right). \tag{2.4}$$

The g_{ad} term adds an extra conductance after each spike, i.e. after the spike:

$$\begin{aligned} V_{\mathrm{m}} &\to V_{\mathrm{r}} \\ g_{\mathrm{ad}} &\to g_{\mathrm{ad}} + g_{\mathrm{ad_{inc}}}. \end{aligned} \tag{2.5}$$

Both AHP and adaptation conductances ($g_{\mathrm{AHP}}(t)$ and g_{ad} respectively) decay exponentially:

$$\begin{aligned} \dot{g}_{\mathrm{AHP}} &= -\frac{g_{\mathrm{AHP}}}{\tau_{\mathrm{AHP}}} \\ \dot{g}_{\mathrm{ad}} &= -\frac{g_{\mathrm{ad}}}{\tau_{\mathrm{ad}}}. \end{aligned} \tag{2.6}$$

In equations (2.2) and (2.4), the term Δ_{T} is defined as the spike slope factor (Fourcaud-Trocmé et al., 2003) and it measures the sharpness of the spike initiation. The closer this parameter is to zero, the faster spike initiation will happen when V_{m} gets close to V_{T}. For the exponential integrate and fire neuron, in the limit $\Delta_{\mathrm{T}} \to 0$, the model becomes equivalent to a leaky integrate and fire neuron (Fourcaud-Trocmé et al., 2003).

The synaptic current for each neuron is a sum of the AMPA, NMDA and $\mathrm{GABA_A}$ synaptic currents collected from spikes of all other neurons:

$$\begin{aligned} I_{\mathrm{syn}}(t) = {} & g_{\mathrm{GABA_A}}(t)(E_{\mathrm{GABA_A}} - V_{\mathrm{m}}) + g_{\mathrm{AMPA}}(t)(E_{\mathrm{AMPA}} - V_{\mathrm{m}}) \\ & + g_{\mathrm{NMDA}}(t)(E_{\mathrm{NMDA}} - V_{\mathrm{m}}) \end{aligned} \tag{2.7}$$

Note that the connectivity in this model is not all-to-all, as for instance there are no E $\to$ E and no I $\to$ I connections. Therefore, effectively, for the stellate cells $g_{\mathrm{AMPA}} = g_{\mathrm{NMDA}} = 0$, and for FS interneurons $g_{\mathrm{GABA_A}} = 0$. The synaptic conductances g_{AMPA}, g_{NMDA} and $g_{\mathrm{GABA_A}}$ of a postsynaptic neuron i were modelled as exponentials with user defined time constants (see table 2.3 for the values of parameters used in these simulations):

$$\begin{aligned} \dot{g}^i_{\mathrm{AMPA}} &= -\frac{g_{\mathrm{AMPA}}}{\tau_{\mathrm{AMPA}}} + \sum_j w^{ij}_{\mathrm{AMPA}} \delta(t - t_j) \\ \dot{g}^i_{\mathrm{NMDA}} &= -\frac{g_{\mathrm{NMDA}}}{\tau_{\mathrm{NMDA}}} + \sum_j w^{ij}_{\mathrm{NMDA}} \delta(t - t_j) \\ \dot{g}^i_{\mathrm{GABA_A}} &= -\frac{g_{\mathrm{GABA_A}}}{\tau_{\mathrm{GABA_A}}} + \sum_j w^{ij}_{\mathrm{GABA_A}} \delta(t - t_j). \end{aligned} \tag{2.8}$$

After each spike of a presynaptic neuron j, each corresponding conductance was incremented by w^{ij}.

In MEC layer II, basket cells receive a potent, NMDA-mediated synaptic excitation (Jones and Buhl, 1993). These NMDA responses are slow, lasting several tens of ms (Jones and Buhl, 1993). In this work, NMDA synapses are thus represented by an exponentially decaying conductance (g_{NMDA}), with a 100 ms time constant (Table 2.3). Both the voltage dependence and slow kinetics have been suggested to help maintain persistent activity in working memory networks (Wang, 1999). Here, it is the slow kinetics of g_{NMDA} that is necessary to maintain the state of the network during consecutive theta cycles. Moreover, NMDA receptors are known to be of several variants, depending on the types of the subunits the receptors are composed of (Paoletti et al., 2013). These several receptor variants have different kinetic time scales, and different sensitivity to the concentration of Mg^{2+}. Jones and Buhl (1993) do not report, quantitatively, to what extent the amplitude of the NMDA-mediated synaptic responses are dependent on the Mg^{2+} concentration. Therefore, I assume here that the slow kinetics of g_{NMDA} is sufficient to stabilise the activity of the network.

Finally, the current external to the neuron

$$I_{\mathrm{ext}}(t) = I_{\mathrm{const}}(t) + I_{\theta}(t) + I_{\mathrm{vel}}(t) + I_{\mathrm{place}}(t) \tag{2.9}$$

consists of a constant value (I_{const}), a theta modulated part, modelled as

$$I_{\theta}(t) = A_{\theta} * (1 + \sin(2\pi f_{\theta} t + \phi_{\theta})), \tag{2.10}$$

the velocity modulated current (I_{vel}) that simulates a combination of head-direction input and animal speed input, and an input coming from place cells (I_{place}). The description of the parameters in Equations (2.9) and (2.10) can be found in Table 2.1.

The choices of constant and theta frequency input amplitudes is discussed in Section 2.2.5. The velocity modulated current is described in Section 2.2.6 and the place cell input current in Section 2.2.7. In Chapter 4, the place cell input is realised in a different way, and is described separately (Section 4.2.3). The descriptions of all parameters and their values are in Tables 2.1–2.5.

2.2.3 Connections between layers

Stellate cells in layer II of the MEC do not seem to communicate directly with each other (Dhillon and Jones, 2000; Pastoll et al., 2013; Couey et al., 2013). This observation was used to constrain the connectivity between layers in this model. As

Name	Description	Name	Description
V_{m}	Membrane potential	E_{AMPA}	AMPA reversal potential
C_{m}	Membrane capacitance	g_{NMDA}	NMDA conductance
g_{L}	Leak conductance	E_{NMDA}	NMDA reversal potential
E_{L}	Leak reversal potential	I_{m}	Trans-membrane current
g_{AHP}	AHP conductance	I_{syn}	Synaptic current
τ_{AHP}	AHP time constant	I_{syn}	Synaptic current
E_{AHP}	AHP reversal potential	I_{ext}	External current
Δ_{T}	Spike initiation width	I_{const}	Constant current
V_{T}	Spike initiation threshold	I_{θ}	Theta-modulated current
$g_{\mathrm{GABA_A}}$	GABA conductance	I_{vel}	Velocity current
$E_{\mathrm{GABA_A}}$	GABA reversal potential	I_{place}	Place cell current
g_{AMPA}	AMPA conductance	τ_{AMPA}	AMPA time constant
$\tau_{\mathrm{GABA_A}}$	GABA time constant	τ_{NMDA}	NMDA time constant
g_{ad}	Adaptation conductance	τ_{ad}	Adaptation time constant
$g_{\mathrm{AHP_{max}}}$	AHP maximal value	$g_{\mathrm{ad_{inc}}}$	Adaptation conductance increase
A_{θ}	θ-current amplitude	f_{θ}	θ-current frequency
ϕ_{θ}	θ-current phase		
w_{AMPA}	AMPA synaptic weight	w_{NMDA}	NMDA synaptic weight
$w_{\mathrm{GABA_A}}$	GABA synaptic weight		

Table 2.1: Neuron parameters and their description. For the exact values used in the simulations, refer to tables 2.2-2.4.

mentioned before, the cells in the E populations have no direct recurrent excitatory synapses. Therefore, when I refer to excitation or inhibition, that means synaptic connections from cells in the E population onto cell(s) in the I population or vice versa respectively.

Here, I focus on connectivity between stellate cells, since the experimental evidence for the absence of direct connections is ample. However the model does not contain direct recurrent inhibition between FS interneurons either. This decision was mainly stimulated by computational costs of extra connectivity and the fact that the main aim is to model a form of pyramidal interneuron network gamma (PING) oscillation. In this type of oscillation, the gamma activity and synchronisation between neurons arises from an interplay between excitatory and inhibitory cells and not in-

Name	Units	Value (E cells)	Value (I cells)
C_{m}	pF	211.389	227.3
E_{L}	mV	-68.5	-60
V_{T}	mV	-50	-45
V_{r}	mV	-68.5	-60
g_{L}	nS	22.73	22.73
Δ_{T}	mV	0.4	0.4
E_{AHP}	mV	-80	×
τ_{AHP}	ms	20	×
$g_{\mathrm{AHP_{max}}}$	nS	5	×
τ_{ad}	ms	×	7.5
$g_{\mathrm{ad_{inc}}}$	nS	×	22.73

Table 2.2: Single neuron parameter values for all cells.

Name	Units	Value
E_{AMPA}	mV	0
τ_{AMPA}	ms	1
E_{NMDA}	mV	0
τ_{NMDA}	ms	100
$E_{\mathrm{GABA_A}}$	mV	-75
$\tau_{\mathrm{GABA_A}}$	ms	5

Table 2.3: Parameter values for synapses.

		E-surround		I-surround	
Name	Units	Value (E cells)	Value (I cells)	Value (E cells)	Value (I cells)
I_{const}	pA	300	200	300	200
A_θ	pA	375	25	650	50
ϕ_θ	rad	$-\pi/2$	$-\pi/2$	$-\pi/2$	$-\pi/2$
f_θ	Hz	8	8	8	8

Table 2.4: Parameter values for external inputs.

hibitory cells alone, as in interneuron network gamma (ING) (Whittington et al., 2000). The PING mechanism can be informally characterised by excitatory cells receiving external input significantly higher than their threshold, driving interneurons to spike, which in turn inhibit activity of the excitatory cells, that in turn stop exciting interneurons (Börgers and Kopell, 2003). This has a synchronising effect on both populations with the firing of interneurons slightly lagging excitatory cells by a few milliseconds (Börgers and Kopell, 2003). Addition of fast, I→I connections does not affect the synchronisation properties, although it could increase the frequency of the gamma oscillation (Brunel and Wang, 2003). We can also note that the optogenetic experiment of Pastoll et al. (2013) has exactly the properties of the PING mechanism and that the nested gamma oscillations are abolished with antagonists of either glutamate or GABA

receptors, as expected if the gamma rhythm is generated by an interplay between stellate cells and FS interneurons. Thus, I do not include inhibition between interneurons in this model.

Theoretical results and previous models of continuous attractors suggest, that in order to sustain/generate an attractor, it is necessary that the strength of a synaptic connection follows a form of a Mexican hat pattern (McNaughton et al., 2006; Fuhs and Touretzky, 2006; Burak and Fiete, 2009). Recent work also suggests that inhibitory competition between grid cells can generate stable multi-bump attractors (Couey et al., 2013), in a similar way as in the work done by Burak and Fiete (2009). Both of these concepts have competition in common, i.e. the cells in the attractor compete for activation. If the competition is strong enough, the stable state of such a system is a hexagonal pattern of activity. Activity in the network can be sustained either by recurrent excitation (Fuhs and Touretzky, 2006), or the network receives some form of background excitatory input (Burak and Fiete, 2009; Pastoll et al., 2013; Couey et al., 2013).

In the network presented here (Pastoll et al., 2013), I have adopted the Mexican hat approach, since it has proven stable in several simulation experiments. Couey et al. (2013) have subsequently shown that inhibition with a step-like synaptic profile is feasible to generate stable bump attractors as well. However, Couey et al. (2013) have implemented the model with an inhibitory population of cells only, therefore whether this concept can translate to the scenario presented here is not yet known. It is also important to mention that the mechanism in Couey et al. (2013) generates attractor states with multiple bumps, while, as we shall see, the attractor network presented here simulates only a single bump of activity. It is not clear whether the step-like inhibitory synaptic profile can generate single-bump attractor states. Thus, since the experimental evidence does not conclusively prove or refute either of the concepts, the criterion of a proper synaptic strength profile is somewhat arbitrary. Nevertheless, studying activity of these different network configurations is important, since predictions made by each model may enable future experiments to distinguish between them.

There are several assumptions about the Mexican hat connectivity that need to be considered. Firstly, the question of the boundaries of the network has to be considered. When the bump of activity generated by the network reaches the boundary, it can either fade away (Burak and Fiete, 2009; Witter and Moser, 2006), or the boundaries can be periodic on a torus (Burak and Fiete, 2009). Alternatively, the boundaries can be periodic on a twisted torus, as already mentioned (Guanella et al., 2007; Pastoll

et al., 2013). It is not clear, currently, how either of such connectivities would arise in the MEC, although recent modeling work demonstrated that synaptic plasticity can lead to the formation of the Mexican hat connectivity with non-periodic boundaries (Widloski and Fiete, 2014). The second issue concerns the anatomical organisation of an attractor network model inside the MEC. Here, the assumption is that a single unit (neuron) in the model network maps to a physical neuron, either a stellate cell or a FS interneuron, in layer II. Stellate cells and accompanying interneurons are located inside the cytochrome oxidase stained patches in layer II (Burgalossi et al., 2011). In order for the network to be wired up appropriately it is necessary that axons and dendrites of stellate cells (grid cells) and FS interneurons extend to other grid cells with dissimilar spatial phases. This seems to be the case, since Burgalossi et al. (2011) show axons and dendrites of stellate cells to span several smaller cytochrome oxidase patches, making this hypothesis plausible. Finally, in order to validate the Mexican hat hypothesis it is necessary to devise experiments to test its plausibility. This might require an experiment in which a large amount of grid cells are recorded from during the movement of an animal, and the strength of the connections from these cells need to be determined and cross-correlated with the difference in spatial phases of grid fields. The strength of the connectivity, as a function of phase difference between the cells, must then resemble the Mexican hat function. If it does not, a different mechanism would have to be considered.

2.2.4 Synaptic connection profiles

The model I have developed was implemented in one of two possible configurations. The first one, which I refer to as the *E-surround* configuration, assumes that excitatory cells provide surround excitation, *onto inhibitory* cells (Figure 2.3A, Appendix 2.2.4), while connectivity of inhibitory cells has a Gaussian profile (Figure 2.3A). In the E-surround configuration, synapse strengths of connections originating from E cells are generated by a Gaussian-like function with values dependent on the distance between a presynaptic (j) and postsynaptic (i) cell on the twisted torus:

$$w^{ij}_{\mathrm{AMPA}} = g_{\mathrm{E}} \exp\left(\frac{-(d(i,j,\mathbf{C},\mathbf{e}^j_p)-\mu)^2}{2\sigma^2_{\mathrm{exc}}}\right), \tag{2.11}$$

$$d(i,j,C,\mathbf{e}_p) = |\mathbf{u}_i - \mathbf{u}_j - C \circ \mathbf{e}_p|_{\mathrm{torus}}, \tag{2.12}$$

$$w^{ij}_{\mathrm{NMDA}} = C_{\mathrm{NMDA}} w^{ij}_{\mathrm{AMPA}}. \tag{2.13}$$

Name	Units	Value
μ	normalised	0.433
σ_{exc}		0.0834
σ_{inh}		0.0834
C (E-cells)		$0.03 \rightarrow 0.11$
C (I-cells)		$0.059 \rightarrow 0.147$
λ_{grid}	cm	60

Table 2.5: Parameter values for synaptic profiles. These parameters are valid for both the E-surround and I-surround configuration.

In these equations, μ is the distance of the excitatory surround from the position of presynaptic neuron, σ_{exc} is the width of the excitatory surround and $|\cdot|_{\text{torus}}$ is a distance on the twisted torus that takes the boundaries of the torus into account. The parameter values for equation (2.11) are in Table 2.5. Note that the values of μ, σ_{exc} and C are normalized by the vertical size of the torus, in order to account for potential changes in the network size.

The excitatory connections are composed of the equivalent amount of NMDA synaptic conductances. The synaptic strengths of NMDA is specified by a fractional constant C_{NMDA}. In all simulations, the NMDA amount constituted 2% of the AMPA conductance. The model itself requires a minimal amount of slow currents (NMDA) that function as a short term memory to maintain the bump attractor during the lulls of the theta rhythm. Also, the presence of NMDA receptors has been shown to stabilize attractor network dynamics (Wang, 1999). At the same time, in order to generate nested gamma oscillations, there will be an upper bound of the proportion of the NMDA currents, since they have a desynchronizing effect (Compte et al., 2000). While Jones and Buhl (1993) report potent NMDA-mediated synaptic excitation of the basket-like interneurons, they do not qualitatively report the ratio of AMPA to NMDA postsynaptic potentials. It is however possible that a large NMDA proportion could abolish the nested gamma oscillations in the model. This scenario remains to be tested by additional simulations in the future work.

$\mathbf{e}_p$ in eq. (2.12) determines the shift of the centre of the outgoing synaptic strength profile on the torus, and was used to couple the velocity of the bump with the simulated animal velocity (Burak and Fiete, 2009; Pastoll et al., 2013). The velocity modulated input is described in more detail in Section 2.2.6.

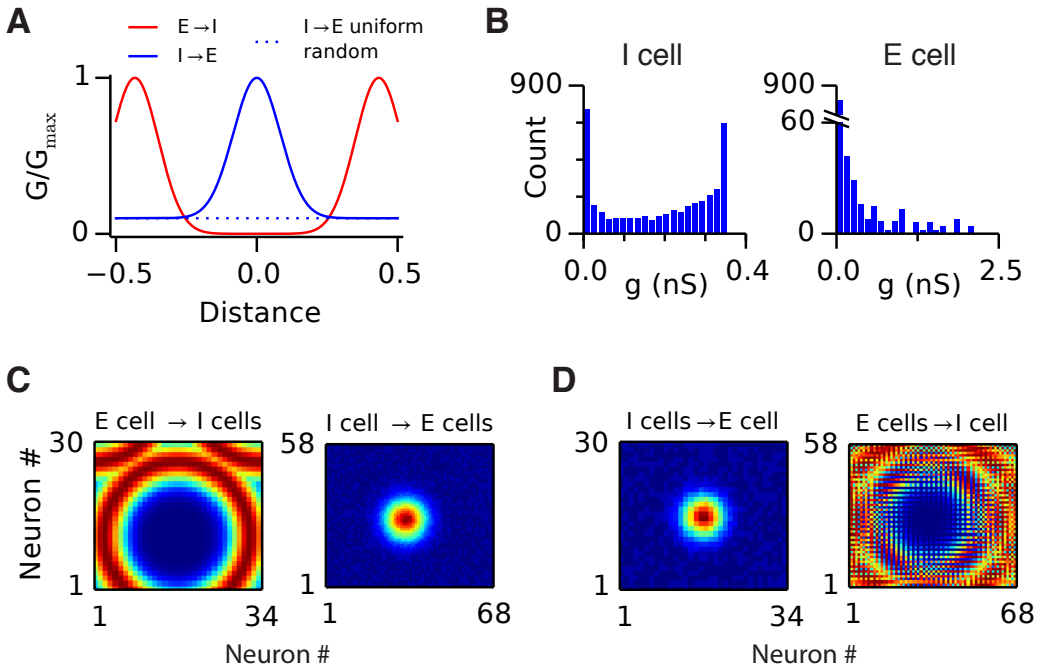

Figure 2.3: **Synaptic strengths in the E-surround network configuration. (A)** Normalised synaptic conductance is plotted as a function of distance between neurons normalised to the size of the neural sheet for connections from E cells to I cells (excitation, red) and from I cells to E cells (inhibition, blue). **(B)** Histograms of synapse strengths for all inputs to one randomly selected I cell (left, excitation) and E cell (right, inhibition). **(C)** Outgoing synaptic strength profiles of an E cell (left) and an I cell (right) in the middle of the twisted torus. **(D)** Input synaptic strength profiles for an E cell (left) and an I cell (right) in the middle of the twisted torus. The synaptic profile parameters were for (C) $\mu = 0.433$, $\sigma_{\text{exc}} = 0.0834$, $C = 0.03$ and for (D) $\sigma_{\text{inh}} = 0.0834$, $C = 0$ (Table 2.5). All values are in units normalized with respect to the number of neurons of the shorter side of the torus.

The network thus effectively implements the Mexican hat profile, if viewed from the point of view of a "composite" inhibition between stellate cells. However, E and I cells in this model receive convergent input and send divergent connections onto the population of neurons they are paired with. This divergent-convergent connectivity makes the model distinct from the single-population Mexican hat implementations.

Synapse strengths of connections from I cells (E-surround configuration) were generated by a Gaussian function

$$w^{ij}_{\text{GABA}_\text{A}} = g_\text{E} \exp\left(\frac{-d(i,j,\mathbf{C},\mathbf{e}^j_p)^2}{2\sigma^2_{\text{inh}}}\right), \tag{2.14}$$

that takes a distance between the pre- and post-synaptic neurons ($d(i, j, \mathbf{C}, \mathbf{e}_p^j)$) and a width of the Gaussian (σ_{inh}) as parameters. As can be seen from eq. (2.14), inhibitory neurons do not have shifts in their outgoing synaptic profiles. In order to facilitate the generation of gamma oscillations (Section 3.2.2), the inhibitory profile contains, in addition to the distance dependent synaptic profile, a uniform component (dashed line in Figure 2.3A). This component is uniformly added to the Gaussian inhibitory input. The probability of connection from an I cell to an E cell was set to 0.4. The strength of the synapse is then a fraction of the maximal inhibitory conductance (Eq. (2.14)). Thus, the network contains a fine-tuned feedback inhibition, as well as a non-specific inhibitory feedback. The parameters for Eq. (2.14) are in Table 2.5. Again, the values of σ_{inh} and C are normalized with respect to the vertical size of the torus in order to account for potential changes in network size.

Since neurons in the network are laid-out on a twisted torus, the connectivity rules must take the toroidal boundaries into account as well. Figure 2.3C illustrates *outgoing* synaptic profiles of an excitatory cell (left) and an inhibitory cell (right) in the middle of the torus. We can see that the middle part at the bottom of the torus is repeated at the top, but it is shifted *half-way* through the horizontal size of the torus, as described earlier. Thus the bottom part of the excitatory ring appears at the edges of the top end of the torus. Note that the excitatory profile is shifted a certain amount of neurons. In the particular configuration shown in Figure 2.3C, the shift is 4 neurons downwards. This introduces an asymmetry that allows the network to track the movement of the animal using an external, velocity-modulated current. A more detailed description will follow (Section 2.2.6; see also Burak and Fiete, 2009; Welinder et al., 2008). As a result of a translationally invariant outgoing connection profiles, the input profiles to the neurons are almost identical to the outgoing ones (Figure 2.3D). Note that due to the (outgoing) excitatory profiles being shifted, the input profiles of inhibitory neurons reflect those shifts, but in a scrambled way (Figure 2.3D right).

The second configuration is the *I-surround* configuration. Here the outgoing synaptic profiles of the I cells have a surround structure, while the strength of the outgoing connections of E cells is a Gaussian function (Figure 2.4). We will see that the selection of the type of the centre-surround profile has profound implications on how spatial firing fields of interneurons will look like. More details on the predictions about interneuron firing fields are provided in Section 3.2.6.

In the I-surround configuration, excitatory weights followed the Gaussian function from Eq. (2.14), while inhibitory weights were generated according to the surround

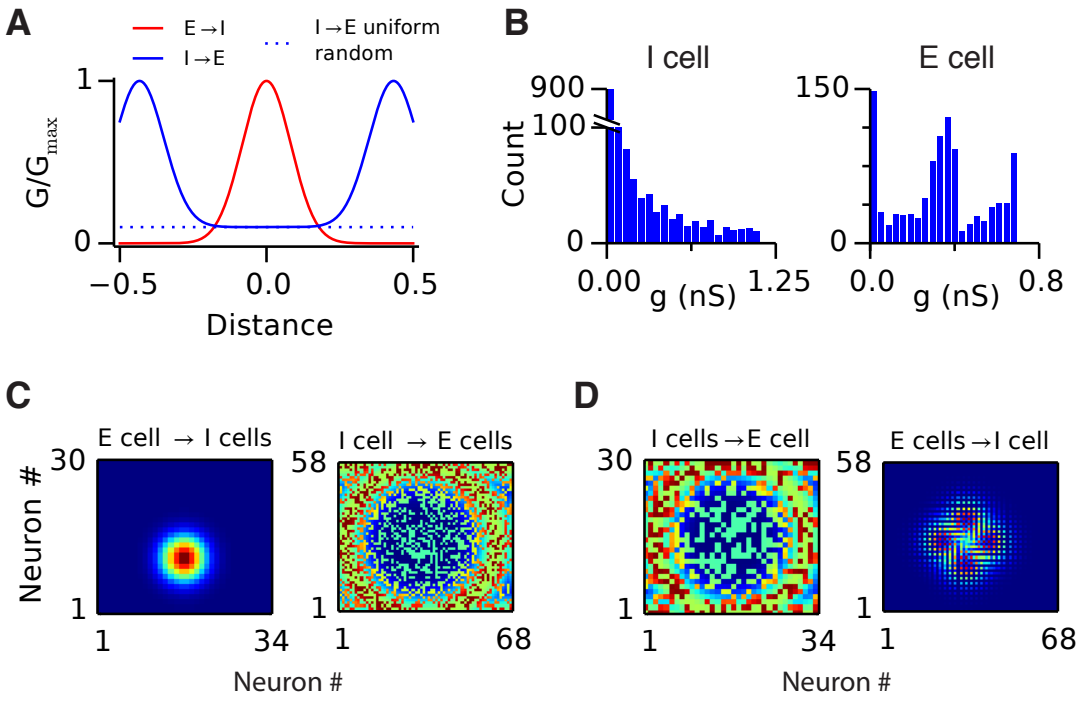

Figure 2.4: **Synaptic strengths in the I-surround network configuration.** **(A)** Normalised synaptic strength is plotted as a function of positional difference ("distance") between neurons normalised to the size of the neural sheet for connections from E cells to I cells (excitation, red) and from I cells to E cells (inhibition, blue). The strength of the uniform connectivity is not in proportion to other synaptic weights (see Appendix 2.2.4 for precise parameters). **(B)** Histograms of synapse strengths for all inputs to one randomly selected I cell (left, inhibition) and E cell (right, excitation). **(C)** Outgoing synaptic strength profiles of an E cell (left) and an I cell (right) in the middle of the twisted torus. **(D)** Input synaptic strength profiles for an E cell (left) and an I cell (right) in the middle of the twisted torus. The synaptic profile parameters were for (C) $\sigma_{\text{exc}} = 0.0834$, $C = 0.03$ and for (D) $\mu = 0.433$, $\sigma_{\text{inh}} = 0.0834$, $C = 0$ (Table 2.5). All values are in units normalized with respect to the number of neurons of the shorter side of the torus.

function in Eq. (2.11) (Figure 2.4). Thus,

$$w^{ij}_{\text{AMPA}} = g_{\text{E}} \exp\left(\frac{-d(i,j,\mathbf{C},\mathbf{e}^j_p)^2}{2\sigma^2_{\text{exc}}}\right) \tag{2.15}$$

$$w^{ij}_{\text{GABA}_\text{A}} = g_{\text{I}} \exp\left(\frac{-(d(i,j,\mathbf{C},\mathbf{e}^j_p)-\mu)^2}{2\sigma^2_{\text{inh}}}\right). \tag{2.16}$$

The parameter choices for these two equations are the same as for the E-surround

configuration and are stated in Table 2.5.

In Chapter 3, the synaptic scaling variables for the E-surround configuration were set to $g_E = 0.343$ nS, $g_I = 2.12$ nS, and the uniform component was set to $0.013/0.4 \times g_I$. In the I-surround configuration (Chapter 3), $g_E = 1.1$ nS, $g_I = 0.39$ nS, and the uniform component was set to $0.3125/0.4 \times g_I$. In Chapter 4, the network was in the E-surround configuration, g_E and g_I varied in the range of 0-6 nS, with the inhibitory uniform component set to $0.013/0.4 \times g_I$.

This centre-surround type of connectivity leads to a specific prediction about the distribution of synaptic strengths between grid cells with the same orientation and spacing, i.e. those cells that are part of a single attractor network. In the E-surround configuration, it predicts a bi-modal distribution for the strengths of excitatory synapses, and a rather uni-modal distribution for the inhibitory synapses (Figure 2.3B), while in the I-surround configuration these roles are reversed (Figure 2.4B).

The choice of synaptic profile parameters (Table 2.5) will influence the type of persistent activity and the shape and diameter of the bump attractor. For instance, Burak and Fiete (2009) include a narrow inhibitory synaptic profile[1] that spans only a fraction of the neural population. This produces a network whose stable states are multiple bumps of activity (Burak and Fiete, 2009). This option was considered during the initial stages of the work, however due to the fact that such networks appeared less stable (data not shown), I have decided to implement a network that produces only a single bump of activity. Such a configuration is similar to the one of Guanella et al. (2007) and requires that the diameter of the surround profile, which is determined by the μ parameter (Eqs. (2.11) and (2.16) for the E- and I-surround configurations respectively), spans a large fraction of the size of the twisted torus. This leads to the specific values presented in Table 2.5. However, this choice is not necessarily rigid and it is possible to change the parameters slightly around the values presented in the table and still acquire qualitatively similar results to those presented in Chapter 3 (data not shown).

2.2.5 Theta-frequency modulated background current

Since the grid cell network does not contain any recurrent excitation, it is necessary to sustain the activity with an excitatory background input. The network thus receives a source of theta-modulated input current (Figure 2.5). The theta frequency modu-

[1] Although note that Burak and Fiete (2009) only model a single population of inhibitory neurons.

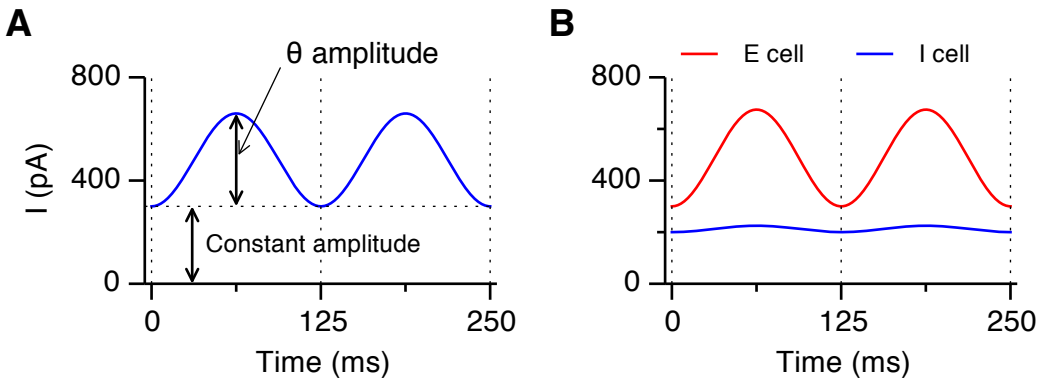

Figure 2.5: **Background and theta excitation current in the attractor model. (A)** The current comprises a constant component and a theta-modulated part. The frequency of theta modulation is 8 Hz in all of the simulations. All the parameters are adjustable. **(B)** Traces of the external currents, as specified in panel (A), fed into E (red) and I (blue) cells. The cells from the two populations receive external currents with different amplitudes.

lated input is composed of a constant component and a theta component (Figure 2.5A) superimposed on top of each other. The theta frequency modulated currents also comprise a noise component. The noise was effectively implemented as white noise current injection per simulation time step. However, due to restrictions of the Brian simulator implementation, in Chapter 3 the amount of noise was defined as variance of the membrane potential. In Chapter 4 the noise is generated by sampling from a Gaussian distribution. Figure 2.5B shows an example of two consecutive theta cycles and their respective theta currents for excitatory (red) and inhibitory (blue) cells.

As can be seen in Figure 2.5B, neurons in the E and I populations do not receive equivalent amount of the theta-frequency modulated currents. While it is as yet unknown where the theta inputs to the MEC originate, or whether the theta signal is generated locally or not, in the model the choice of amplitude and constant component of these currents cannot be arbitrary, due to the amount of inhibitory feedback such a network would generate. Unfortunately, a computer aided optimisation technique could not be used here to fine-tune the parameters of the model, in order to produce bump attractors, due to the computational demands of the simulations. In order to achieve a stable bump attractor state (Section 3.2.1), a manual process involving short simulations of the network and subsequent visualisation of the population activity on the twisted torus was used. During this process, the constant and theta amplitudes, as well as strengths of E and I synapses were changed, until the bump attractor was

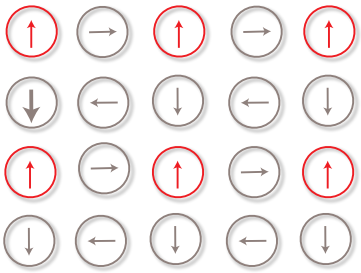

Figure 2.6: **Distribution of preferred directions of neurons on a patch of the neural sheet.** All neurons on the neural sheet (either E cells or I cells, but not both) were assigned a preferred direction of a shift of their outgoing synaptic profile. Each arrow illustrates the direction of $\mathbf{e}_p$, the unit vector from eq. (2.12). Therefore, there are four sub-populations of E cells, determined by their preferred directional vectors. Red colour highlights the sub-population with their outgoing synaptic profiles shifted upwards.

visible on the twisted torus.

2.2.6 Velocity modulated input current

All simulations of grid fields and path integration estimations contain current input modulated by the speed and direction of the simulated animal. In this chapter, velocity modulated input either targets the E cell population or the I cell population. All cells in the targeted population are assigned a preferred direction vector (eq. (2.12)) that shifts the outgoing synaptic profile in the direction specified by the unit vector $\mathbf{e}_p$ in Eq. (2.12). Figure 2.6 shows the distribution of preferred directions on a small patch of E cells on the twisted torus. Cells with similar preferred directions are preferentially excited by the velocity input tuned to movement in that direction.

During simulated movement of the animal, the velocity modulated current injected into the neuron i is computed as follows (here $\cdot$ is a dot product):

$$\begin{aligned} I^i_{vel}(t) &= C_v \mathbf{v}(t) \cdot \mathbf{e}^i_p \\ C_v &= \frac{N_x}{a\lambda_{\text{grid}}}. \end{aligned} \tag{2.17}$$

The gain of the velocity input (C_v) is determined from the number of neurons the bump needs to translate in order to return to the original position (N_x (neurons); on a twisted torus this quantity is effectively the horizontal size of the neural sheet) divided by the product of the expected grid field spacing (λ_{grid} (cm)) and a slope of the relation-

ship between bump speed and injected velocity current magnitude (a (neurons/s/pA)). Therefore, given a desired spacing between grid fields, the gain of the velocity inputs can be calibrated and matched with the place cell input (see next section).

2.2.7 Place cell input

Experiments in which hippocampal input to the MEC is abolished show disappearance of stable grid fields (Fyhn et al., 2004; Bonnevie et al., 2013). The networks considered in this thesis thus contain an extra input that effectively emulates place firing fields. When movements through realistic animal trajectories are simulated, the network receives an input that pushes the bump of activity into a location on the neural sheet that is consistent with the current position of the animal in the simulated arena. In Chapter 3, the place cell input is active only for 100 ms every 10 seconds so that spatial firing is determined primarily by the integration of velocity inputs to the network. The place cell input is implemented as part of the external current source (Eq. (2.9)).

The contribution of place cell input to grid firing in this model is distinct from the one implemented in Bonnevie et al. (2013). Bonnevie et al. (2013) use a tonic excitatory drive from the hippocampus in order to sustain the activity in the bump attractor. When this activity is lowered or abolished, the bump attractor in their network does not form. Since the model is deterministic, its bump attractor does not drift, and only the tonic excitatory drive is necessary to generate stable grid firing fields. In contrast, the hippocampal input in the model presented here also provides spatial input that opposes drift of the activity bump. The excitatory drive from hippocampus that is abolished in the experiment by Bonnevie et al. (2013) is here represented by I_{const} in equation (2.9). If this input is abolished, the model network does not form a bump attractor, which is consistent with the result of the experiment.

2.2.8 Gridness score estimation

Gridness scores are calculated according to previous studies (Sargolini et al., 2006), by taking the spatial autocorrelation of each firing field (a region corresponding to a circle with radius $\lambda_{\text{grid}}/2$ and a centre in the middle of the autocorrelation function has been removed) and rotating in steps of three degrees. For each angle of rotation, a Pearson correlation coefficient of the original autocorrelation with the rotated one is calculated. To calculate the gridness score the maximum of values of the correlation coefficient at 30, 90 and 150 degrees rotation was subtracted from the minimum of the values at 60

and 120 degrees rotation.

2.3 Discussion

This chapter outlined the development of a single-bump continuous attractor network of stellate cells and FS interneurons in layer II of the MEC. The chapter provides information necessary for the understanding of concepts and simulation results outlined in this thesis. Namely, as a result of specific constraints about the connectivity of stellate cells and interneurons, a two population attractor network has been introduced. This network receives theta-frequency modulated currents, which also highlight the necessity of introducing slow, NMDA-like synapses between excitatory and inhibitory populations of neurons. The slow synaptic currents help the network to overcome the lack of activation between consecutive theta cycles, which in turn would force the bump of activity to disintegrate. The chapter also introduced a thorough description of internal, as well as components and inputs that are external to the attractor network itself, thus giving sufficient information for the reader to proceed to the next chapters, which deal with describing the main simulation results.

Chapter 3

Co-existence of theta-nested gamma oscillations and grid firing fields

All figures in this chapter, except for Figure 3.6 appear in, or have been adapted from, Pastoll et al. (2013).

3.1 Introduction

As we have seen in Chapter 1, recent experimental evidence shows that in layer II of the MEC, feedback inhibition dominates the connections between principal stellate cells (putative grid cells) and that direct excitatory synapses between these cells are virtually absent (Pastoll et al., 2013; Couey et al., 2013), at least in adult animals (Couey et al., 2013). These data provide valuable constraints on how a faithful attractor network model of grid cells in layer II should be implemented. While these constraints already give us a substantial amount of information about the connectivity of grid cell networks, a precise quantification of synapse strengths is at this time unknown. Therefore, when building an attractor model, there are two options. The first one is to wait until the complete connectome of MEC is established. The other one is to use the knowledge obtained from higher level theories (e.g. rate models) to gain insight into the dynamics of more detailed models of attractor networks. At the time of publication of this work, there were no biologically plausible continuous attractor models of grid cells that use both spiking neuron models and satisfy the constraints on indirect connectivity between stellate cells in layer II. Only recently there has been progress in applying STDP to develop spiking attractor models of grid cells (Widloski and Fiete, 2014), as well as emergence of hybrid models utilising oscillatory interference and an

attractor network composed of spiking neurons (Schmidt-Hieber and Häusser, 2013; Bush and Burgess, 2014).

LFP recordings from the MEC in rats and mice show a diverse oscillatory activity. *In vivo*, MEC exhibits prominent theta (4-10 Hz) and gamma (30-100 Hz) power peaks during exploratory behaviour and anaesthesia (Chrobak and Buzsaki, 1998; Colgin et al., 2009; Quilichini et al., 2010). Chrobak and Buzsaki (1998) recorded LFPs from superficial layers of entorhinal cortex. In layer II-III, they found theta frequency activity with the highest power, in the range of 6-12 Hz. Superimposed on the theta troughs, gamma LFPs could be seen, whose amplitude was also modulated by theta. Colgin et al. (2009) found gamma oscillations nested within theta in behaving animals as well. In another study, Quilichini et al. (2010) recorded in anaesthetised rats in the entorhinal cortex again, and found the same relationship. These studies thus established phase-amplitude coupling in the MEC.

Gamma oscillations and PAC in the MEC can also be induced *in vitro*. Persistent gamma can be generated by the application of kainaite (Cunningham et al., 2003, 2004). Pastoll et al. (2013) showed that optogenetically activated populations of stellate cells and fast spiking (FS) interneurons in layer II generate nested gamma oscillations when the light activation amplitude is theta-modulated. Different properties of these two forms of gamma activity *in vitro* suggest that they might be mediated by different mechanisms. Firstly, optogenetically induced gamma has a higher frequency than the pharmacologically induced gamma, and, while the light induced gamma is not dependent on the presence of NMDA receptors, Middleton et al. (2008) have demonstrated that the pharmacologically induced gamma oscillations decrease their frequency and are subsequently mediated by interactions between pyramidal cells and inhibitory goblet cells in layer III. Nevertheless, these studies demonstrate forms of gamma activity (Cunningham et al., 2003), as well as phase-amplitude coupling (Pastoll et al., 2013) *in vitro*.

In this chapter, I will present the simulation results of the spiking continuous attractor model that I have outlined in Chapter 2 and which addresses all of these experimental constraints. The network I have developed generates grid-like receptive fields, while entraining both (modelled) populations of stellate cells and FS interneurons into a stable theta-nested gamma rhythm. Moreover, because the model, for the first time, explicitly simulates inhibitory neurons, it allows for specific predictions about the nature of interneuron firing fields. In addition, due to biological plausibility of the simulated neurons, obtained by simulating them as exponential integrate and fire neurons

with conductance based synapses, the model generates specific predictions about the evolution of membrane potential within and outwith a grid field, for neurons in both excitatory and inhibitory populations. The results will show that a common circuit mechanism, feedback inhibition, can support both attractor dynamics and gamma frequency nested oscillations.

3.2 Results

In this section, I present the results of the simulations of the attractor network. I first establish that feedback inhibition alone is sufficient to generate stable attractor states in the model (Section 3.2.1). This analysis also demonstrates that the attractors are sustained during several consecutive theta cycles. Next, in Sections 3.2.2 and 3.2.3, I explore the properties of nested gamma oscillations that the network generates. Finally, in Sections 3.2.4–3.2.8, I demonstrate that the oscillatory networks can generate grid firing fields, and I provide several new and experimentally testable predictions. In the following text, all the simulations were carried out in the E-surround configuration, except where explicitly stated otherwise.

3.2.1 Feedback inhibition alone is sufficient to support attractor states

Continuous attractor models of grid cells or of activity in other areas of the brain were previously either implemented as networks of interneurons directly inhibiting each other (Burak and Fiete, 2009), or by using recurrent excitation in the network (Compte et al., 2000). How does the mechanism of attractor formation translate into networks which contain separate populations of excitatory and inhibitory neurons without recurrent excitatory collaterals? Since stellate cells in layer II do not excite one another, answering such a question should prove important in establishing the plausibility of an attractor network residing in layer II of the MEC.

Figure 3.1 shows the formation of a bump attractor in the E cell layer, after fine-tuning the cellular properties. The network in general generates bumps when the amount of inhibition is sufficient to break the symmetry, otherwise the activity remains uniform across the whole layer (data not shown). Note that the maximal firing rate in the bump in this configuration is around 20 Hz (Figure 3.1A). While in general it is possible to achieve an arbitrary firing rate, I have fine tuned the external input current

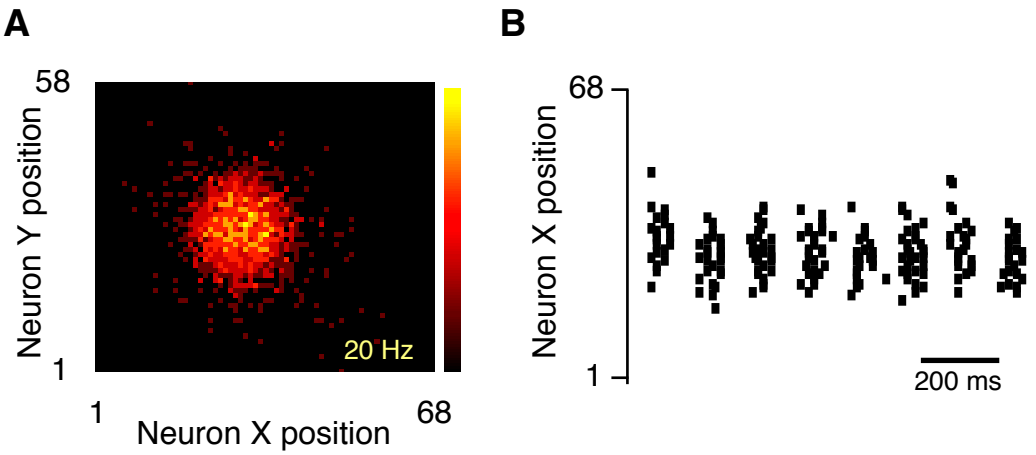

Figure 3.1: **Attractor states emerge in networks without feedback excitation.** **(A)** Activity of the population of E neurons on the twisted torus with the size of 68×58 neurons. The simulation was performed in the E-surround configuration. **(B)** Spike rasters from 68 neurons corresponding to row 29 in (A), showing that the bump is stable during successive theta cycles.

and the cellular properties to match a generally observed, rather lower, average firing rates of stellate cells (<~20 Hz) *in vivo* (Hafting et al., 2005; Sargolini et al., 2006).

Figure 3.1B illustrates the stability of the bump over 8 consecutive theta cycles. Since the bump is a two dimensional structure the panel only shows a slice through row 29 in the E cell layer (middle of the neural layer). The panel also illustrates how the activity is restricted to only those parts of theta cycles where the input current is maximal. Note that while the bump is being sustained over consecutive theta cycles, its position in the excitatory layer might still drift over time. This can be seen in Figure 3.1A. The bump was initialised to be positioned in the centre of the torus, however it is clear that after certain amount of time (the time of the snapshot) the bump has "wandered" slightly away from the centre of the torus.

The raster plot in Figure 3.1B also highlights the necessity of the NMDA-like slow component in the network. At each end of the theta input period the E cells stop firing and thus the network needs to "remember" the position of the bump from the previous theta cycle in order to initialize itself towards the next theta cycle. This is accomplished by the slow NMDA conductance with a time constant that outlasts the duration of the theta cycle (in the model here the time constant of NMDA synapses is 100 ms). The NMDA synapses that were activated from the neurons inside the bump during a theta cycle will carry on the structured information about which neurons were

activated. These neurons will then be more likely to spike in the next theta cycle, while other neurons will be inhibited. Thus, in the model, NMDA synapses are required to maintain persistent activity in the network.

The need for a slow synapse is confirmatory with the presence of a powerful NMDA-mediated excitation of basket cells in layer II of the entorhinal cortex. In addition, this requirement provides clear testable predictions about the gridness score of grid cells in this layer. For instance, abolishing the NMDA currents in layer II should decrease the gridness score of the firing fields of stellate cells. The manipulation of time constant relative to the period of local theta rhythm should also influence the gridness score of the cells in this layer. If the time constant of NMDA currents can be made much shorter than that of the theta rhythm, this should lead to a decrease in gridness score. On the contrary, increased time constant of NMDA currents could in principle lead to a stabilisation of the grid firing field.

3.2.2 Feedback inhibition enables co-existence of attractor states and theta-nested gamma oscillations

Section 3.2.1 has indicated that externally imposed theta oscillations together with a lack of direct excitatory synapses between model stellate cells are enough to support stable attractor states. This result is largely consistent with the work on one dimensional attractors in the head direction system (Boucheny et al., 2005; Song and Wang, 2005). It is not clear, however, whether bump attractor states can also support oscillatory network dynamics in attractor models.

In its default configuration (Figure 2.3), the network indeed generates oscillatory activity in the gamma range (30-100 Hz), together with stable attractor states. Figure 3.2A illustrates inhibitory and excitatory synaptic currents recorded from two cells in the network. Both traces show regular beats at theta frequency (the blue trace stands for excitation onto an inhibitory cell and vice versa for the red trace). When theta stimulation is maximal (presumably corresponding to the troughs of the LFP theta signal), the synaptic currents exhibit fast nested gamma frequency oscillations.

How does the timing of synaptic currents in both populations compare to *in vivo* and *in vitro* experimental results? Quilichini et al. (2010) have recorded from principal cells and interneurons (among other cells) in layer II of the MEC. Their results show short latency positive peaks in cross-correlograms between these cells, indicating that the activity of interneurons is driven by input from principal cells. Similarly, Pastoll

et al. (2013) have performed an optogenetic stimulation of stellate cells and interneurons in layer II. The results also show a peak in the cross-correlogram of synaptic currents between these two types of cells, thus indicating that excitation to interneurons consistently leads inhibition to stellate cells (Pastoll et al., 2013). Similarly to these experimental results, simulation outputs from the model show a short latency lag between excitatory and inhibitory synaptic currents. Figure 3.2B shows the synaptic currents across the duration of one gamma cycle, illustrating that excitation precedes inhibition with a lag of a few milliseconds. Cross correlation between excitation and inhibition in the model (Figure 3.2C) also shows a peak at a few millisecond lag, confirming that the results of the simulation are qualitatively similar to the experiment. The attractor model with feedback inhibition thus establishes a sufficiency condition for the generation of nested gamma oscillations, based on propagation of synaptic activity from E cells to FS interneurons.

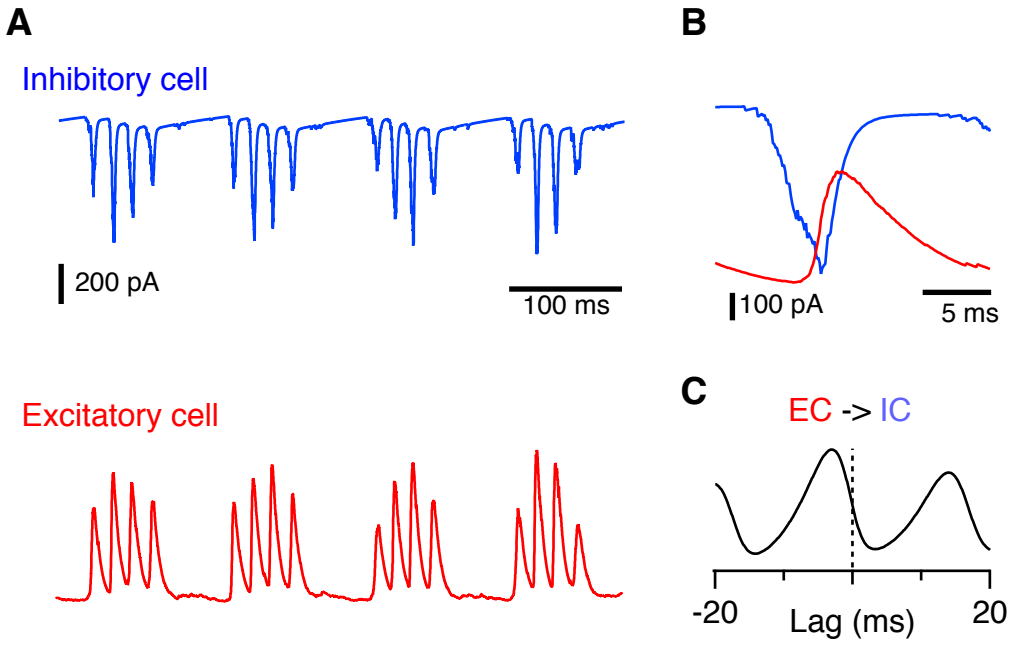

Figure 3.2: **Attractor states co-exist with theta-nested gamma oscillations.** **(A)** Examples of synaptic currents recorded from E and I cells at the centre of the twisted torus in Figure 3.1. **(B)** Synaptic currents during a single gamma cycle, illustrating that excitation precedes inhibition. **(C)** Cross-correlation between synaptic currents recorded from E and I neurons. Excitatory input to interneurons precedes inhibitory input to excitatory neurons. Both examples in (B) and (C) are from the neuron pair in (A).

3.2.3 Nested gamma oscillations have clock-like properties

Recent work postulates that the cross-frequency coupling between theta and gamma oscillations has an important role in information coding (Lisman, 2005). Lisman has proposed that an ensemble of neurons firing synchronously during a gamma cycle carries information about the place of an animal. The successive gamma cycles within a theta cycle therefore carry information about the relative timing of two "pieces" of information. This mechanism can be translated into the context of grid fields, if we assume that each gamma cycle in the entorhinal grid cell network carries an information about the position of the animal. For these coding schemes to work, a precise relationship between the phase of spiking of a neuron relative to theta phase is important (Lisman, 2005).

Interestingly, optogenetic stimulation *in vitro* also shows that nested gamma oscillations induced by a light source with amplitude modulated at theta frequency, can result in a precise relationship between gamma frequency synaptic currents and theta phase (Pastoll et al., 2013). This timing relationship can be consistent even during tens of successive theta cycles (Pastoll et al., 2013).

In this section I show that the experimental result of Pastoll et al. (2013) holds in the grid cell model as well. Figure 3.3A shows inhibitory synaptic currents onto a stellate cell during 40 consecutive theta cycles. The peaks of gamma current are strongly aligned with each other during the duration of the simulation. Interestingly, as Lisman (2005) proposes, the theta signal has a meaning here: it provides an absolute reference frame both for establishing a sequence as well as providing a timing signal to synchronise a population of grid cells during a gamma cycle.

Precise timing of spike output from E cells is also illustrated in Figure 3.3B. Here, the raster plot of action potentials during the same consecutive theta cycles as in Figure 3.3A shows that spikes are aligned during these theta cycles. In order for the absolute reference frame mechanism to work properly, the frequency of nested (gamma) oscillations must be higher than a certain threshold. This is needed in order to accommodate at least a few gamma cycles within a theta cycle. The simulation results show that nested gamma frequency in the model is ~55 Hz. While this is a little lower than what is observed *in vivo* (Chrobak and Buzsaki, 1998; Colgin et al., 2009; Quilichini et al., 2010) and in the optogenetic *in vitro* study of Pastoll et al. (2013), the frequency is in the gamma range (40–100 Hz) and it is higher than the frequency of persistent gamma observed by application of kainate in the MEC slices (Cunningham et al., 2003). It

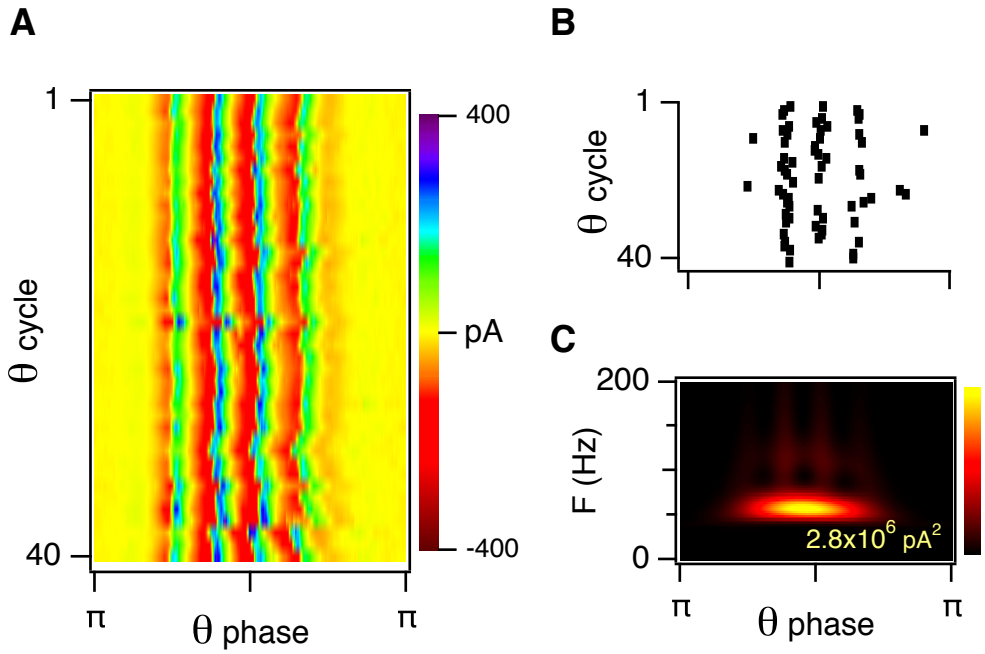

Figure 3.3: **Gamma oscillations in the model have clock-like properties.** **(A)** Inhibitory synaptic currents onto E cells, plotted during 40 consecutive theta cycles, indicate that the timing of nested gamma oscillations is consistent across theta cycles. Data are from an excitatory neuron at the centre of the twisted torus in the network described in Figures 3.1 and 3.2. Similar clock-like nested gamma oscillations are observed from neurons at all locations. **(B)** Raster plot shows action potentials of a neuron at the centre of the twisted torus as in (A), for 40 consecutive theta cycles. A spike emitted by a neuron may or may not be part of every gamma cycle. Thus, the timing of action potentials is consistent during consecutive theta cycles, but the number of action potentials may vary from cycle to cycle. **(C)** Example scalogram of the inhibitory synaptic current during 40 consecutive theta cycles for the neuron in (A and B).

should be noted however, that the model contains many free parameters that could affect the frequency of nested gamma oscillations and their relationship might not be easily predictable. These are investigated further in Chapter 4.

3.2.4 Bump movement and velocity inputs

This section addresses the question of whether, and how, the configuration of velocity inputs influences path integration in the model. Grid cells are currently widely believed to represent self-location (Moser et al., 2008). There are several possible mechanisms

of how the representation of location can be accomplished in the nervous system. The model implemented here adopts the working hypothesis that grid fields are computed by integrating self-motion signals, a process known as path integration (Etienne and Jeffery, 2004; McNaughton et al., 2006). The path integration mechanism in previous attractor models is in general realised by moving the activity bump on the neural sheet in accordance with the movement of the animal (Song and Wang, 2005; Fuhs and Touretzky, 2006; Burak and Fiete, 2009). If the relationship between movement speed of the animal and bump speed is linear, the network will perform path integration accurately. Here, the bump movement in response to velocity inputs was implemented by including asymmetries into the synaptic weight function, similarly as has been done in Burak and Fiete (2009). More details can be found in Appendix 2.2.4.

This model, unlike previous models of grid cells (Fuhs and Touretzky, 2006; Burak and Fiete, 2009), contains two separate populations of neurons, in line with the experimental evidence from MEC layer II (Dhillon and Jones, 2000; Pastoll et al., 2013; Couey et al., 2013). Thus, in order to move the bump attractor along the animal's instantaneous direction of movement, it is possible to target the velocity input onto either the population of E cells, the population of I cells, or in fact to target both populations. This can be accomplished by including the synaptic profile asymmetries into either of the target populations. Since targeting both populations is a matter of linear combination of both variants, I will focus on describing the two options separately.

Figure 3.4 shows the speed of the bump as a function of simulated movement speed, for different amounts of the synaptic profile shift. I have implemented the network so that the velocity input targets either the population of E cells (Figure 3.4A) or I cells (Figure 3.4B). In both cases, with lower shifts, the relationship saturates, and the slope of the saturation depends on the shift of the synaptic profile (Figure 3.4). However, when E cells are targeted and the synaptic profile shift is 4 neurons (Figure 3.4A), the bumps speed is linearly dependent on the movement speed in the whole simulated region of movement speeds (0–100 cm/s). On the other hand, when I cells are targeted, the saturation of bump vs. movement speed relationship is, in the best scenario when the synaptic shift is 10 neurons, around 50 cm/s. In these simulations, the synaptic shift in the case of I cells cannot be greater than $\sim$10 neurons, since the bump attractor becomes unstable at that point (unpublished observations during fine-tuning of the network).

Thus, in this setup, both variants of targeting velocity inputs are capable of linearly integrating the simulated movement speed, the saturation onset depends on the amount

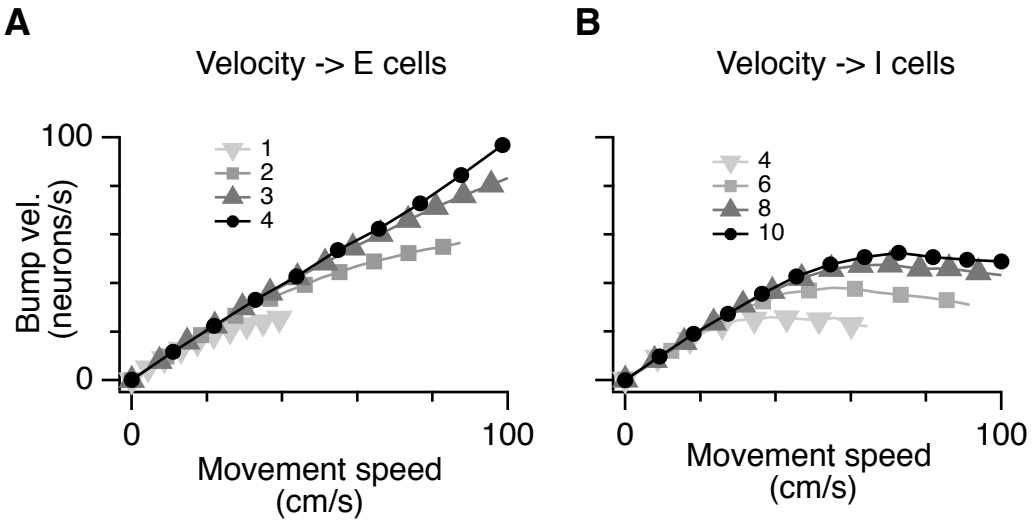

Figure 3.4: **Velocity inputs can target both excitatory and inhibitory cells. (A)–(B)** Bump attractor speed as a function of the simulated movement of an animal, for networks with different outgoing synaptic profile shifts. Networks in which the velocity-modulated input is connected to E cells (A) have a wider linear response range than networks in which the velocity-modulated input drives the I cell population (B).

of synaptic profile shift, and when I cells are targeted by the velocity input, the linear range of velocity integration is smaller, compared to the case when E cells are targeted. The smaller linear range of velocity integration when I cells are targeted is probably due to the fact that increased inhibition loses its effect once E cells are already silenced. This restricts the range of animal velocities that can be used for accurate path integration in these networks. As we will see in Section 3.2.5, both of the variants outlined here can generate stable grid firing fields, indicating that velocity inputs *in vivo* could in principle target either population.

3.2.5 Theta-nested gamma oscillations co-exist with grid firing fields

The simulations so far show that the networks are able to generate persistent attractor states that co-exist with theta-nested gamma oscillations. This section shows that the networks are able to path integrate and therefore produce grid firing fields. As previously, I will cover the two outlined cases of velocity input targets. For each one, I run 10 simulations with different random seeds. At first I simulate the network with

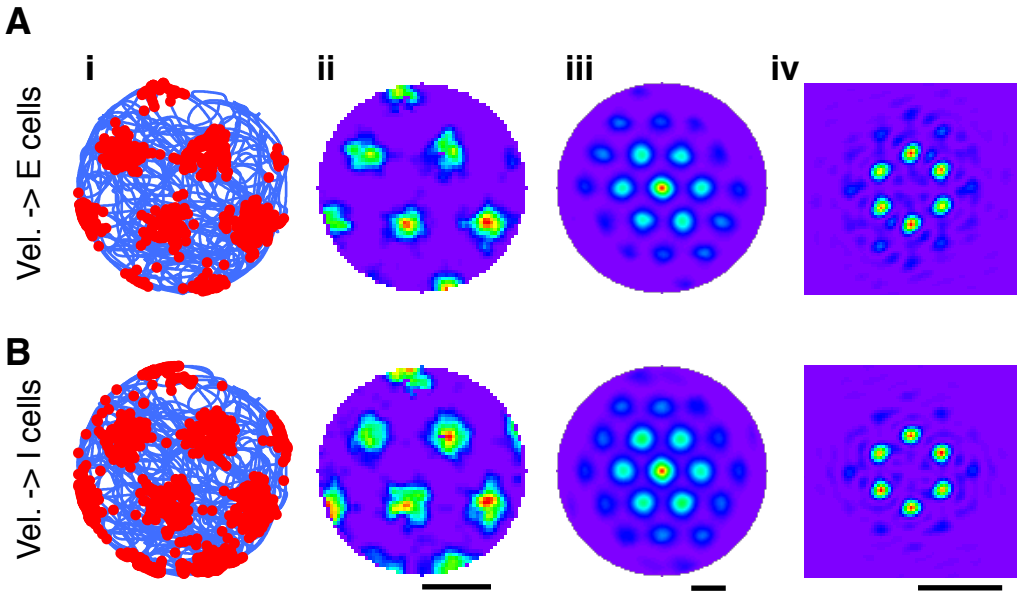

Figure 3.5: **Theta-nested gamma oscillations coexist with grid firing fields.** Example spike positions (dots) superimposed on simulated animal trajectories (lines) **(i)**, corresponding smoothed firing rate maps **(ii)**, autocorrelation plots **(iii)**, and 2D Fourier power spectra **(iv)** generated by the attractor model during simulated exploration of a circular arena. Velocity inputs were connected either to E cells **(A)** or I cells **(B)**. Gridness scores of networks with velocity inputs targeting E cells (1.1 ± 0.01, n = 10) are similar to gridness scores extracted from networks in which velocity inputs target I cells (1.12 ± 0.01, n = 10, p = 0.25). Scale bars represent 60 cm for the spiking, rate, and autocorrelation plots, and 4 m^{-1} for the Fourier spectrograms.

velocity inputs targeting the E cell population. Figure 3.5A shows an example simulation run that lasted for 1200 seconds. We can clearly see that the example neuron's firing field has a hexagonal structure. The example in Figure 3.5A shows simulations in which the synaptic profile shift has been set to 4 neurons.

The second case, in which velocity inputs target I cells, is shown in Figure 3.5B. Here the synaptic profile shift has been set to 10 neurons. At this amount of shift, the bump speed has the largest linear response as a function of animal speed (Figure 3.4B). As in the previous case, this variant is capable of producing grid firing fields as well. In both cases, the networks have almost indistinguishable gridness scores (1.1 ± 0.01, n = 10 for velocity inputs targeting E cells, and 1.12 ± 0.01, n = 10, for velocity inputs targeting I cells), in fact statistically they do not differ (p = 0.25, t-test). Therefore, grid

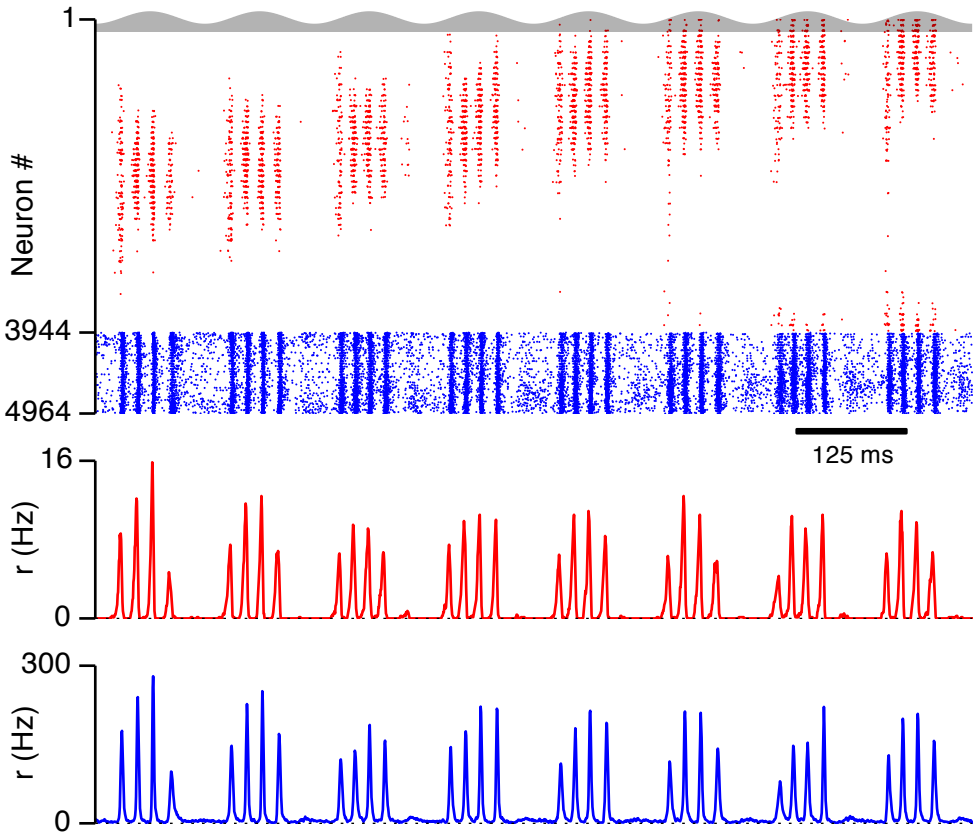

Figure 3.6: **Theta-nested gamma oscillations and population-level activity.** *Top*: Action potential raster plot of all E (red) and I (blue) cells during 8 consecutive theta cycles of the simulation of animal movement. The twisted torus has been linearised in a row-wise manner to plot action potentials of all neurons and thus the movement of the activity bump might not reflect the actual direction of the animal movement. *Centre* and *bottom*: Population average firing rate of E cells (red) and I cells (blue) estimated from the raster plot (rectangular sliding window; 2ms length and 0.5ms time step) demonstrates gamma frequency synchronisation on a population level. Theta input is illustrated in grey.

cell attractor networks can co-exist with theta-nested gamma oscillations and velocity inputs can target either E or I cells or potentially both populations. To better illustrate the co-existence of nested gamma oscillations with the attractor states that generate grid firing fields, Figure 3.6 shows action potentials of all neurons in network (top), together with the respective population-average firing rates of E and I cells (centre and bottom). This figure illustrates that nested gamma oscillations are generated together with the attractor states, but also demonstrates that gamma oscillation persists during

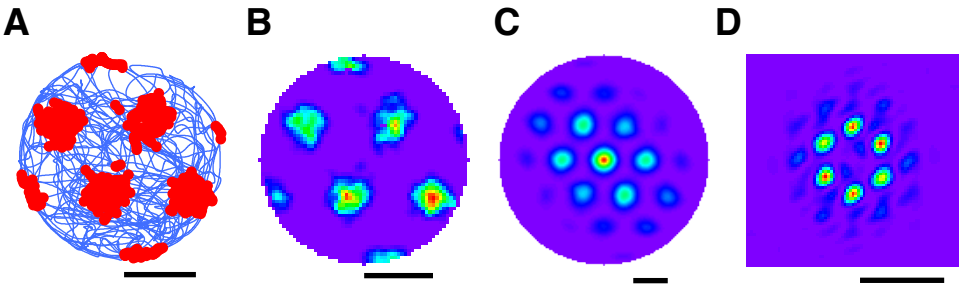

Figure 3.7: **Theta oscillations are not necessary for generation of grid fields.** Plots show grid firing fields in condition with theta oscillation replaced with a constant background current with the same mean amplitude. *Left to right:* Example spike positions (dots) superimposed on simulated animal trajectories (lines) **(A)**, corresponding firing rate maps **(B)**, autocorrelation plots **(C)**, and 2D Fourier power spectra **(D)** generated from networks with velocity inputs connected to excitatory cells and theta oscillation replaced by a constant input with the same amount of charge per theta cycle injected into cells. The gridness score of the networks without theta input is 1.11 ± 0.01, similar to grid fields in Figure 3.5 (n = 10, p = 0.43). Scale bars represent 60 cm for the spiking, rate, and autocorrelation plots, and 4 m^{-1} for the Fourier spectrograms.

the movement of the bump of activity.

All the networks presented so far contain the theta frequency modulated background excitation current. Theta oscillations are prevalent in MEC in rodents (Quilichini et al., 2010; Schmidt-Hieber and Häusser, 2013; Domnisoru et al., 2013), however there is evidence for grid cells in non-rodent species such as Egyptian fruit bats, which do not posses LFP theta oscillations (Yartsev et al., 2011). The model in this work is consistent with both of these results. Figure 3.7 shows grid fields from simulations in which the theta modulated input has been replaced with a constant drive that delivers the same amount of charge per unit time as theta modulated input currents. These simulations show that theta oscillations are not necessary for generation of grid fields. The networks form grid firing fields (Figure 3.7), with gridness score similar to grid fields from networks with theta oscillations (gridness score 1.11 ± 0.01, n=10 simulation trials, p=0.43)

Taken together, these results demonstrate that theta-nested gamma oscillations can co-exist with bump attractor states and that networks in which these two phenomena coexist are capable of path integration and computation of grid firing fields. Moreover, theta oscillations are not necessary for computation of grid fields, since in this model

they are an externally imposed input to the network.

3.2.6 Firing fields of interneurons

This section describes specific predictions about the firing fields of interneurons in layer II of the MEC. The implementation of a two population network is a specific step forward in studying the possible algorithms performed by a grid cell network. As we will see, in the current configuration, the nature of interneuron firing fields depends on the configuration of the centre-surround synaptic profile (Figures 2.3 and 2.4, Eqs. (2.11) and (2.14)). In the following text, I will present results from both E- and I-surround organisation of synaptic profiles.

3.2.6.1 E-surround firing fields

Synaptic profiles in the E-surround configuration have surround-centre arrangement. Synapses from E cells onto I cells are strongest between neurons that are far apart on the torus (given the twisted-torus boundaries). On the other hand, synapses from I cells onto E cells are strongest between neurons that are closest on the torus (Figure 2.3A). In the E cell population, this configuration generates the activity bump. The activity in the I cell population, however, results in a structure inverted with respect to the E cell population (described in more detail in Figure 3.13). As a result, firing fields of interneurons are also inverted with respect to firing fields of excitatory cells. The firing fields of interneurons are shown in Figure 3.8, along with smoothed firing rate maps, spatial autocorrelations and 2D Fourier spectrograms of the autocorrelation function.

3.2.6.2 I-surround firing fields

Excitatory cells in the I-surround configuration still have the standard grid-like firing fields (Figure 3.9A). This is not surprising, since the population activity of E cells is bump-like, as the shape of the total (indirect) inhibition does not change (cf. synaptic profile functions in Figure 2.4A). However, since the excitatory synaptic profile is now a Gaussian, inhibitory cells become active at the same positions as excitatory cells. In fact they also form a bump of activity (Figure 3.14A). Therefore, spatial firing fields of interneurons are also grid-like (Figure 3.9B), with the same orientation and spacing as grid fields of excitatory cells.

Interestingly, the differences between interneuron firing fields are an inevitable implication of the class of attractor models that lack direct feedback excitation. While in

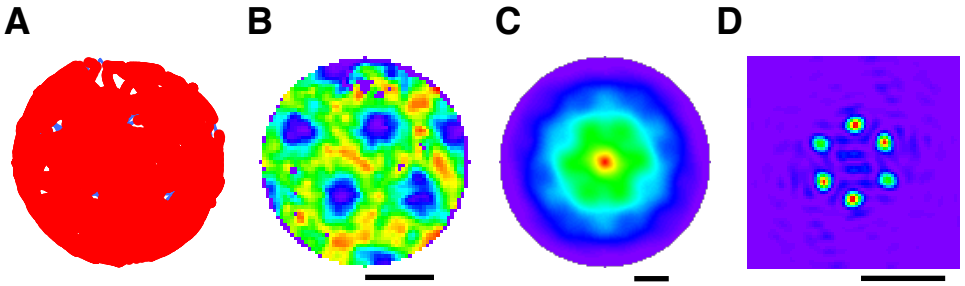

Figure 3.8: **Interneurons in the E-surround configuration have "inverted" grid-like fields.** Example spike positions (dots) superimposed on simulated animal trajectories (lines) **(A)**, corresponding firing rate maps **(B)**, autocorrelation plots **(C)**, and 2D Fourier power spectra **(D)** of the interneuron firing fields in the E-surround configuration (Figure 2.3). Scale bars represent 60 cm for the spiking, rate, and autocorrelation plots, and 4 m^{-1} for the Fourier spectrograms.

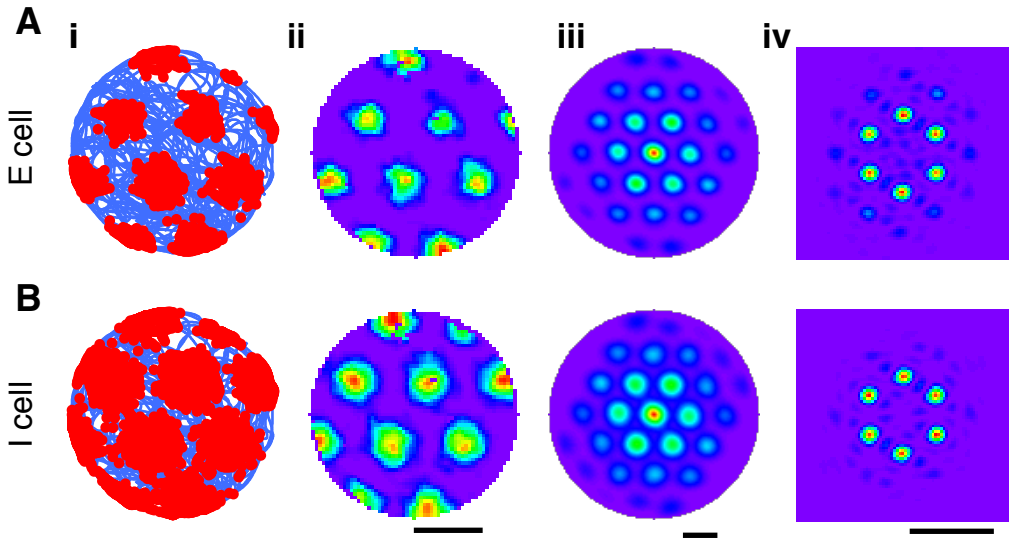

Figure 3.9: **Interneurons in the I-surround configuration have grid-like firing fields.** Example spike positions (dots) superimposed on simulated animal trajectories (lines) **(i)**, corresponding firing rate maps **(ii)**, autocorrelation plots **(iii)**, and 2D Fourier power spectra **(iv)** generated by the simulated animal movement in the I-surround synaptic configuration, for an excitatory cell **(A)** and an interneuron **(B)**. Scale bars represent 60 cm for the spiking, rate, and autocorrelation plots, and 4 m^{-1} for the Fourier spectrograms.

networks with recurrent excitation it is possible to not have spatial tuning in inhibitory cells (Compte et al., 2000), due to the fact that recurrent inhibition only serves to pre-

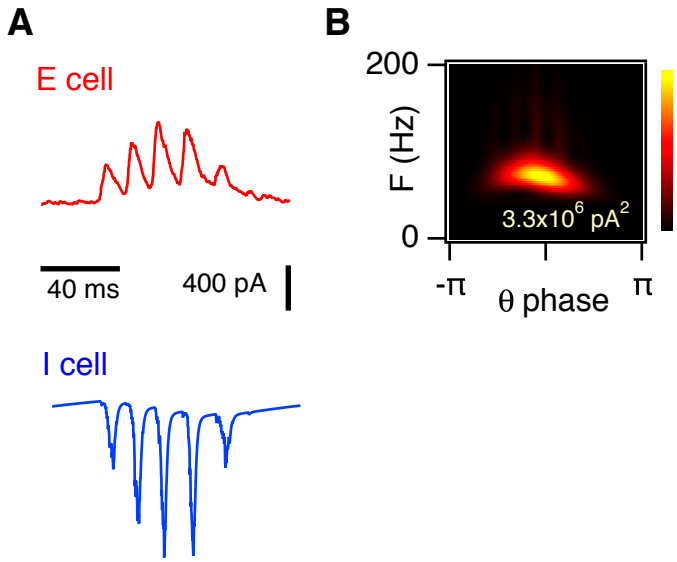

Figure 3.10: **Theta-nested gamma oscillations in networks with I-surround configuration. (A)** Examples of synaptic inhibitory (red) and excitatory (blue) currents of an E (top) and I (bottom) cell, respectively, in the network which is in the I-surround configuration. **(B)** Scalogram of the inhibitory synaptic activity as a function of theta cycle phase for the neuron in (A).

vent the network from runaway excitation, here inhibition serves a role in the tuning properties of the bump attractor and therefore interneurons must inherit spatial tuning from the excitatory cells. In the case of the E-surround configuration, interneurons will thus have "inverted" grid receptive fields. In the case of the I-surround configuration, interneurons will have grid-like receptive fields.

3.2.6.3 Nested gamma oscillations

Networks in the I-surround configuration generate nested gamma oscillations as well. Figure 3.10A shows an example of one theta cycle of inhibitory synaptic currents of an excitatory cell (red trace) aligned with excitatory current impinging onto an inhibitory cell (blue trace). We can see that the oscillations are qualitatively similar to the E-surround variation of the model, with frequency in the same range, as shown in the scalogram in Figure 3.10B.

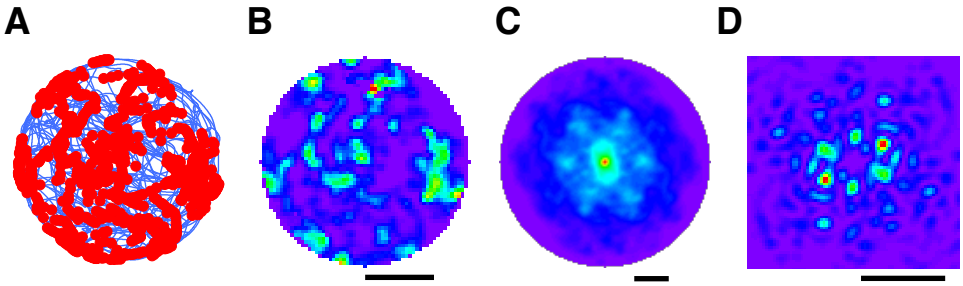

Figure 3.11: **Hippocampal place cell input is necessary for generation of grid fields.** Example spike positions (dots) superimposed on simulated animal trajectories (lines) **(A)**, corresponding firing rate maps **(B)**, autocorrelation plots **(C)**, and 2D Fourier power spectra **(D)** generated by simulations in the absence of place input. The gridness score generated by the networks is 0.22 ± 0.07, which is considerably less than the gridness score in Figure 3.5 (p = 1.16×10^{-9}, n = 15), indicating that grid firing is abolished. Scale bars represent 60 cm for the spiking, rate, and autocorrelation plots, and 4 m^{-1} for the Fourier spectrograms.

3.2.7 Hippocampal input is necessary to prevent drift of the bump attractor

This section highlights the necessity of resetting the phase of the bump attractor during the simulation, in order to produce spatial firing fields with high gridness score. Most of the grid cell attractor networks contain a source of uniform excitatory input that drives the activity of the neurons (Burak and Fiete, 2009; Couey et al., 2013), or comprise recurrent excitatory collaterals that sustain the activity of the bump without external intervention (Fuhs and Touretzky, 2006). These models are primarily implemented as rate models and thus they might not accurately capture the effect of noise, discreteness of spiking and inaccuracies of synaptic weights on the stability of bump attractors over long periods of simulation time. The results from the model implemented here show that spatially tuned inputs are necessary in order to produce grid fields with high gridness score. The network contains a source of place-like input, active every 10 seconds, that pushes the bump attractor towards the correct position. The correct positions are determined by the desired spacing between grid firing fields.

Figure 3.11 shows an example grid field from a simulation of 15 trials, in which this place cell-like input has been switched off. The average gridness score is 0.22 ± 0.07, indicating that in this case the network does not compute grid firing fields, as compared

to simulations in which place cell input is active (Section 3.2.5, $p = 1.16 \times 10^{-9}$, $n = 15$). It is currently unclear, whether the loss of grid fields without the phase resetting of bump attractor is due to any of the network or synaptic properties highlighted in the beginning of this section. A detailed discussion can be found in Section 3.3.5.

3.2.8 Membrane potential predictions

This section describes predictions of membrane potential and synaptic current dynamics in the model. One of the main goals of this work is to explore the properties of a biologically more plausible model of grid cells that captures anatomical properties of layer II of the MEC. In contrast to previous models, simulations with exponential integrate and fire neurons enable predictions of intracellular membrane potential and current dynamics. The current implementation thus provides a relatively detailed insight into the dynamics of the model and makes detailed predictions that can be tested experimentally with patch-clamp as well as extracellular recording methods.

3.2.8.1 Excitatory cells in the E-surround configuration

First, let us focus on predictions stemming out of the model in the E-surround configuration. Figure 3.12A shows a snapshot of the population activity of E cells on the twisted torus. The activity in the population forms a bump (similarly to the one in Figure 3.1A) with a peak firing rate of 20 Hz. Figure 3.12B plots membrane potential (top) and synaptic currents (bottom, inhibition) during two consecutive theta cycles, of a cell that is in the centre of the bump attractor. This cell will fire with an average firing rate of 8 Hz (one spike every theta cycle on average), and it receives nested-gamma oscillations. Note that the synaptic currents do not show the constant and theta component of the drive to the cell. Since cells outwith the bump attractor must remain silent (Figure 3.12C, top), they receive substantially larger post-synaptic currents (Figure 3.12C, bottom).

Note that in this configuration, the model not only predicts large amplitude oscillatory synaptic currents with gamma frequency, but also that the membrane potential fluctuates in the gamma frequency range. This is reflected in the membrane potential traces (Figure 3.12B,C top). *In vivo* recordings to date have only examined fluctuations in the theta frequency range (Domnisoru et al., 2013; Schmidt-Hieber and Häusser, 2013) and not gamma range. Also note that the amplitude of inhibitory post-synaptic potentials depends on the GABA reversal potential of the inhibitory synapses and thus

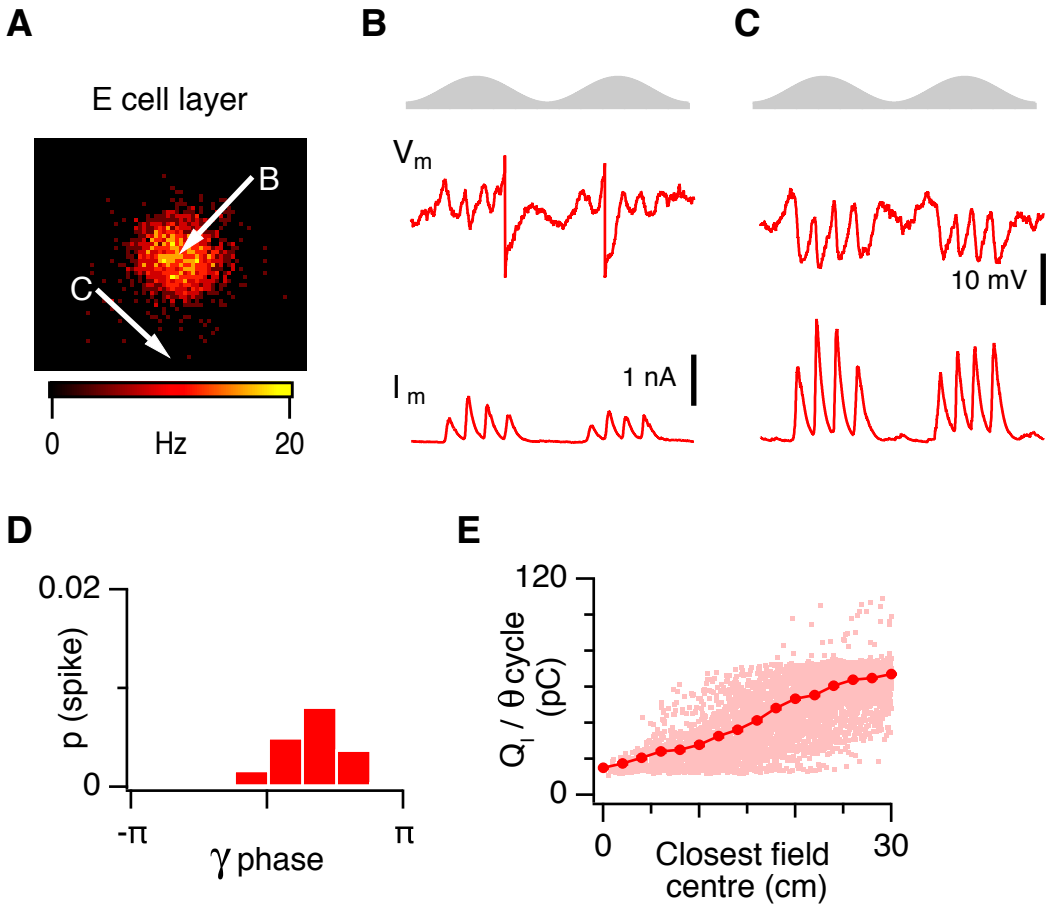

Figure 3.12: **Predicted membrane potential dynamics of E cells in the E-surround configuration. (A)** Firing rate maps showing the bump activity on the twisted torus, together with the locations of neuron examples with respect to the activity bump. The colour scale represents the firing rate of neurons. The network is in the E-surround configuration, but networks in the I-surround configuration will also generate bumps and thus the results will be qualitatively similar. **(B)–(C)** Membrane potentials and inhibitory synaptic currents of the two neurons highlighted by arrows in (A), for two consecutive theta cycles. Both neurons receive nested gamma frequency inhibitory input, but the input is lower for the neuron in the centre of the activity bump. This enables the external theta frequency drive to trigger action potentials when the simulated animal is traversing the grid field. **(D)** Spike probability as a function of gamma phase for the excitatory neurons. **(E)** Total inhibitory charge during each theta cycle, for an E cell, plotted as a function of the instantaneous animal distance from the cell's closest grid firing field.

if the inhibition is shunting, it will not reveal gamma oscillations in neuron membrane potential.

Figure 3.12D illustrates that E cells in the model tend to spike at a preferred gamma phase. Note that some *in vivo* work suggests that excitatory cells in layer II of the entorhinal cortex have a weak gamma phase modulation (Quilichini et al., 2010). However, LFP potentials *in vivo* might be much more noisy than the "idealised" synaptic currents in the model in this work, and thus the gamma phase modulation as seen in experiments can be diminished as compared to results from simulations.

The dependence of synaptic current amplitudes on neuron position within the torus is translated into the spatial dimension as well. Figure 3.12E shows total charge of inhibitory synaptic input during each theta cycle, as a function of distance from the centre of the excitatory cell's nearest grid firing field during that cycle. This relationship shows that E neurons inside their grid firing field receive minimal amount of inhibition as compared to when the animal is positioned outside the cell's firing field. In other words the model predicts that inhibition, and not excitation, controls the firing of grid cells.

3.2.8.2 Inhibitory cells in the E-surround configuration

The firing rate of I cells in the E-surround configuration is an inverse image of the population firing rate of E cells. Figure 3.13A shows a snapshot of the population firing rate for the same simulation as in Figure 3.12. We can see that as compared to excitatory cells, inhibitory cells form an "inverted" bump attractor, i.e. interneurons are active in positions on the torus where excitatory cells are silent, reflecting the synaptic profile functions (Figure 2.3). The membrane potential responses have similar properties (Figure 3.13B,C top).

As for excitatory cells, both active and inactive interneurons receive gamma modulated synaptic currents that are excitatory (Figure 3.13B,C bottom), with amplitudes reflecting positions of interneurons on the twisted torus. Spiking activity of interneurons (Figure 3.13D) is also modulated by gamma. This is consistent with the relatively fixed phase relationship of excitatory and inhibitory synaptic currents, as shown previously in Figure 3.2B,C.

Given the inverted nature of the firing of E cells in the attractor network, the relationship of total excitatory charge per theta cycle into the interneuron, as a function of the distance from the nearest grid field of an excitatory cell to whom the interneuron makes strongest connections, is inverted. Again, this is a direct result of the E-surround

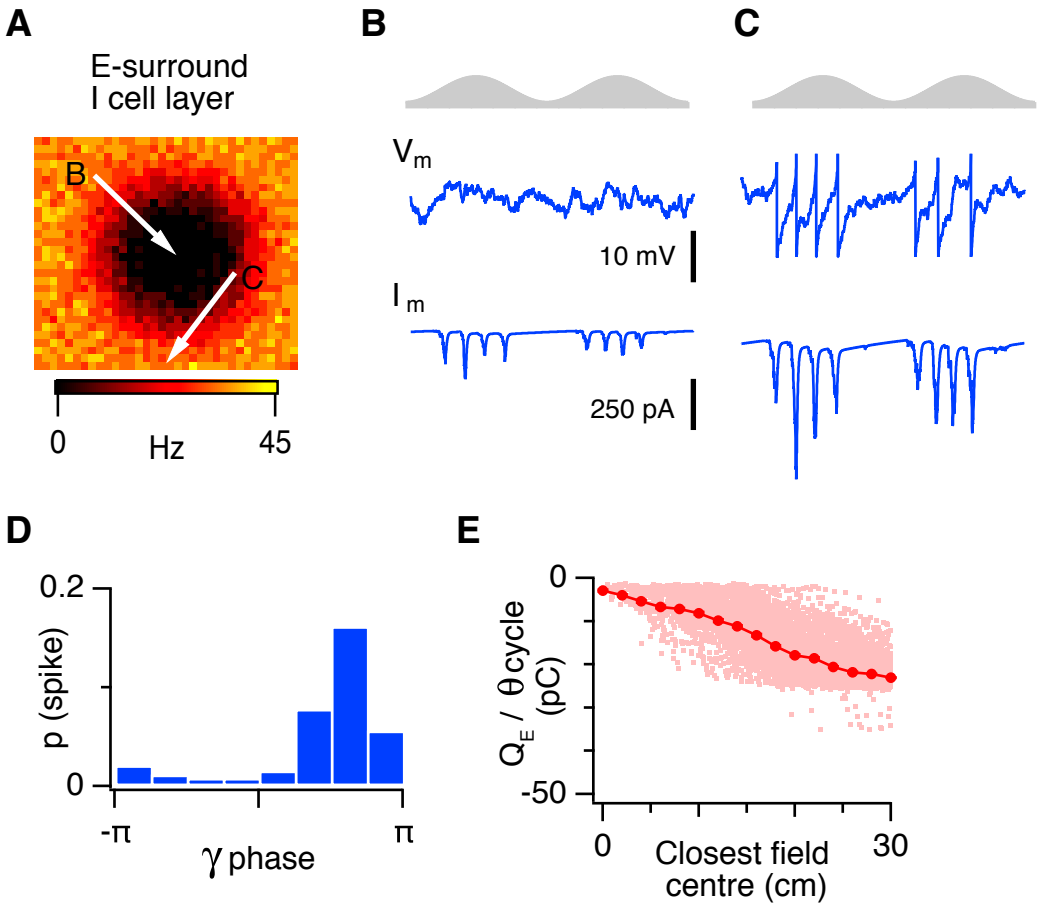

Figure 3.13: **Predicted membrane potential dynamics of I cells in the E-surround configuration. (A)** Firing rate maps showing the activity bump on the twisted torus, together with the locations of neuron examples with respect to the activity dip. The colour scale represents the firing rate of neurons. The network is in the I-surround configuration **(B)**–**(C)** Membrane potentials and excitatory synaptic currents for the two neurons highlighted in (A). Both neurons received nested gamma frequency excitatory input, however, the gamma input is lower for I neurons that project onto E cells at the centre of the bump. **(D)** Spike probability as a function of gamma phase for the inhibitory neurons. **(E)** Total excitatory charge during each theta cycle, of the excitatory synaptic input to an I cell, plotted as a function of the instantaneous distance of the animal to the nearest grid field of the E cell onto which the I cell makes strongest connections.

synaptic configuration.

3.2.8.3 Inhibitory cells in the I-surround configuration

In contrast to the E-surround configuration, interneurons in the I-surround configuration have all the membrane potential and synaptic relationships reversed. Here I show only the results for the inhibitory neurons, since E cells have qualitatively the same characteristics as in the E-surround configuration.

Again, due to the nature of synaptic strength function (Figure 2.4), both excitatory cells and inhibitory cells form a bump (Figure 3.14A). Interneurons in the centre of the bump fire at the depolarising phase of the theta cycle (Figure 3.14B top) and they receive a substantial amount of excitatory gamma burst currents (bottom). On the other hand, interneurons outside the (inhibitory) bump do not receive any inputs from the excitatory cells, due to the fact that they have to remain silent in order to form the bump. Thus, their do not receive any synaptic gamma currents.

Finally, interneurons that spike, have a similar gamma phase preference as in the E-surround configuration (Figure 3.14D) and the relationship of total charge per theta cycle as a function of distance during that theta cycle from the centre of the nearest grid firing field is again inverse to the E-surround configuration (Figure 3.14E).

3.3 Discussion

In this chapter, I have presented a spiking attractor network model of grid cells in layer II of the MEC. This is one of the most comprehensive models of grid cells in this layer as it takes into account the connectivity and circuit dynamics of principal cells and interneurons (see Widloski and Fiete (2014) for a more recent spiking attractor network of grid cells and Bush and Burgess (2014) for a hybrid interference/attractor model composed of spiking neurons).

The network reproduces several known experimental results from the MEC. Firstly, single-neuron spatial receptive fields of excitatory cells in the model are grid-like, similar to firing fields of grid cells found mostly in superficial layers of the MEC (Fyhn et al., 2004; Hafting et al., 2005; Fyhn et al., 2008; Yartsev et al., 2011; Buetfering et al., 2014). Moreover, when theta frequency input drives the network activity, membrane currents recorded from model cells show gamma oscillations nested within the theta rhythm (~55 Hz). The frequency is similar to the gamma recorded in behaving

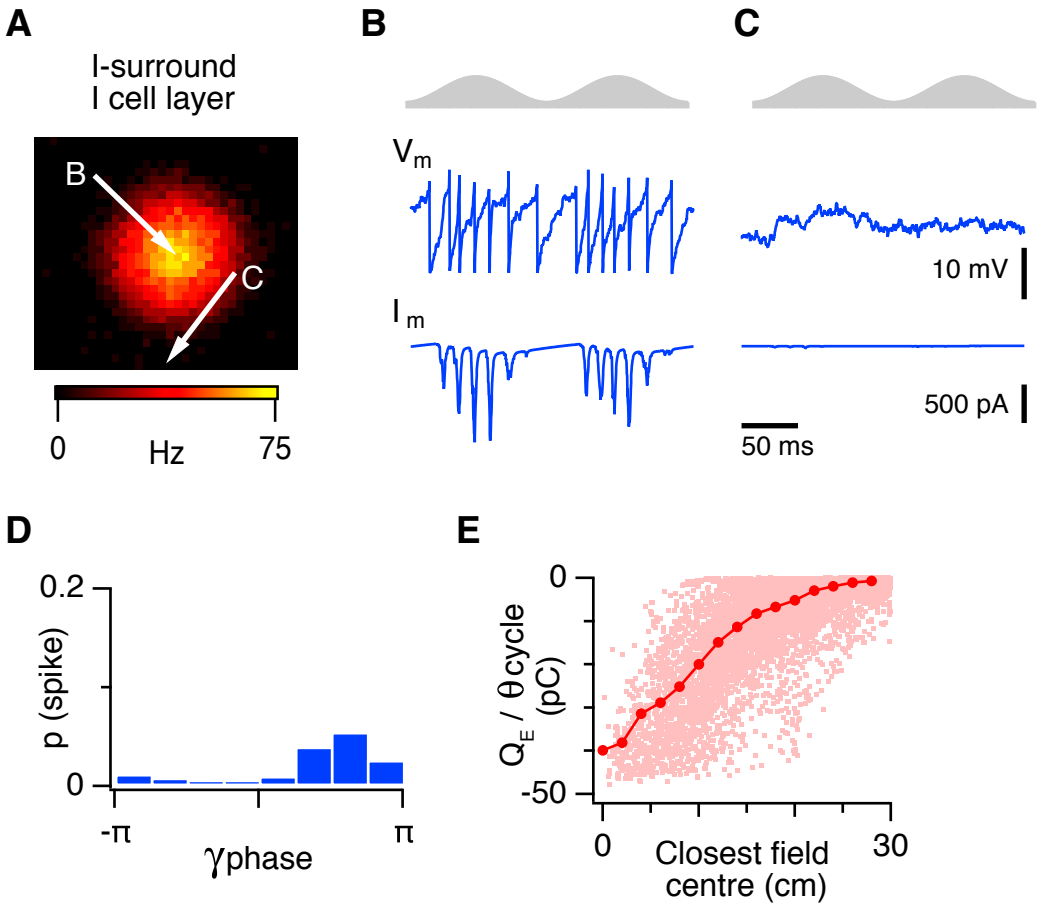

Figure 3.14: **Predicted membrane potential dynamics of I cells in the I-surround configuration.** **(A)** Colour plots show the firing rate of the population of neurons on the twisted torus, together with locations of neurons used for analysis in this figure. The network is in the I-surround synaptic configuration and the activity of I cells forms a bump. **(B)–(C)** Membrane potential and current during two theta cycles for neurons at the locations indicated in (A). Neurons inside the inhibitory bump receive nested gamma frequency excitatory input, while neurons outside of the activity bump receive little or no excitation (C) **(D)** Spike probability as a function of gamma phase for the inhibitory neurons. **(E)** Total charge of the excitatory synaptic input during each theta cycle onto an I cell, plotted as a function of the instantaneous animal distance from the firing field of the E cell to which the interneuron makes the strongest connections.

animals (~89 Hz in Chrobak and Buzsaki, 1998; ~65–140 Hz in Colgin et al., 2009), as well as gamma induced by light activation of stellate cells and FS interneurons in MEC slices (~64-100 Hz; Pastoll et al., 2013). At the same time, the frequency is higher than in pharmacologically induced gamma oscillations *in vitro* (~46 Hz; Cunningham et al., 2003, 2004). In the model, action potentials of E and I cells are phase locked to theta and gamma in the same way as is observed *in vivo* (Chrobak and Buzsaki, 1998; Colgin et al., 2009; Quilichini et al., 2010) and *in vitro* (Pastoll et al., 2013) and their relative timing is also consistent with these studies (Quilichini et al., 2010; Pastoll et al., 2013). The model thus successfully combines the attractor network theory with the concept of theta-nested gamma oscillations, and demonstrates that in principle these phenomena can co-exist together in a single system.

3.3.1 Oscillations and intrinsic properties

The network implementation in this work is based on an exponential integrate and fire neuron model (Fourcaud-Trocmé et al., 2003), which does not take into account the intrinsic properties of stellate cells (e.g. I_h current, sag), although the model of E cells incorporates a simple mechanism of after-spike hyperpolarisation. The model thus only demonstrates a sufficient condition for the generation of nested gamma oscillations by the means of a synaptic mechanism, the mechanism of pyramidal-interneuronal gamma, and as such does not require the specific components present in stellate cells in MEC layer II (see e.g. Pastoll et al., 2012). While stellate cells possess resonance properties at theta frequency (Haas and White, 2002; Erchova et al., 2004; Schreiber et al., 2004; Pastoll et al., 2012) their time constants are too long to contribute to gamma oscillations which are in the range of 30-100 Hz.

The theta frequency resonance properties could, however, contribute to the generation of the theta rhythm. The theta rhythm in this work is assumed to originate from the medial septum, since lesions of this area abolish theta oscillations in the MEC (Brandon et al., 2011; Koenig et al., 2011). The presence of resonance properties in E cells in the model could thus enhance the power of theta oscillations, although in the current implementations the theta frequency input is modeled as “ideal”, i.e. it takes the form of a noise-less cosine function. The model however does not rule out the possibility that part, or even all of the power at theta frequency could be induced from within the network itself, given appropriate mechanisms.

3.3.2 Amplitude of E and I theta inputs

In the model, the amplitude of theta frequency modulation was not chosen arbitrarily. In principle, it was favorable to set the theta input amplitude of E cells to a higher value than that of I cells, to prevent excessive excitation of I cells that would in turn mostly silence the E cells and thus abolish activity in the network. This also seemed as a configuration which was the most consistent one with the experiment performed in Pastoll et al. (2013). Thus, it might seem that the firing of I cells in the network model is only weakly modulated by theta input. This would be inconsistent with the data of Quilichini et al. (2010) that shows a comparable magnitude of theta modulation of both principal cells and interneurons in layer II of the entorhinal cortex. However, because I cells in the model receive also strong excitatory input from the E cells, their theta modulation will also be at least as strong as that of the E cells (data not shown). Thus, while the amplitude of external theta inputs might differ for the two populations, their theta modulation index will be similar due to the more complex synaptic interactions in the model.

On the other hand, the choice of the relative amplitudes of the theta inputs to the E and I populations might affect the dynamics of the network. For instance, if the external theta modulation of I cells is strong and superthreshold, I cells will fire spontaneously even without the need of excitation from the E cells. In order to sustain the firing of E cells and as a consequence the generation of a stable bump state, it would be necessary to also increase the tonic or phasic theta modulation of E cells in order to compensate for the increase in inhibition. Another possibility would be to provide a tonic input to E cells (without theta modulation) and only modulate I cells strongly in the theta frequency range. This would induce theta modulation of both populations and produce similar results as the current model does. The choice of the relative strengths of the external theta frequency modulation should therefore not be crucial for the performance of the network to generate grid firing fields and theta nested gamma oscillations.

3.3.3 Oscillatory activity, coding and information transmission

The attractor model in this work enables co-existence of theta-nested gamma oscillations with the attractor states generated by the network. The presence of gamma oscillations in the network has several implications for information transmission and coding. In this section, I will describe how the results of the model relate to the possibility of selective information transmission between brain regions (Akam and Kull-

mann, 2010), potential role of theta and gamma oscillations in working memory (Lisman and Idiart, 1995; Jensen and Lisman, 1996) and cognitive functioning (Singer, 1999). I will also discuss the lack of theta-phase precession and the relationship of the model to other work that incorporates phase precession into attractor networks.

3.3.3.1 Selective information transmission

What is the oscillatory activity in the model useful for? It has been hypothesised that nervous systems could exploit oscillatory activity for selective information transmission. For instance, Akam and Kullmann (2010) describe simulations in which a filtering network can selectively multiplex between outputs of several sender networks. The sender networks implement population codes that are either oscillating at different frequencies or asynchronous. Since the receiving network acts as a filter resonant at a specific frequency, it can band-pass filter the combined activity from the sender networks. The output of the receiving network is thus a population activity of one of the sender networks. This type of multiplexing is known as frequency division multiplexing (FDM) and is widely used in telecommunication.

The model presented in this work is consistent with the implementation of FDM by Akam and Kullmann (2010). The population activity in the model and grid firing fields represent spatial information, in the form of a multi-peaked tuning curves, while nested gamma oscillations assign a frequency band to the population coded signal that is assumed to be transmitted to a downstream population acting as a receiver. Note, however, that the attractor model in this chapter does not reproduce all the parts necessary to implement FDM in Akam and Kullmann (2010), since I do not implement the downstream filtering network. The model here only demonstrates that the grid cell system composed of the attractor network and feedback inhibition could be a part of the FDM system.

3.3.3.2 Phase precession

There is a wealth of experimental evidence suggesting that the precise phase of action potential firing with respect to ongoing LFP oscillation is important to convey information. In the hippocampus, the phase of spiking of place cells relative to theta oscillation advances as the rat passes through the cell's firing field (O'Keefe and Recce, 1993). The same phenomenon has been observed in layer II, but not layer III in the MEC (Hafting et al., 2008). Thus, the phase of spiking relative to ongoing theta rhythm

could potentially enhance coding capabilities of hippocampal and entorhinal networks.

While the network presented here contains a source of theta-modulated input, the model does not generate phase precession. Other work, however, suggests that it might be feasible to incorporate phase precession into an attractor network model of path integration. For instance, Navratilova et al. (2012) used a spiking implementation of an attractor network augmented with an after-spike depolarisation (ADP) mechanism to implement phase precession. The model consisted of a line attractor layer that generated a bump of activity. The movement of the bump was performed by a layer that contained cells sensitive to space as well as being modulated by head direction (the conjunctive grid by head direction cells (Sargolini et al., 2006)). The model also received an 8 Hz theta frequency input. In this model, phase precession was generated by a so-called look-ahead mechanism, in which the conjunctive cells drive the bump of activity ahead of the current position of the animal. At the end of the theta cycle, the bump dies out and it is subsequently regenerated by the ADP, as well as the NMDA synaptic component, present in the cells. This mechanism causes the action potentials of cells to precess when the simulated animal traverses a grid field. In another study, Schmidt-Hieber and Häusser (2013) combined velocity coupled oscillators with an attractor network. The interference between the oscillators enabled the action potentials to precess with respect to LFP theta, consistently with the observed data. In addition, Bush and Burgess (2014) implemented a hybrid oscillatory interference/attractor network model, in which the attractor network received input from several velocity controlled oscillators. In this model, the path integration itself is performed by the oscillatory interference mechanism, while the attractor network prevents the divergence of the relative phases of the velocity controlled oscillators. This enabled grid cells to generate grid firing fields, as well as phase precess with respect to theta oscillation as well. Thus, there are at least two possible mechanisms by which path integration and theta phase precession can occur. The first one is path integration performed by an attractor network, which is augmented with a precession mechanism, such as the one in Navratilova et al. (2012). The other one is that phase precession itself is implemented by the oscillatory interference mechanism (Bush and Burgess, 2014) and the network itself is augmented with a stabilizing attractor dynamics.

The mechanism of path integration and network dynamics in the model presented in this thesis is distinct from those of Navratilova et al. (2012) and Schmidt-Hieber and Häusser (2013). In contrast to Navratilova et al. (2012), the attractor network here does not generate the look-ahead mechanism and the ADP is not present in the

simulated stellate cells in this model. The precession in Schmidt-Hieber and Häusser (2013) and Bush and Burgess (2014) is generated by an interference mechanism which is not present in the network here either. Thus, the model here does not contain any additional mechanism necessary to generate phase precession, and as demonstrated in Schmidt-Hieber and Häusser (2013), the continuous attractor network on its own does not generate phase precession.

3.3.3.3 The theta-gamma code

Nested gamma oscillations have been suggested to participate in more complex temporal coding schemes (Lisman and Idiart, 1995). Lisman and Idiart (1995) have demonstrated that simple circuits with feedback inhibition can realise a short term memory mechanism consistent with psychophysical experiments. In their work, a network of pyramidal (excitatory) cells receives a subthreshold input in the form of theta frequency modulated signal, together with a suprathreshold informational input that sets the ordering of "memories". The after-depolarisation present in excitatory neurons then maintains the collective ordering of memories encoded by the firing of the cells. This process requires inhibition as well (Lisman and Idiart, 1995).

Such temporal coding schemes require precise relationship between theta and gamma oscillations, and neuronal spike timing. The attractor model here demonstrates that grid cell attractor networks are compatible with this temporal code. The timing of nested gamma oscillations in the network is preserved during consecutive theta cycles (Section 3.2.3), similarly to the experiment performed in MEC slices (Pastoll et al., 2013). At present, the timing of action potentials of single neurons is not conserved during consecutive gamma periods (Figure 3.3B). This could be due to the fact that the excitatory neurons in the network here lack the after-spike depolarisation component that is necessary to preserve relative timing of action potentials during gamma cycles (Lisman and Idiart, 1995). Another possible mechanism to ameliorate this situation would be the presence of theta phase precession, which could assign a preferred theta phase to spikes of neurons, as a function of animal position (O'Keefe and Recce, 1993; Hafting et al., 2008). Other models deal with combining phase precession with attractor models (Navratilova et al., 2012; Schmidt-Hieber and Häusser, 2013; Bush and Burgess, 2014). This would make, in principle, possible to preserve relative spike timing of neurons, similarly to Lisman and Idiart (1995). Therefore, the combination of an attractor network and theta-nested gamma oscillations is compatible with temporal coding schemes which require precise relationship of a fast and slow oscillation.

3.3.3.4 Neural synchrony and perceptual binding

The combination of attractor states and theta-nested gamma oscillations suggests that rate and temporal coding can co-exist together (Pastoll et al., 2013). In principle, the synchrony generated by the nested gamma oscillations could be used for various perceptual tasks. Theories have been devised that propose that synchrony plays a critical role in perceptual binding (Von Der Malsburg, 1981; Singer, 1999). The temporal binding hypothesis proposes that the apparent conundrum of how different objects are considered to be related together by the nervous system, i.e. bound into a single percept, can be solved by neural synchrony (Singer, 1999). Here, objects are separated by space (e.g. in the primary visual cortex), but represented by synchronous activity of two or more ensembles of neurons. This synchronous spiking can thus more effectively drive the activity of a downstream population representing the percept.

While this work is conceptually consistent with the temporal binding hypothesis, it only provides a possible substrate for such a mechanism. In fact, the temporal binding hypothesis has been substantially criticized for actually not solving the binding problem (Shadlen and Movshon, 1999). For instance, the temporal binding hypothesis does not describe how binding is computed, only how it is signalled; the temporal binding hypothesis is presented as primarily occurring in early stages of cortical processing, while Shadlen and Movshon (1999) argue that the binding problem is rather computed by a high-level computational process; the correlated neural activity, an argument used in favour of the binding by synchrony hypothesis, has not been convincingly shown to be related to the binding problem (Shadlen and Movshon, 1999). Thus, while the attractor model here can generate synchronised neural activity, this might not be directly related to theories that propose perceptual binding by synchrony.

3.3.4 What is the nature of the velocity signal?

Attractor networks that perform an integrator function require a representation of the integrated quantity as an input to the network. This is regardless of whether the networks function as angular integrators, e.g. in the models of head direction system (Taube et al., 1990a,b; Song and Wang, 2005; Xie et al., 2002; Zhang, 1996; Boucheny et al., 2005) or as path integrators (Conklin and Eliasmith, 2005; Fuhs and Touretzky, 2006; McNaughton et al., 2006; Burak and Fiete, 2009; Pastoll et al., 2013; Couey et al., 2013).

The current attractor models, including the one implemented in this thesis, con-

sider only simplified and idealistic implementations of velocity inputs. Firstly, most of the initial implementations (Fuhs and Touretzky, 2006; Burak and Fiete, 2009) and the implementations derived thereof (Navratilova et al., 2012; Pastoll et al., 2013; Couey et al., 2013) have current based inputs. These inputs are usually computed from velocity vectors represented as a difference of simulated positions of animals (Eq. (2.17); Burak and Fiete, 2009). The extent to which these representations of velocities are biologically plausible and the amount of experimental data are quite limited. Thus the mechanistic plausibility of path integration implemented in the brain still remains elusive.

How could the velocity input to the path integrator be implemented in real brains in animals? Pyramidal cells in hippocampus have been shown to correlate their firing rate with running speed of animals running on linear tracks (Huxter et al., 2003). Cells linearly sensitive to speed have also been observed in the hippocampus (O'Keefe et al., 1998) and in the medial entorhinal cortex (Kropff et al., 2014). Also, cells whose firing rates are modulated by movement direction have been reported (Welday et al., 2011). If the output of a population of such speed sensitive cells was fed into an attractor model and the connections between hippocampus and grid cells were set up by an appropriate plasticity mechanism, this speed modulated input could in theory provide information about the speed of an animal that can be used to drive the bump attractor. On the other hand, Sargolini et al. (2006) reported speed modulation of grid, head-direction, and conjunctive grid vs. head-direction cells in the MEC as well. This could point to a source of a speed signal that is rather generated locally and could readily be integrated into the attractor network present in layer II.

While both Huxter et al. (2003) and Sargolini et al. (2006) report positive correlations between speed of movement and firing rate of various cells in hippocampus and MEC, the reported correlation coefficients are low. Huxter et al. (2003) report that the Pearson's correlation coefficient is 0.2, while in Sargolini et al. (2006) the correlation coefficient between speed, head-direction, and conjunctive cells are 0.24, 0.14, and 0.42 respectively. On the contrary, the theoretical models of grid cells, including the model presented here, rely on a precise speed input that either modulates the frequency of oscillators (Burgess et al., 2007), or translates the bump of activity in accordance with the position of the animal (Fuhs and Touretzky, 2006; Burak and Fiete, 2009). Therefore, it needs to be determined, whether the speed signals reported in Huxter et al. (2003) and Sargolini et al. (2006) can be considered as an accurate source of velocity input to path integrators.

Even though Huxter et al. (2003) report certain relationship between speed and firing rate of hippocampal pyramidal cells, their recordings were performed in CA1 and CA3 and dentate gyrus. While CA1 has extensive projections to entorhinal cortex (Witter and Amaral, 2004), these are mostly into deeper layers and not to layer II or perhaps even layer III, where the majority of grid cells are found (Hafting et al., 2005; Sargolini et al., 2006).

Recently, CA2 has been suggested to have direct connections to layer II in the MEC (Rowland et al., 2013). However, the results have not been confirmed by other recent studies that mapped output connectivity of the CA2 region (Hitti and Siegelbaum, 2014). Moreover, it is not clear whether there are any speed modulated cells in CA2. Thus the evidence of an extra-hippocampal speed input is currently not confirmed.

While putative speed cells might code for the magnitude of an animal's motion, the attractor model hypothesis requires a directional input. This input can be realised in the form of cells that are sensitive to movement direction. Thus, the situation is more viable here, since the MEC itself, as well as areas surrounding it, contain head direction cells (Sargolini et al., 2006; Taube et al., 1990a,b). In the MEC, deeper layers contain both conjunctive grid-by-head direction cells as well as pure head direction cells (Sargolini et al., 2006), however it has not been established yet whether head direction cells in the deeper layers project directly to stellate cells, a necessary condition for the current implementations of the attractor models. At the same time, it is known that presubiculum has projections to layer II (Witter and Amaral, 2004), but again, any direct connection to functionally identified grid cells has not been investigated.

Recently, Raudies et al. (2013) raised an issue about the relevance of head direction cells for the coding of movement direction. Raudies et al. (2013) have analysed recorded movement trajectories and firing of head direction cells, and found that head direction cells in fact do not encode movement direction. Nor did the authors find any tuning to the difference between movement and head direction in these cells. Raudies et al. (2013) thus subsequently show that an oscillatory interference model of grid cells that uses the head direction information instead of movement direction has low gridness scores. The authors thus question the relevance of head directional input to grid field computation that implements path integration.

In summary, the substrate supporting the attractor based path integration mechanism is present, but the precise details that could directly support or refute the existence of this kind of mechanisms have not been elucidated yet. The future experimental and

perhaps modelling work related to attractor models of grid cells thus needs to answer two fundamental questions: how are the velocity and movement direction signals reported in the above mentioned text connected to an attractor network, and whether these velocity signals are precise enough to support path integration over longer distances.

3.3.5 Hippocampal input

It is well known that attractor networks suffer from drift of the position of bump of activity over time even when it is supposed to remain stable (Eliasmith, 2005; Burak and Fiete, 2009). Such drift, whether it is systematic or caused by noise in the system, inevitably leads to the blurring or complete disappearance of grid fields.

Naturally, drift must occur in the attractor model in this work as well. This could be due to the source of noise in the network or imperfections in the synaptic profile strengths caused by finite network size or synaptic profile shifts. The model thus uses an "absolute" allocentric input that resets the bump attractor position periodically. The resetting input is realised as an input coming from place cells in the hippocampus. The model currently demonstrates that gridness score drops on average to zero, measured over the time period of 20 minutes, when the place cell input is disconnected from the network. At the same time, the input from place cells is not the sole driver of grid activity in the attractor network. The input is active only for 100 ms every 10 seconds. This is sufficient to reset the position of the bump of activity, but the grid pattern is generated primarily by integration of velocity inputs.

The necessity of hippocampal input for the stability of firing fields in superficial layers of the MEC has been demonstrated earlier by lesions of hippocampus (Fyhn et al., 2004). While Fyhn et al. (2004) do not treat firing fields of cells in the MEC as grid fields, a later study has shown that input from hippocampus is necessary for achieving high gridness scores of grid cells, since temporary inactivation of hippocampus abolished grid fields (Bonnevie et al., 2013). However, it is not clear to what extent the abolished hippocampal input contains spatially tuned components and to what extent the input was only a source of a uniform, background excitation current.

Is it anatomically plausible that such input could target actual stellate cells in layer II of the MEC? As was mentioned before, it is known from anatomical studies that the CA1 region projects to deeper layers of the MEC (Witter and Amaral, 2004). Therefore it is likely that neurons in superficial layers receive the place input from somewhere

else. A candidate region could be CA2 which has recently been shown to have direct connections to principal cells in layer II of the MEC (Rowland et al., 2013; although see Hitti and Siegelbaum (2014) which reports that CA2 does not project to layer II in the MEC). At the same time, it is not clear from the limited experimental evidence, whether CA2 pyramidal cells are place cells. Thus, more experimental evidence is needed on the contribution of hippocampus to the firing fields of grid cells.

3.3.6 Do interneurons have regular firing fields?

The two population attractor model that I implemented is the first one to provide direct predictions about the firing fields of interneurons in two dimensional arenas. Earlier, and more recent models of grid cells implement reduced versions of attractors, in which grid cells make direct inhibitory (Burak and Fiete, 2009; Couey et al., 2013), or both excitatory and inhibitory connections (Fuhs and Touretzky, 2006). While this already violates Dale's law, which states that a neuron can only make excitatory or inhibitory connections, but not both at the same time, it is possible to implement the attractor without excitation, by appropriately setting up the Mexican hat connectivity (Burak and Fiete, 2009).

It is however well known that stellate cells, most likely being the majority of grid cells in layer II of the MEC, do not connect directly with each other, but indirectly via fast spiking interneurons (Dhillon and Jones, 2000; Pastoll et al., 2013; Couey et al., 2013). The reduced models however do not provide any information about the firing fields of interneurons. The two population attractor model does. And in the configuration where direct excitation is missing, it makes specific predictions about the firing fields of interneurons. Namely, the model predicts, that, depending on whether the excitatory/inhibitory connections are surround/centre or centre/surround, interneurons should have either inverted firing fields (Figure 3.8) or firing fields with the same spacing and orientation as those of grid cells they connect to (Figure 3.9). It is important to note that the excitation and inhibition here is not simply a naïve implementation of the purely inhibitory model of Burak and Fiete (2006), in which one inhibitory cell would correspond to an inhibitory synapse from a grid cell. The excitatory and inhibitory synapses have a wide, divergent or convergent connectivity and this connectivity is shared by the FS interneurons in the network. Thus, the implementation of a Mexican hat profile without recurrent excitation predicts that firing fields of FS interneurons in layer II of the MEC have a regular structure.

Recent recordings from parvalbumin positive FS interneurons in the MEC have provided some information about their firing fields in two dimensional arenas (Buetfering et al., 2014). Buetfering et al. (2014) have recorded from hundreds of parvalbumin positive interneurons and grid cells in the MEC of mice and have shown that the majority of interneurons do not have hexagonal firing fields, since their gridness score was close to zero (Buetfering et al., 2014). Is it possible that the firing fields of interneurons in the Buetfering et al. (2014) study are instead the "inverted" grid fields, as predicted by the I-surround configuration in the model presented here? It is unlikely that the gridness score analysis of the interneuron firing fields would yield a high gridness score. The reason is that the autocorrelation function of the inverted fields has only a single peak in the centre (Figure 3.8). Therefore, the rotations of the autocorrelations, as performed by the gridness score computing algorithm (Hafting et al., 2005), would only yield a constant correlation coefficient between the rotated autocorrelations, regardless of the rotation angle. Thus, the difference between the maxima of the correlation coefficients at 30, 90, and 150 degrees and the minima at 60 and 120 degrees would result in low gridness scores. An alternative way to examine the hexagonality of the inverted firing fields is to use the 2D Fourier transform of the spatial firing field (Krupic et al., 2012). For the inverted fields, 2D Fourier transform shows three distinct peaks separated by 60 degrees (Figure 3.8D). While purely visual analysis of the interneuron firing fields in the Buetfering et al. (2014) study does not suggest any periodicity, they have not performed this analysis.

Adding to their result, however, Buetfering et al. (2014) show that some FS interneurons which do not have grid fields receive input from grid cells, and thus it is likely that they are part of the mechanism of feedback inhibition identified in earlier studies (Pastoll et al., 2013; Couey et al., 2013).

The results of Buetfering et al. (2014) thus suggests there are at least two possibilities of how a grid cell network could be implemented. First, grid cells in layer II could be part of a larger grid cell network that spans several layers of the MEC. In particular, the connectivity between stellate cells in layer II and cells in layer III, in which some of the pyramidal cells also have grid fields, has not been elucidated yet. This interaction with the deeper layer would allow for more extensive connections than only pure feedback inhibition between stellate cells in layer II. The second option is that the current implementation of the two population grid cell attractor model is perhaps too simplified and there are connectivity rules that allow for building stable attractors that do not require interneurons to have regular firing fields. Indeed, Buetfering et al.

(2014) show that while the majority of interneurons in layer II do not have grid fields, their firing fields carry a certain amount of spatial information. A final possibility is that grid fields are generated by some other mechanism that is not yet conceived of. Currently, there does not seem to be further evidence that would favour any of these hypotheses and thus there is room for more experiments and modelling to elucidate the role of excitation and inhibition in the grid cell network.

3.3.7 Related work

The idea of attractor models is by no means a new one. Before grid cells were discovered (Hafting et al., 2005), line attractors were used for modelling responses of head direction cells (Boucheny et al., 2005; Song and Wang, 2005; Zhang, 1996; Goodridge and Touretzky, 2000; Xie et al., 2002) and two dimensional attractor models were proposed as a path integration mechanism for place cells (McNaughton et al., 2006). However, continuous attractors predicted a regularly repeating structure, which was not observed in the single firing fields of place cells. Moreover global and rate remapping of place cells (Leutgeb et al., 2005) did not correspond with a "fixed metric space" of a path integrator. Thus, after the introduction of grid cells (Hafting et al., 2005), attention has shifted onto implementations of attractor models to reproduce the firing fields of grid cells.

There are various ways in which attractor network implementations might vary. For instance, some models of grid cells implement continuous attractors with multiple bumps of activity (Fuhs and Touretzky, 2006; Burak and Fiete, 2009; Couey et al., 2013), while others only have a single bump (Guanella et al., 2007; the model presented in this work and published in Pastoll et al., 2013). Multiple-bump attractor models can further be distinguished based on the specific implementation of boundaries. These can either be periodic (Burak and Fiete, 2009; Couey et al., 2013; Guanella et al., 2007), or non-periodic (Fuhs and Touretzky, 2006; Burak and Fiete, 2009). Since the arrangement of bumps on the neural layer is already hexagonal, both the periodic and the non-periodic variants are sufficient to also generate hexagonal firing fields. On the other hand, single bump models require periodic boundaries in order to obtain the hexagonal structure of firing fields, since the hexagonality is not inherently present in the population activity (Guanella et al., 2007; Pastoll et al., 2013). In terms of biological detail, most attractor models of grid cells are rate-based (Fuhs and Touretzky, 2006; Burak and Fiete, 2009; Couey et al., 2013) or only implement a limited form of spik-

ing activity (Burak and Fiete (2009); although see some more recent spiking models by Bush and Burgess (2014) and Widloski and Fiete (2014)). Moreover, these models do not take into account the presence of separate excitatory and inhibitory populations of neurons. Instead, they either implement connectivity rules in which excitatory cells send both excitatory and inhibitory synapses to other cells in the network (Fuhs and Touretzky, 2006), or the networks are implemented as inhibitory neurons only (Burak and Fiete, 2009; Couey et al., 2013). In the following text I will describe previous and current models of grid cells (or models originally intended to reproduce activity of place cells), and compare their architecture to the work presented here.

The attractor model of grid cells presented in this work is derived from the early and more recent works of two dimensional bump attractors that were proposed to model path integration in the hippocampal system. Perhaps the first to accomplish this was the work by Samsonovich and McNaughton (1997), in which the authors proposed a "multichart map-based path integrator" (MPI). MPI comprises a set of sub-networks that model a sensory array, place cells, a layer of integrators, a head direction system, and a layer of cells sensitive to movement. Place cells and integrator cells consist of several "charts", each being responsible for one environment an animal moves in. The network was the first attempt to comprehensively describe the putative path integration system in rodents, however, it focused on place cells. The place cell sub-network consisted of a continuous attractor network that generated a bump of activity, while the integrator sub-network provided the network with a velocity-dependent movement of the place cell bump layer. This architecture was later implemented in a one-dimensional model of grid cells and phase precession in Navratilova et al. (2012) that was discussed in Section 3.3.3.2. Later, Conklin and Eliasmith (2005) proposed a path integration model based on the earlier developed neural engineering framework (Eliasmith and Anderson, 2004). Their model results in a two dimensional toroidal attractor model (of place cells), that is capable of path integration. The synaptic profiles are Gaussian, with shifts in their centres, similar to Fuhs and Touretzky (2006) and Burak and Fiete (2009). The model of Conklin and Eliasmith (2005) was a move forward, when compared to the MPI architecture of Samsonovich and McNaughton (1997). The model was more compact and with better robustness to noise. In contrast to the work presented here, their model is still a simplified version, since it is composed of only a single population of excitatory cells.

The works of Samsonovich and McNaughton (1997) and Conklin and Eliasmith (2005) were done before the hexagonal properties of medial entorhinal cells were iden-

tified, even though Fyhn et al. (2004) would already suggest this. After Hafting et al. (2005) was published, it was obvious that the repeating nature of grid firing fields could be easily implemented by two dimensional attractor networks with or without toroidal boundaries. This was accomplished by Fuhs and Touretzky (2006) for non-toroidal boundaries, while Burak and Fiete (2009) have later shown that the model of Fuhs and Touretzky (2006) suffers from too much drift and rotations of the hexagonal population firing rate patterns (Burak and Fiete, 2006) and proposed a refined version of the path integrator implemented both with and without repeating boundaries. Their model could path integrate with realistic rodent trajectories recorded in experimental sessions (Burak and Fiete, 2009). Thus, the first attractor models that explicitly reproduced the firing fields of grid cells were composed of rate-based neurons that were either purely excitatory or inhibitory, but did not model interneurons explicitly, as was done in this work.

The attractor networks proposed in the more recent models of path integration in the MEC (McNaughton et al., 2006; Fuhs and Touretzky, 2006; Burak and Fiete, 2009) all generate multiple bumps of activity that are more or less spread in a hexagonal pattern on a sheet of neurons. This is, however, not the only solution to generate hexagonal firing fields. Guanella et al. (2007) observed that a single bump of activity on a twisted torus can accomplish the same task. This simplifies the design of the attractor model considerably and allows for robust implementations of bump attractor models with fewer neurons than attractors with multiple bumps, as was done in Fuhs and Touretzky (2006) and (Burak and Fiete, 2009). The bump attractor model in this work and in Pastoll et al. (2013) uses the same principle, since it is simpler, computationally less expensive, and thus allowing for a greater level of biological detail in modelling.

The current work thus builds on top of the previously implemented rate models of grid cells (Fuhs and Touretzky, 2006; Burak and Fiete, 2009) and the idea of using a twisted torus topology for achieving the hexagonal structure of firing fields of grid cells (Guanella et al., 2007). However, unlike this previous work, the model presented here is implemented with exponential integrate and fire neurons, and extends all of the previous network architectures with an explicitly modelled population of FS interneurons (also see work by Bush and Burgess (2014) who have built a hybrid oscillatory interference/attractor network model, and Widloski and Fiete (2014) who explore attractor networks of grid cells in a developmental context). The usage of integrate and fire neurons was motivated by their biological plausibility, which allowed me to reproduce theta-nested gamma oscillations that were similar to those present in the MEC

in behaving animals (Chrobak and Buzsaki, 1998; Quilichini et al., 2010) and *in vitro* (Pastoll et al., 2013). The explicit inclusion of the FS interneurons in the model, on the other hand, provided specific predictions about the firing fields of these cells in behaving animals. These predictions were already tested in mice (Buetfering et al., 2014).

The combination of continuous attractor properties, strong inhibitory feedback, and theta modulation makes the model presented here distinct from more reduced models (Onslow et al., 2014) and rate and spiking models that simulate oscillatory bumps but do not generate grid firing fields (Roxin et al., 2005, 2006). Onslow et al. (2014) explored the properties of a rate model in which the dynamics was reduced to a two dimensional dynamical system with a sigmoid activation function. Thus, there are two main distinctions between the model here and by Onslow et al. (2014). First, the rate model in Onslow et al. (2014) is a two dimensional dynamical system and therefore cannot describe the emergence of bump attractors. Second, the rate model investigated in Onslow et al. (2014) does not contain any delays and thus requires presence of E-E connections to generate a stable limit cycle. In the model presented here, the presence of E-E connectivity has been explicitly excluded from the model, due to the constraints imposed by experimental evidence from the MEC (Dhillon and Jones, 2000; Pastoll et al., 2013; Couey et al., 2013). Other models (Roxin et al., 2005, 2006) explore rate dynamics in networks with delays, complemented with simulations of spiking networks. The model presented here is qualitatively consistent with the analytical derivation of stable states in these networks. For instance, Roxin et al. (2005) show that strong uniform inhibitory feedback is necessary for the network to achieve an "oscillatory bump" state in the rate implementation, as well as in the spiking implementation (Roxin et al., 2005). The same principle had to be used in this work to generate bump states that co-exist with theta-nested gamma oscillations. However, a distinctive feature between the model here and in Roxin et al. (2005) is that here the network functions under the conditions of theta-modulated inputs, and also generates grid firing fields. Thus, I believe the work presented in this chapter helps to provide significant contributions to the question of how grid fields, as well as theta-nested gamma oscillations are generated in the medial entorhinal cortex.

Chapter 4

Intrinsic noise promotes independent control of gamma oscillations and grid firing by the strength of recurrent inhibitory and excitatory synaptic connections

4.1 Introduction

Noise is ubiquitous in nervous systems (Faisal et al., 2008) and neural circuits face the challenge of optimising their parameters in order to perform useful computations in the face of this noise. In general, noise is considered to have a detrimental effect on signal transmission (Shannon, 1956). Only a few studies so far have addressed possible positive effects of noise (Longtin et al., 1991; Benzi et al., 1999; Shu et al., 2003) and they have only dealt with signal transmission. Thus, the impact of noise on actual computation performed by neural circuits remains elusive.

In neocortical circuits, noise is usually considered detrimental for information transmission due to abundant excitatory reverberation mechanisms (Faisal et al., 2008). On the other hand, stellate cells in layer II of the MEC, unlike excitatory cells in many neocortical regions, are connected exclusively by feedback inhibition mediated by fast spiking interneurons (Dhillon and Jones, 2000; Pastoll et al., 2013; Couey et al., 2013). The impact of noise on computations performed by such a circuit has not been investigated yet.

Local field potential recordings from MEC show a prominent phase-amplitude coupling effect between theta (4-10 Hz) and gamma (30-100 Hz) oscillations (Quilichini et al., 2010). In this circuit, the power of gamma oscillations is temporally modulated by the phase of an ongoing theta rhythm. Changes in power and/or frequency of oscillations could be linked to certain psychological disorders (Buzsáki et al., 2013). For instance, changes in the ratio of excitation and inhibition and accompanying abnormalities in the oscillatory activity have been suggested as a possible cause for cognitive disorders such as autism and schizophrenia (Rubenstein and Merzenich, 2003; Lewis et al., 2012). However, the mechanistic relationships between cognitive function, changes in amounts of synaptic excitation and/or inhibition, neural network dynamics, and neural network computations, are not known.

In this chapter, I use the attractor network model of grid cells developed in Chapter 3 to explore these issues. I have optimised the previous version of the attractor network in order to support large scale simulations of animal movement in which the synaptic strengths between the excitatory (E) and inhibitory (I) populations can be freely varied. I find that both gamma oscillations and grid fields are sensitive to variations in the synaptic strengths between the E and I populations, but their relationship differs. The properties of gamma provide very little information about the network's ability to form bump attractors or generate grid firing fields. Thus, gamma activity does not predict rate-coded computation well. Unexpectedly, the simulations show that this relationship is noise-dependent. In networks without noise the range of E and I synaptic strengths that support gamma and grid fields is restricted. With addition of a moderate amount of noise, the range of the E and I synaptic couplings that supports grid firing and gamma is massively expanded. These results identify noise as a critical factor for generation of grid fields and gamma oscillations, as well as suggest that, while the rate and temporal coded computations share the same neural substrate, their roles in cognitive processes might nevertheless differ.

This chapter is organised into several sections. Section 4.2 describes the differences between the original model presented in Chapter 3, and the model used in this part of the thesis. Section 4.3 describes the results of the simulations, namely how noise and variations in global synaptic couplings between the excitatory and inhibitory populations influences the dynamics of the network. This section deals mostly with how both the computation of grid fields and nested gamma oscillations are affected by the respective changes in parameters. Finally, Section 4.4 provides some concluding remarks for this chapter.

4.2 Attractor network model extensions and analysis methods

This section describes, in detail, extensions of the attractor model from Chapter 3. While the previous chapter dealt with implementing an attractor model with feedback inhibition and showing that the dynamics of the model resembles *in vivo*-like theta-nested gamma oscillations, in this chapter I build upon this previously developed architecture. I explore the dynamics of the model as a function of global synaptic coupling between the excitatory and inhibitory populations, as well as levels of noise in the network.

The model that has been simulated in this chapter is conceptually equivalent to Chapter 3 and Pastoll et al. (2013). However there are a number of differences and extensions that need to be mentioned to fully understand the implications of the results. These differences are described in the following text.

4.2.1 General network architecture

In this chapter, a two-population network of integrate and fire neurons has been simulated (Figure 4.1A). A detailed description of the membrane potential dynamics can be found in Appendix 2.2.2. Both populations of neurons are arranged on a twisted torus, that can be visualised as two separate layers of neurons, as shown in Figure 4.1A. Since the topology is a twisted torus, the boundaries wrap around in a way illustrated in Figure 2.1B. Figure 4.1A only shows the torus unwound, and separate for each population. Here, I follow the same convention as in Chapter 3, in which all plots and panels related to excitatory cells are painted in red colour, while all data related to inhibitory cells are painted in blue, except for cases where the colour is unrelated to the identity of the neuronal population. Thus, the topology of the network is equivalent to the version presented in Chapter 3.

The number of E cells in this chapter is different from the networks simulated in Chapter 3, where the neurons were arranged on a twisted torus with dimensions 68×58 neurons, in total 3944 neurons. Here, each population consists of 1024 neurons. These are arranged on the twisted torus such that its sizes are 34×30 neurons in vertical and horizontal directions, respectively. The sole motivation for decreasing the number of excitatory cells was to reduce the computational demands of the model. The decrease in the number of E neurons fourfold can be compensated by increasing the strength

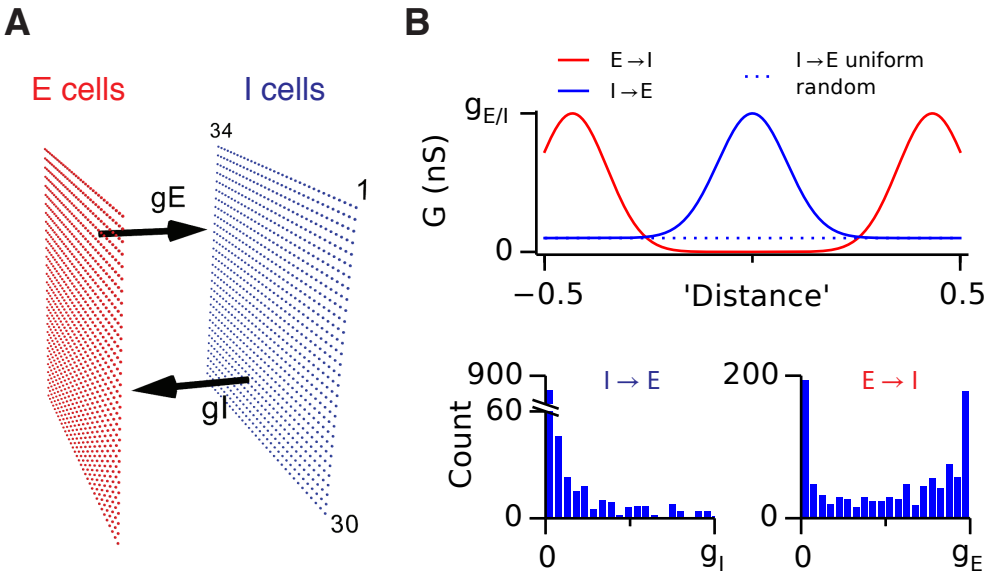

Figure 4.1: **(A)** A schematic of populations of excitatory cells (E cells, red) and inhibitory cells (I cells, blue) on a twisted torus of size 34x30 neurons. The synaptic coupling between the two populations was parameterised by the inter-population peak synaptic conductances g_E (E → I synapses) and g_I (I → E synapses), used through out the text. **(B)** `Top`: Plots illustrate peak synaptic conductances of excitatory (red) and inhibitory (blue) synapses, as a function of the distance of pre-synaptic and post-synaptic neurons on the twisted torus. Dotted blue line illustrates a non-specific source of inhibition that is distance independent (synaptic strength not in proportion to solid lines). `Bottom`: Distributions of synaptic weights from all I cells onto an E cell in the model (left) and from all E cells onto an I cell (right). g_E and g_I determine maximal values of these distributions.

of excitatory synapses by the same amount. Thus, an I cell in an equivalent network receives the same amount of total excitation. This ensures that the properties of gamma and attractor formation are the same in both versions of the network. Thus, the decrease in the number of E neurons made systematic exploration of large parameter spaces feasible, without affecting the results from Chapter 3 and Pastoll et al. (2013).

The synaptic weight profile in the model considered in this chapter follows the E-surround configuration (Figure 4.1B, also see Figure 2.3). Thus, on the twisted torus, excitatory connectivity has a ring-like profile of surround excitation, while inhibitory connectivity has a local, Gaussian profile (Figure 4.1B top). This connectivity profile generates interneuron firing fields that are inverted with respect to grid fields of the E cells (Figure 3.8). The synaptic coupling between the populations was thus parame-

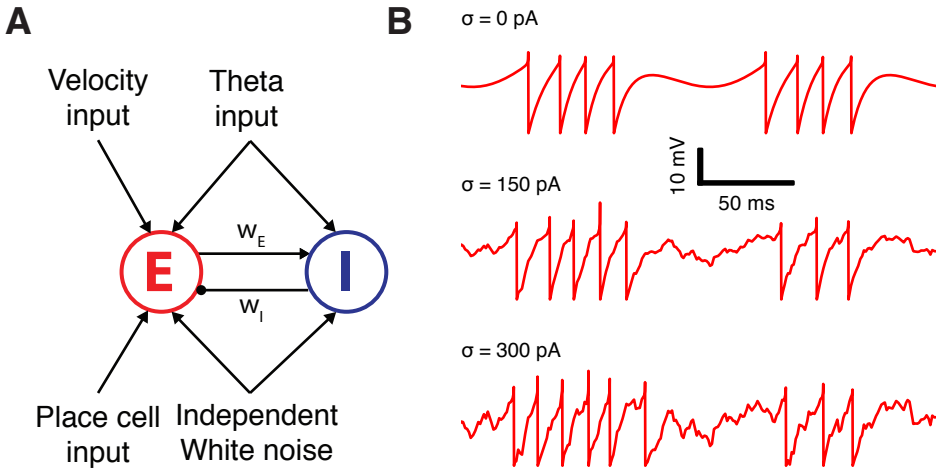

Figure 4.2: **(A)** A schematic of the external inputs in the attractor model, reprinted from Figure 2.1A. Here, place cells have been modelled as a set of spike generators with Gaussian receptive fields. Each neuron in the attractor network received an independent source of Gaussian white noise, parameterised by the standard deviation of the Gaussian. **(B)** Examples of membrane potential time course of an isolated E cell during two consecutive theta cycles, without noise (white noise input current standard deviation σ = 0 pA), with an intermediate amount of noise (σ = 150 pA) and with noise level doubled (σ = 300 pA). The neuron in this example only received the theta modulated input current (Eq. (2.10)) and noise. All other inputs to the network were disabled.

terised by the g_{E} and g_{I} parameters, that determine the peak of the synaptic weight function. The actual connections can thus follow a unimodal distribution of excitatory and a bimodal distribution of inhibitory synaptic weights, with the maximal values determined by g_{E} and g_{I} (Figure 4.1B bottom).

4.2.2 External inputs and the definition of noise

Similarly to Pastoll et al. (2013), the network received several types of external inputs. As Figure 4.2A shows, each neuron receives (i) an 8Hz, theta frequency modulated current, (ii) velocity input on which to perform path integration, (iii) place cell input to oppose attractor drift and (iv) a source of Gaussian white noise current. The theta frequency modulated current and velocity input are described in Sections 2.2.5 and 2.2.6. However, the implementation of the place cell input in this chapter has changed. It is described in detail in Section 4.2.3. Noise was implemented by injecting current

into each neuron in the attractor network independently. Each time step, the amount of current injected was determined by sampling from a Gaussian distribution with a zero mean and an appropriate standard deviation. If not mentioned otherwise, σ in the text and figures in this chapter will determine the three noise levels that were simulated: (i) either a deterministic network, in which $\sigma = 0$ pA; (ii) networks with an intermediate level of noise ($\sigma = 150$ pA); (iii) and networks with noise level doubled ($\sigma = 300$ pA). Figure 4.2B shows a membrane potential response of an isolated E cell in the network, with theta modulated external input and the three simulated levels of noise, determined by σ.

4.2.3 Place cell input

Previous modelling work of spiking continuous attractor networks of grid cells shows that grid cell networks might not be capable of generating stable grid firing fields for a longer time periods (Pastoll et al., 2013). This is consistent with the loss of firing fields when hippocampal input has been abolished (Fyhn et al., 2004; Bonnevie et al., 2013).

The model presented in this chapter thus contains a source of (allocentric) spatially tuned input, most likely originating from place cells. In the parameter exploration experiments, the mechanism of place cell simulation was updated in order to increase biological plausibility of resetting the state of bump attractors and to counter-balance their drift. Place cells were simulated as independent inhomogeneous Poisson spiking generators, whose rate was modulated by a Gaussian function of the simulated animal location. Thus, the firing rate of an i^{th} place cell, $r_i(t)$ was:

$$r_i(t) = r_{\max} \exp\left(-\frac{|\mathbf{l}(t) - \boldsymbol{\mu}_i|^2}{2\sigma^2_{\text{field}}}\right), \tag{4.1}$$

where $r_{\max}$ is the firing rate in the centre of the place field, $\mathbf{l}$ is an instantaneous position of the simulated animal, $\boldsymbol{\mu}_i$ is the centre of the place field and σ_{field} is the width of the place field. In all simulations, there were 900 place cells, with $r_{\max} = 50$ Hz, and $\sigma_{\text{field}} = 20$ cm. Spikes emitted by place cells were thus generated by independent Poisson processes with rate $r_i(t)$ in eq. (4.1), and the centres of individual place fields were uniformly distributed in the arena the simulated animal was moving in. The connection weights from place cells were arranged in a divergent manner, so that a place cell had strongest connections with neurons whose firing fields were aligned (in real space) with the firing field of the place cell. The connection weight (maximum of the synaptic conductance) from place cell i to a grid cell j decayed according to a

Gaussian function

$$g_{ji} = G_{\mathrm{PC}}^{\max} \exp\left(-\frac{|\boldsymbol{\mu}_{\mathrm{PC}}^{i} - \boldsymbol{\mu}_{\mathrm{G}}^{j}|^2}{2\sigma_{\mathrm{PC}}^2} \right), \tag{4.2}$$

where $G_{\mathrm{PC}}^{\max}$ is the maximal connection strength between two fully aligned grid and place fields, $\boldsymbol{\mu}_{\mathrm{PC}}^{i}$ is the centre of the place field of the i^{th} place cell, $\boldsymbol{\mu}_{\mathrm{G}}^{j}$ is the centre of the grid field of the j^{th} grid cell that is nearest to the place cell, σ_{PC} is the width of the synaptic profile. The parameters were set to $G_{\mathrm{PC}}^{\max} = 0.5$ nS and $\sigma_{\mathrm{PC}} = 7$ cm. Connections from place cell were modelled as AMPA conductances (Eq. 2.8).

Place cell input was active only during the full grid field simulations (Section 4.3.1) and during simulations in which the effectivity of the place cell input was assessed (Section 4.3.5.3). Simulations of the stationary bump networks and estimations of bump attractor velocity responses (all other result sections in this chapter) were performed with the place cell input switched off. However see also section 4.2.4 for the use of place cell input during bump attractor initialisation.

4.2.4 Bump attractor initialisation

Each simulation contains an initialisation section that tries to set the model into the desired state, i.e. a bump attractor. During this stage, the theta-modulated input is switched off and the network receives only the constant input source (see eq. (2.9)). The bump attractor might not form spontaneously, and instead the network could persist in a uniform firing rate regime (Compte et al., 2000). However, it might be possible that when forced into the attractor state, the network will persist (data not shown). Therefore, I used the place cell input as a spatially-tuned input that served (i) as an initialisation input in order to drive the network into an attractor state if this does not happen spontaneously and (ii) to initialise the bump attractor position so that it is correctly "synchronised" with the place cell input. The initialisation phase lasted for the first 500 ms of simulation time, during which the firing rate of place cells were doubled, and the connections from place cells to grid cells were increased ten-fold.

4.2.5 Simulation protocols

4.2.5.1 Simulations of animal movement

Simulations of animal movement have been carried out for 600 seconds (section 4.3.1). Here, for each value of g_{E} and g_{I}, the main simulation run is preceded by a number of

shorter simulations with certain data analysis steps. The analysis of the shorter simulation runs determines how much current needs to be injected in order for the bump of activity to track the simulated movement of an animal. This determines the gain of the velocity input current in order to produce grid fields with a specified spacing between the peaks in the firing field. The result is a single number in units of neurons/s/pA, which determines the speed of the bump as a function of injected velocity input. An algorithmic description of the estimation procedure is in Appendix A. The spacing between the blobs of the grid firing fields was set to 60 cm in all of the simulations.

During the main simulation run, the animal movement is simulated for 600 s. Each of the runs is repeated 3 times. These simulations use the estimated velocity response gain in order to calibrate the spacing between the grid firing fields. After the simulation is finished, a neuron in the bottom-left corner of the torus is selected for analysis. For this cell the gridness score of its firing field is computed (Section 2.2.8). The reasoning behind choosing only a single cell to estimate the gridness score is as follows. The grid firing fields in the network are a result of coordination of activity of the network as a whole. If the network forms a bump attractor that is able to accurately track animal movement, all cells in the network will have grid-like firing fields that differ only in their phases. On the other hand, if the bump attractor does not form, is unstable, or does not accurately track the position of the animal, the gridness score of all cells will be low. Grid fields could form without a bump attractor only if the firing of the cells was driven by input from place cells. However, place cell input in this model is not strong enough to drive the activity of the neurons on its own and would not result in gridness score significantly higher than chance (data not shown). Thus, the firing field of a single cell in the network represents grid field computation in the network as a whole. Moreover, this cell can be selected arbitrarily.

4.2.5.2 Short simulation runs without animal movement

Some of the simulation runs were used to estimate properties of bump attractors and nested gamma oscillations (Sections 4.3.2, 4.3.4, 4.3.5, and 4.3.6). In these experiments, instead of simulating animal movement, a shorter, ten second simulation, was run. The velocity and place cell input were disabled. Thus, the network is expected to only produce a static bump attractor and does not perform path integration. The setup is equivalent to removing the "Velocity input" and "Place cell input" components from the model, as shown in Figure 4.2. For each parameter setting (determined by g_{E}, g_{I}, and the noise level), 5 simulations were performed. For each simulation run,

post-synaptic currents were recorded from 25 randomly selected excitatory cells in the model. Thus, on each run, different cells could be picked up for analysis. It is in principle possible to record membrane currents from all the neurons. However, the amount of data generated by such simulations quickly becomes overwhelming (on the order of several terabytes per parameter exploration experiment). Thus the approach chosen here was to sample from the population of neurons and store the recorded state variables of only a subset of these. This allowed for unrestricted analysis and visualisation of the recorded state variables.

4.2.6 Analysis of gamma oscillations

The estimation of power and frequency of gamma oscillations was accomplished by analysing the post-synaptic currents recorded during the simulation. First, the synaptic current was band-pass filtered between 20 and 200 Hz. Subsequently, an autocorrelation of the filtered signal was computed for each of the 25 selected cells in the network (see Section 4.2.5.2). The power and frequency of an oscillation for a single cell was computed by detecting the first local maximum of the autocorrelation function. The correlation value at the point of the local maximum then determined the strength of the underlying oscillation, while the time lag at the maximal value determined the frequency of the oscillation. Two other methods were assessed to estimate the power and frequency of nested gamma oscillations before deciding to use the autocorrelation analysis (data not shown). The first one was to apply power spectral analysis on the recorded postsynaptic currents. This proved infeasible, since the recorded currents during gamma oscillations and non-gamma states deviated from sinusoidal shapes, and thus generated many harmonic peaks in the power spectrum. This made automatic detection of power peaks infeasible. The other method, the wavelet transform, relies on fitting a wavelet function onto the signal. However the shape of the wavelet might not always match the analysed signal and thus it would require designing the wavelets a priori before the analysis. This also proved impractical and not easily verifiable for an automatic analysis. Thus, autocorrelation analysis of the recorded membrane currents was chosen to estimate the power and frequency of nested gamma oscillations.

4.2.7 Analysis of bump attractor states

4.2.7.1 Gaussian function fitting

I used the short simulation runs described in Section 4.2.5.2 to estimate whether the attractor networks formed bump states. I then estimated an instantaneous population firing rate at various successive points in the simulation (using a 250 ms wide sliding window). All the results use only population firing rate from the excitatory neurons.

The properties of a bump-like population activity (if it is a bump) where then estimated by fitting a symmetric Gaussian function to the population firing rate, using the maximum likelihood estimator, assuming Gaussian noise:

$$B(\mathbf{X}) = A \exp\left(\frac{-\|\mathbf{X}-\boldsymbol{\mu}\|^2}{2\sigma_{\text{bump}}^2}\right), \tag{4.3}$$

where A was the height of the Gaussian function, $\mathbf{X}$ was neuron position on the twisted torus, $\boldsymbol{\mu}$ was the centre of the Gaussian, σ_{bump} was the width of the Gaussian, and $\|\cdot\|$ represents a distance metric on the twisted torus.

4.2.7.2 Bump attractor formation metric

Initially, I examined whether the standard deviation of the fitted Gaussian functions (σ_{bump}) provides any information about bump formation. I reasoned that bump attractors that have successfully formed will have a lower value of σ_{bump} than either a homogeneous activity or activity that is scattered over the toroidal neural layer. In the two latter cases, if the activity is homogeneous, the fitting process has to set the value of σ_{bump} to much greater than the size of the torus, in order to spread the Gaussian function over the whole neural sheet. If the activity is scattered, it will also force the fitting process to widen the Gaussian function and thus increase the value of σ_{bump}. This will be in contrast to bumps of activity that are confined to only a small, continuous subregion of the torus, in which case σ_{bump} will stay low.

In Appendix B I briefly describe the result of using the reciprocal value of σ_{bump} to estimate the presence of bump attractors. While this reciprocal can provide a visual indication of how wide the bump attractor is (Figure B.1A) and the extreme values correspond to visual images of population activity on the torus (Figure B.1B), it is not straightforward to determine automatically whether the bump attractor forms and how stable it is during the course of the simulation. This is due to the fact that the actual width of the bump depends on the amplitude A of the Gaussian function in Eq. (4.3).

In order to determine the width of the bump it is necessary to take into account both σ_{bump} and A in Eq. (4.3).

Here, I provide a measure that determines the width of the Gaussian, and compares it with the size of the twisted torus. The bump is considered to form when the width of the Gaussian is less than a threshold, otherwise the population activity is very close to uniform and thus cannot form a bump. The width of the Gaussian is determined as a radius around the centre of the function for which its value is equal to a threshold rate, R_T:

$$\begin{aligned} R_T = f(x,y) &= A\exp\left(-\frac{x^2+y^2}{2\sigma^2}\right) \\ -\frac{x^2+y^2}{2\sigma^2} &= \ln\frac{R_T}{A} \\ d^2 = x^2+y^2 &= -2\sigma^2\ln\frac{R_T}{A} \\ d &= \sigma\sqrt{-2\ln\frac{R_T}{A}}. \end{aligned} \tag{4.4}$$

Here, A and σ are the estimated parameters of the Gaussian function fitted onto the population activity on the twisted torus.

The procedure uses a hard threshold to determine whether the bump has formed or not: if $d < T$, the population activity is considered to form a bump, otherwise not. The estimation parameters have been chosen as $R_T = 0.1$ Hz, and the diameter threshold was set to a minimum of the sizes of the twisted torus, i.e. $T = 30$ neurons. These parameters yielded the best results when validated visually on a small subset of simulations (Figure C.2B). When the bump classification procedure is performed for several consecutive snapshots of population activity, we can determine the fraction of the simulation time the attractor network persisted in a bump state, regardless of the position of the bump attractor (here reported as P(bump)).

4.3 Results

This section describes the results of the simulations that took place in the parameter regions of excitatory (g_{E}) and inhibitory (g_{I}) synaptic scaling parameters, further parameterised by the three simulated levels of noise. In Section 4.3.1, I estimate the ability of the attractor network to generate stable grid firing fields given variations of g_{E} and g_{I} and level of noise in the network. In Section 4.3.2 I explore how the power

and frequency of gamma oscillations changes given the same parameters. I also determine the relationship between grid field computations and the power and frequency of nested gamma oscillations in the network (Section 4.3.3) and show that gamma oscillations carry little information about the gridness scores generated by the network. Section 4.3.4 shows that a successful formation of a bump attractor state is necessary but not sufficient for high gridness score. Section 4.3.5 provides a detailed analysis of bump attractor position drift and the extent to which the position can be controlled by inputs from modelled place cells. This information is important in order to dissect the mechanisms that contribute to the generation of stable grid firing fields. In Section 4.3.6 I demonstrate that the positive effect of noise on grid field and gamma computations is primarily mediated by braking down epileptic-like states in networks without noise.

4.3.1 Moderate noise reduces the sensitivity of grid fields to variations in global synaptic strengths

The simulations in Chapter 3 demonstrated that attractor networks with feedback inhibition and theta frequency modulated background input are capable of producing grid-like firing fields, with the help of a resetting mechanism realised by the input from (model) place cells. The network in Chapter 3 contained an intrinsic source of noise simulated as fluctuations of membrane potential, while in this chapter noise was simulated as current injections into all cells.

I therefore investigated how the dynamics of the grid cell attractor network evolves when noise levels are changed. I first simulated the attractor networks using the protocol described in Section 4.2.5.1, extracted the spatial firing field from a selected neuron, and calculated its gridness score.

At first, I ran simulations in which noise was absent (Figure 4.3, $\sigma = 0$ pA), the excitatory synaptic strength factor (g_{E}) was set to 3 nS and the inhibitory strength (g_{I}) was lower and set to 1 nS (Figure 4.3Aa). These networks generated firing fields with gridness score comparable to the ones obtained from *in vivo* recordings from rats and mice (Hafting et al., 2005; Sargolini et al., 2006; Buetfering et al., 2014). I next swapped the values of E and I connections, i.e. set $g_{\mathrm{E}} = 1$ nS and $g_{\mathrm{I}} = 3$ nS, thus increasing inhibition by a factor of 3, while decreasing excitation by the same amount. In this configuration, networks without noise failed to produce grid firing fields (Figure 4.3Ab). These results suggest that the ability of the networks to generate grid firing

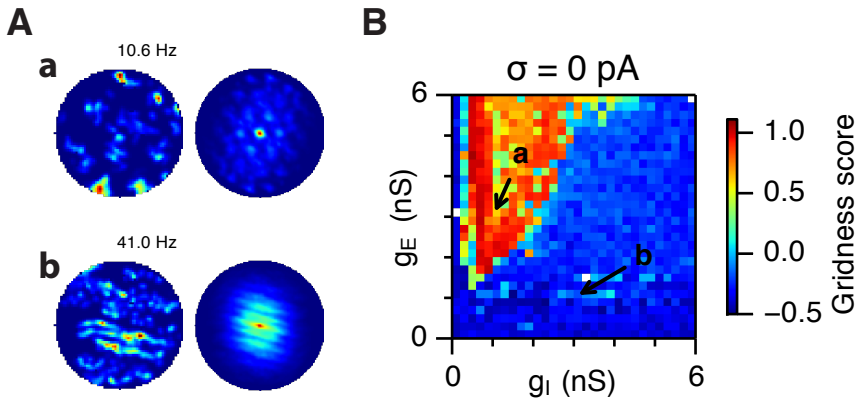

Figure 4.3: **Networks without noise generate grid fields only in a restricted region of E-I parameter spaces. (A)** Examples of spatial firing fields (left) and their autocorrelations (right) in simulations highlighted by arrows in panel (B). **(B)** Gridness score in the parameter space of excitatory (g_E) and inhibitory (g_I) synaptic scaling parameters. Each item in the colour plot is an average gridness score of at most three simulation runs. Networks where inhibition is high do not produce grid firing fields.

fields depends on the relative strengths of excitatory and inhibitory synapses.

In order to determine the contribution of g_E and g_I to the ability of the network to compute grid firing fields, I have performed the simulation protocol in a wide range of excitatory and inhibitory synaptic strengths (0-6 nS for both parameters) and extracted gridness score from each of the simulations. I performed 3 trials for each combination of the g_E and g_I parameters. Figure 4.3B shows that the range of g_E and g_I where gridness score is high in networks without noise is restricted to values where inhibition is low. Thus, generation of grid firing fields in networks with feedback inhibition requires specific tuning of synaptic strengths.

Since neural systems are inherently noisy, I expected the limited region in which grid firing fields are supported to shrink with addition of noise. I therefore set the noise level to σ = 150 pA and repeated the simulation runs. Unexpectedly, I found an opposite effect, in that the range of the simulated parameter region supporting grid firing fields greatly expanded (Figure 4.4A,B). Figure 4.4B shows that the region with high gridness score had a crescent-like shape, in that both regions where inhibition is low and excitation is high, and vice versa, produce networks in which spatial firing fields have a high gridness score. Examples of grid fields from these two situations are in Figure 4.4A. Next, I increased the standard deviation of noise current twofold, and

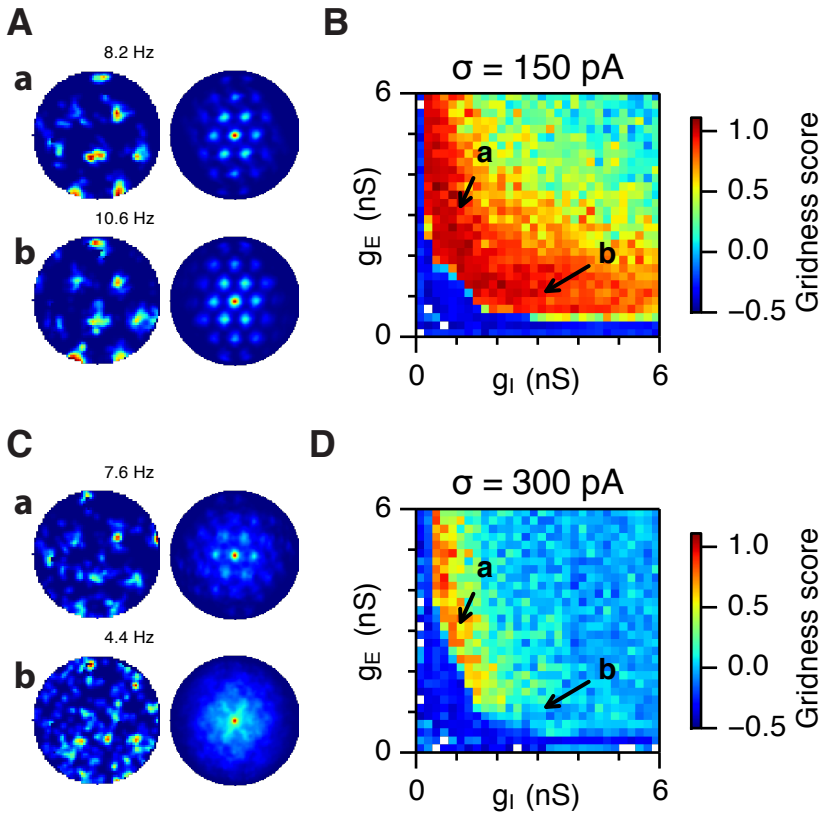

Figure 4.4: **Noise increases the range of synaptic strengths that support grid firing. (A)** Spatial firing fields (left) and their autocorrelations (right) of E cells from simulation runs highlighted by arrows in panel (B). **(B)** Gridness score plotted in parameter spaces of excitatory (g_{E}) and inhibitory (g_{I}) strengths of synaptic conductances, for networks where noise level was set to $\sigma = 150$ pA. Each item in the colour plot is an average gridness score of at most three simulation runs. **(C, D)** As for (A, B) but with noise level set to $\sigma = 300pA$.

observed that for most values of g_{E} and g_{I} the gridness score dropped profoundly into levels close to zero (Figure 4.4C,D). This result is consistent with the detrimental role of noise in path integration systems (Eliasmith, 2005; Conklin and Eliasmith, 2005; Zhang, 1996). Thus, in the simulations presented here, the intermediate noise level is the one most suited for producing attractor networks that generate stable grid fields.

The simulations thus show that presence of noise can influence the computation of grid fields in two ways. In some cases, consistent with the current view about noise (Faisal et al., 2008), presence of noise is detrimental for the generation of grid fields. This type of computation is largely influenced by the amount of excitatory and inhibitory coupling between the two populations in the network. When a simulation

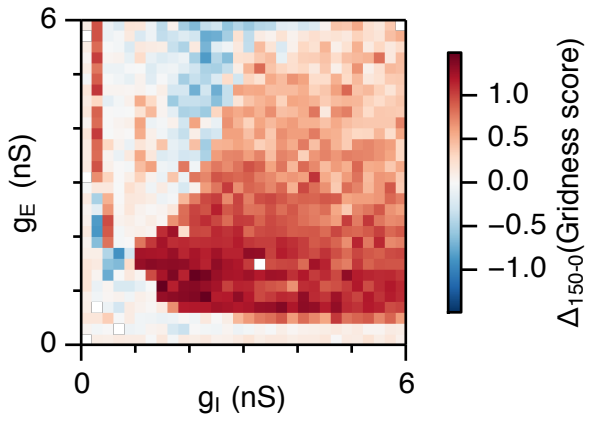

Figure 4.5: **Noise promotes grid field computations in networks with strong inhibition.** Parameter plot shows difference of gridness scores in networks with $\sigma = 150$ pA and networks with $\sigma = 0$ pA in simulations from Figures 4.3B and 4.4B.

with $g_E = 3$ nS and $g_I = 1$ nS is considered, we can observe that networks without noise and with noise level set to $\sigma = 150$ pA are both capable of producing receptive fields with high gridness score. This situation is highlighted by letter "a" in the plots in Figures 4.3 and 4.4. When the noise is increased to $\sigma = 300$ pA, the fields become blurred (Figure 4.4Ca,D). On the contrary, when g_E and g_I are set to 1 and 3 nS respectively, we can see that deterministic networks and networks with σ set to 300 pA fail to produce grid fields, while networks with σ set to 150 pA produce grid fields with gridness score comparable to the previous case. This situation is highlighted by letter "b" in Figures 4.3 and 4.4. Thus, noise can be beneficial or detrimental for grid field computation, depending on the amount of inhibition present in the network.

A more quantitative assessment of the transitions from low to high gridness scores, or vice versa, in the parameter region of excitatory and inhibitory synaptic couplings is shown in Figure 4.5. Here, the difference of gridness scores between networks with $\sigma = 150$ and $\sigma = 0$ pA has been computed. The figure shows that most of the gridness score gain occurs in regions when inhibition is high. When either of the synaptic couplings is close to zero, the change is also close to zero. Interestingly, when inhibition is low (g_I set to 0.2 nS) and excitation is high (> 3 nS), we can observe a strong increase in gridness score in the noisy networks ($\sigma = 150$ pA). This small stripe which does not "fit well" with the rest of the changes in the parameter space currently cannot be explained fully due to a high complexity of the network. This beneficial effect of noise when $g_I = 0.2$ nS could potentially be caused by an interaction of the

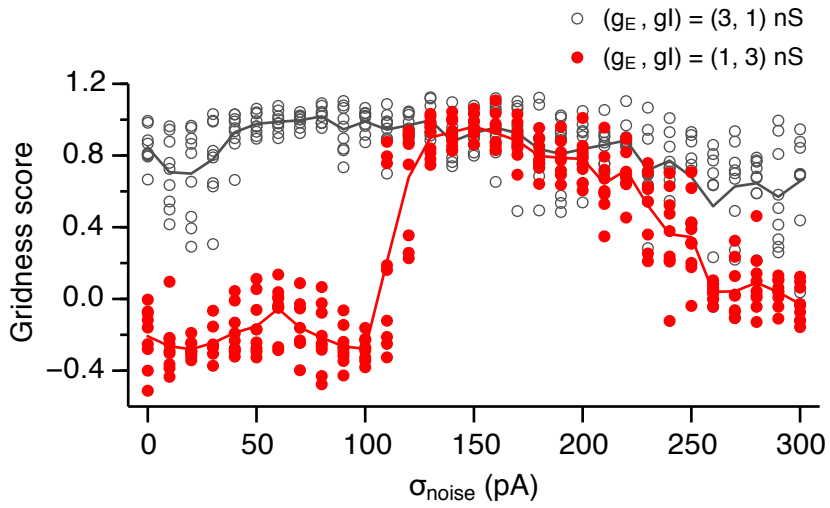

Figure 4.6: **Minimal amount of noise is required to support grid field computations in networks where inhibition is strong.** Gridness score plotted as a function of the standard deviation of intrinsic noise. Each noise level comprises simulations from a rectangular patch of 9 locations in the parameter space, whose centres were located where inhibition is low and excitation is high (grey; g_E = 3 nS, g_I = 1 nS), and where inhibition is high and excitation is low (red; g_E = 1 nS, g_I = 3 nS). Each point represents an average of 3 simulation runs.

bump of activity and place cell input connected to the network.

How does the ability of the networks to produce grid fields compare when simulated with much finer differences in levels of noise? I have simulated the attractor networks in a neighbourhood of 8 g_E and g_I values surrounding the locations highlighted by arrows in Figure 4.4a-b, with noise levels ranging from 0 to 300 pA, in steps of 10 pA (Figure 4.6). As before, when g_E and g_I were set to 3 and 1 nS respectively, there was a decrease of gridness score with increasing level of noise (grey trace in Figure 4.6). On the other hand, with g_E and g_I set to 1 and 3 nS respectively, the networks with $\sigma < 100$ pA had an average gridness score close to zero, followed by a sharp transition to the highest gridness scores simulated, subsequently followed by a steady decrease, similar to the previous condition (red trace in Figure 4.6). Thus, under the current modelling conditions, when inhibition is high, one can identify a threshold in noise that allows the network to perform accurate computation of animal's positions, which in turn results in stable grid firing fields.

The simulations also show that a minimal amount of coupling between the two populations is necessary for any computation performed by the network (Figure 4.4).

This is understandable, since if the coupling is too weak, no bump attractor will form in the network, and thus the gridness score will be low, regardless of a noise level present in the network.

In summary, the simulations in this section show that noise in networks with feedback inhibition and an external source of theta frequency input expands parameter regions in which successful grid field computations take place, that it makes the grid field landscape more robust to changes in the strengths of excitatory and inhibitory synapses and that there is an optimal level of noise necessary for this to occur.

4.3.2 Presence of noise supports generation of theta-nested gamma oscillations.

How do different levels of white noise affect generation of theta-nested gamma oscillations in this attractor model? I have conducted a separate set of shorter simulations to assess the power and frequency of nested gamma oscillations generated by the model (Sections 4.2.5.2 and 4.2.6). In the case of grid field computation, the excitatory-inhibitory parameter regions of deterministic networks contained a relatively low proportion of high gridness score, which was expanded when noise was introduced into the simulations. Since the attractor network, when properly configured, can generate nested gamma oscillations (cf. Chapter 3), I investigated how the changes in g_{E} and g_{I}, and noise level shape the dynamics of gamma oscillations.

To assess the properties of gamma oscillations in the model I used inhibitory post-synaptic currents recorded from E cells. Figures 4.7A and 4.8A,D illustrate the post-synaptic currents of E cells from simulations located in different points in the parameter space. Following the convention introduced in Section 4.2.1, inhibitory currents *onto* excitatory cells are coloured red, while excitatory currents onto inhibitory cells are coloured blue. These currents are a result of a simulated voltage clamp experiment, with a clamp potential of -50 mV. Thus, an inward (excitatory) current has a negative sign. The currents are snapshots of two theta cycles of the excitatory or inhibitory activity of most of the population. The examples of post-synaptic currents are located in the same positions in the parameter spaces as in the case of Figures 4.3 and 4.4.

As with the grid field simulations, I first examined the oscillations in deterministic networks, in regions where excitation is high and inhibition is low (g_{E} = 3 nS, g_{I} = 1 nS), and vice versa (Figure 4.7A). Contrary to the grid field simulations, we can see that with both synaptic strength settings, gamma oscillations looked disrupted. The post-

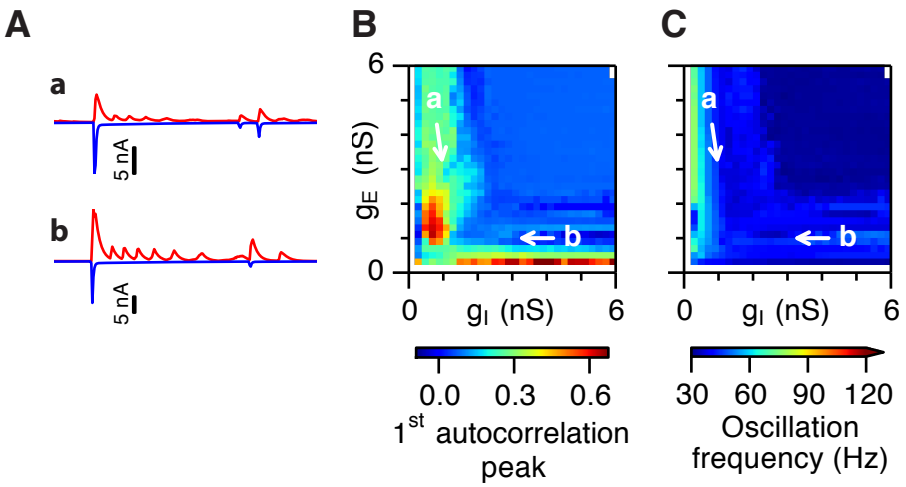

Figure 4.7: **Networks without noise support gamma oscillations only in a limited region of E-I spaces. (A)** Examples of inhibitory (red) and excitatory (blue) synaptic currents recorded from two respective excitatory and inhibitory neurons from simulations highlighted by arrows in panels (B,C). **(B)** A correlation value at the first local maximum of an autocorrelation of inhibitory synaptic currents (I → E cells, 25 randomly selected E cells), plotted in the E-I parameter space, for networks without noise ($\sigma = 0$ pA). **(C)** Frequency at the first autocorrelation peak, corresponding to (B).

synaptic currents were dominated by large spikes at the beginnings of theta cycles. These large spikes in synaptic currents are best illustrated in Figure C.4. I therefore performed the short simulations without animal movement in the same range of g_E and g_I as for the simulations of grid fields. The estimations of gamma power show that the range of g_E and g_I that support gamma oscillations is limited (Figure 4.7B) and confined to the portion of the parameter space where both excitation and inhibition are weak. In fact, the frequency of the detected oscillations were well below the fast gamma range, and mostly at the low end of the slow gamma range (Figure 4.7C; see also Buzsáki and Draguhn (2004) for the range of frequencies).

I next investigated the properties of the nested gamma oscillations in networks with a moderate noise level. With the introduction of noise into the network, the parameter region with high gamma power was greatly expanded, and it covered most of the simulated space of g_E and g_I (Figure 4.8B). I next superimposed a contour plot of gridness score in Figure 4.4B onto the gamma power and frequency plots in Figure 4.8B,C. The isoclines show regions in which gridness score equals 0.5. In these plots, neither power, nor frequency of gamma oscillations followed the crescent-like shape

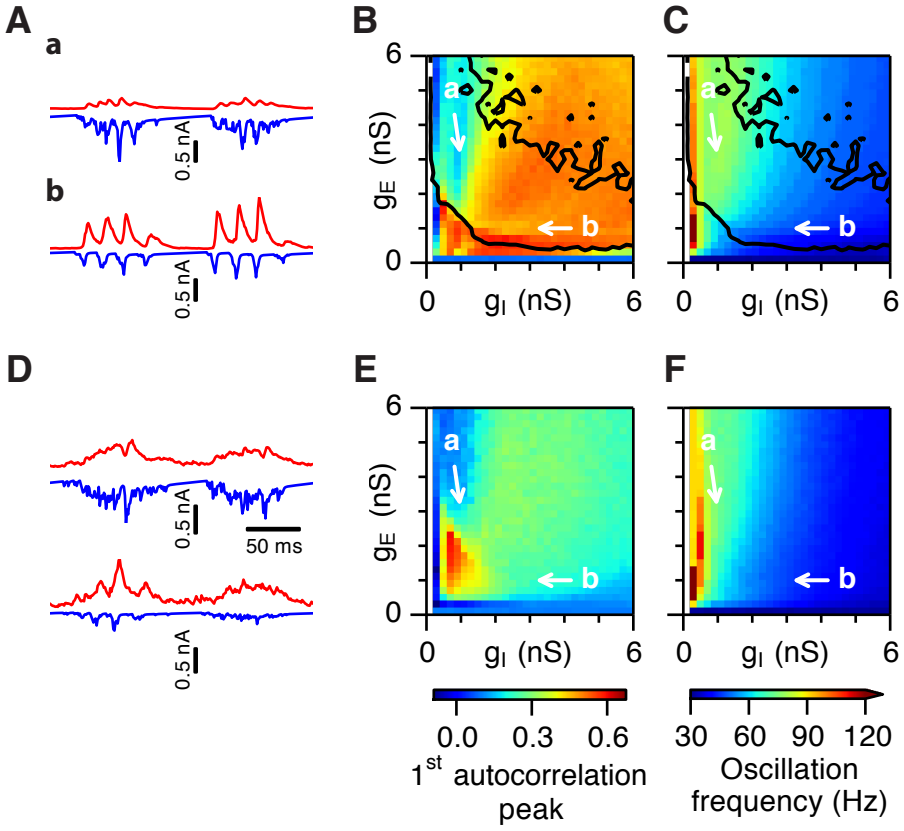

Figure 4.8: **Presence of an intermediate level of noise expands the parameter region supporting emergence of theta-nested gamma oscillations. (A)** Examples of inhibitory (red) and excitatory (blue) synaptic currents recorded from two respective excitatory and inhibitory neurons from simulations highlighted by arrows in panels (B,C). **(B)** A correlation value at the first local maximum of an autocorrelation of inhibitory synaptic currents (I → E cells, 25 randomly selected E cells), plotted in the E-I parameter space, for networks with noise level set to σ = 150 pA. **(C)** Frequency at the first autocorrelation peak, corresponding to (B). Black lines indicate isoclines of gridness score from Figure 4.4B equal to 0.5. **(D-F)** As for (A-C), but with noise level set to σ = 300 pA.

of high gridness score represented by the isoclines, suggesting a weak relationship between grid field computation and power and frequency of nested gamma oscillations. In addition, when the networks were simulated with noise level set to σ = 300 pA, the gamma correlation values decreased in most of the parameter region (Figure 4.8D-F), in line with my initial expectations about the detrimental effect of noise. These results thus support the conclusion that a moderate amount of noise is beneficial for the computations and dynamics that the network generates.

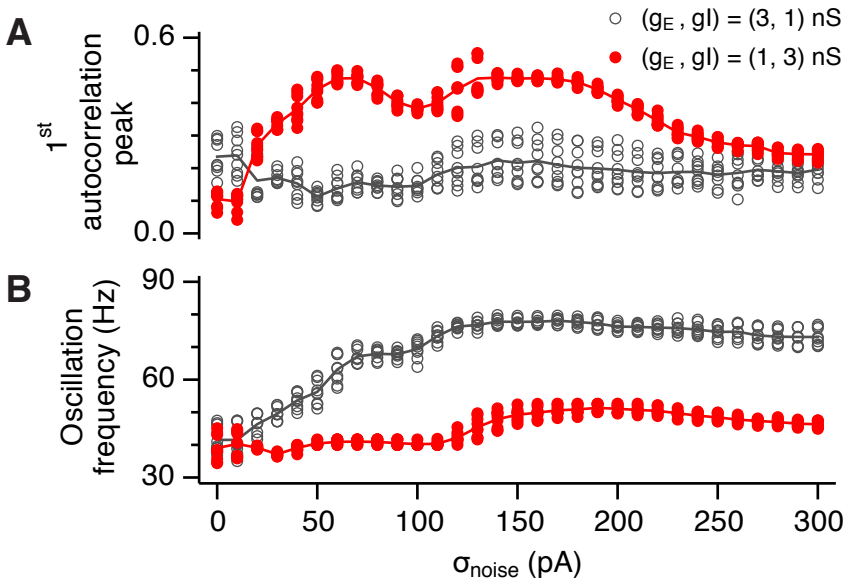

Figure 4.9: **Theta-nested gamma oscillations require presence of intrinsic noise when inhibition is high. (A)** Correlation value at the first autocorrelation peak of the inhibitory post-synaptic current as a function of standard deviation of the noise current. Grey colour indicates simulations with g_E = 3 nS, g_I = 1 nS. Red colour indicates simulations with g_E = 1 nS, g_I = 3 nS. **(B)** Same as (A), but the plot shows frequency corresponding to the detected autocorrelation peak.

Can we draw any mechanistic insights about the role of excitation and inhibition in stable gamma oscillations and grid firing fields? In noisy networks (Figure 4.8A-C) high g_I is beneficial for nested gamma oscillations with high power. In the parameter region around g_E = 1 nS and g_I = 3 nS (Figure 4.8Bb) gamma oscillations have high power together with the stable grid firing fields. Thus, naturally, a minimal amount of inhibition in the network is necessary for stable oscillatory dynamics and when this amount is not reached (Figure 4.8Ba) inhibitory neurons fail to illicit synchronous activity in the network. Interestingly, high inhibition is detrimental for both gamma oscillations and grid firing fields when networks are noise-less. The mechanistic reason for this is discussed in Section 4.3.6.

In order to assess how the power and frequency of nested gamma oscillations changes as a function of much finer difference of noise levels, the simulations of a static bump attractor have been repeated with noise values ranging from 0 to 300 pA, in steps of 10 pA (Figure 4.9). For each noise level, 9 values of g_E and g_I were simulated. The values included a point in the centre of a selected location in the parameter space (described next) and 8 values surrounding the centre point. The plot in Figure

4.9 shows values from a region with high excitation and low inhibition (grey colour, g_E = 3 nS, g_I = 1 nS), and from a region with low excitation but strong inhibition (g_E = 1 nS, g_I = 3 nS). In the region with strong excitation and weak inhibition, the power of nested gamma oscillations stays low and does not change with increasing noise. However, the frequency in this case increased from a low gamma (~40 Hz; σ = 0 pA) to a high gamma region (~75 Hz; $\sigma \geq 150$ pA). On the contrary, in regions where inhibition is high, the power of nested gamma oscillations as a function of noise has a non-monotonic shape. Interestingly, and compared to the gridness score data in Figure 4.6, the maxima lie in regions with intermediate noise levels (red trace in Figure 4.9A). In this case, however, the frequency stays in the low gamma range, with a slight increase towards higher noise levels (red trace in Figure 4.9B).

While I have presented specific data about the beneficial role of noise for the generation of nested gamma oscillations, these data do not yet explain the mechanistic reason of this beneficial effect. The question of why noise is beneficial for gamma oscillations is addressed in Section 4.3.6.

4.3.3 Independent control of gamma oscillations and grid firing by the strength of recurrent connections

Having data that allow us to analyse both the oscillatory dynamics and the quality of grid fields in the network, we can ask whether there is a relationship between them. In this case, we can plot a scatter plot of the gridness score with oscillation power, as is shown in Figure 4.10. The figure shows data combined from Figures 4.3, 4.4, 4.7 and 4.8. In order to highlight the differences between how much noise was injected into the network, different noise levels were plotted with different colours. We can see from the figure, that determining the relationship between the two quantities is not straightforward, but the data do not seem to be related.

In order to assess this relationship quantitatively, I have computed the maximal information coefficient (MIC; Reshef et al., 2011) between the gridness score and oscillation power and its frequency. MIC is a measure of dependence between two variables that captures a wide range of relationships. When the relationship is functional, the MIC value roughly equals the coefficient of determination of the underlying regression. MIC can be determined in the range of $\langle 0,\ 1 \rangle$, where 0 means that the two quantities are statistically independent, while 1 indicates a prefect functional relationship. To calculate the MIC score, I used the freely available *minepy* Python package

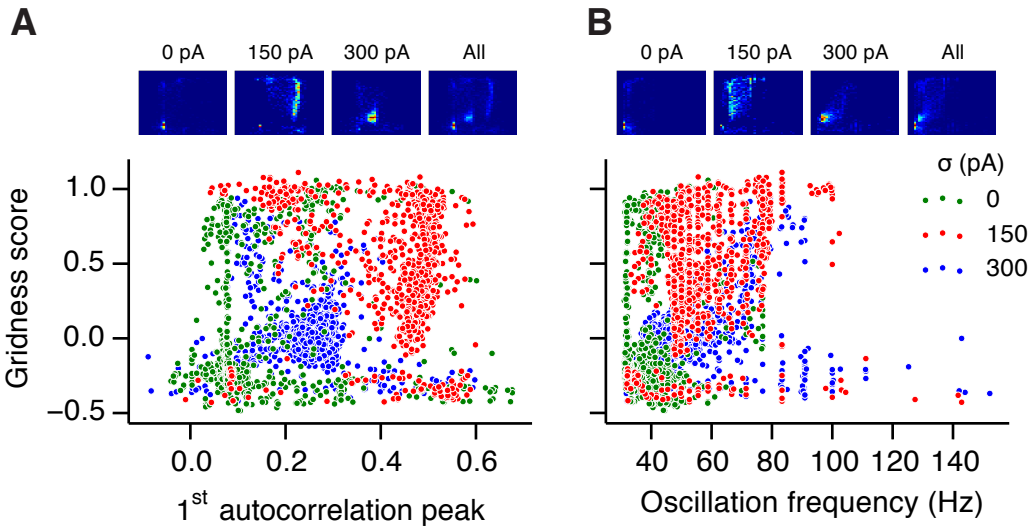

Figure 4.10: **Grid field computation does not show any straightforward relationship to the power of nested gamma oscillations. (A)** Scatter plot shows gridness score as a function of gamma oscillation power for simulations with noise absent (green), with an intermediate level of noise (red) and highest simulated noise level (blue). Each dot represents data from simulations of a stationary bump (Figures 4.7 and 4.8) and simulations of animal movement (Figures 4.3 and 4.4). The stationary simulations and simulations of animal movement comprise two separate runs. Insets show probability density functions for each noise level separately and all noise levels aggregated. **(B)** Same as for (A), but for gridness score vs. oscillation frequency.

(Albanese et al., 2013). In many cases mutual information (MI) is also a useful measure of dependence between two variables. However, the absolute value of MI depends on the discretisation of the probability density function and thus makes it hard to interpret. On the other hand, MIC does not suffer from this problem. I thus provide values of both MIC and MI so that comparisons can be made between the two cases.

I first analysed the relationship between gamma power and gridness score (Figure 4.10A, C.5, and Table 4.1). The MIC score is rather low irrespective of whether we consider the noise levels separately or combined together (MIC <= 0.319 for all conditions). Mutual information follows the same trend as the MIC score and the linear fit explains only a small portion of the total variance ($r^2 < 0.113$ for all combinations). We can estimate a similar trend in the data from Figure 4.10B which shows a scatter plot of gridness score and oscillation frequency. The relationship between these two quantities is also weak, as shown in Table 4.1. Gridness scores are thus unlikely

Gridness score vs. oscillation power				vs. oscillation frequency		
σ (pA)	MIC	MI	r^2	MIC	MI	r^2
0	0.3	2.016	0.025	0.309	1.952	0.071
150	0.301	1.987	0.002	0.299	1.848	0.079
300	0.285	1.975	0.015	0.352	1.983	0.064
All together	0.319	1.276	0.113	0.325	1.12	0.117

Table 4.1: **Information measures between gridness score and oscillation power and its estimated frequency.** Maximal information coefficient (MIC), mutual information (MI) and coefficient of determination (r^2) for data in Figure 4.10.

to be predicted from the power or frequency of gamma oscillations, since the MIC score show only a weak, and potentially a non-linear relationship, given that the linear regression explains only a small portion of the total variance of the data (Table 4.1).

The data presented here therefore suggest that information about gamma power or frequency in the model does not reliably predict the grid field computations performed by the network. The data rather suggest that changes in power and frequency of gamma oscillations are independent of gridness score in the region where gridness score is high (gridness score > 0.5). This is highlighted in Figure 4.8B,C. The black contour highlights a region where gridness score is higher than 0.5. We can see that this region contains a wide range of oscillation power and frequency spanning the region where stable grid fields are generated. This suggests that local grid cell neural circuits may be able to fine-tune their gamma strength and frequency without disrupting the grid field computations.

In summary, noise qualitatively changes the power and frequency of nested gamma oscillations in networks with feedback inhibition and theta frequency modulated input current. Similar to the case of grid firing fields, the parameter sub-region supporting nested gamma oscillations is larger in networks with an optimal level of noise. However, an accurate computation of grid fields in the network is not related to the power and frequency of nested gamma oscillations. Rather, gamma power and frequency can be fine-tuned across a relatively wide range without disrupting the stability of grid firing fields.

4.3.4 Bump attractors are necessary but not sufficient for stable grid fields

I wondered what properties of the attractor networks determine the gridness score when g_E, g_I, and noise levels are being changed (cf. Section 4.3.1 for the analysis of grid fields). One possibility is that networks that have low gridness score fail to form stable bump attractors and thus path integration in such networks does not happen. I therefore decided to test to what extent this hypothesis is true. In this section I consider how the formation of bump attractors changes as a function of the strength of excitatory and inhibitory global synaptic coupling between the E and I populations. The stability of bump attractors is determined as a proportion of theta cycles during which the population activity of E cells is classified to form a bump (P(bumps); see Section 4.2.7 for the estimation procedure).

In networks with noise absent, and low inhibition, I found that bump attractors formed successfully, but the firing rate range inside the bump of activity appeared rather discrete (Figure 4.11Aa; also compare with bumps in Figure 4.11c-e). However, the bump was stable, and showed very little drift during the course of the simulation (see also Figure 4.13B for information about intrinsic stability of bump attractors). In this parameter region, gridness score was high (Figure 4.3). This is consistent with the successful attractor formation. On the contrary, when inhibition was increased threefold and excitation decreased by the same amount, bump attractors failed to form and the population activity of E cells was dominated by unstable patterns of activity (Figure 4.11Ab). In fact, further examining the parameter region of g_E and g_I showed that when inhibition is low bumps may fail to form, whereas bumps form successfully when inhibition is low (Figure 4.11B and C.2Bb,c).

While networks without noise have a rather restricted ability to form stable bump attractors, when noise was switched on (σ = 150 pA), most of the parameter region was dominated by bump attractors (Figure 4.11Ac and C) except where the amount of synaptic inhibition or excitation was not sufficient to produce activity necessary for bump formation. The transition between networks with low coupling and no bumps to networks with bumps was, however, sharp. When noise level was increased to σ = 300 pA, the parameter space had a similar organisation (Figure 4.11Ad,e and D).

I next tried to determine whether there is any correlation between the formation of bump attractors and successful generation of grid fields. I first examined the correspondence between regions with high gridness score and regions with high bump score. I

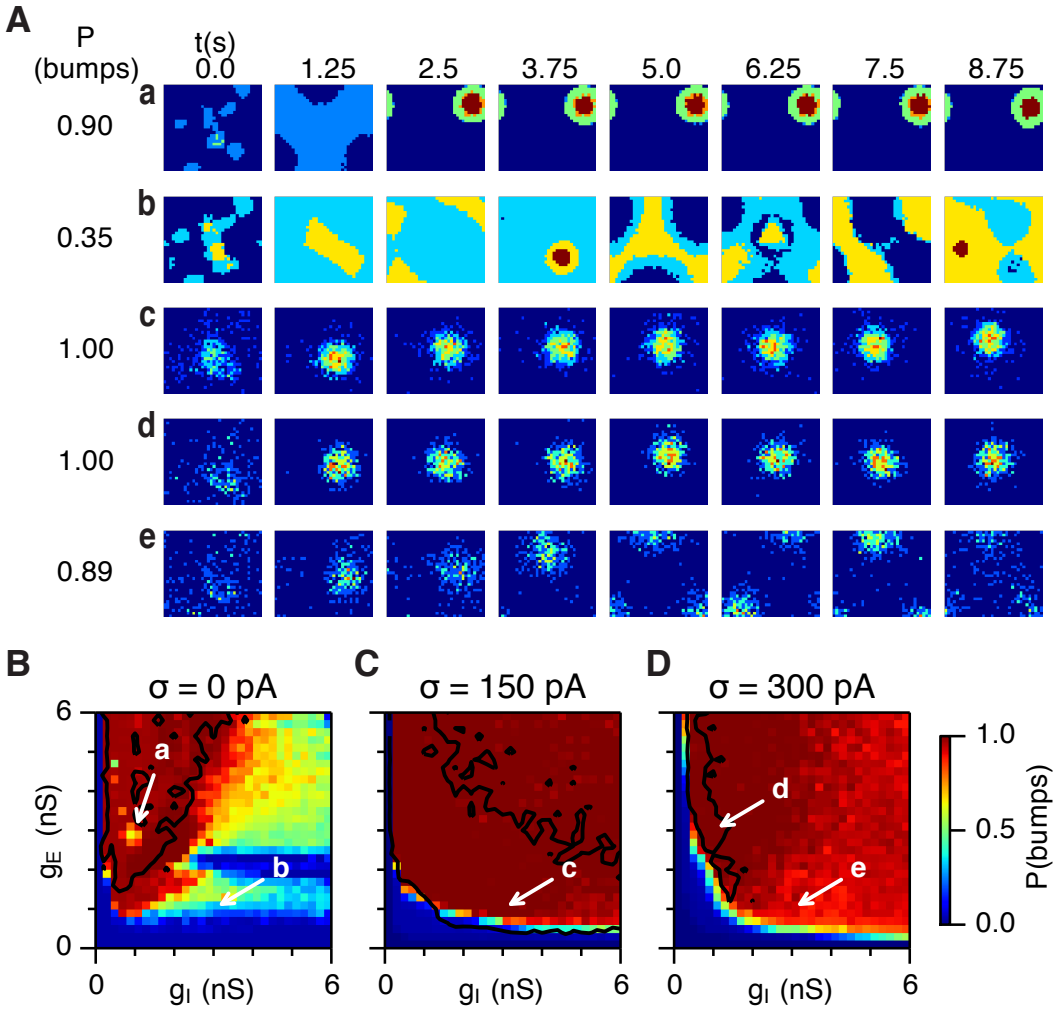

Figure 4.11: **Bump attractors are necessary, but not sufficient for grid field computations. (A)** Examples of E cell population firing rate snapshots from simulations in (B), as highlighted by the arrows (a-e) and the corresponding proportion of snapshots classified as bump attractors, for that particular simulation run (P(bumps)). The snapshots are evenly subsampled in time to 1.25 s, in order to cover the whole ten second simulation run. **(B)** Colour plots show proportion of snapshots of population firing rates classified as bump attractors (sliding rectangular window with 250 ms duration and 125 ms time step; Section 4.2.7), for the three simulated levels of noise and the range of strengths of recurrent synaptic coupling. Arrows show positions in the parameter space of the examples in panel (A).

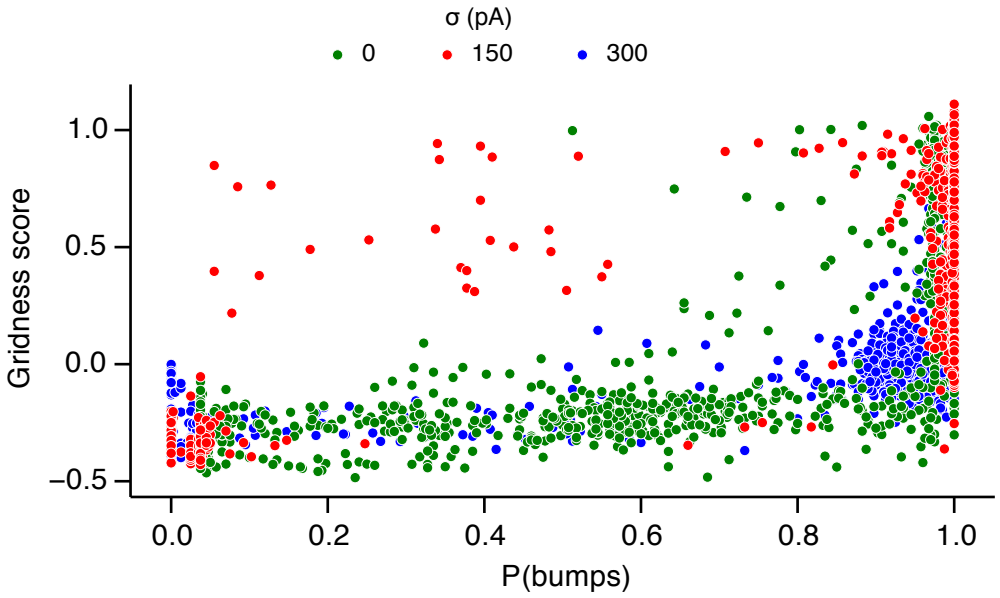

Figure 4.12: **Formation of bump attractors does not imply high gridness score.** Relationship between gridness score computed from the grid field simulation runs (Figures 4.3 and 4.4) and proportion of snapshots of population firing rates classified as bump attractors (Figure 4.11B). Each colour represents one noise level and each dot in the scatter plot is an average of three and five simulation runs of grid field simulations and simulations from Figure 4.11B respectively. The plot shows that successful formation of a bump attractor is necessary but not sufficient for computation of grid fields. A scatter plot with data from different noise levels in separate panels is in Figure C.3.

superimposed a contour plot that highlights a boundary where gridness score is greater than 0.5, onto the plots of bump score in Figure 4.11B-D. In networks without noise, the region of high bump score mostly corresponded with the region of high gridness score (Figure 4.11B). However, near the transition from high to low bump score there were networks that successfully formed bumps, but did not form grid fields. This condition is apparent also in Figure 4.12 (green colour), where networks with high bump score have a relatively wide distribution of gridness scores. This is also most apparent in a separate scatter plot in Figure C.3A (dark and light green colour), where the high bump score region with low gridness scores tightly corresponds with the E-I region highlighted by the contours in Figure 4.11B. I also applied MIC to data in Figure 4.12. However, the MIC values are rather inconclusive in determining the relationship between grid field computation and bump attractor stability, although the MIC values

σ (pA)	MIC	MI	r^2
0	0.551	1.889	0.483
150	0.471	0.914	0.438
300	0.418	1.66	0.288
All together	0.573	1.225	0.391

Table 4.2: **Information measures between gridness score and bump formation score.** The table shows the maximal information coefficient (MIC), mutual information (MI) and the coefficient of determination of a linear fit (r^2) of data in Figure 4.12 (see also Figure C.3 for a detailed plot).

are not close to zero ($MIC_{\sigma=0pA} = 0.551$) and the coefficient of determination of linear fit is moderate ($r^2 = 0.483$, Table 4.2). The data thus suggest that in the case of networks without noise, the formation of bump attractors does not necessarily imply high gridness score.

I next examined the same relationship for networks with noise. Already the first glance on the contour plot in Figure 4.11C,D reveals that most of the parameter region is dominated by successfully formed bump attractors, but the region where gridness score is high does not overlap with the region where bump attractors form. Again, a more thorough examination of the relationship reveals that in both of the noisy cases (σ = 150 and 300 pA), successful formation of bump attractors is not sufficient for stable grid fields, since there is a wide distribution of gridness scores when P(bumps) $\approx$ 1 (Figure 4.12; see also detailed scatter plots in Figure C.3B,C). This interpretation is also supported by the fact that the MIC score drops when noise level is set to 150 and 300 pA (MIC = 0.471 and 0.418 for σ = 150 and 300 pA respectively). In summary, bump attractor formation is necessary, but not sufficient for generation of stable grid fields.

4.3.5 Bump drift and controllability of bump position by external inputs

The method that estimates the presence of a bump in the attractor model only determines whether the bump attractor forms or not. It does not give any information about the stability and controllability of the bump. I have therefore performed an extra set of simulations in which I investigate the spontaneous drift of the bump attractor, as

well as the extent to which the position of the bump can be controlled by the place cell activity.

4.3.5.1 Spontaneous drift of the bump state

In this section I investigate how stable the positions of the centres of the bump attractors are when global synaptic strengths and levels of noise are varied. For data analysis, I used the short, 10 second simulation runs of the stationary bumps (Section 4.2.5.2). Before discussing the data, let us first describe the simulation protocol, illustrated in Figure 4.13A. Every simulation comprises an initialisation phase, that lasts for the first 500 ms of the simulation run. Theta input is switched off and replaced with a constant current. As in every simulation run in this chapter, the network also receives a spatially tuned place cell input that is expected to place the bump attractor into the correct position and switch the activity on the torus into a bump state if it does not form spontaneously (Section 4.2.4). The onset of theta input is at 500 ms. The place cell input is turned off after the end of the initialisation phase.

In this protocol, I determine the drift of the bump attractor as a difference between the estimated position of the bump near the beginning and end of the simulation, that is, at 1 and 9 seconds of the simulation time. The time points of position estimation are illustrated in green in Figure 4.13A.

The parameter space plots of bump drifts yield an interesting result. Figure 4.13B left shows that deterministic networks have a region with very stable bump attractors, when inhibition is low (dark blue region). The rest of the parameter space is dominated by a high drift of the bump (bright values). This can be explained by the fact that bumps do not form in this region, and it is consistent with the data from Section 4.3.4, which shows that bump attractors fail to form in the absence of noise when inhibition is high. With introduction of both intermediate and high levels of noise, the parameter spaces become varied. In the case of σ = 150 pA, we can see an increase of the spontaneous drift in most of the parameter space, with a lower drift in regions where inhibition is low. When σ = 300 pA, the parameter space becomes even more varied, with regions of low drift intermingled with regions of high drift.

Why do noisy networks drift less when g_{E} is high and σ = 150 pA (Figure 4.13B centre)? There are at least two possible explanations. The first one is that strong excitatory synapses will increase the firing rate of interneurons and thus the information about which neurons are dis-inhibited (and thus form a bump) or inhibited (and these are silent) is transferred more readily across the two populations. This will allow for

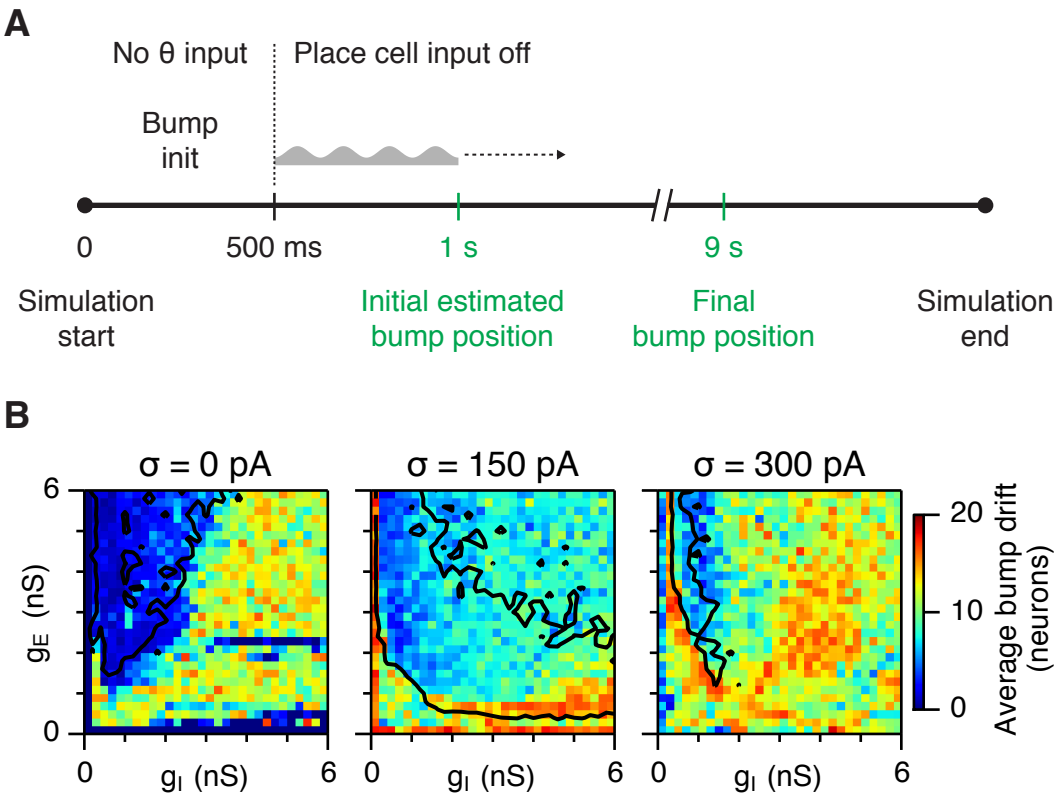

Figure 4.13: **Sensitivity of bump attractor spontaneous drift to variations in synaptic strengths and noise levels. (A)** Schematic of the bump attractor drift estimation procedure. The first 500 ms of a simulation trial are used to initialise the bump attractor. Onset of theta modulated input current was at 500 ms. The estimated centres of bump attractors measured by the least squares fit of symmetric Gaussians were at 1 s (initial position) and 9 s (final position). The drift was then estimated as the distance on twisted torus between the initial and final position. Simulation time was 10 s. **(B)** Colour plots show bump attractor drifts averaged over 3 simulation trials, for the simulated ranges of excitatory and inhibitory synaptic strengths and levels of noise. Networks without noise can form stable bump attractors in a subset of their parameter region. Networks with noise suffer from attractor drift in majority of the parameter region. Black contours show isoclines of gridness score equal to 0.5.

a stable bump attractor. The second, related, reason for increased stability with high g_E is that the increased amount of excitation will also increase the NMDA drive onto interneurons. The increased NMDA currents will thus last for a longer period of time and will retain the information about the bump attractor that is then ready during the next theta cycle. On the other hand both variants produce grid firing fields with high

gridness score (black contours in Figure 4.13B centre). We should note here that the drift can be compensated for by the place cell input and thus the network might be capable of generating stable grid firing fields even when drift is high. The amount of drift will then influence the stability of gridness score when visual cues are not sufficiently salient (e.g. grid cell recordings in darkness; Hafting et al., 2005).

In summary, while networks without noise produce stable and robust bumps in a smaller sub-region of the parameter space than networks with an intermediate level of noise, when bumps are formed in the deterministic networks, their position remains stable and is "immune" to the effects of spontaneous drift that is prevalent in networks with noise.

4.3.5.2 Effectivity of the bump position initialisation

In this section, I investigate how effective the initialisation protocol is (see detailed description in Section 4.2.4). The correct position of the activity bump in the beginning of a simulation run is important for proper synchronisation of place cell input with the actual bump position. If the place cell input is only just strong enough to oppose attractor drift, but not enough to control the position of bump attractors, incorrect initial position of the bump might decrease the gridness score of grid cells.

I therefore ran another set of simulations of a stationary bump (i.e. with the velocity and place cell inputs switched off) and estimated the position of the bump 250 ms after the end of the initialisation phase, that is after 750 ms of simulation time (Figure 4.14A). The 250 ms delay was selected to avoid a transient phase after the end of bump initialisation. This delay is only two theta cycles and in principle should not affect the position of the bump attractor. After the simulation run I computed the difference between the reset coordinates on the twisted torus ([0, 0]) and the actual position of the bump at 750 ms. The distance between these two quantities reflects how effective the initialisation protocol was.

In networks without noise, I found that the initialisation effectivity was low, since the initialisation error was close to half of the torus size (Figure 4.14B left). Thus, in most of the cases, a bump starts at a random position. Note that the bump might not form when inhibition is high, and thus one always has to take into account the data from Figure 4.11. On the contrary, with the intermediate level of noise (σ = 150 pA), the initialisation protocol was effective (Figure 4.14B centre). However, we can see that the initialisation error increases diagonally with the increase in excitation and inhibition. This is interesting, since it could give us a hint on why the gridness score

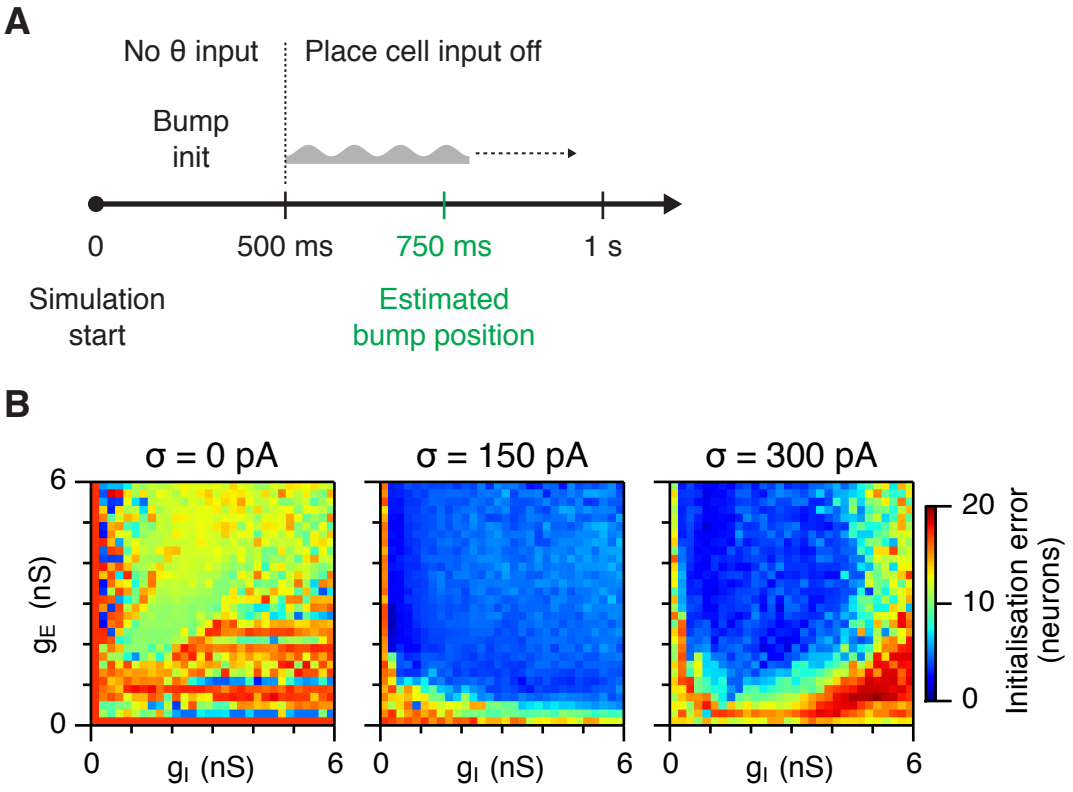

Figure 4.14: **Changes in effectivity of the initialisation protocol as a function of global synaptic coupling and noise level**. **(A)** The protocol used to estimate bump position immediately after the initialisation of the bump attractor was performed. The desired position of the bump was at (0, 0) coordinates on the neural sheet. Bump position was estimated at 750 ms. **(B)** Colour plots show the distance between the required and initialised position of the bump on the twisted torus. Networks without noise mostly fail to initialise the bump into the correct position.

decreases when both excitation and inhibition is high (compare this data with colour plots in Figure 4.4A centre). Networks with noise level set to σ = 300 pA have a higher initialisation error at the edges of the simulated parameter space. There does not seem to be a direct correspondence between gridness score in Figure 4.4A and the initialisation in these simulations.

4.3.5.3 Effectivity of the place cell resetting mechanism

We next turn our focus on how the place cell mechanism influences the position of the bump attractor in the network. This is necessary, since both experimental results (Bonnevie et al., 2013) and modelling work (Pastoll et al., 2013) suggest that grid cells

require an input from the hippocampus in order to generate grid firing fields with high gridness score.

I therefore estimated how effective the place cell input was in keeping the attractor state at a constant position. Again, I simulated 5 trials of 10 second duration, with a 500 ms initialisation phase. Place cell input was then switched on for the duration of the simulation. Velocity input was disabled. Starting at 1 s, the positions of the bumps were then estimated until the end of the 10 s simulation run. These positions were then compared to positions imposed by the place cell resetting mechanism. The average distance between the desired and estimated positions of the bumps thus gave the error of the place cell input.

Figure 4.15B shows the results of the simulations. It is interesting to see that, as in all previous cases in this section, it is relatively hard to control the bump attractor with external inputs when there is no noise in the model. Simulations with $\sigma = 0$ pA show that the average distance from the reset position is again on the order of half the size of the neural sheet, demonstrating that the bump is not controlled by the place cell input (Figure 4.15B left). With the introduction of noise, place cell input is effective in most of the parameter region (Figure 4.15B centre). Interestingly, when both excitation and inhibition are strong, the distance from reset position increases. This is relevant, since it again suggests that the decrease of gridness score, as shown in data from Figure 4.4A in networks with $\sigma = 150$ pA might be related to the effectivity of initialisation and place cell inputs to reset the bump attractor position. When noise was set to $\sigma = 300$ pA, place cell input became even less effective (Figure 4.15B right), and the region with low resetting error was similar to the parameter region with high gridness score, as shown in colour plots in Figure 4.4A right.

Since bump attractors drift in all noise situations (Section 4.3.5.1) place cell input in this model is necessary for the generation of stable grid fields. It is not yet clear why in the noise-free case (Figure 4.15B left) the place cell resetting mechanism is ignored and this would perhaps require additional simulations. However, the seizure-states in Section 4.3.6 could provide an intuitive explanation: the place cell input is extremely small when compared to the postsynaptic currents flowing through the membrane, due to the increased synchronous behavior of neurons and thus will not affect the position of the activity bump. In noisy networks, increased coupling between the populations (whether g_{E} and g_{I} separately, or both increased at the same time) probably contribute to the instability of the bump attractor position. In this cases, increased strength of connections from place cells could potentially ameliorate the inability of the place cell

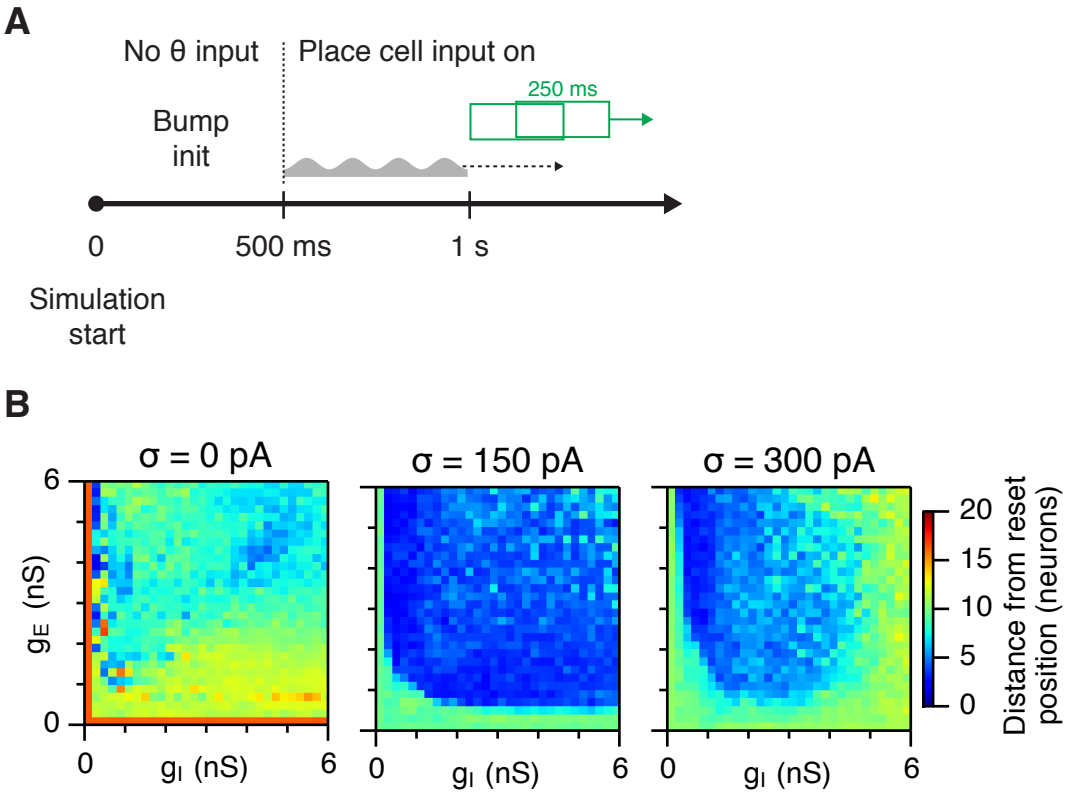

Figure 4.15: **Effectivity of the place cell resetting mechanism as a function of global synaptic couplings and noise level. (A)** Illustration of the procedure to estimate the difference between the "reset" position induced by place cells and estimated position of the bump state, by using a sliding window with 250 ms duration and 125 ms time step. The resulting distance from the reset position, in one simulation run, was then an average over all sliding windows. **(B)** Colour plots show the effectivity of place cell mechanism for an average of 5 simulation runs with 10 s duration. Place cells are most effective in networks with an intermediate amount of noise.

input to compensate for the drift of the attractor.

In summary, in the model with feedback inhibition, changes in noise levels have a profound effect on how the excitatory-inhibitory parameter spaces look like, and thus how well the network performed in computational tasks, such as computation of grid fields.

4.3.6 Seizure-like states in noiseless networks and benefits of noise

How are the changes of noise levels reflected in action potential activity of both E and I populations? To answer this question, I have analysed the activity of all neurons in the network in regions where excitation is weak and inhibition is high (g_E = 1 nS and g_I = 3 nS). Figure 4.16 shows raster plots and population-average firing rates during two consecutive theta cycles. In this location in the parameter space, deterministic networks suffer from hyper-synchronous "packets" of activity at the beginning of theta cycles (Figure 4.16A). When E cells fire in this manner, they immediately trigger a spike or a burst in the whole I population, which in turn inhibits the E cell population for the rest of the theta cycle. The long response of I cells is due to the NMDA component in the excitatory connections (traces not shown). The situation now repeats during the next theta cycle. This way, the bump attractor either does not form at all, or the population activity is unstable (cf. Figure 4.11A).

We can see in Figure 4.16B that introduction of noise stabilises the dynamics of the model. The plot shows that when a bump state has formed in the network, neurons are synchronised and phase locked to both theta and gamma oscillations and the maximal firing rate during theta cycles drops by an order of magnitude. Note that in the case of these simulations no parameters in the model have changed at all, other than the standard deviation of the Gaussian distribution of the noise current. As expected, when noise level was set to σ = 300 pA, the network activity approached the asynchronous state, and nested gamma oscillations did not occur (Figure 4.16C). Note however, that in the case of the example in Figure 4.16, when σ = 300 pA, the average firing rate of E cells decreased as compared to the intermediate noise level. This happened due to the fact that interneurons started to fire spontaneously when noise level increased to σ = 300 pA (Figure 4.16C, blue raster plot and firing rate trace).

In the case of the noise-free network (Figure 4.16A), interneurons fire a burst that resembles gamma activity and we can also observe spike frequency adaptation during the rest of the theta cycle. This burst of activity is due to the super-threshold NMDA synaptic currents mediated by the highly synchronous activation of E cells (red trace in the figure in panel A). The I cells are thus over-excited and the adaptation mechanism affects their firing rate in this case (cf. Section 2.2.2). It is important to note that a different scenario takes place in noisy networks (Figure 4.16B,C). Here, the population firing rates of neurons are approximately an order of magnitude lower than in the

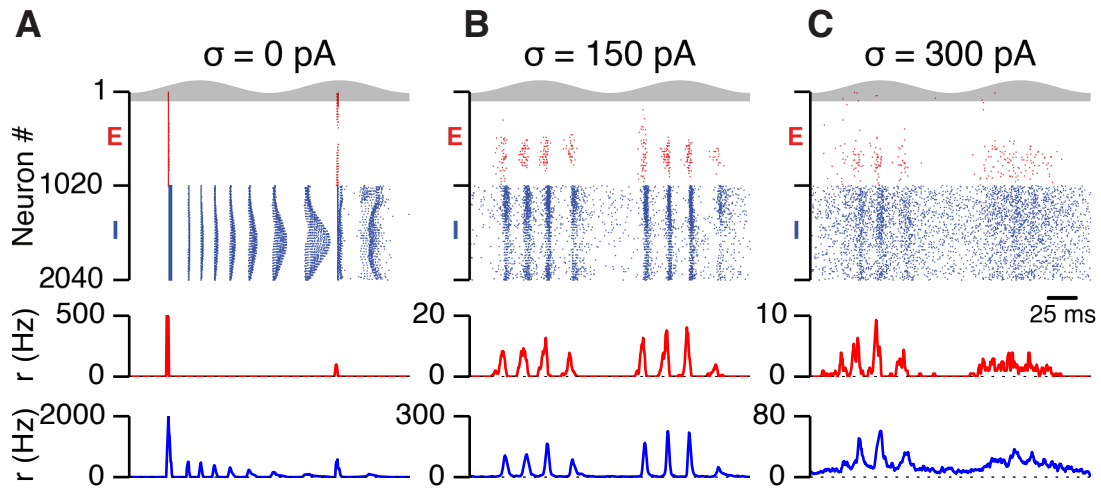

Figure 4.16: **Networks with feedback inhibition can suffer from seizure-like activity when noise is absent.** Raster plots show activity of all neurons in the excitatory (red) and inhibitory (blue) populations for the duration of two theta cycles (top), along with the average population firing rates for both populations (centre and bottom; sliding rectangular window with 2 ms duration and 0.5 ms time step), for the three simulated levels of noise (σ = 0, 150, and 300 pA). Simulations were performed in the absence of simulated animal movement, with g_E = 1 nS and g_I = 3 nS. In this configuration, networks without noise tend to suffer from a hyper-synchronous firing of E cells that prevents formation of bump attractor (cf. Figure 4.11).

noise-free case (centre and bottom traces in panel B in the figure), and thus the synchronisation effect in the network is mediated by the pyramidal-interneuron gamma mechanism. Here, the intrinsic properties, such as membrane and synaptic time constants can in principle affect e.g. the frequency of the generated gamma oscillation.

I next turned to investigate what proportion of the excitatory-inhibitory parameter space was dominated by a strong synchronous spiking activity, especially in networks without noise. I again used the simulations of the stationary bump (Section 4.2.5.2), and extracted the maximal population firing rate during each simulation run. The firing rates were estimated by a sliding rectangular window with a 2 ms duration and a 0.5 ms time step. In order to account for possible spiking artefacts during the initialisation phase, I have excluded the first 500 ms of the simulation runs.

Figure 4.17 shows the parameter space plots extracted from the simulated data. As expected from Figure 4.16, most of the parameter space in networks with σ = 0 pA is occupied by networks in which at least one theta cycle had a population-average

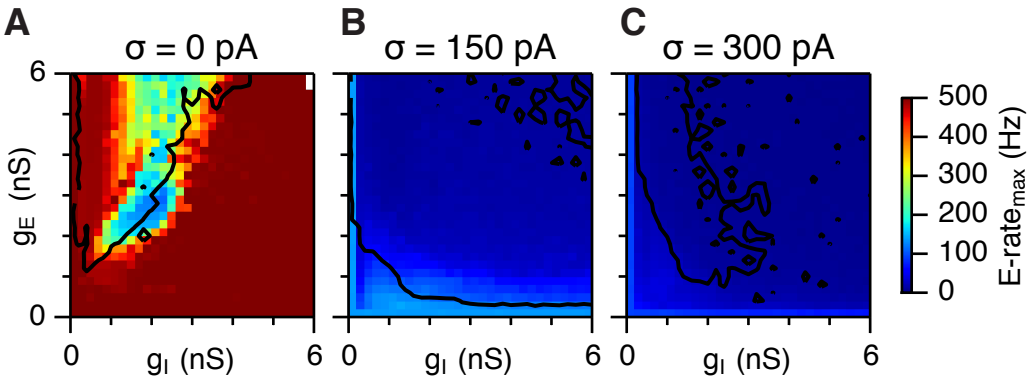

Figure 4.17: **Seizure-like activity in the parameter spaces of global synaptic couplings and noise.** Maximal average population firing rate of E cells estimated from the whole simulation run (10 s, 500 ms at the beginning of the simulation excluded) for each simulated level of noise. Most of the parameter region in networks without noise has at least one hyper-synchronous firing burst. Each point in the parameter region is an average of maxima from 5 simulation runs. Black lines show isoclines of gridness score equal to 0.1, indicating, for networks without noise, only a partial overlap of a region with high gridness score and a region with seizure activity.

firing rate of 500 Hz. That means that during 10 s of simulated time, at least one theta cycle in these networks was dominated by a synchronous spiking of almost all E neurons during a 2 ms window (Figure 4.17A). This kind of activity is prevented by introducing both intermediate and high levels of noise, since the maximal firing rate during the simulations dropped markedly (Figure 4.17B,C).

The maximal firing rate throughout the *whole* simulation is a rough measure of incidence of seizure-like states in the network. However, when I superimposed the contour plot of gridness score onto the parameter space in Figure 4.17A (black lines are isoclines that equal gridness score of 0.1), I noticed that many networks had the maximal firing rate saturated at 500 Hz/0.2ms, even though they generated stable grid firing fields. Some networks, especially on the boundaries of the gridness score isoclines, did not suffer from strong seizure-like states but did not generate stable grid fields (Figure 4.17A).

I therefore refined the firing rate measures by estimating the maximal firing rate per theta cycle, instead of for the whole simulation. I used a simple, threshold-based classifier to classify each theta cycle: if the firing rate during the theta cycle was higher than 300 (i.e. more than 60% of cells firing during a 2ms time interval), the cycle was

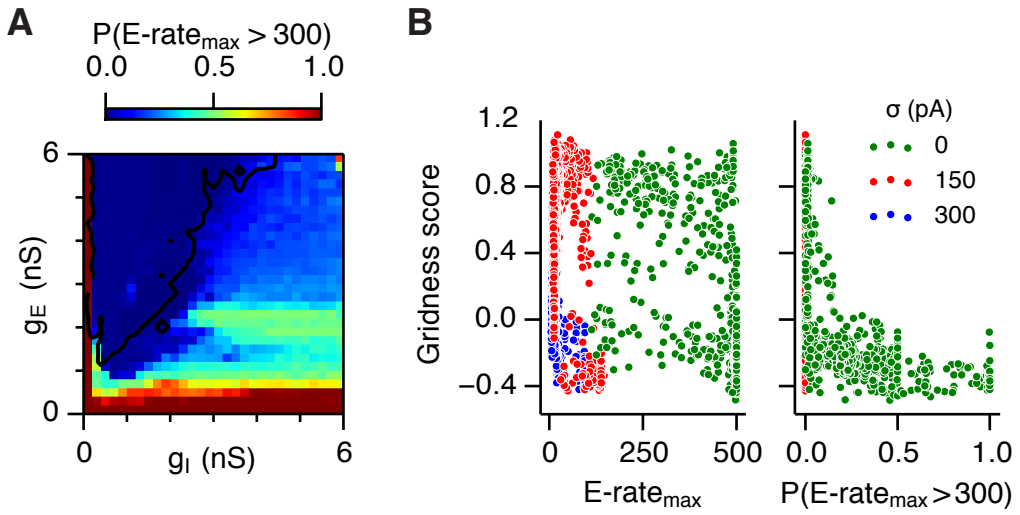

Figure 4.18: **Incidence of seizure-like states determines gridness scores in networks without noise. (A)** Proportions of theta cycles in the simulation runs classified as seizures, i.e. those theta cycles in which the population-average firing rate was greater than 300 Hz/2ms interval. Isoclines show regions where gridness score equals 0.1. **(B)** Scatter plot of gridness score vs. the maximal firing rate during whole simulation run (left) and the proportion of theta cycles classified as seizures (right).

classified as containing a seizure, otherwise it did not. I then estimated the fraction of theta cycles during the simulation that were classified as seizures (P(E-rate$_{max}$ > 300)).

After applying the seizure incidence measure to the data I noticed that networks without noise suffer from a large number of seizure-like states when inhibition is strong (Figure 4.18A) and that this region roughly corresponds with low gridness score in Figure 4.3B. At the same time, when inhibition is low, the incidence of seizures declines rapidly. The isocline plots of gridness score are aligned well to the region with low incidence of seizure states in the network as well (Figure 4.18A), suggesting that in networks without noise the presence of hyper-synchronous firing is mostly responsible for the loss of stable grid fields. This is corroborated by the higher MIC values, suggesting a stronger relationship between gridness score and seizure incidence (MIC = 0.603 for σ = 0 pA; Table 4.3). Note that E-rate$_{max}$ does not predict gridness score as well (MIC = 0.523), which is consistent with the colour plot in Figure 4.17A. For P(E-rate$_{max}$ > 300) and σ = 150 and 300 pA the MIC is zero, since noisy networks do not suffer from seizures at all, and thus the incidence of seizures is irrelevant to gridness score in these networks.

Gridness score vs. E-rate$_{max}$				vs. P(E-rate$_{max}$ > 300)		
σ (pA)	MIC	MI	r^2	MIC	MI	r^2
0	0.523	1.498	0.314	0.603	1.949	0.359
150	0.499	2.073	0.240	0	0	0
300	0.404	1.965	0.109	0	0	0
All together	0.49	1.413	0.122	0.37	0.635	0.192

Table 4.3: **Information measures between gridness score and seizure scores.** The table shows the maximal information coefficient (MIC), mutual information (MI), and the coefficient of determination of a linear fit (r^2) for data from Figures 4.17 and 4.18.

I thus conclude that noise is beneficial to break down seizure-like spiking of both E and I cells in deterministic grid cell networks with feedback inhibition and theta-nested gamma oscillations. This, in many cases, helps to stabilise the dynamics of the spiking network and thus helps in formation of stable bump attractors. In the deterministic networks, the seizure-like states are largely responsible for the failure to form stable bump attractors and thus perform accurate path integration. In networks with noise, there are no seizure-like states present, and thus changes in gridness score and/or power and frequency of gamma oscillations are very likely attributed to changes in the strengths of excitatory and inhibitory synaptic connections, or, as we have seen in Section 4.3.5, to the sensitivity of the attractor networks to noise-induced drift and the ability of place cell input to correct for this drift.

4.4 Discussion

In this chapter, I have shown that the presence of an optimal level of noise in a model inspired by anatomical and functional evidence from layer II in the MEC is beneficial for computations of grid fields and emergence of nested gamma oscillations in this circuit. I have simulated a two-population neural network model in a large two-dimensional space of global synaptic strengths between excitatory and inhibitory populations. The network received different levels of white noise, specified by standard deviation of the Gaussian distribution the noise was sampled from.

The simulations show that the attractor network without noise has a limited subregion in the parameter space in which grid field computations take place, while most

of the parameter space did not produce grid fields in these networks. When an intermediate level of noise was present, the region supporting the formation of grid fields covered most of the parameter space. With even higher level of noise present in the network, gridness score dropped to low values in most of the parameter space. Similar, in fact stronger effects, were observed, when power of nested gamma oscillations was analysed.

I have shown that these effects are partially attributed to the fact that networks without noise fail to form continuous attractors in parts of the parameter space with low gridness score, which in turn affects the quality of path integration performed by these networks. Moreover, the sub-regions with low gridness score in deterministic networks were dominated by epileptic-like hyper-synchronous firing of E and I cells which is very likely the reason why the attractor networks presented here failed to produce stable continuous attractor states.

These results thus suggest that noise can play an important role in pattern formation in neural circuits both in time and space. Given the widely believed role of grid cells in spatial navigation (Barry and Burgess, 2014; Moser et al., 2014), and the role of oscillations in cognition and various psychological disorders (Traub and Whittington, 2010; Uhlhaas and Singer, 2010; Buzsáki et al., 2013; Kopell et al., 2014), the results show that the presence of noise might be an important aspect of a correct functioning of the nervous system.

4.4.1 Signal transmission versus pattern formation

In communication systems, noise degrades the amount of information that can be transmitted through a communication channel (Shannon, 1956; Cover and Thomas, 2006). Noise in the nervous system can come from various sources and in general is believed to distort the fidelity of transmitted signals (Faisal et al., 2008). In some cases, stochastic resonance can increase the signal-to-noise ratio during signal propagation (Longtin et al., 1991; Benzi et al., 1999; Shu et al., 2003). In this work, the grid cell attractor network has a role distinct from solely propagating input signals. In fact, the network has to create a pattern of population activity, the activity bump, and transform this pattern into single neuron grid firing fields. In the absence of noise, the network, due to periodic theta frequency input, does not generate stable attractors necessary for the velocity integration process that generates grid firing fields. Thus, the role of noise in the attractor network lies in abolishing strong inhibitory feedback from interneurons,

which allows the network to generate stable bump states.

This role of noise could be explored here due to the explicit representation of spiking dynamics and fast and slow synapses in the network. This is different from other models of theta-nested gamma oscillations that simulate a two-dimensional dynamical system of E and I populations with theta modulated inputs to the network (Onslow et al., 2014). The main difference lies in the fact that the state of the network in such models is represented by a firing rate variable, and synaptic input influences this firing rate instantaneously. In contrast, the model presented here has AMPA-, NMDA- and fast GABA-mediated synapses which allow for much richer synaptic dynamics than the firing rate models. Thus, while these highly reduced models allow for analytical explorations, they do not represent the spiking dynamics in the network presented here and do not allow to study generation of spatio-temporal patterns, such as grid firing fields.

4.4.2 Independent gamma and rate-coded computation

Neural mechanisms that underlie cognitive performance and deficits are currently not known. Experimental models of autism and schizophrenia suggest that cognitive deficits in these disorders can be attributed to changes in the balance between excitation and inhibition (Rubenstein and Merzenich, 2003; Lewis et al., 2012). At the same time, the communication by coherence hypothesis proposes that functional connectivity can be accomplished by increased coherence between distinct brain areas (Fries, 2005). The natural consequence of this idea is that cognitive deficits would be linked to abnormalities in oscillatory activity (Uhlhaas and Singer, 2012). Oscillatory activity could also be used for simply routing information from different upstream brain regions, into a single receiver capable of filtering information based on frequency. It has been demonstrated by modelling that such effects are viable (Akam and Kullmann, 2010).

Grid cells are believed to be part of a wider cognitive circuit composed of hippocampus and surrounding areas, and thus the model presented here allows us to relate the mechanistic substrates of grid field computation and gamma oscillations to changes in the strengths of excitatory and inhibitory connections. The results in this chapter show that in a realistic scenario when networks contain certain amount of noise, there is a dissociation between the power and frequency of gamma oscillations from the rate coded computations performed by the attractor part of the network (Section 4.3.3). In the theta-gamma attractor network, it is possible to tune the power and frequency of

nested gamma oscillations by changing the values of g_{E} and g_{I}, without disrupting the rate coded computation of grid fields in the neural circuit. These results are thus more consistent with a currently abstract concept of communication by coherence (Fries, 2005; Akam and Kullmann, 2012) in which changes in coherence between two brain regions influence the ability of the regions to mutually communicate. Similarly, the combination of rate-coded computation and gamma oscillations in the network could be utilised by a downstream region that selectively filters information based on the oscillation frequency of the upstream area (Akam and Kullmann, 2010). This filtering scenario is further supported by the independence of the rate-coded grid computations and gamma frequency oscillations as reported in this chapter. If one assumes that cognitive processes are solely the result of a rate-coded mechanism, in which the grid-like tuning curves could participate, then the dissociation between nested gamma oscillations and grid field computation in the model here would imply that these two phenomena might be related only weakly. This would be in contrast with the underlying hypothesis that the observed perceptual weaknesses in cognitive disorders are linked to abnormalities in the power of gamma oscillations (Rubenstein and Merzenich, 2003; Lewis et al., 2012). On the other hand, under assumption of the communication by coherence hypothesis, oscillatory activity is necessary to ensure information transfer between two brain areas. In that case, the presence of both rate-coded tuning curves and gamma oscillations is necessary for correct functioning of the nervous system. Then, the networks such as the grid cell network modelled here, need specific fine-tuning of their parameters in order to perform their tasks accurately, and disruption of oscillatory activity itself is sufficient to render the transfer of the rate-coded information ineffective.

While in the model here the exploration of theta-nested gamma oscillations and grid firing fields was motivated by changes in the ratio of excitation and inhibition, other parameters of the model could be responsible for different dynamical states in the attractor network. Onslow et al. (2014) have recently shown that different theta amplitudes and the strength of a tonic drive (here represented as I_θ and I_{const} in Eqs. (2.10) and (2.9)) could also contribute to different variants of theta-nested gamma oscillations. For instance, in Onslow et al. (2014), when theta input to the E population was below a certain threshold, the model did not generate nested gamma oscillations. If the input was too strong, the network generated gamma oscillation only on the rising and descending phases of theta. However, due to their reduced nature, it is not clear to what extent such rate implementations correspond to the spiking attractor network

presented here.

4.4.3 Robustness of the network during fine-tuning of synaptic strengths

The presence or absence of noise in an attractor network as highlighted in this work is relevant with respect to the need to self-organise the grid cell circuit. I have shown that the attractor network with feedback inhibition, the neural circuit that has been suggested to reside in the layer II of the MEC (Pastoll et al., 2013; Couey et al., 2013; Yoon et al., 2013), has improved properties in terms of neural computation when noise is included in the network. Networks with noise have a much higher gridness score as a function of the strengths of global excitatory and inhibitory synaptic strengths as opposed to networks that do not receive any source of noise. This means that noisy networks are much more robust to changes in the total strengths of couplings between the excitatory and inhibitory populations. In turn the plasticity mechanisms that need to fine-tune the network into a usable state, have a much "simpler task".

4.4.4 Trade-off between stability, correct attractor formation, and controllability

We have seen in Section 4.3.5.1 that there are differences between the stability of bump attractors formed in networks without noise and attractors in noisy networks. There are a number of interesting points to consider when comparing these two model variations. The simulations show that even though networks with noise can form stable bump attractors easily (Figure 4.11), these attractors can suffer from a considerable amount of spontaneous drift, as shown in the central part of Figure 4.13B. Thus, it is necessary to include a certain resetting mechanism into networks with noise. This has been accomplished by connecting the attractor model with place cell input from hippocampus. This input opposes attractor drift.

On the contrary, in networks without noise (Figure 4.13B left), we can see that the bump attractor, in locations in the parameter spaces where bumps form, remains stable. In fact, the blue region in Figure 4.13B left is close to zero, indicating that the bump attractor does not move during the simulation. This apparent stability has drawbacks, in that it might lead to states during which neurons fire in a hyper-synchronous way (Figure 4.17).

Therefore, there is a trade-off. Networks with noise accumulate error and are thus not able to path-integrate for a long time, but they are more robust to changes in global synaptic coupling between the excitatory and inhibitory populations. In addition, even though networks without noise are more stable than networks with noise, they require a specific tuning of the recurrent synaptic strengths. It would be interesting to investigate experimentally which one of these scenarios would be more plausible in terms of coding and spatial navigation in rodents.

4.4.5 Implementation of noise

The noise in this chapter was implemented as a current input drawn from a Gaussian distribution. Thus, it is an abstract way to represent variability in the system. As we have seen, it is this variability that in certain configurations prevents the network from forming the seizure-like states. In other words, the presence of variability breaks the symmetry of the system, and allows the network to successfully form bump states and use them for path integration. Although Gaussian white noise is the means of noise implementation in this work, it is possible that other sources of inhomogeneities would be sufficient to prevent the seizure-like states as well. For instance, noise in the amplitude or phase of the theta inputs could in principle be sufficient to induce enough variability to prevent the hyper-synchronous firing of E cells which in turn hyper-excite the I cells. Another possibility is the inhomogeneities in the synaptic properties of neurons, e.g. introducing noise in the excitatory and inhibitory synaptic profiles. It should however be noted that these inhomogeneities could also impair the path integration mechanism or bump state formation to such an extent that this could profoundly impair basic dynamics of the network as such. Additional simulations would thus be required to quantitatively assess the effect of other sources of variability on network dynamics in this model.

Chapter 5

Conclusion and future work

5.1 Conclusion

In this thesis, I have presented results about the possible dynamics of attractor networks of grid cells in layer II of the MEC. The networks are based on the hypothesis that the local grid cell circuit performs path integration, i.e. the integration of angular and speed signals somehow represented in the brain.

Since the discovery of grid cells, there have been many attempts to model the local microcircuit of the medial entorhinal cortex. Most of the modelling work can be divided into two classes: one of them uses interference of velocity controlled oscillators (O'Keefe and Recce, 1993; Burgess et al., 2007), while the other approach is based on attractor dynamics (Fuhs and Touretzky, 2006; Burak and Fiete, 2009). Here, I adopted the approach that assumes that the underlying microcircuit in layer II consists of an attractor network, and, as mentioned earlier and throughout the work, that this attractor network performs integration of the velocity inputs impinging on it. The reasons for adopting the attractor approach were twofold.

Firstly, oscillatory interference models have received substantial critique from the modelling and experimental community. Namely, it has been argued that the basic analytical model as suggested in O'Keefe and Recce (1993) and Burgess et al. (2007) is not plausible when realistic neural dynamics are considered (Remme et al., 2010). Moreover, recent experimental evidence from *in vivo* whole cell recordings suggests that the depolarisation effect when an animal is traversing the grid field is caused by slow ramps rather than changes in amplitudes of theta oscillations (Domnisoru et al., 2013; Schmidt-Hieber and Häusser, 2013) as predicted by the interference model (Burgess et al., 2007). Also, intrinsic theta oscillations are rather unstable themselves (Dod-

son et al., 2011), while the relative phase-stability of the velocity controlled oscillators is an imminent prerequisite for the correct functioning of these types of models (although see work by Burgess and Burgess (2014) that ameliorates this issue). While this critique is rather substantial, I consider the ability to quantitatively evaluate the interference model as its strength. Indeed, this has spawned important conceptual advances in terms of how the oscillatory interference mechanism could be implemented in a more biologically plausible way. For instance, it is possible to model velocity controlled oscillators as independent networks of oscillators, each with its preferred direction, which solves the issue of phase locking of the dendritic oscillators (Zilli and Hasselmo, 2010). In fact, recent work has attempted to create hybrid models that combined the interference mechanism with attractor networks (Bush and Burgess, 2014).

The second reason is that network interactions are at the core of the attractor models and so inevitably the dynamics are more complicated and harder to test experimentally. Therefore, the attractor models of grid cells mostly received attention at the level of firing rate models (Fuhs and Touretzky, 2006; Burak and Fiete, 2009; Couey et al., 2013). In contrast, models of head direction cells (Song and Wang, 2005) and spatial working memory (Compte et al., 2000) have been pushed forward in the direction of implementing spiking versions of attractors. While rate models are rather simpler to deal with, they do not allow to consider the full spectrum of dynamics as the spiking models and their predictive power is also lower. Thus, even despite the current evidence in favour of the attractor models of grid cells (Yoon et al., 2013), there remains a lot of work to be done in order to validate their biological plausibility.

In broader terms, the latter reason was a motivation to build a two-population spiking attractor model of grid cells. In Chapter 3, I have shown that some of the simulation outputs are directly testable in an experimental setting. For instance, the predicted membrane potential dynamics of the integrate and fire neuron I have used to model single neurons can be directly measured in *in vivo* or *in vitro* conditions, albeit this is technically still challenging (Domnisoru et al., 2013; Schmidt-Hieber and Häusser, 2013). By simulating an idealised voltage clamp, I have also shown that the theta-nested gamma oscillations activated by light in slices of the MEC can be faithfully reproduced in the attractor model (Pastoll et al., 2013), also providing a step forward in assessing the biological plausibility of the model and its predictive power with respect to experimental work.

The results presented in this work constitute a step forward in validating the attractor model in light of the anatomical constraints on layer II in the MEC. For instance,

it has been shown that principal cells in layer II communicate with each other only via feedback inhibition (Pastoll et al., 2013; Couey et al., 2013). This poses specific challenges for the attractor model, since tuning curves in attractor models are mostly assumed to arise from excitatory interactions between excitatory cells, while inhibition might or might not be spatially tuned (Compte et al., 2000). Building on previous work on rate (Fuhs and Touretzky, 2006; Burak and Fiete, 2009) and spiking models (Song and Wang, 2005), I have shown that the circuit which contains only feedback inhibition is sufficient to generate stable attractor states and networks that are capable of path integration. Moreover, by implementing the excitatory and inhibitory populations separately, the work here has provided important predictions about the firing rates of interneurons, that have already been tested in an experimental study (Buetfering et al., 2014). While the predictions show that interneurons have to have spatial firing fields that are either grid-like or have an "inverted" grid structure, Buetfering et al. (2014) have shown that spatial firing fields of the majority of parvalbumin positive interneurons (in mice) are neither of these, although they carry certain spatial information. Hence, one possibility is that the basic idea of an attractor model has to be advanced by future modelling studies that show whether it is possible to build attractor networks without feedback inhibition in which interneurons do not have regular spatial firing fields. An alternative possibility is that the hexagonal or "inverted hexagonal" firing fields will be recorded in other types of interneurons present in layer II of the MEC (Canto et al., 2008).

While the advancements in terms of higher biological plausibility and satisfaction of anatomical constraints in the proposed attractor network model are compelling, the results of the work do not end there. I have shown that the attractor network based on feedback inhibition reproduces the cross-frequency coupling of theta and gamma oscillations observed *in vivo* (Chrobak and Buzsaki, 1998; Quilichini et al., 2010). The model is also consistent with data from optogenetically activated *in vitro* microcircuits, that generate theta-nested gamma oscillations, in a controlled manner (Pastoll et al., 2013). I show that, in the same way as in the slice preparation in Pastoll et al. (2013), the model network can generate synchronised bursts of population activity in the gamma range in a manner that is dependent on the phase of theta oscillation, with a clock-like precision. These aspects are important, because they support several cognitive theories of information transmission in the brain. For instance, the model could be compatible with some of the proposals about how theta and gamma oscillations could be used to carry out working memory operations (Jensen and Lisman, 1998, 1996).

At the same time, the model has important implications for the implementations of the communication-by-coherence concept (Fries, 2005), since it directly shows how a rate-coded mechanism could be combined with spike timing in order to allow for efficient functional communication between different areas. This efficient communication could also be modulated by filtering networks, as suggested in Akam and Kullmann (2010).

In Chapter 4 I explored how variations in noise and synaptic strengths between the excitatory and inhibitory populations influence the correct functioning of the network with respect to grid field computation and theta-nested gamma oscillations. I have shown that the presence of noise promotes generation of stable grid firing fields, mostly by breaking the network off from seizure-like states that prevent formation of stable bump attractors. I have also shown that networks with noise much more readily engage in stable theta-nested gamma oscillations, also a result of breaking down the seizure-like states.

In addition, I have shown that noise promotes differential sensitivity of nested gamma oscillations and grid field computations to changes in excitatory and inhibitory synaptic strengths in the network. Namely, in the attractor network presented here it is possible to tune the power and frequency of nested gamma oscillations independently of the way the network generates stable grid firing fields. These results are relevant to the current theories of disorders such as autism and schizophrenia that postulate that changes in the balance between excitation and inhibition may result in cognitive deficits (Rubenstein and Merzenich, 2003; Lewis et al., 2012). In the attractor model presented here, it is possible to dissociate the power of gamma oscillations from the grid field cognitive circuit suggesting that, at least in the specific model presented here, gamma oscillations co-exist, but do not contribute to the rate-coded computation performed by the attractor network.

5.2 Future work

Among other topics, one of the central points of this work was to build a prototype of a spiking attractor network model of grid cells. This has been accomplished fully and I now possess a comprehensive set of software tools to simulate and explore the properties of these networks in different computational contexts.

One of the immediate predictions of the two-population attractor model presented here is that the fast spiking interneurons in layer II of the MEC have regular spatial

firing fields. This has been shown to be the case for only a subset of parvalbumin interneurons (Buetfering et al., 2014), although firing fields of other interneuron types are currently unknown. Thus a question arises whether it is possible to build attractor models in which excitatory cells only communicate via feedback inhibition, and inhibitory cells do not have any regular spatial organisation (in our case the fast spiking interneurons). This is one of the possible future directions.

The attractor models, and not only of grid cells, have been criticised to be biologically implausible due to the complicated nature of connection weights. In fact, most of the models rely on an intricate synaptic profile functions, and thus it is not clear how such circuits would arise developmentally. With models of path integration, there is an added complication of the network having to perform as an accurate path integrator, which adds up to the complicated set of features the network has to perform (Fuhs and Touretzky, 2006; Burak and Fiete, 2009). Only very recently have there been attempts to "develop" the grid cell attractor model by using STDP and spatially tuned inputs, and the networks perform well only under specific and well-tuned conditions, and in some cases may suffer from positive feedback loops that do not allow the network to self organise (Widloski and Fiete, 2014). Thus, one of the directions of the future work are to test the validity of attractor networks of grid cells in the developmental context.

In conclusion, the work presented in this thesis is a step forward in demonstrating the plausibility of the existence of continuous attractor networks in layer II of the MEC and in the brain in general. The spiking implementation allowed me to explore questions about specific mechanistic implementations of theta-nested gamma oscillations in a region such as the MEC and demonstrated the advantages of using spiking neural networks to make predictions about intra- and extra-cellular recordings in the brain. Therefore, I believe that my work has provided valuable insights into the computations performed by the nervous system.

Appendix A

Estimating the velocity response of bump attractors

In order to estimate the precision of velocity integration in a continuous attractor, I have performed shorter simulations in which a constant velocity input (in the horizontal direction) has been injected into E cells for a period of 10 seconds. Based on this set of simulations, the slope of the bump speed vs. strength of the injected velocity current has been estimated (in units of neurons/s/pA). The estimation was based on the following algorithm:

1. Estimate the range of bump speeds that need to be covered (Figure A.1).

$$s^i_{\text{bump}} = \frac{N_x}{\lambda_{\text{grid}}} * s^i_{\text{animal}}, \tag{A.1}$$

   where s_i are the speeds of the animal/bump, estimated from forward differences of the trajectory of the simulated animal (Figure A.1A), N_x is the horizontal size of the neural sheet (neurons), and λ_{grid} is the grid field spacing (cm). These speeds will form a distribution of bump speeds that the attractor must achieve in order to path integrate without error (figure A.1B).

2. Pick a specified percentile from this distribution (here, the 99^{th} percentile was used), i.e. the maximal speed of the bump, in order to account for the specified fraction of animal velocities, set this as s_{max}. The range of target bump speeds will be $< 0, s_{\text{max}} >$.

3. For each $I_{\text{vel}} \in \{0, 10, .., 100\}$ pA, estimate the bump speed by tracking its position on the neural sheet, using the Gaussian fitting procedure described in Section

4.2.7.1. Repeat this step 10 times. This step acquires data for estimating the slope of bump speed vs. injected velocity current relationship.

4. For each $I_{\text{vel}}^{\max} \in \{10, 20, .., 100\}$ pA, estimate a line fit on data samples with the velocity current in the range of $I_{\text{vel}} \in < 0, I_{\text{vel}}^{\max} >$, i.e. fit the line to only a subset of velocity current data points.

5. Remove all fits that do not fit at least $< 0, s_{\max} >$ on the bump velocity axis.

6. If there are any lines left, select line with the minimal error of fit (normalized by the number of data points used); otherwise select line (from the original list) that covers the maximal range of bump speeds.

7. Calculate the slope of the selected line and finish.

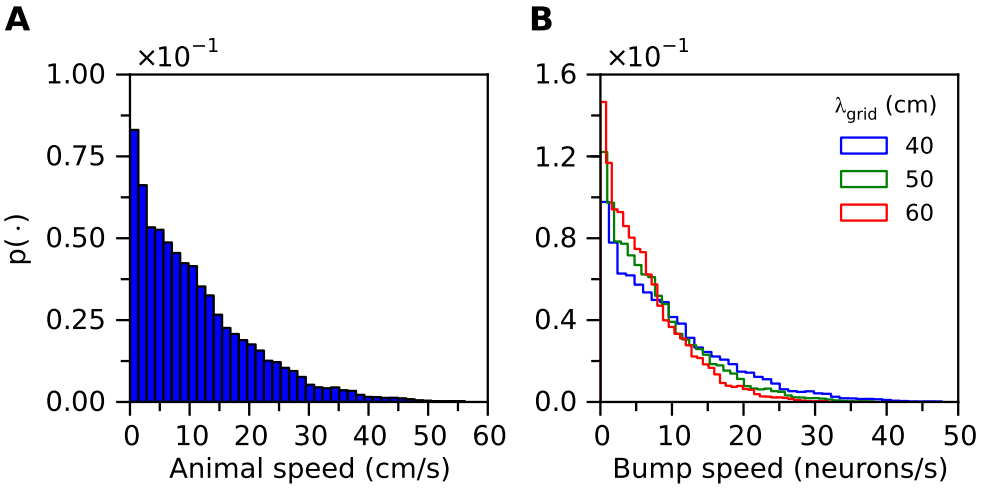

Figure A.1: **Animal and bump speeds necessary to achieve accurate path integration. (A)** Histogram of velocities of a simulated animal. **(B)** Histogram of bump speeds derived from the animal velocities estimated in eq. (A.1), for different grid field spacings.

Appendix B

Standard deviation of fitted Gaussians as a bump formation measure

I have estimated snapshots of population firing rate at the end of shorter, 10 second, simulation runs (5 trials). For each run, the population firing rate on the twisted torus was estimated by a sliding rectangular window with a duration of 250 ms and a 125 ms time step. For each of the snapshots, the fitting procedure estimated the parameters of the Gaussian function described in Eq. (4.3) in Section 4.2.7.1). In this method, only the reciprocal of the standard deviation of the Gaussian functions was taken into account ($\sigma_{\text{bump}}^{-1}$). The resulting reciprocal value, for one simulation run, was determined as a mean value for all the sliding windows during that particular simulation run.

Note that when $\sigma_{\text{bump}}^{-1} = 0$, the bump width is theoretically infinite, i.e. the activity on the torus would be uniform, while when $\sigma_{\text{bump}}^{-1} = \infty$, the bump would be infinitely narrow. Thus, the interpretation of this measure is that $\sigma_{\text{bump}}^{-1}$ is close to the width of the bump, with values close to zero representing wide bumps, and high values representing narrow bumps. The measure of taking the reciprocal of σ_{bump} makes sense when one wants to take an average values of several bump estimates during a simulation run. If only σ_{bump} was considered, activity close to uniform, i.e. all neurons firing with a very similar firing rate, would inevitably bias the resulting number towards very wide bumps.

Figure B.1 shows the g_{E} and g_{I} parameter spaces of the reciprocal of σ_{bump} (averaged over 5 trials). The results here are similar to Figure 4.11. However, as mentioned in Section 4.2.7.2, this measure is hard to interpret and I thus used the more sophisti-

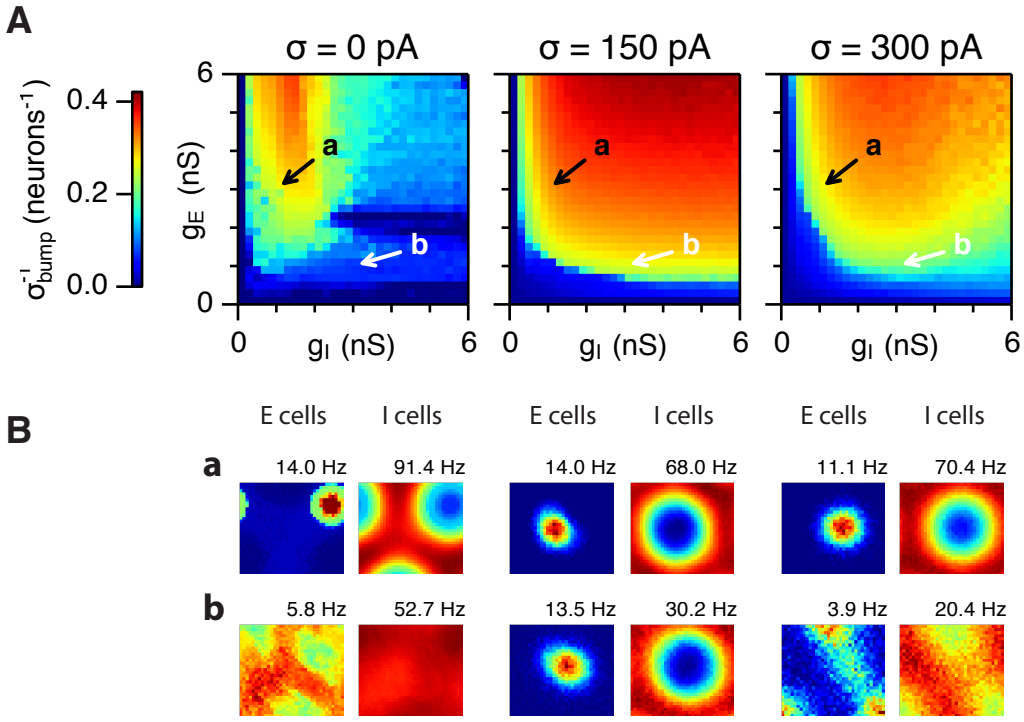

Figure B.1: **Estimating the presence of bump attractors.** Short, ten second simulations have been run and population firing rate of E cells has been estimated, with a 250 ms rectangular window and 125 ms (one θ cycle) window time step. Symmetric Gaussian functions were then fitted onto each snapshot and standard deviation was estimated (σ_{bump}). **(A)** Shows an average of $\sigma^{-1}_{\text{bump}}$ of all the snapshots in one simulation for all the simulated strengths of synaptic couplings (g_{E} and g_{I}) and noise levels. The final values were averages of 5 simulation trials. **(B)** Representative average population firing rates of both populations during the whole course of one of the simulation trials in the parameter regions highlighted by arrows in panel (A). While this simple metric allows for a rough estimate of the "presence" of bumps by quantifying the standard deviation of the fitted Gaussian functions, it might not be adequate to reliably determine whether, and for what period of time during the simulation, a stable bump attractor forms.

cated estimation of the presence of bump attractors in order to study their stability and relationship to grid field computations and gamma oscillations.

Appendix C

Detailed figures for the parameter exploration simulations

This appendix provides several detailed plots of the dynamics of the network presented in Chapter 4. These plots are locations in the excitatory-inhibitory parameter spaces that illustrate the spiking activity and computation of the network.

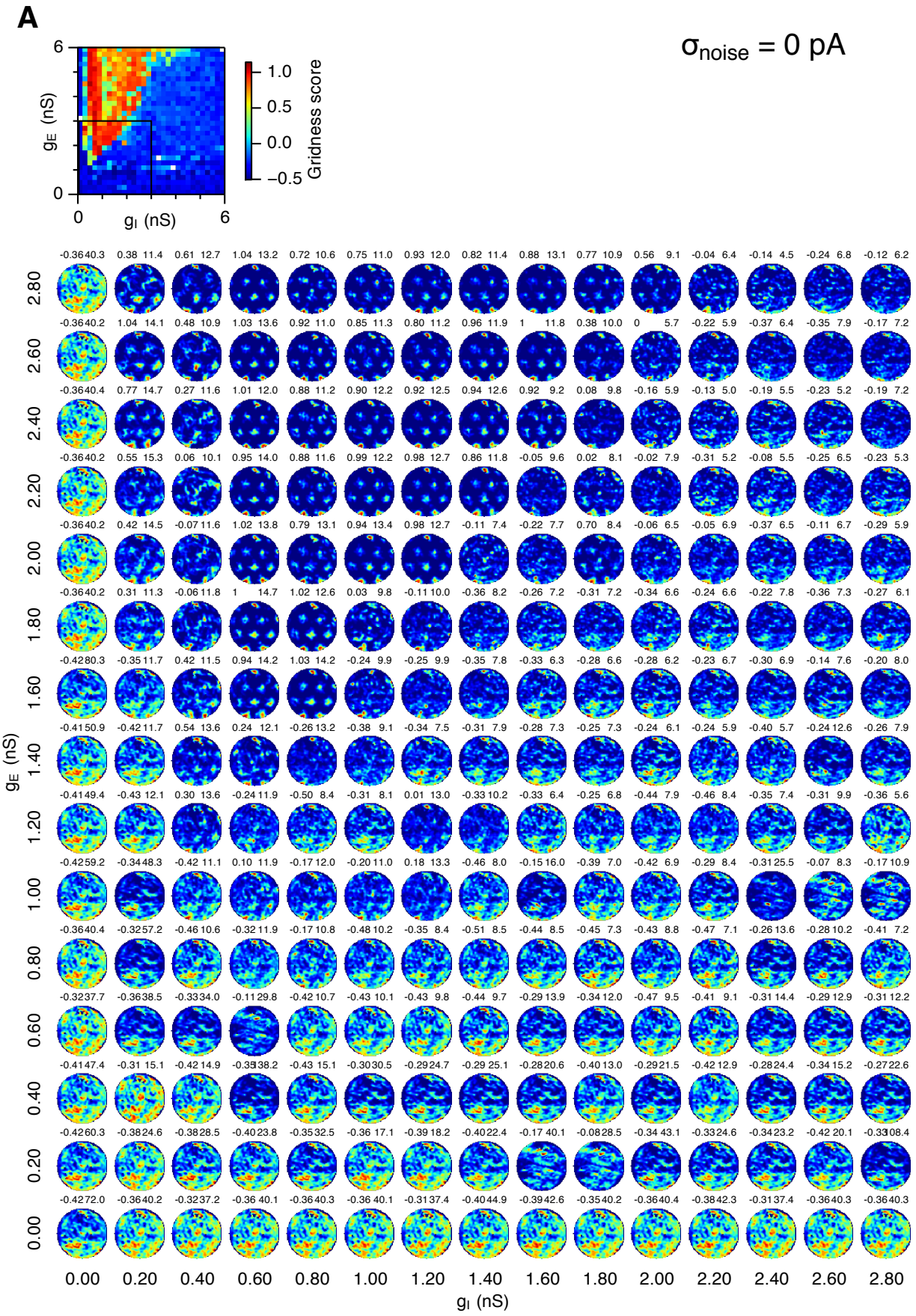

Figure C.1: **Examples of spatial firing fields.** Firing fields of one cell in the network (one trial), in the parameter region highlighted by the rectangle. Above each firing field is the estimated gridness score (left) and maximal firing rate in the firing field (right). Blank (white) locations in the parameter space are simulations that did not finish in the pre-specified time limit (5 h). Figure continues on next pages.

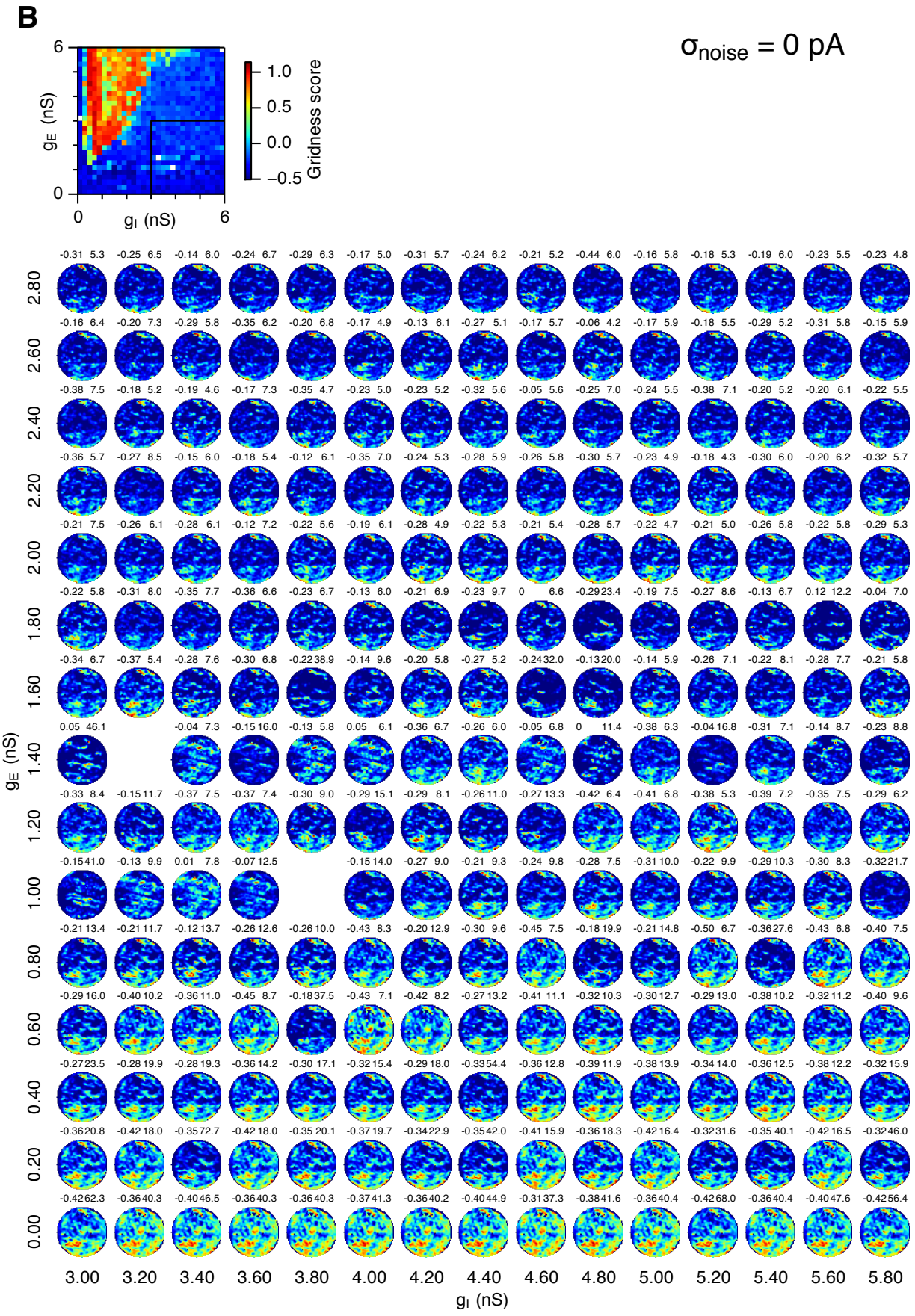

Figure C.1 (cont.)

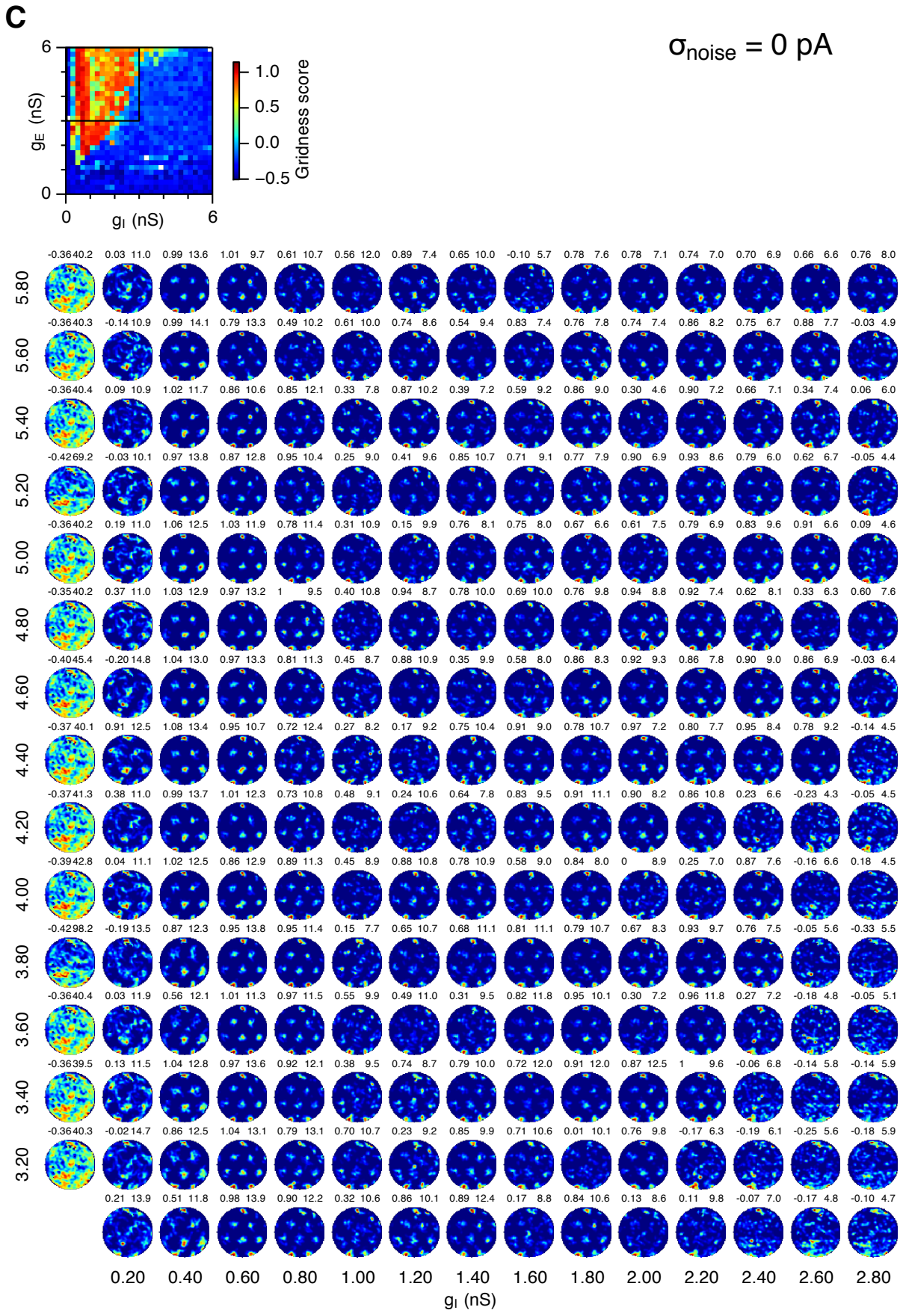

Figure C.1 (cont.)

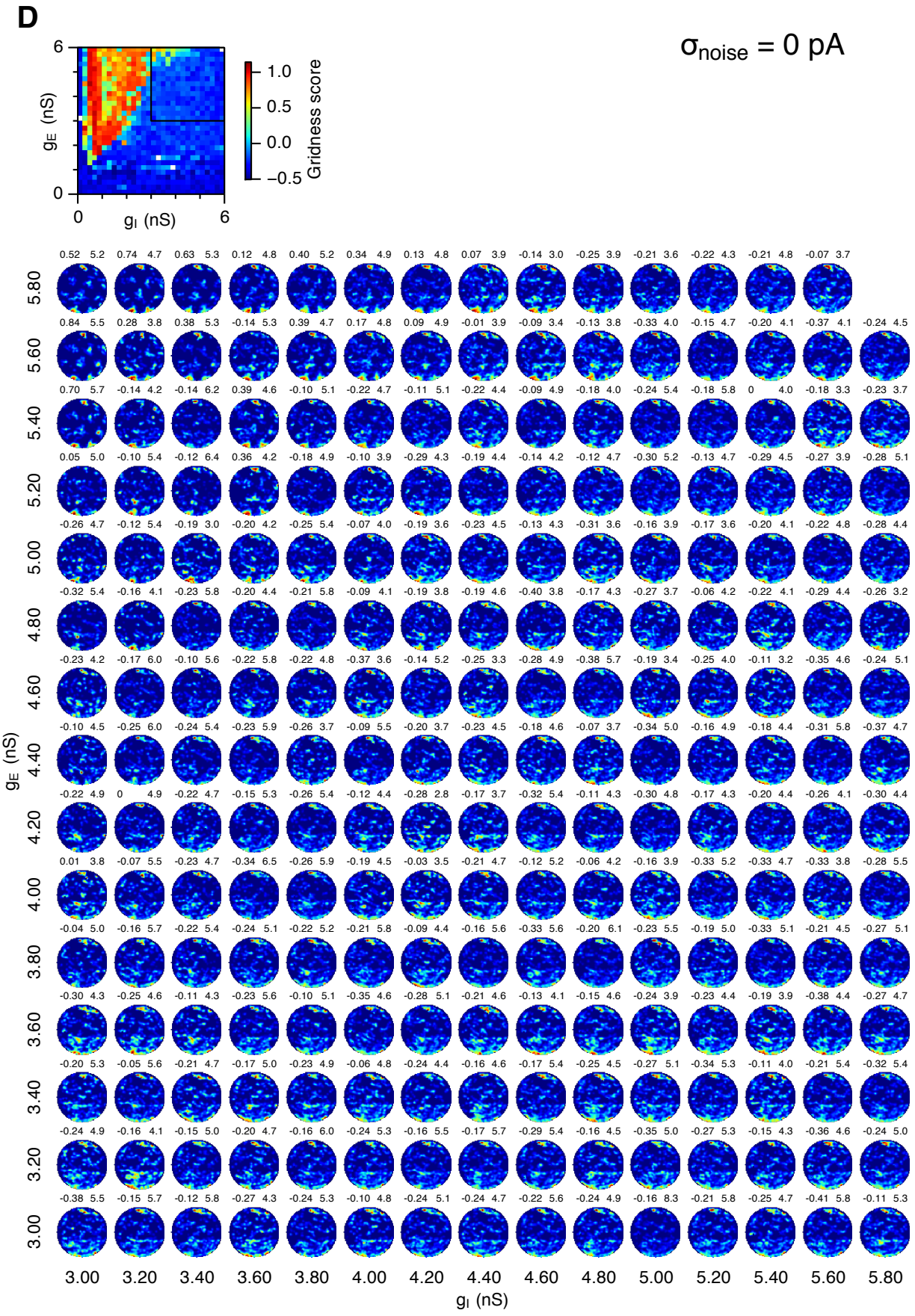

Figure C.1 (cont.)

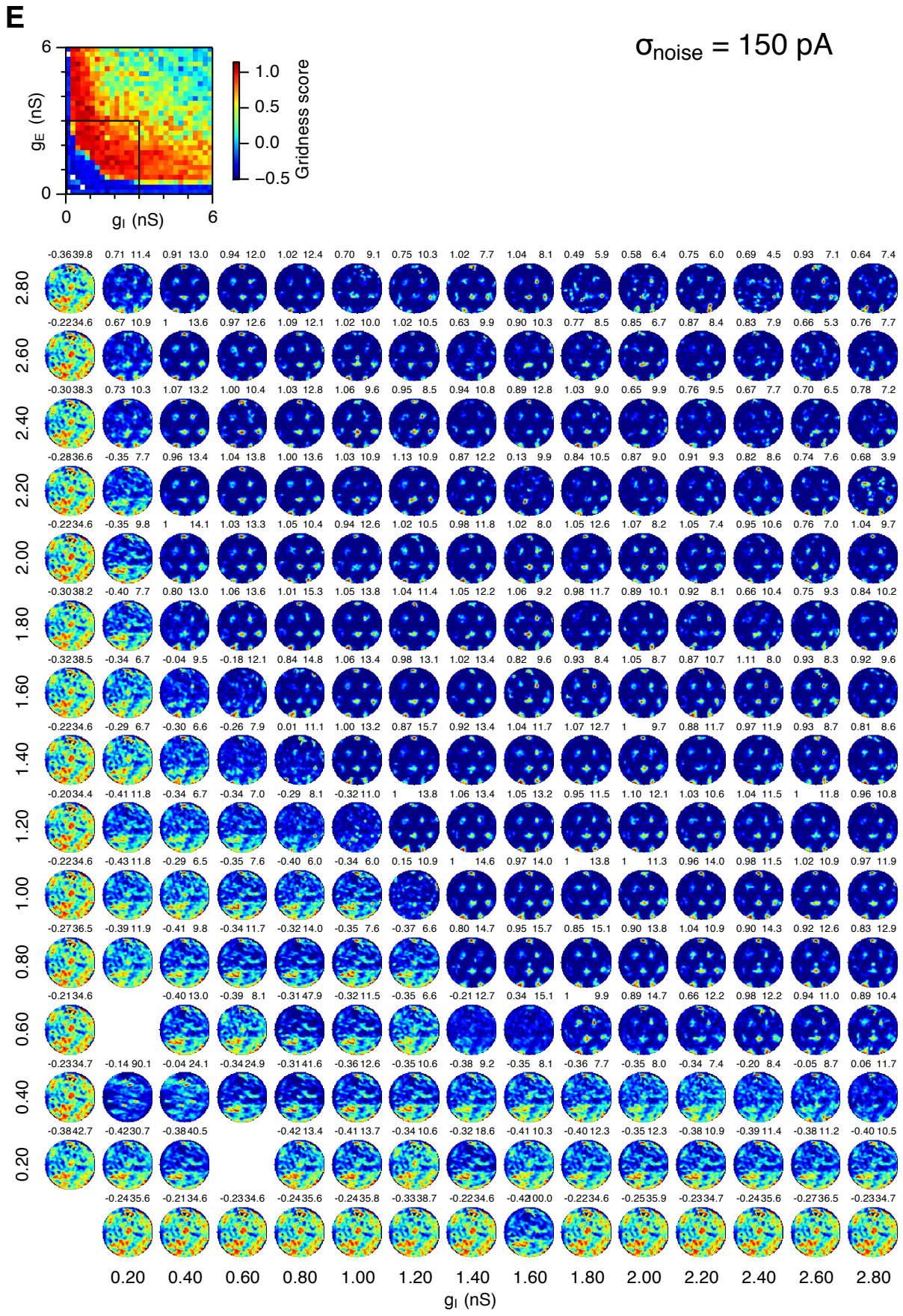

Figure C.1 (cont.)

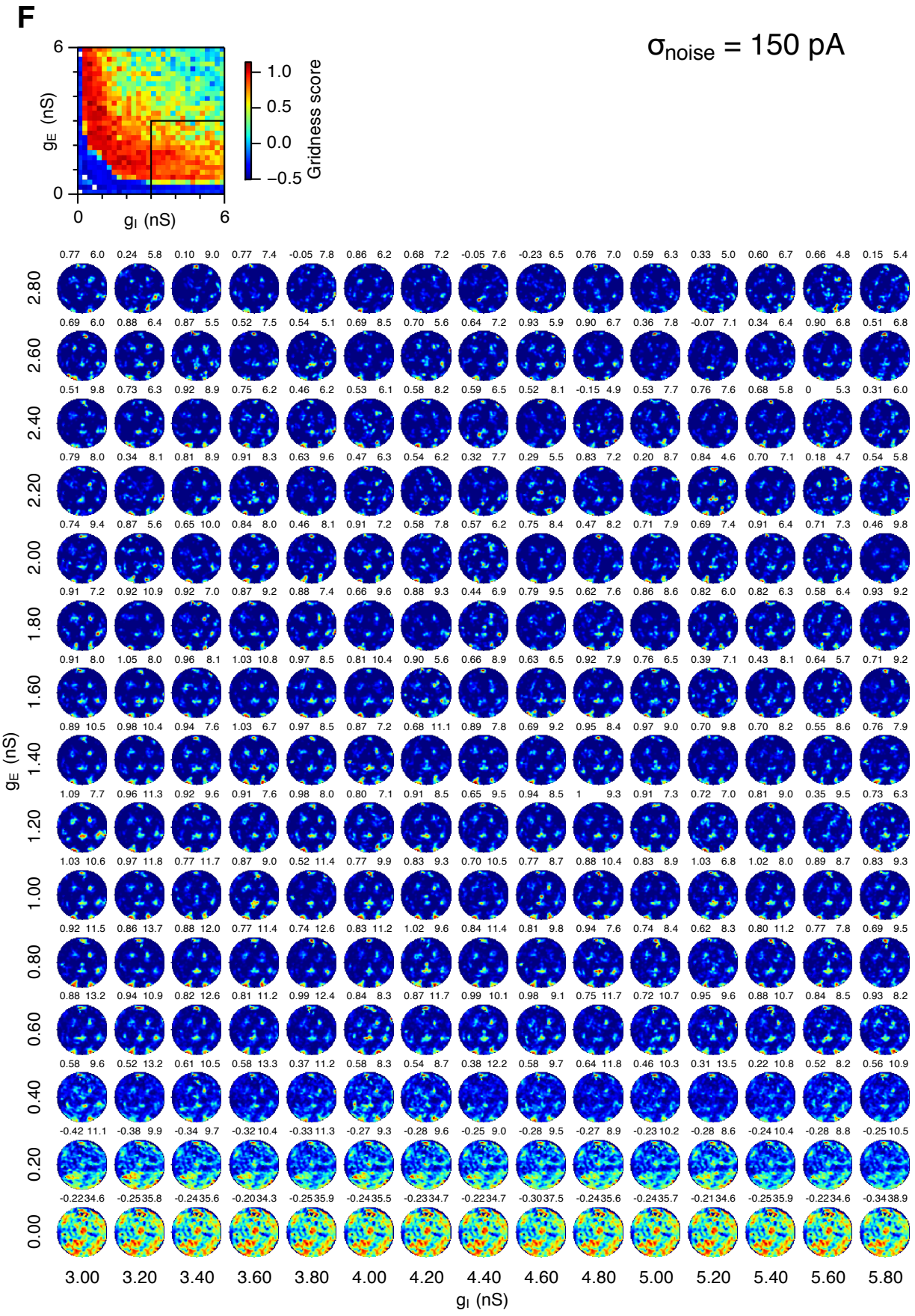

Figure C.1 (cont.)

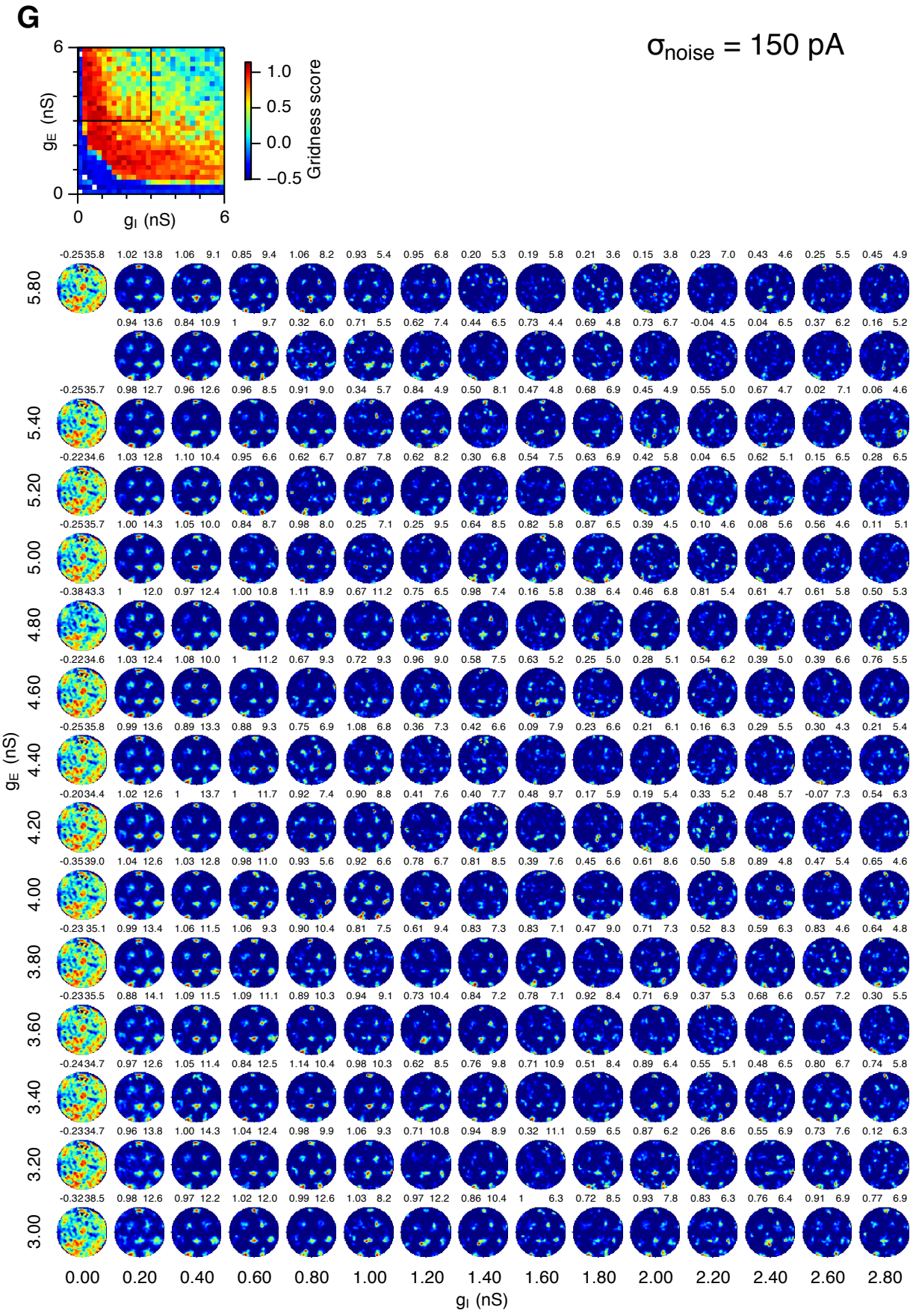

Figure C.1 (cont.)

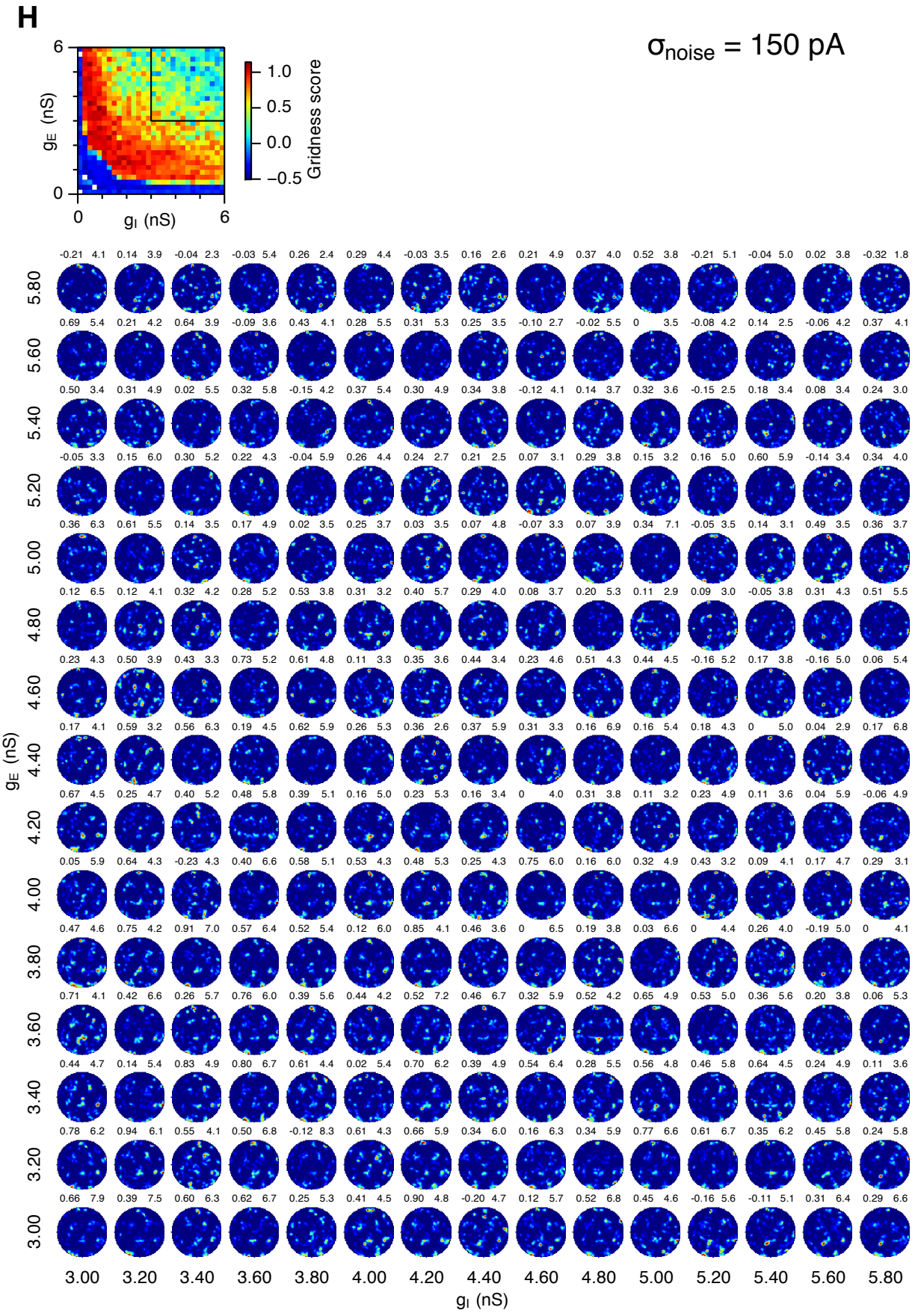

Figure C.1 (cont.)

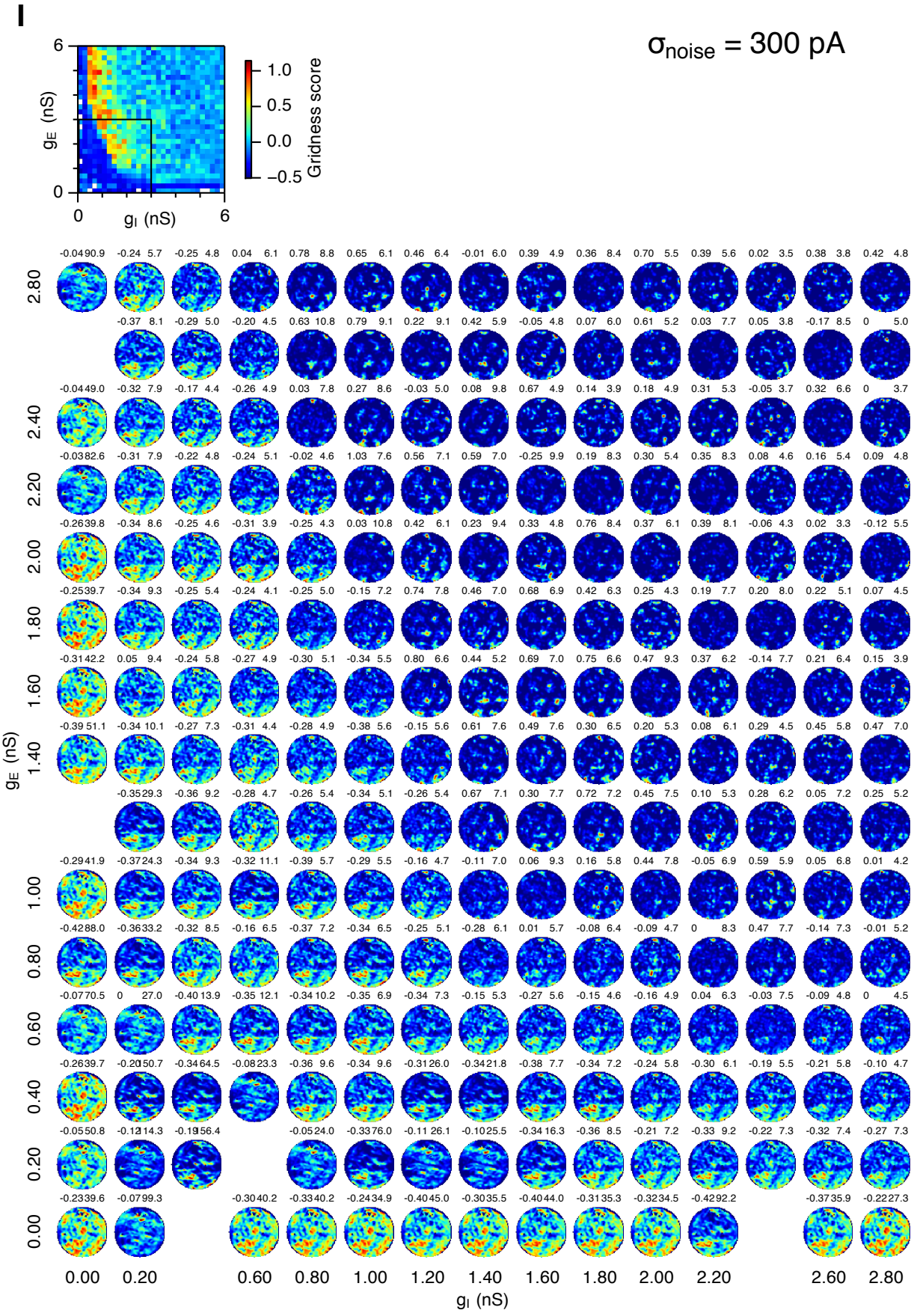

Figure C.1 (cont.)

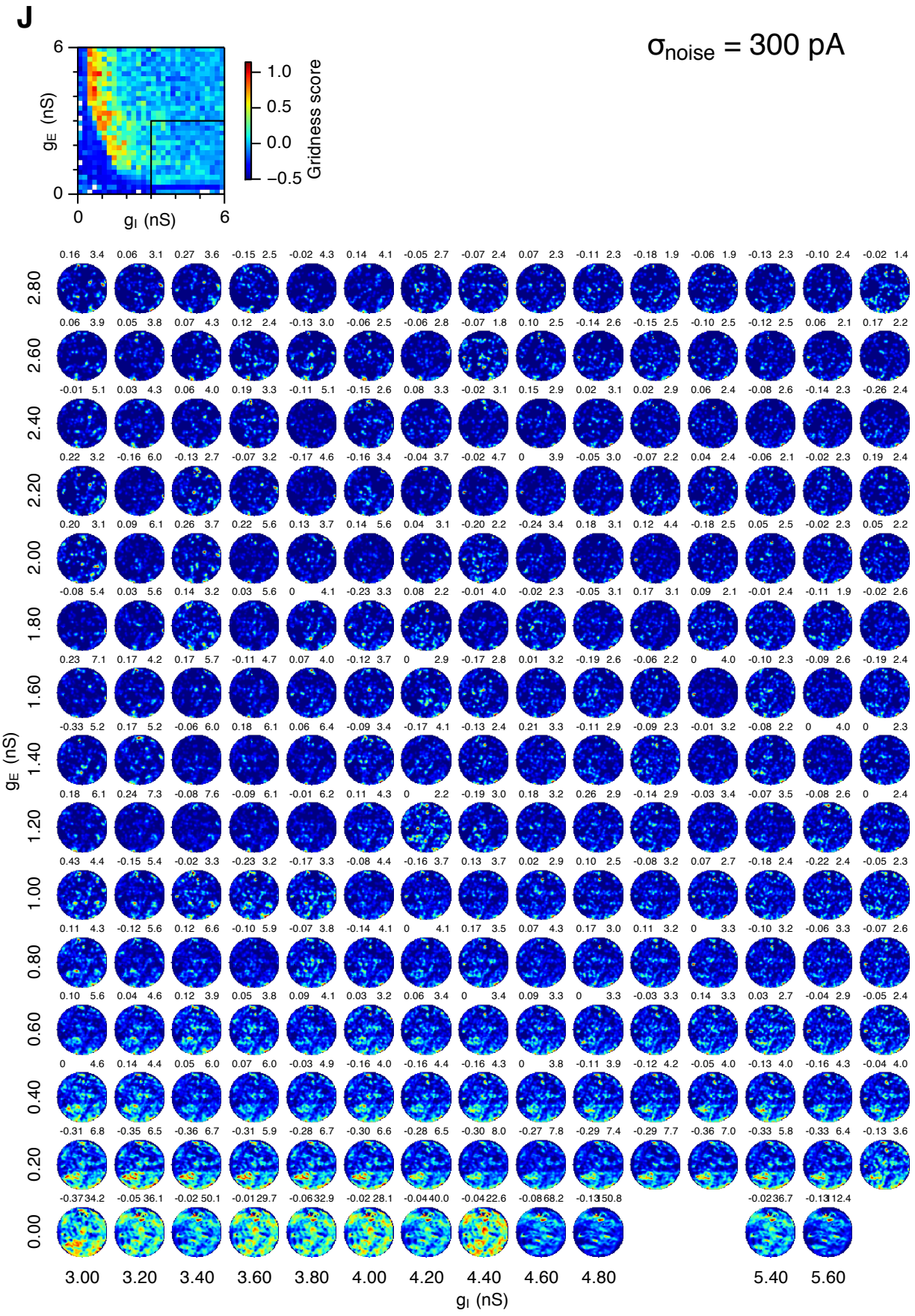

Figure C.1 (cont.)

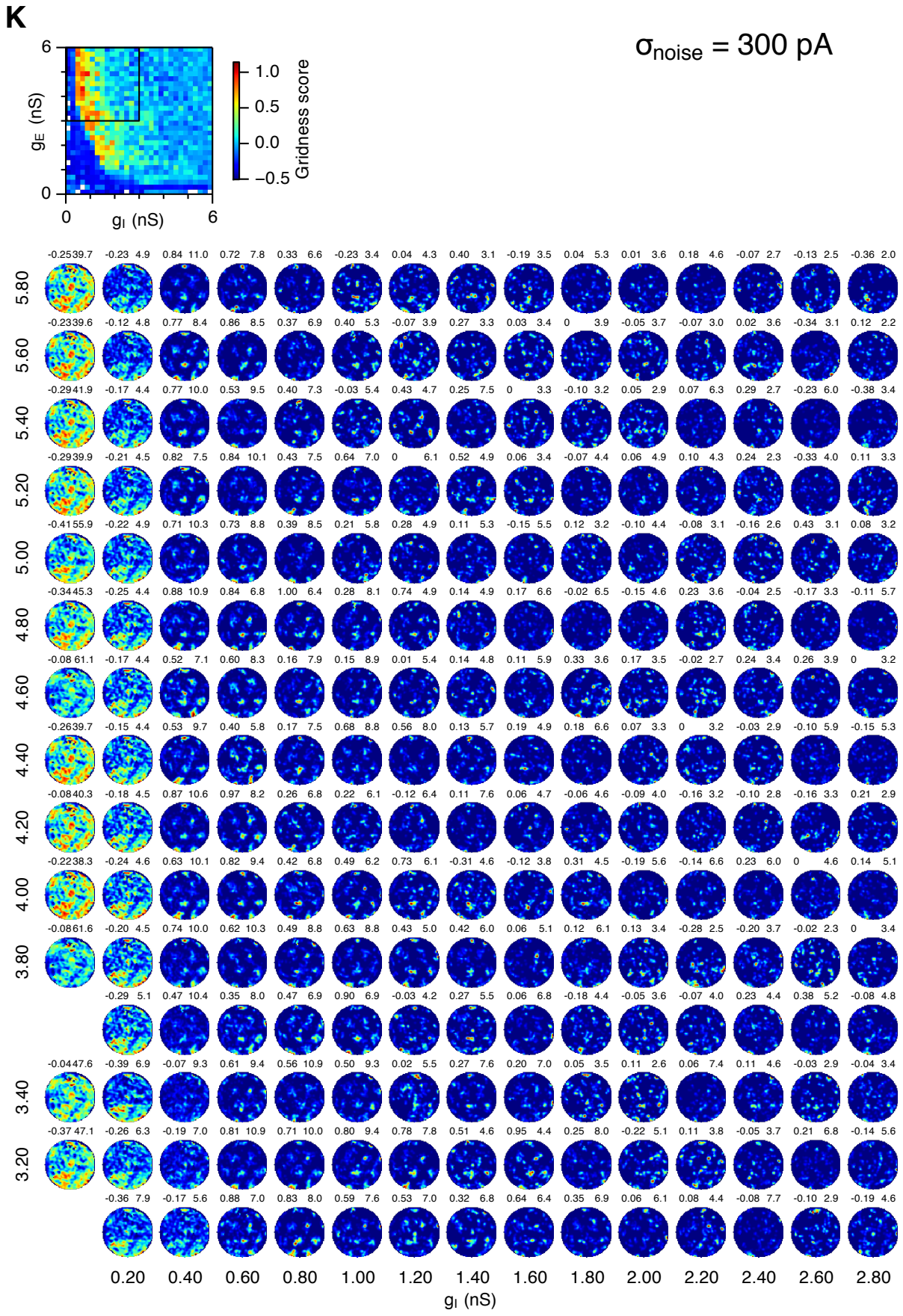

Figure C.1 (cont.)

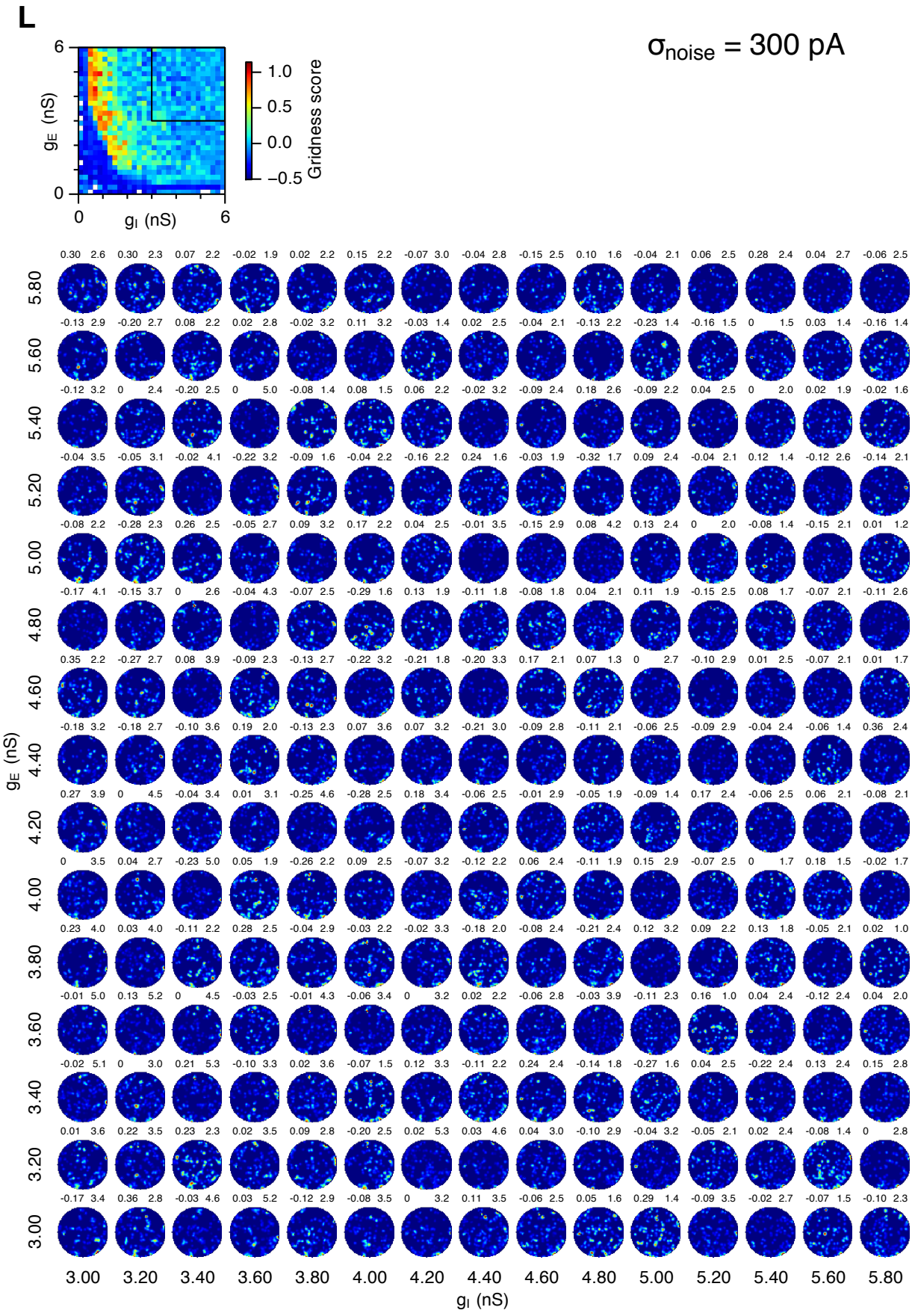

Figure C.1 (cont.)

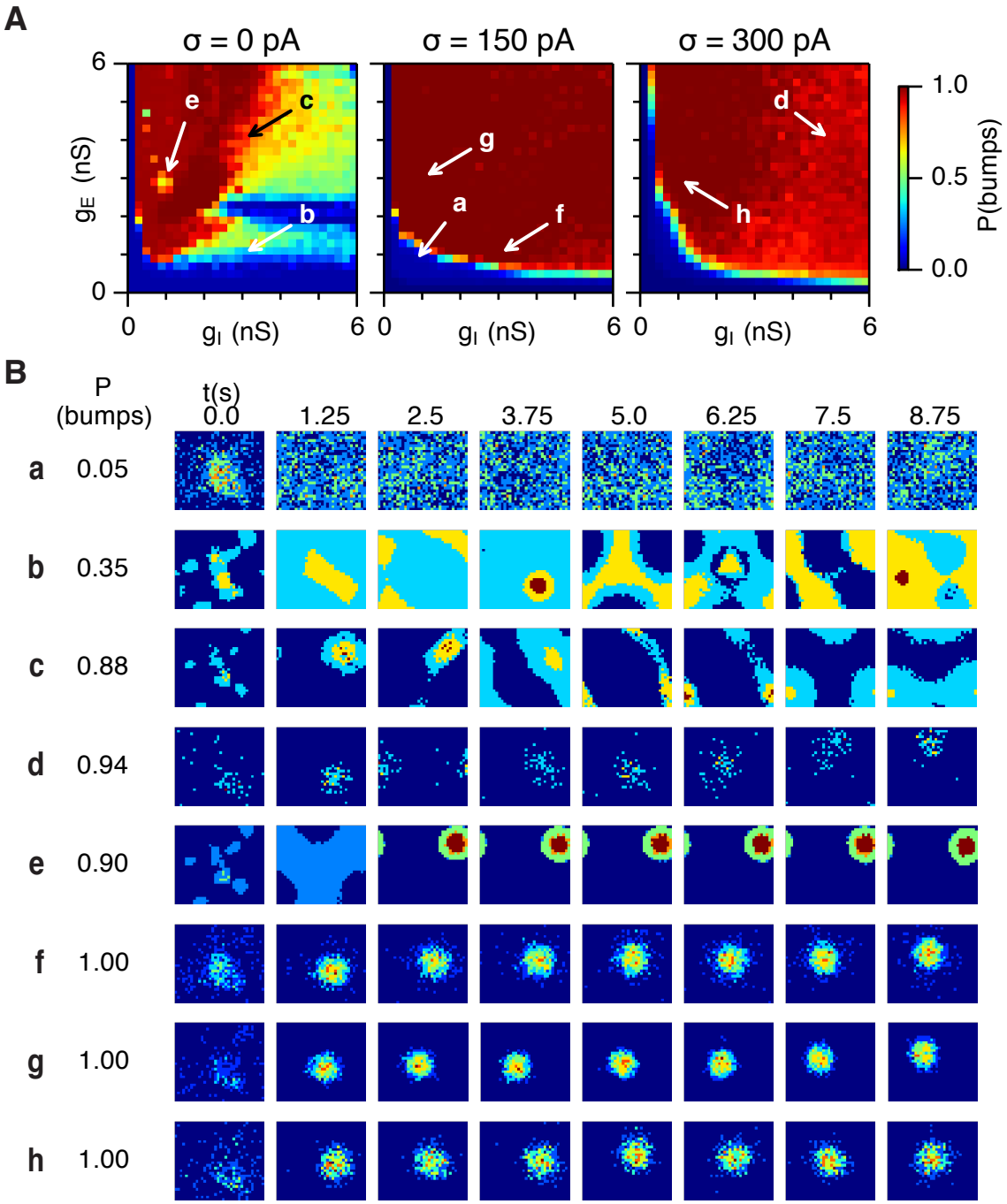

Figure C.2: **Examples of bump attractor stability in various locations in the parameter spaces of g_E, g_I and noise levels. (A)** Colour plots show proportion of snapshots of population firing rates classified as bump attractors (sliding rectangular window with 250 ms duration and 125 ms time step), for the three simulated levels of noise and the range of strengths of recurrent synaptic coupling. Each colour point is an average of five, ten second, simulation runs with the velocity inputs switched off. Arrows show positions in the parameter space of examples in panel (B). **(B)** Examples of E cell population firing rate snapshots from simulations in (A), as highlighted by the arrows (a-h) and the corresponding proportion of snapshots classified as bump attractors, for that particular simulation run (P(bumps)). The snapshots are evenly subsampled in time to 1.25 s, in order to cover the whole ten second simulation run.

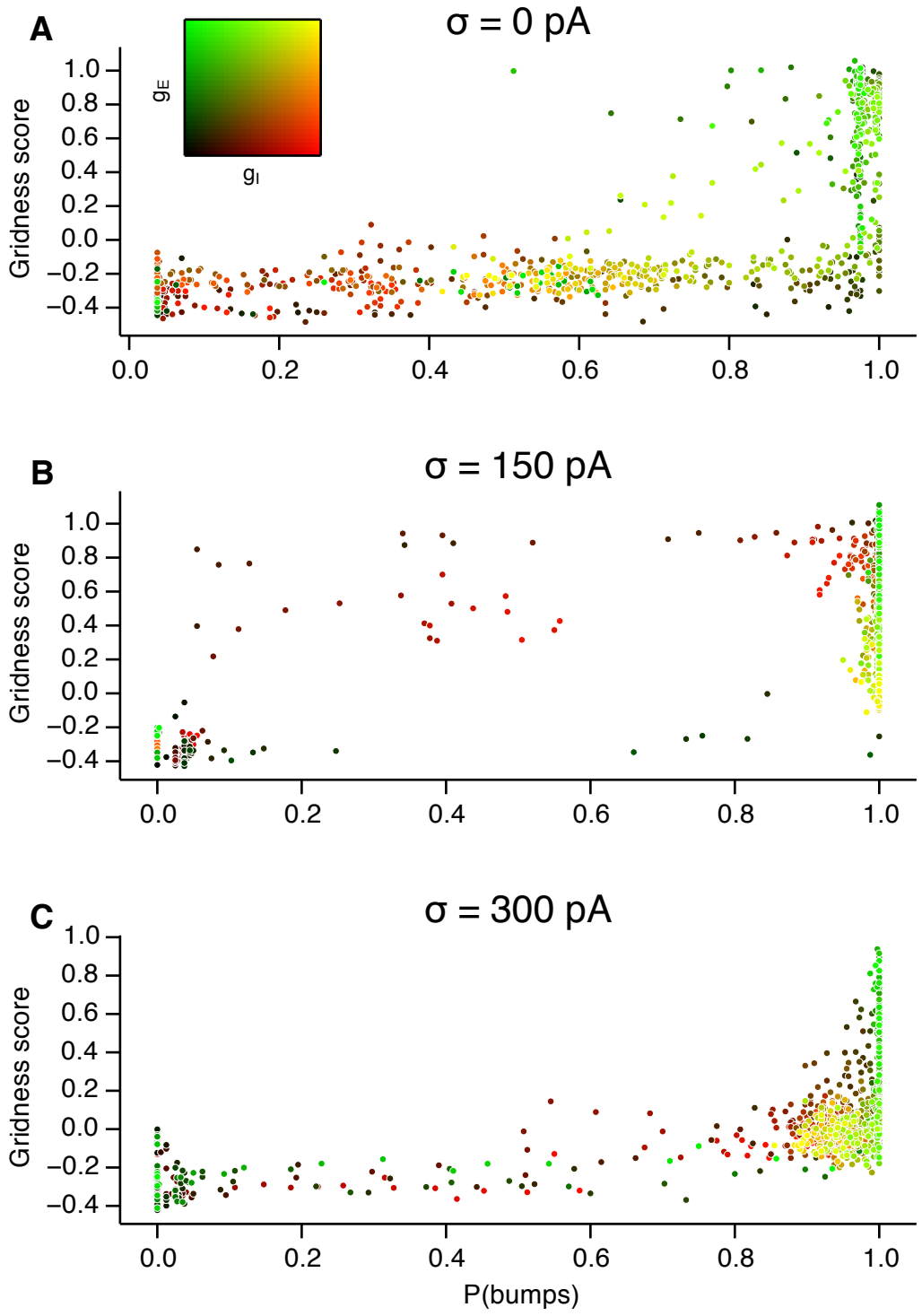

Figure C.3: **Scatter plots of gridness score vs. bump formation score.** See Section 4.3.4. **(A-C)** The plots show relationships between grid field computations (gridness score) and the ability of attractor networks to form stable bump attractors (P(bumps)). P(bumps) determines the proportion of simulation time the activity in the E population was classified as a bump attractor. Colour coding determines the value of g_{E} and g_{I} as shown in the 2D colorbar.

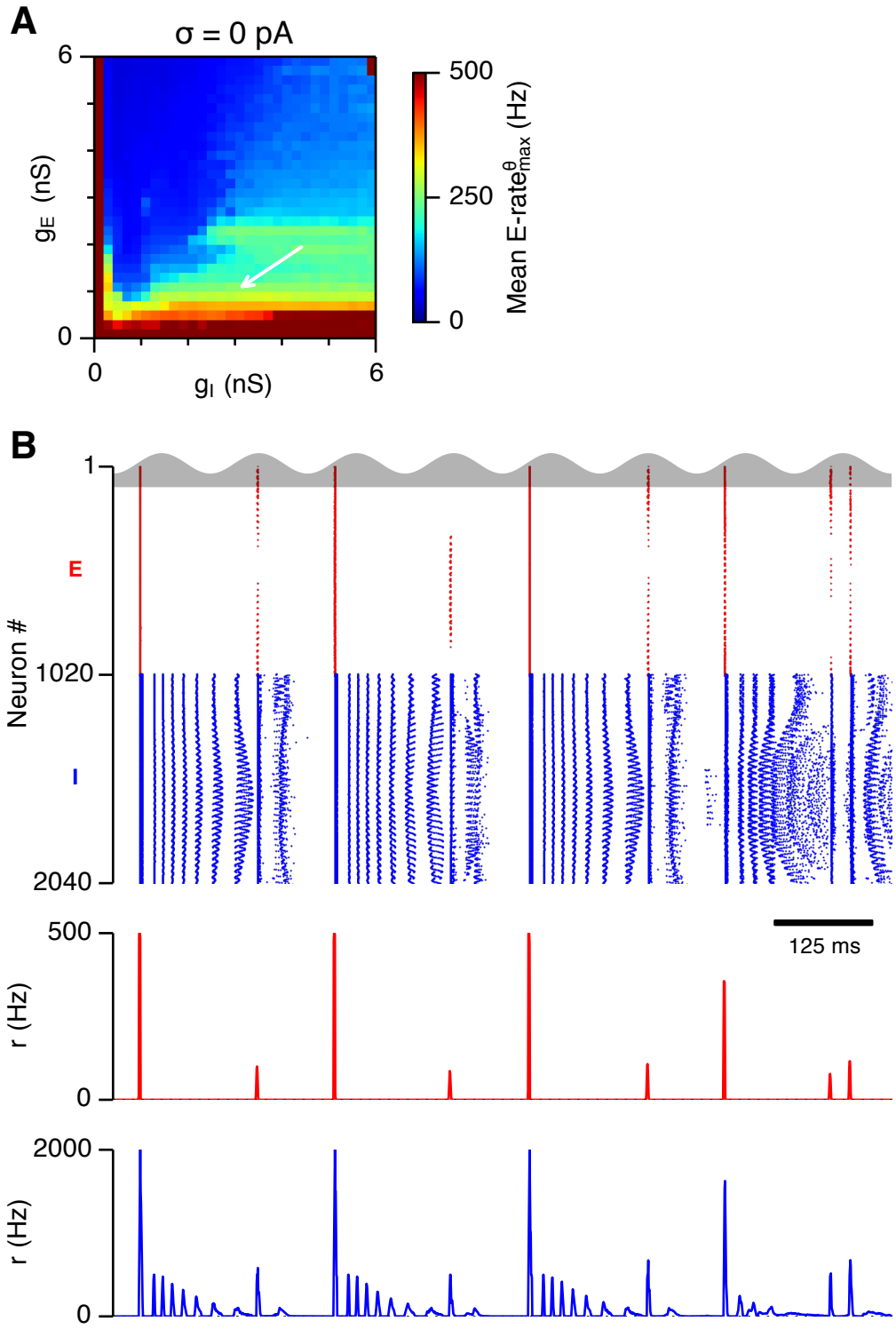

Figure C.4: **Examples of activity in the network**. **(A)** Mean maximal firing rate per theta cycle (average over 5 trials). **(B)** Raster plots and population-average firing rates of selected locations in the excitatory-inhibitory parameter spaces during 8 consecutive θ cycles. The position in the parameter space is highlighted by an arrow. Figure continues on next pages.

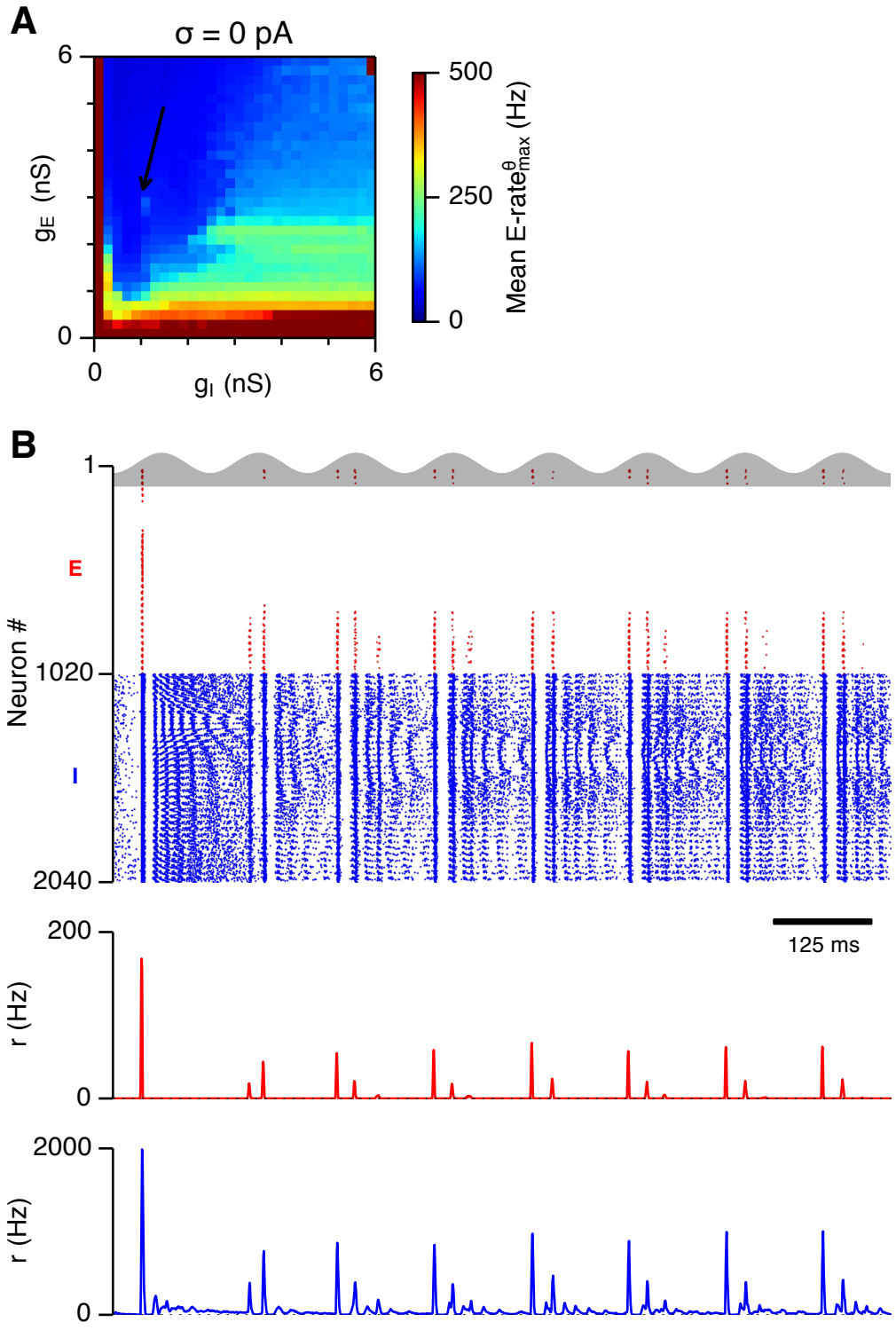

Figure C.4 (cont.)

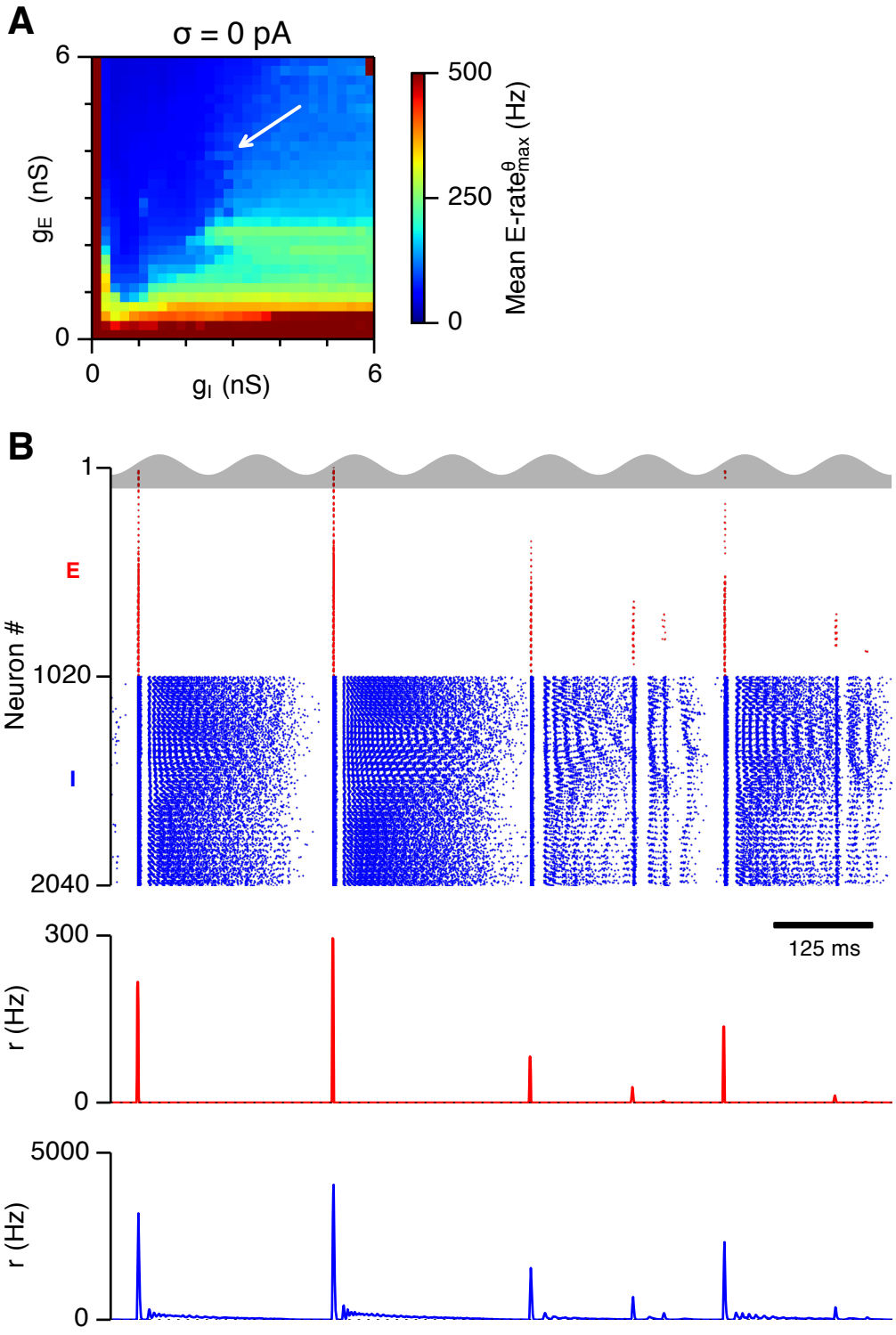

Figure C.4 (cont.)

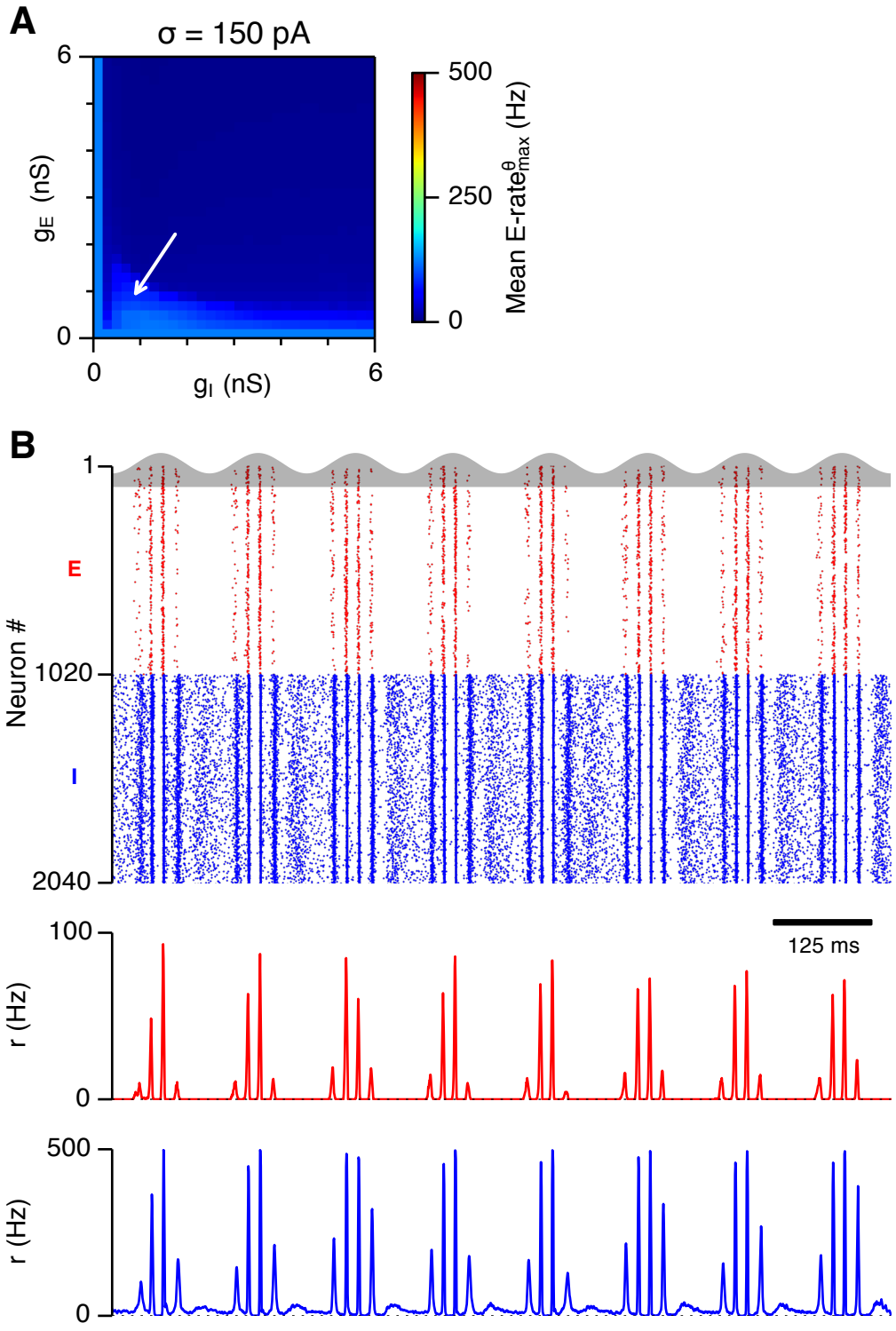

Figure C.4 (cont.)

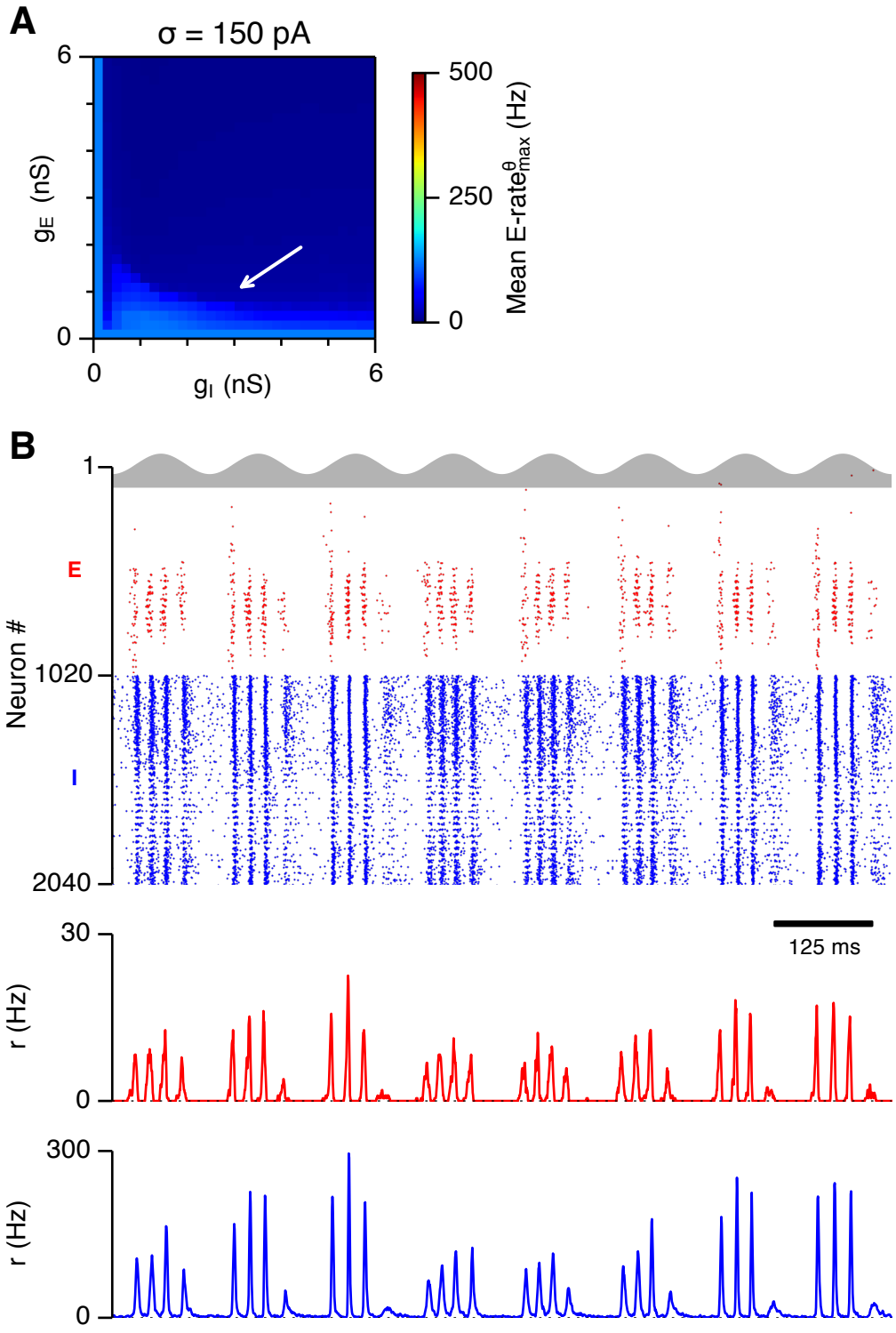

Figure C.4 (cont.)

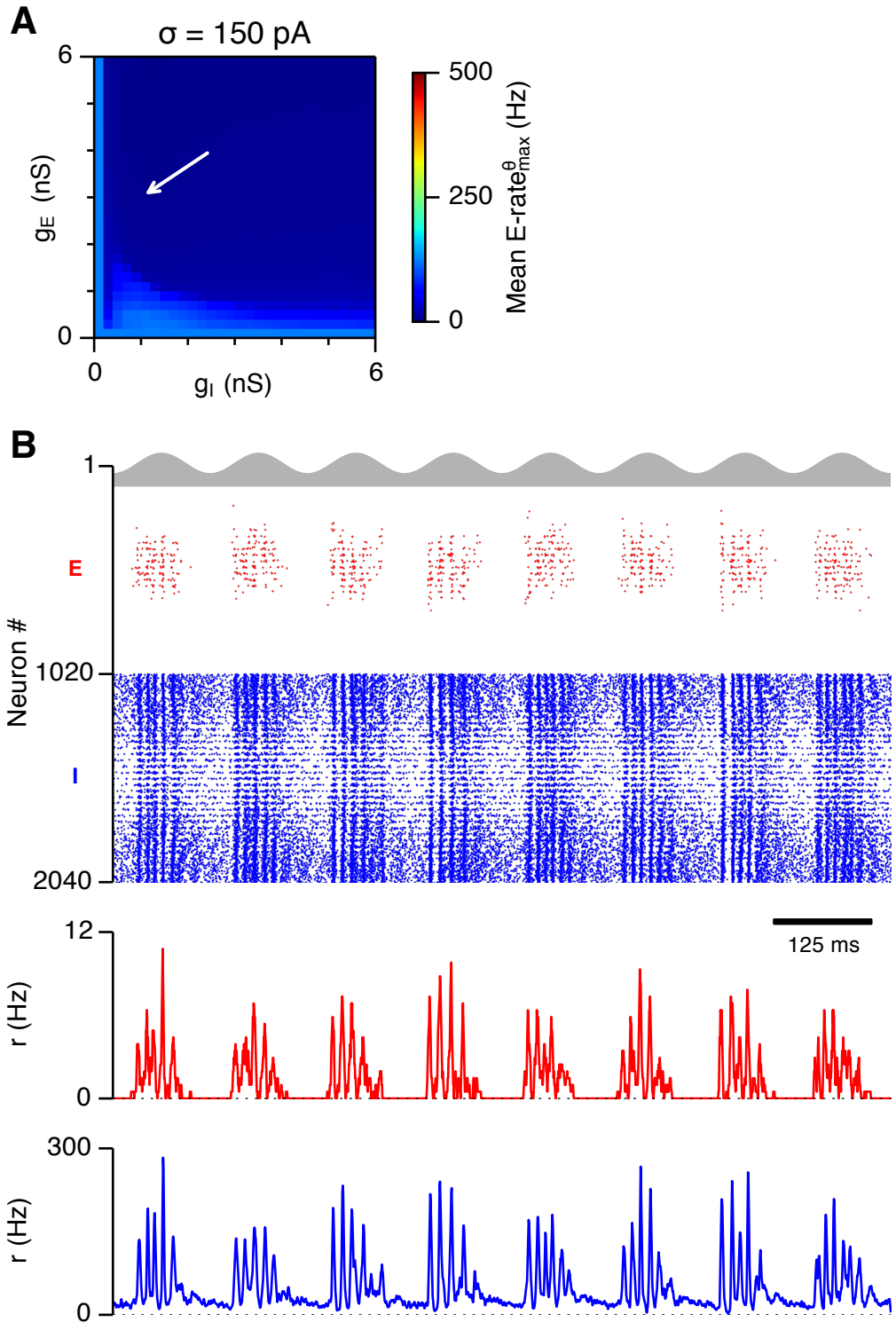

Figure C.4 (cont.)

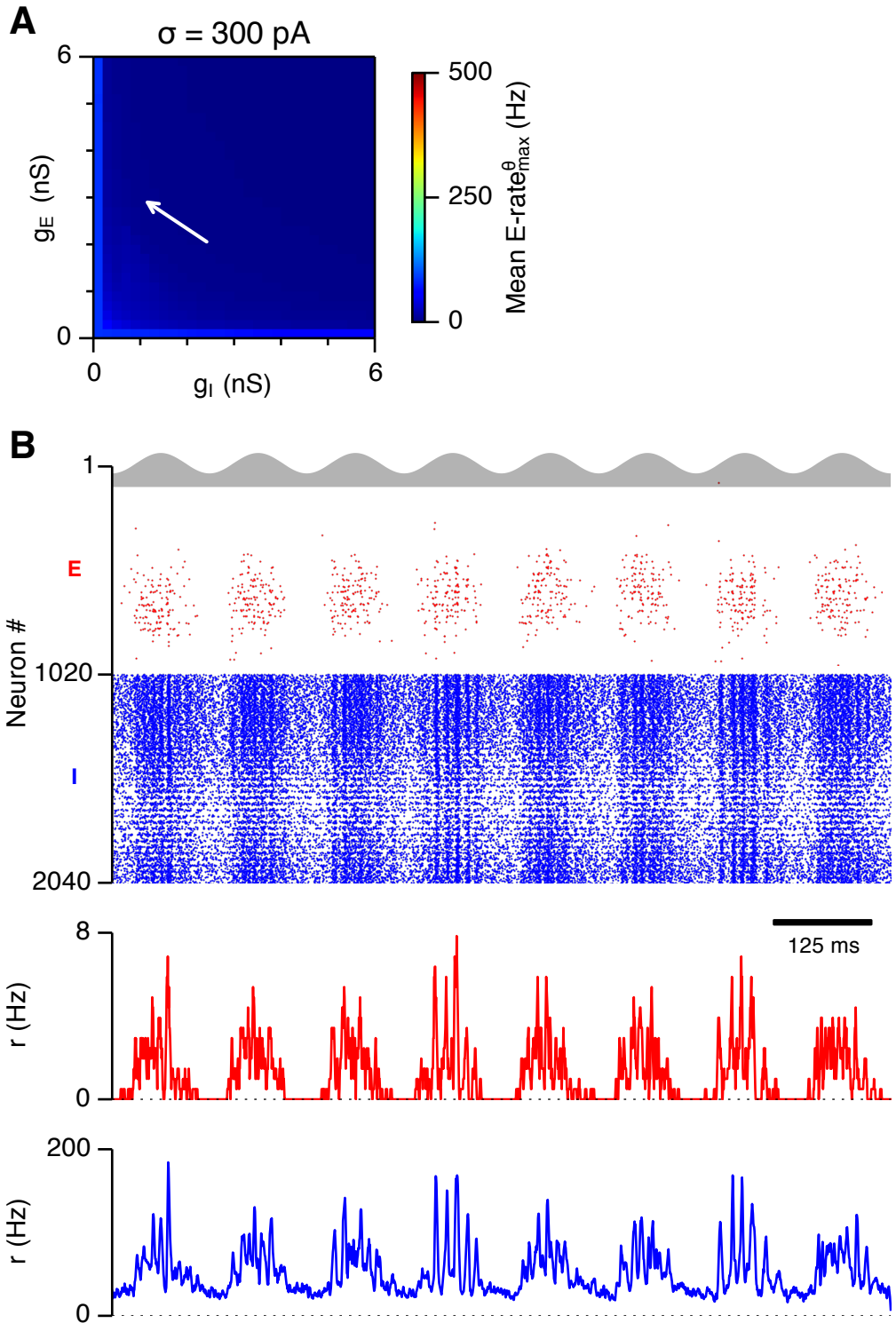

Figure C.4 (cont.)

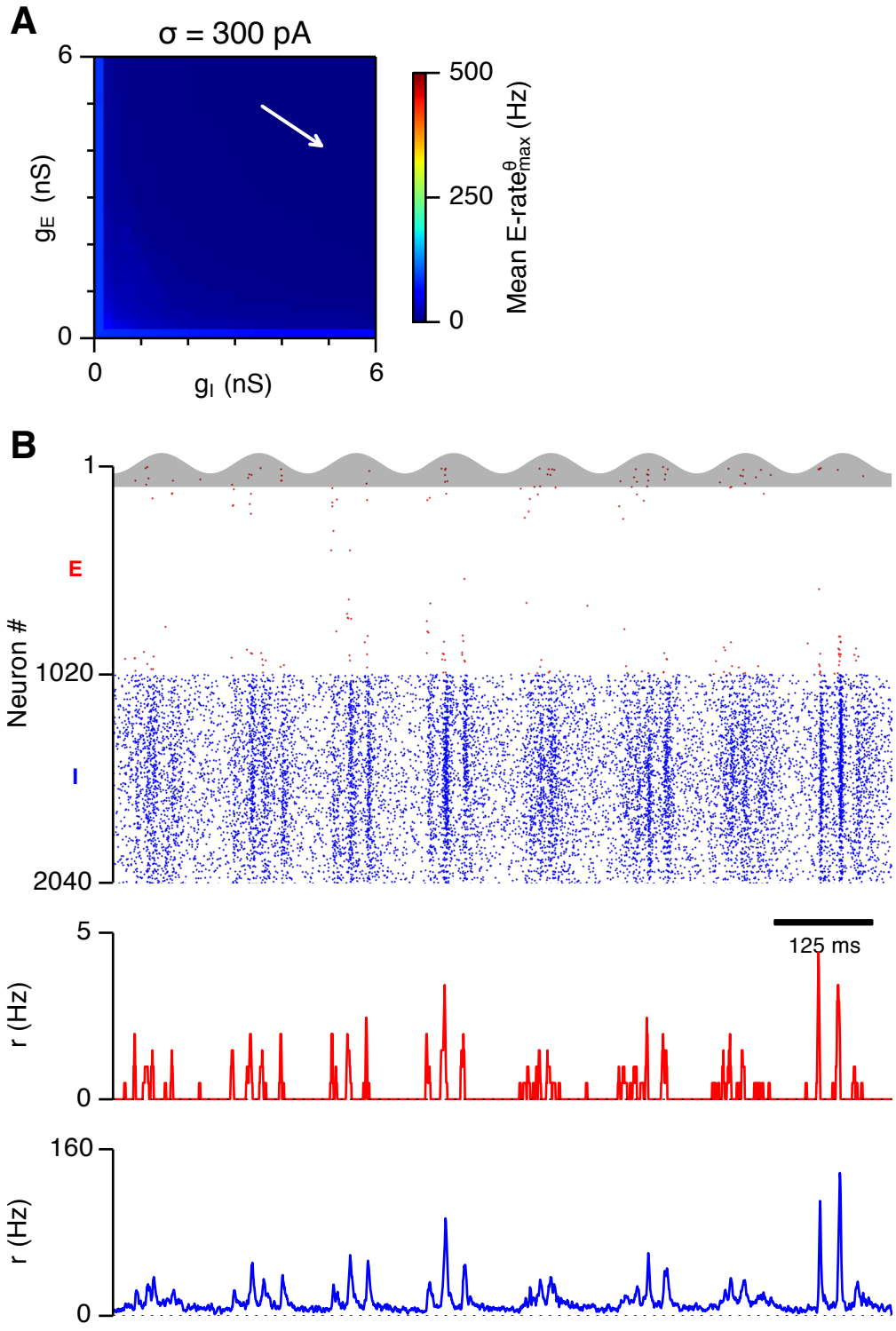

Figure C.4 (cont.)

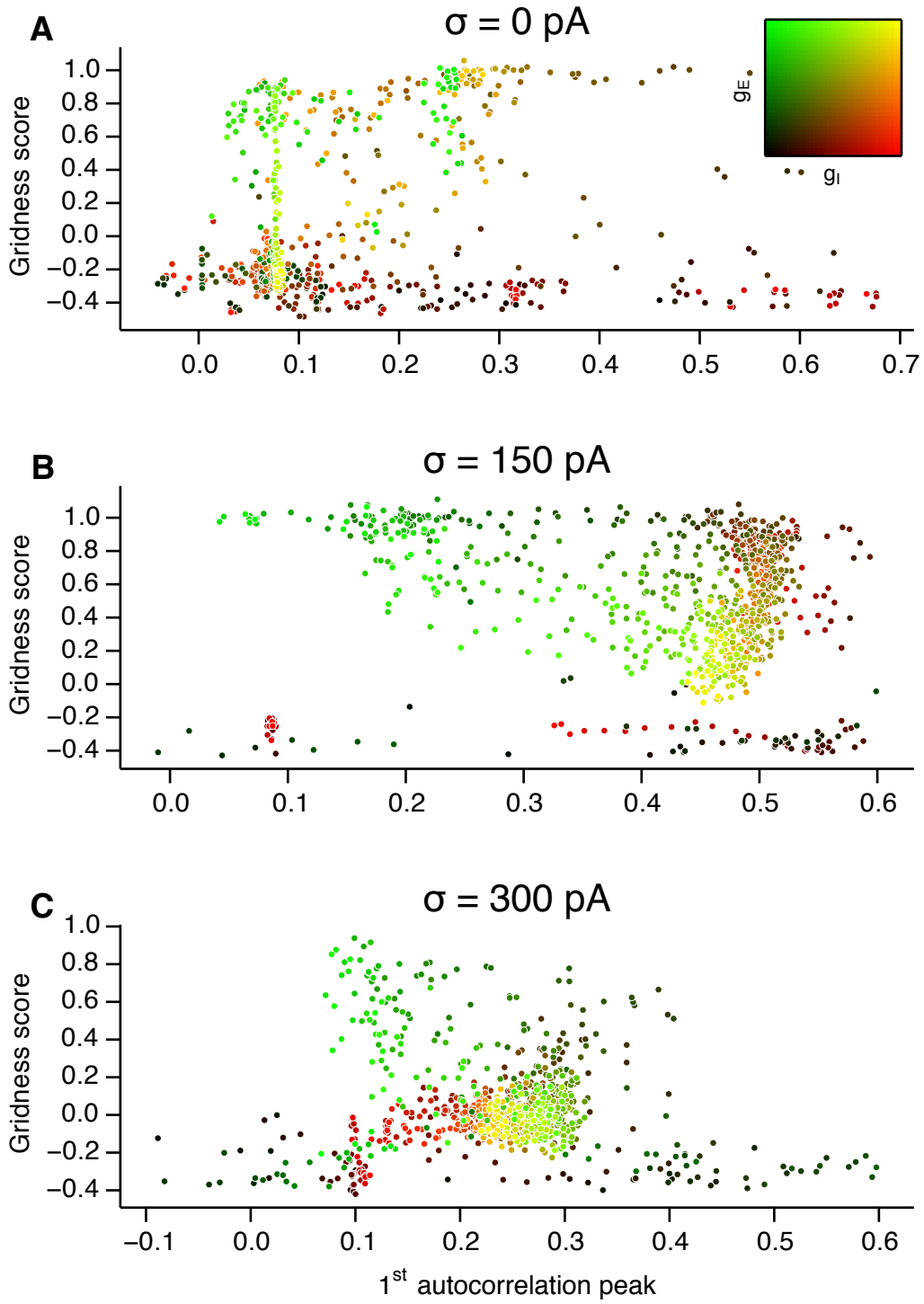

Figure C.5: **Scatter plots of gridness score vs. power of gamma oscillations.** See section 4.3.2. **(A-C)** The plots show relationships between grid field computations (gridness score) and the power of nested gamma oscillations. The strength of the oscillation was determined by autocorrelation analysis (Section 4.2.6). Colour coding determines the values of g_{E} and g_{I}, as shown in the 2D colorbar.

Bibliography

Akam, T. and Kullmann, D. M. (2010). Oscillations and Filtering Networks Support Flexible Routing of Information. *Neuron*, 67(2):308–320.

Akam, T., Oren, I., Mantoan, L., Ferenczi, E., and Kullmann, D. M. (2012). Oscillatory dynamics in the hippocampus support dentate gyrus–CA3 coupling. *Nature Neuroscience*, 15(5):763–768.

Akam, T. E. and Kullmann, D. M. (2012). Efficient "communication through coherence" requires oscillations structured to minimize interference between signals. *PLOS Computational Biology*, 8(11):e1002760.

Albanese, D., Filosi, M., Visintainer, R., Riccadonna, S., Jurman, G., and Furlanello, C. (2013). Minerva and minepy: a C engine for the MINE suite and its R, Python and MATLAB wrappers. *Bioinformatics (Oxford, England)*, 29(3):407–408.

Alonso, A. and Klink, R. (1993). Differential electroresponsiveness of stellate and pyramidal-like cells of medial entorhinal cortex layer II. *Journal of Neurophysiology*, 70(1):128–143.

Alonso, A. and Llinás, R. R. (1989). Subthreshold Na+-dependent theta-like rhythmicity in stellate cells of entorhinal cortex layer II. *Nature*, 342(6246):175–177.

Amari, S. (1977). Dynamics of pattern formation in lateral-inhibition type neural fields. *Biological cybernetics*, 27(2):77–87.

Amit, D. J. and Brunel, N. (1997). Model of global spontaneous activity and local structured activity during delay periods in the cerebral cortex. *Cerebral Cortex*, 7(3):237–252.

Barry, C. and Burgess, N. (2014). Neural mechanisms of self-location. *Current biology*, 24(8):R330–9.

Barry, C., Hayman, R., Burgess, N., and Jeffery, K. J. (2007). Experience-dependent rescaling of entorhinal grids. *Nature Neuroscience*, 10(6):682–684.

Ben-Yishai, R., Bar-Or, R. L., and Sompolinsky, H. (1995). Theory of orientation tuning in visual cortex. *Proceedings of the National Academy of Sciences of the United States of America*, 92(9):3844–3848.

Benzi, R., Sutera, A., and Vulpiani, A. (1999). The mechanism of stochastic resonance. *Journal of Physics A: Mathematical and General*, 14(11):L453–L457.

Bi, G. Q. and Poo, M. M. (1998). Synaptic modifications in cultured hippocampal neurons: dependence on spike timing, synaptic strength, and postsynaptic cell type. *Journal of Neuroscience*, 18(24):10464–10472.

Bjerknes, T. L., Moser, E. I., and Moser, M.-B. (2014). Representation of Geometric Borders in the Developing Rat. *Neuron*, 82(1):71–78.

Bonnevie, T., Dunn, B., Fyhn, M., Hafting, T., Derdikman, D., Kubie, J. L., Roudi, Y., Moser, E. I., and Moser, M.-B. (2013). Grid cells require excitatory drive from the hippocampus. *Nature Neuroscience*, 16(3):309–317.

Börgers, C. and Kopell, N. (2003). Synchronization in Networks of Excitatory and Inhibitory Neurons with Sparse, Random Connectivity. *Neural Computation*, 15(3):509–538.

Boucheny, C., Brunel, N., and Arleo, A. (2005). A continuous attractor network model without recurrent excitation: maintenance and integration in the head direction cell system. *Journal of computational neuroscience*, 18(2):205–227.

Brandon, M. P., Bogaard, A. R., Libby, C. P., Connerney, M. A., Gupta, K., and Hasselmo, M. E. (2011). Reduction of theta rhythm dissociates grid cell spatial periodicity from directional tuning. *Science*, 332(6029):595–599.

Brun, V. H., Solstad, T., Kjelstrup, K. B., Fyhn, M., Witter, M. P., Moser, E. I., and Moser, M.-B. (2008). Progressive increase in grid scale from dorsal to ventral medial entorhinal cortex. *Hippocampus*, 18(12):1200–1212.

Brunel, N. and Wang, X.-J. (2003). What determines the frequency of fast network oscillations with irregular neural discharges? I. Synaptic dynamics and excitation-inhibition balance. *Journal of Neurophysiology*, 90(1):415–430.

Buetfering, C., Allen, K., and Monyer, H. (2014). Parvalbumin interneurons provide grid cell-driven recurrent inhibition in the medial entorhinal cortex. *Nature Neuroscience*, 17(5):710–718.

Burak, Y. and Fiete, I. (2006). Do We Understand the Emergent Dynamics of Grid Cell Activity? *Journal of Neuroscience*, 26(37):9352–9354.

Burak, Y. and Fiete, I. R. (2009). Accurate path integration in continuous attractor network models of grid cells. *PLOS Computational Biology*, 5(2):e1000291.

Burgalossi, A. and Brecht, M. (2014). Cellular, columnar and modular organization of spatial representations in medial entorhinal cortex. *Current opinion in neurobiology*, 24:47–54.

Burgalossi, A., Herfst, L., von Heimendahl, M., Förste, H., Haskic, K., Schmidt, M., and Brecht, M. (2011). Microcircuits of Functionally Identified Neurons in the Rat Medial Entorhinal Cortex. *Neuron*, 70(4):773–786.

Burgess, C. P. and Burgess, N. (2014). Controlling phase noise in oscillatory interference models of grid cell firing. *Journal of Neuroscience*, 34(18):6224–6232.

Burgess, N. (2008). Grid cells and theta as oscillatory interference: Theory and predictions. *Hippocampus*, 18(12):1157–1174.

Burgess, N., Barry, C., and O'Keefe, J. (2007). An oscillatory interference model of grid cell firing. *Hippocampus*, 17(9):801–812.

Bush, D. and Burgess, N. (2014). A hybrid oscillatory interference/continuous attractor network model of grid cell firing. *Journal of Neuroscience*, 34(14):5065–5079.

Buzsáki, G. and Draguhn, A. (2004). Neuronal oscillations in cortical networks. *Science*, 304(5679):1926–1929.

Buzsáki, G., Logothetis, N., and Singer, W. (2013). Scaling Brain Size, Keeping Timing: Evolutionary Preservation of Brain Rhythms. *Neuron*, 80(3):751–764.

Camperi, M. and Wang, X. J. (1998). A model of visuospatial working memory in prefrontal cortex: recurrent network and cellular bistability. *Journal of computational neuroscience*, 5(4):383–405.

Canolty, R. T. and Knight, R. T. (2010). The functional role of cross-frequency coupling. *Trends in cognitive sciences*, 14(11):506–515.

Canto, C. B., Wouterlood, F. G., and Witter, M. P. (2008). What does the anatomical organization of the entorhinal cortex tell us? *Neural plasticity*, 2008:381243.

Chen, G., King, J. A., Burgess, N., and O'Keefe, J. (2013). How vision and movement combine in the hippocampal place code. *Proceedings of the National Academy of Sciences*, 110(1):378–383.

Chrobak, J. J. and Buzsaki, G. (1998). Gamma oscillations in the entorhinal cortex of the freely behaving rat. *Journal of Neuroscience*, 18(1):388–398.

Cohen, H. S. (2000). Vestibular disorders and impaired path integration along a linear trajectory. *Journal of vestibular research : equilibrium & orientation*, 10(1):7–15.

Colgin, L. L., Denninger, T., Fyhn, M., Hafting, T., Bonnevie, T., Jensen, O., Moser, M.-B., and Moser, E. I. (2009). Frequency of gamma oscillations routes flow of information in the hippocampus. *Nature*, 462(7271):353–357.

Colgin, L. L. and Moser, E. I. (2010). Gamma oscillations in the hippocampus. *Physiology (Bethesda, Md.)*, 25(5):319–329.

Compte, A., Brunel, N., Goldman-Rakic, P. S., and Wang, X. J. (2000). Synaptic mechanisms and network dynamics underlying spatial working memory in a cortical network model. *Cerebral cortex*, 10(9):910–923.

Conklin, J. and Eliasmith, C. (2005). A controlled attractor network model of path integration in the rat. *Journal of computational neuroscience*, 18(2):183–203.

Couey, J. J., Witoelar, A., Zhang, S.-J., Zheng, K., Ye, J., Dunn, B., Czajkowski, R., Moser, M.-B., Moser, E. I., Roudi, Y., and Witter, M. P. (2013). Recurrent inhibitory circuitry as a mechanism for grid formation. *Nature Neuroscience*, 16(3):318–324.

Cover, T. M. and Thomas, J. A. (2006). *Elements of Information Theory*. John Wiley & Sons.

Cunningham, M. O., Davies, C. H., Buhl, E. H., Kopell, N., and Whittington, M. A. (2003). Gamma oscillations induced by kainate receptor activation in the entorhinal cortex in vitro. *Journal of Neuroscience*, 23(30):9761–9769.

Cunningham, M. O., Halliday, D. M., Davies, C. H., Traub, R. D., Buhl, E. H., and Whittington, M. A. (2004). Coexistence of gamma and high-frequency oscillations in rat medial entorhinal cortex in vitro. *The Journal of physiology*, 559(Pt 2):347–353.

Derdikman, D., Whitlock, J. R., Tsao, A., Fyhn, M., Hafting, T., Moser, M.-B., and Moser, E. I. (2009). Fragmentation of grid cell maps in a multicompartment environment. *Nature Neuroscience*, 12(10):1325–1332.

Deuchars, J., West, D. C., and Thomson, A. M. (1994). Relationships between morphology and physiology of pyramid-pyramid single axon connections in rat neocortex in vitro. *The Journal of physiology*, 478 Pt 3:423–435.

Dhillon, A. and Jones, R. S. (2000). Laminar differences in recurrent excitatory transmission in the rat entorhinal cortex in vitro. *Neuroscience*, 99(3):413–422.

Dickson, C. T., Magistretti, J., Shalinsky, M. H., Fransén, E., Hasselmo, M. E., and Alonso, A. (2000). Properties and Role of I h in the Pacing of Subthreshold Oscillations in Entorhinal Cortex Layer II Neurons. *Journal of Neurophysiology*, 83(5):2562–2579.

Dodson, P. D., Pastoll, H., and Nolan, M. F. (2011). Dorsal-ventral organization of theta-like activity intrinsic to entorhinal stellate neurons is mediated by differences in stochastic current fluctuations. *The Journal of physiology*, 589(Pt 12):2993–3008.

Doeller, C. F., Barry, C., and Burgess, N. (2010). Evidence for grid cells in a human memory network. *Nature*, 463(7281):657–661.

Domnisoru, C., Kinkhabwala, A. A., and Tank, D. W. (2013). Membrane potential dynamics of grid cells. *Nature*, 495(7440):199–204.

Eliasmith, C. (2005). A unified approach to building and controlling spiking attractor networks. *Neural Computation*, 17(6):1276–1314.

Eliasmith, C. and Anderson, C. H. (2004). *Neural engineering: Computation, representation, and dynamics in neurobiological systems*. MIT Press.

Erchova, I., Kreck, G., Heinemann, U., and Herz, A. V. M. (2004). Dynamics of rat entorhinal cortex layer II and III cells: characteristics of membrane potential resonance at rest predict oscillation properties near threshold. *The Journal of physiology*, 560(Pt 1):89–110.

Etienne, A. S. and Jeffery, K. J. (2004). Path integration in mammals. *Hippocampus*, 14(2):180–192.

Faisal, A. A., Selen, L. P. J., and Wolpert, D. M. (2008). Noise in the nervous system. *Nature Reviews Neuroscience*, 9(4):292–303.

Feldmeyer, D. and Sakmann, B. (2000). Synaptic efficacy and reliability of excitatory connections between the principal neurones of the input (layer 4) and output layer (layer 5) of the neocortex. *The Journal of physiology*, 525(1):31–39.

Fiete, I. R., Burak, Y., and Brookings, T. (2008). What grid cells convey about rat location. *Journal of Neuroscience*, 28(27):6858–6871.

Fourcaud-Trocmé, N., Hansel, D., van Vreeswijk, C., and Brunel, N. (2003). How spike generation mechanisms determine the neuronal response to fluctuating inputs. *Journal of Neuroscience*, 23(37):11628–11640.

Fries, P. (2005). A mechanism for cognitive dynamics: neuronal communication through neuronal coherence. *Trends in cognitive sciences*, 9(10):474–480.

Fries, P. (2009). Neuronal gamma-band synchronization as a fundamental process in cortical computation. *Annual review of neuroscience*, 32:209–224.

Fuhs, M. C. and Touretzky, D. S. (2006). A spin glass model of path integration in rat medial entorhinal cortex. *Journal of Neuroscience*, 26(16):4266–4276.

Fyhn, M., Hafting, T., Treves, A., Moser, M.-B., and Moser, E. I. (2007). Hippocampal remapping and grid realignment in entorhinal cortex. *Nature*, 446(7132):190–194.

Fyhn, M., Hafting, T., Witter, M. P., Moser, E. I., and Moser, M.-B. (2008). Grid cells in mice. *Hippocampus*, 18(12):1230–1238.

Fyhn, M., Molden, S., Witter, M. P., Moser, E. I., and Moser, M.-B. (2004). Spatial representation in the entorhinal cortex. *Science*, 305(5688):1258–1264.

Garden, D. L. F., Dodson, P. D., O'Donnell, C., White, M. D., and Nolan, M. F. (2008). Tuning of synaptic integration in the medial entorhinal cortex to the organization of grid cell firing fields. *Neuron*, 60(5):875–889.

Gatome, C. W., Slomianka, L., Lipp, H. P., and Amrein, I. (2010). Number estimates of neuronal phenotypes in layer II of the medial entorhinal cortex of rat and mouse. *Neuroscience*, 170(1):156–165.

Gewaltig, M.-O. and Diesmann, M. (2007). NEST (NEural Simulation Tool). *Scholarpedia*, 2(4):1430.

Giocomo, L. M. and Hasselmo, M. E. (2008a). Computation by oscillations: Implications of experimental data for theoretical models of grid cells. *Hippocampus*, 18(12):1186–1199.

Giocomo, L. M. and Hasselmo, M. E. (2008b). Time constants of H current in layer II stellate cells differ along the dorsal to ventral axis of medial entorhinal cortex. *Journal of Neuroscience*, 28(38):9414–9425.

Giocomo, L. M., Zilli, E. A., Fransén, E., and Hasselmo, M. E. (2007). Temporal frequency of subthreshold oscillations scales with entorhinal grid cell field spacing. *Science*, 315(5819):1719–1722.

Goodman, D. and Brette, R. (2008). Brian: a simulator for spiking neural networks in python. *Frontiers in neuroinformatics*, 2:5.

Goodridge, J. P. and Touretzky, D. S. (2000). Modeling attractor deformation in the rodent head-direction system. *Journal of Neurophysiology*, 83(6):3402–3410.

Green, J. D. and Arduini, A. A. (1954). Hippocampal Electrical Aactivity In Arousal. *Journal of Neurophysiology*, 17(6):533–557.

Grossberg, S. (1976). Adaptive pattern classification and universal recoding: I. Parallel development and coding of neural feature detectors. *Biological cybernetics*, 23(3):121–134.

Grossberg, S. and Seitz, A. (2003). Laminar development of receptive fields, maps and columns in visual cortex: the coordinating role of the subplate. *Cerebral Cortex*, 13(8):852–863.

Guanella, A., Kiper, D., and Verschure, P. (2007). A model of grid cells based on a twisted torus topology. *International Journal of Neural Systems*, 17(4):231–240.

Haas, J. S. and White, J. A. (2002). Frequency Selectivity of Layer II Stellate Cells in the Medial Entorhinal Cortex. *Journal of Neurophysiology*, 88(5):2422–2429.

Hafting, T., Fyhn, M., Bonnevie, T., Moser, M.-B., and Moser, E. I. (2008). Hippocampus-independent phase precession in entorhinal grid cells. *Nature*, 453(7199):1248–1252.

Hafting, T., Fyhn, M., Molden, S., Moser, M.-B., and Moser, E. I. (2005). Microstructure of a spatial map in the entorhinal cortex. *Nature*, 436(7052):801–806.

Henrie, J. A. and Shapley, R. (2005). LFP power spectra in V1 cortex: the graded effect of stimulus contrast. *Journal of Neurophysiology*, 94(1):479–490.

Hitti, F. L. and Siegelbaum, S. A. (2014). The hippocampal CA2 region is essential for social memory. *Nature*, 508(7494):88–92.

Huxter, J., Burgess, N., and O'Keefe, J. (2003). Independent rate and temporal coding in hippocampal pyramidal cells. *Nature*, 425(6960):828–832.

Jacobs, J., Weidemann, C. T., Miller, J. F., Solway, A., Burke, J. F., Wei, X.-X., Suthana, N., Sperling, M. R., Sharan, A. D., Fried, I., and Kahana, M. J. (2013). Direct recordings of grid-like neuronal activity in human spatial navigation. *Nature Neuroscience*, 16(9):1188–1190.

Jeewajee, A., Barry, C., O'Keefe, J., and Burgess, N. (2008). Grid cells and theta as oscillatory interference: Electrophysiological data from freely moving rats. *Hippocampus*, 18(12):1175–1185.

Jensen, O. and Colgin, L. L. (2007). Cross-frequency coupling between neuronal oscillations. *Trends in cognitive sciences*, 11(7):267–269.

Jensen, O. and Lisman, J. E. (1996). Novel lists of 7 +/- 2 known items can be reliably stored in an oscillatory short-term memory network: interaction with long-term memory. *Learning & memory*, 3(2-3):257–263.

Jensen, O. and Lisman, J. E. (1998). An oscillatory short-term memory buffer model can account for data on the Sternberg task. *Journal of Neuroscience*, 18(24):10688–10699.

Jones, R. and Buhl, E. H. (1993). Basket-like interneurones in layer II of the entorhinal cortex exhibit a powerful NMDA-mediated synaptic excitation. *Neuroscience letters*, 149(1):35–39.

Jones, R. S. G. (1994). Synaptic and intrinsic properties of neurons of origin of the perforant path in layer II of the rat entorhinal cortex in vitro. *Hippocampus*, 4(3):335–353.

Killian, N. J., Jutras, M. J., and Buffalo, E. A. (2012). A map of visual space in the primate entorhinal cortex. *Nature*, 491(7426):761–764.

Kitamura, T., Pignatelli, M., Suh, J., Kohara, K., Yoshiki, A., Abe, K., and Tonegawa, S. (2014). Island cells control temporal association memory. *Science*, 343(6173):896–901.

Klink, R. and Alonso, A. (1997). Morphological characteristics of layer II projection neurons in the rat medial entorhinal cortex. *Hippocampus*, 7(5):571–583.

Kloosterman, F., van Haeften, T., Witter, M. P., and Lopes da Silva, F. H. (2003). Electrophysiological characterization of interlaminar entorhinal connections: an essential link for re-entrance in the hippocampal-entorhinal system. *European Journal of Neuroscience*, 18(11):3037–3052.

Koenig, J., Linder, A. N., Leutgeb, J. K., and Leutgeb, S. (2011). The spatial periodicity of grid cells is not sustained during reduced theta oscillations. *Science*, 332(6029):592–595.

Köhler, C. (1986). Intrinsic connections of the retrohippocampal region in the rat brain. II. The medial entorhinal area. *The Journal of comparative neurology*, 246(2):149–169.

Kopell, N. J., Gritton, H. J., Whittington, M. A., and Kramer, M. A. (2014). Beyond the Connectome: The Dynome. *Neuron*, 83(6):1319–1328.

Kropff, E., Carmichael, J. E., Moser, E. I., and Moser, M. B. (2014). Speed cells in the medial entorhinal cortex. In *Society for Neuroscience (SfN)*.

Kropff, E. and Treves, A. (2008). The emergence of grid cells: Intelligent design or just adaptation? *Hippocampus*, 18(12):1256–1269.

Krupic, J., Burgess, N., and O'Keefe, J. (2012). Neural representations of location composed of spatially periodic bands. *Science*, 337(6096):853–857.

Kumar, S. S., Jin, X., Buckmaster, P. S., and Huguenard, J. R. (2007). Recurrent circuits in layer II of medial entorhinal cortex in a model of temporal lobe epilepsy. *Journal of Neuroscience*, 27(6):1239–1246.

Leutgeb, S., Leutgeb, J. K., Barnes, C. A., Moser, E. I., McNaughton, B. L., and Moser, M.-B. (2005). Independent codes for spatial and episodic memory in hippocampal neuronal ensembles. *Science*, 309(5734):619–623.

Lewis, D. A., Curley, A. A., Glausier, J. R., and Volk, D. W. (2012). Cortical parvalbumin interneurons and cognitive dysfunction in schizophrenia. *TRENDS in Neurosciences*, 35(1):57–67.

Lisman, J. (2005). The theta/gamma discrete phase code occuring during the hippocampal phase precession may be a more general brain coding scheme. *Hippocampus*, 15(7):913–922.

Lisman, J. E. and Idiart, M. A. (1995). Storage of 7 +/- 2 short-term memories in oscillatory subcycles. *Science*, 267(5203):1512–1515.

Longtin, A., Bulsara, A., and Moss, F. (1991). Time-interval sequences in bistable systems and the noise-induced transmission of information by sensory neurons. *Physical review letters*, 67(5):656–659.

Markram, H., Lübke, J., Frotscher, M., Roth, A., and Sakmann, B. (1997). Physiology and anatomy of synaptic connections between thick tufted pyramidal neurones in the developing rat neocortex. *The Journal of physiology*, 500 (Pt 2):409–440.

Mathis, A., Herz, A. V. M., and Stemmler, M. (2012). Optimal population codes for space: grid cells outperform place cells. *Neural Computation*, 24(9):2280–2317.

McNaughton, B. L., Battaglia, F. P., Jensen, O., Moser, E. I., and Moser, M.-B. (2006). Path integration and the neural basis of the 'cognitive map'. *Nat Rev Neurosci*, 7(8):663–678.

Middleton, S., Jalics, J., Kispersky, T., LeBeau, F. E. N., Roopun, A. K., Kopell, N. J., Whittington, M. A., and Cunningham, M. O. (2008). NMDA receptor-dependent switching between different gamma rhythm-generating microcircuits in entorhinal cortex. *Proceedings of the National Academy of Sciences*, 105(47):18572–18577.

Mittelstaedt, M. L. and Mittelstaedt, H. (1980). Homing by path integration in a mammal. *Naturwissenschaften*, 67(11):566–567.

Mizuseki, K., Sirota, A., Pastalkova, E., and Buzsáki, G. (2009). Theta oscillations provide temporal windows for local circuit computation in the entorhinal-hippocampal loop. *Neuron*, 64(2):267–280.

Moser, E. I., Kropff, E., and Moser, M. B. (2008). Place cells, grid cells, and the brain's spatial representation system. *Annual review of neuroscience*, 31:69–89.

Moser, E. I., Roudi, Y., Witter, M. P., Kentros, C., Bonhoeffer, T., and Moser, M.-B. (2014). Grid cells and cortical representation. *Nature Reviews Neuroscience*, 15(7):466–481.

Navratilova, Z., Giocomo, L. M., Fellous, J.-M., Hasselmo, M. E., and McNaughton, B. L. (2012). Phase precession and variable spatial scaling in a periodic attractor map model of medial entorhinal grid cells with realistic after-spike dynamics. *Hippocampus*, 22(4):772–789.

Nolan, M. F., Dudman, J. T., Dodson, P. D., and Santoro, B. (2007). HCN1 channels control resting and active integrative properties of stellate cells from layer II of the entorhinal cortex. *Journal of Neuroscience*, 27(46):12440–12451.

O'Keefe, J. (1976). Place units in the hippocampus of the freely moving rat. *Experimental neurology*, 51(1):78–109.

O'Keefe, J. and Burgess, N. (2005). Dual phase and rate coding in hippocampal place cells: Theoretical significance and relationship to entorhinal grid cells. *Hippocampus*, 15(7):853–866.

O'Keefe, J., Burgess, N., Donnett, J. G., Jeffery, K. J., and Maguire, E. A. (1998). Place cells, navigational accuracy, and the human hippocampus. *Philosophical Transactions of the Royal Society B: Biological Sciences*, 353(1373):1333–1340.

O'Keefe, J. and Dostrovsky, J. (1971). The hippocampus as a spatial map. Preliminary evidence from unit activity in the freely-moving rat. *Brain research*, 34(1):171–175.

O'Keefe, J. and Recce, M. L. (1993). Phase relationship between hippocampal place units and the EEG theta rhythm. *Hippocampus*, 3(3):317–330.

Onslow, A. C. E., Jones, M. W., and Bogacz, R. (2014). A canonical circuit for generating phase-amplitude coupling. *PLoS ONE*, 9(8):e102591.

Paoletti, P., Bellone, C., and Zhou, Q. (2013). NMDA receptor subunit diversity: impact on receptor properties, synaptic plasticity and disease. *Nature Reviews Neuroscience*, 14(6):383–400.

Pastoll, H., Ramsden, H. L., and Nolan, M. F. (2012). Intrinsic electrophysiological properties of entorhinal cortex stellate cells and their contribution to grid cell firing fields. *Frontiers in Neural Circuits*, 6:17.

Pastoll, H., Solanka, L., van Rossum, M. C. W., and Nolan, M. F. (2013). Feedback inhibition enables theta-nested gamma oscillations and grid firing fields. *Neuron*, 77(1):141–154.

Petsche, H., Stumpf, C., and Gogolak, G. (1962). The significance of the rabbit's septum as a relay station between the midbrain and the hippocampus. I. The control of hippocampus arousal activity by the septum cells. *Electroencephalography and Clinical Neurophysiology*, 14:202–211.

Pilly, P. K. and Grossberg, S. (2012). How do spatial learning and memory occur in the brain? Coordinated learning of entorhinal grid cells and hippocampal place cells. *Journal of cognitive neuroscience*, 24(5):1031–1054.

Pilly, P. K. and Grossberg, S. (2013). Spiking neurons in a hierarchical self-organizing map model can learn to develop spatial and temporal properties of entorhinal grid cells and hippocampal place cells. *PLoS ONE*, 8(4):e60599.

Quilichini, P., Sirota, A., and Buzsáki, G. (2010). Intrinsic circuit organization and theta-gamma oscillation dynamics in the entorhinal cortex of the rat. *Journal of Neuroscience*, 30(33):11128–11142.

Raudies, F., Brandon, M. P., Chapman, G. W., and Hasselmo, M. E. (2013). Movement direction is not coded by the firing of most entorhinal cells but required by grid cell models. In *Society for Neuroscience*, San Diego.

Remme, M. W. H., Lengyel, M., and Gutkin, B. S. (2010). Democracy-Independence Trade-Off in Oscillating Dendrites and Its Implications for Grid Cells. *Neuron*, 66(3):429–437.

Reshef, D. N., Reshef, Y. A., Finucane, H. K., Grossman, S. R., McVean, G., Turnbaugh, P. J., Lander, E. S., Mitzenmacher, M., and Sabeti, P. C. (2011). Detecting novel associations in large data sets. *Science*, 334(6062):1518–1524.

Roudi, Y. and Latham, P. E. (2007). A balanced memory network. *PLOS Computational Biology*, 3(9):1679–1700.

Rowland, D. C., Weible, A. P., Wickersham, I. R., Wu, H., Mayford, M., Witter, M. P., and Kentros, C. G. (2013). Transgenically targeted rabies virus demonstrates a major monosynaptic projection from hippocampal area CA2 to medial entorhinal layer II neurons. *Journal of Neuroscience*, 33(37):14889–14898.

Roxin, A., Brunel, N., and Hansel, D. (2005). Role of delays in shaping spatiotemporal dynamics of neuronal activity in large networks. *Physical review letters*, 94(23):238103.

Roxin, A., Brunel, N., and Hansel, D. (2006). Rate models with delays and the dynamics of large networks of spiking neurons. *Progress of Theoretical Physics Supplement*, 161:68–85.

Rubenstein, J. L. R. and Merzenich, M. M. (2003). Model of autism: increased ratio of excitation/inhibition in key neural systems. *Genes, Brain and Behavior*, 2(5):255–267.

Samsonovich, A. and McNaughton, B. L. (1997). Path integration and cognitive mapping in a continuous attractor neural network model. *Journal of Neuroscience*, 17(15):5900–5920.

Sargolini, F., Fyhn, M., Hafting, T., McNaughton, B. L., Witter, M. P., Moser, M.-B., and Moser, E. I. (2006). Conjunctive representation of position, direction, and velocity in entorhinal cortex. *Science*, 312(5774):758–762.

Schmidt-Hieber, C. and Häusser, M. (2013). Cellular mechanisms of spatial navigation in the medial entorhinal cortex. *Nature Neuroscience*, 16(3):325–331.

Schreiber, S., Erchova, I., Heinemann, U., and Herz, A. V. M. (2004). Subthreshold Resonance Explains the Frequency-Dependent Integration of Periodic as Well as Random Stimuli in the Entorhinal Cortex. *Journal of Neurophysiology*, 92(1):408–415.

Shadlen, M. N. and Movshon, J. A. (1999). Synchrony unbound: a critical evaluation of the temporal binding hypothesis. *Neuron*, 24(1):67–77– 111–25.

Shannon, C. E. (1956). A Mathematical Theory of Communication. *Bell System Technical Journal*, 27(4):623–656.

Shu, Y., Hasenstaub, A., Badoual, M., Bal, T., and McCormick, D. A. (2003). Barrages of synaptic activity control the gain and sensitivity of cortical neurons. *Journal of Neuroscience*, 23(32):10388–10401.

Singer, W. (1999). Neuronal synchrony: a versatile code for the definition of relations? *Neuron*, 24(1):49–65.

Skaggs, W. E., McNaughton, B. L., Wilson, M. A., and Barnes, C. A. (1996). Theta phase precession in hippocampal neuronal populations and the compression of temporal sequences. *Hippocampus*, 6(2):149–172.

Solstad, T., Boccara, C. N., Kropff, E., Moser, M.-B., and Moser, E. I. (2008). Representation of geometric borders in the entorhinal cortex. *Science*, 322(5909):1865–1868.

Somers, D. C., Nelson, S. B., and Sur, M. (1995). An emergent model of orientation selectivity in cat visual cortical simple cells. *Journal of Neuroscience*, 15(8):5448–5465.

Song, P. and Wang, X.-J. (2005). Angular path integration by moving "hill of activity": a spiking neuron model without recurrent excitation of the head-direction system. *Journal of Neuroscience*, 25(4):1002–1014.

Sreenivasan, S. and Fiete, I. (2011). Grid cells generate an analog error-correcting code for singularly precise neural computation. *Nature Neuroscience*, 14(10):1330–1337.

Stackman, R. W. and Herbert, A. M. (2002). Rats with lesions of the vestibular system require a visual landmark for spatial navigation. *Behavioural Brain Research*, 128(1):27–40.

Stensola, H., Stensola, T., Solstad, T., Frøland, K., Moser, M.-B., and Moser, E. I. (2012). The entorhinal grid map is discretized. *Nature*, 492(7427):72–78.

Stumpf, C., Petsche, H., and Gogolak, G. (1962). The significance of the rabbit's septum as a relay station between the midbrain and the hippocampus II. The differential influence of drugs upon both the septal cell firing pattern and the hippocampus theta activity. *Electroencephalography and Clinical Neurophysiology*, 14(2):212–219.

Taube, J. S., Muller, R. U., and Ranck, J. B. (1990a). Head-direction cells recorded from the postsubiculum in freely moving rats. I. Description and quantitative analysis. *Journal of Neuroscience*, 10(2):420–435.

Taube, J. S., Muller, R. U., and Ranck, J. B. (1990b). Head-direction cells recorded from the postsubiculum in freely moving rats. II. Effects of environmental manipulations. *Journal of Neuroscience*, 10(2):436–447.

Terrazas, A., Krause, M., Lipa, P., Gothard, K. M., Barnes, C. A., and McNaughton, B. L. (2005). Self-motion and the hippocampal spatial metric. *Journal of Neuroscience*, 25(35):8085–8096.

Traub, R. and Whittington, M. (2010). *Cortical oscillations in health and disease*. Oxford University Press.

Uhlhaas, P. J. and Singer, W. (2010). Abnormal neural oscillations and synchrony in schizophrenia. *Nature Reviews Neuroscience*, 11(2):100–113.

Uhlhaas, P. J. and Singer, W. (2012). Neuronal Dynamics and Neuropsychiatric Disorders: Toward a Translational Paradigm for Dysfunctional Large-Scale Networks. *Neuron*, 75(6):963–980.

van der Linden, S. and Lopes da Silva, F. H. (1998). Comparison of the electrophysiology and morphology of layers III and II neurons of the rat medial entorhinal cortex in vitro. *The European journal of neuroscience*, 10(4):1479–1489.

van Haeften, T., Baks-te Bulte, L. n., Goede, P. H., Wouterlood, F. G., and Witter, M. P. (2003). Morphological and numerical analysis of synaptic interactions between neurons in deep and superficial layers of the entorhinal cortex of the rat. *Hippocampus*, 13(8):943–952.

Varga, C., Lee, S. Y., and Soltesz, I. (2010). Target-selective GABAergic control of entorhinal cortex output. *Nature Neuroscience*, 13(7):822–824.

Von Der Malsburg, C. (1981). The correlation theory of brain function. Technical Report 81, Dept. of Neurobiology, Max-Planck-Institute for Biophysical Chemistry, Goettingen.

Wallace, D. G., Hines, D. J., Pellis, S. M., and Whishaw, I. Q. (2002). Vestibular information is required for dead reckoning in the rat. *Journal of Neuroscience*, 22(22):10009–10017.

Wang, X. J. (1999). Synaptic basis of cortical persistent activity: the importance of NMDA receptors to working memory. *Journal of Neuroscience*, 19(21):9587–9603.

Welday, A. C., Shlifer, I. G., Bloom, M. L., Zhang, K., and Blair, H. T. (2011). Cosine directional tuning of theta cell burst frequencies: evidence for spatial coding by oscillatory interference. *Journal of Neuroscience*, 31(45):16157–16176.

Welinder, P. E., Burak, Y., and Fiete, I. R. (2008). Grid cells: the position code, neural network models of activity, and the problem of learning. *Hippocampus*, 18(12):1283–1300.

Whittington, M. A., Traub, R. D., Kopell, N., Ermentrout, B., and Buhl, E. H. (2000). Inhibition-based rhythms: experimental and mathematical observations on network dynamics. *International journal of psychophysiology : official journal of the International Organization of Psychophysiology*, 38(3):315–336.

Widloski, J. and Fiete, I. R. (2014). A Model of Grid Cell Development through Spatial Exploration and Spike Time-Dependent Plasticity. *Neuron*, 83(2):481–495.

Witter, M. P. and Amaral, D. G. (2004). *The rat nervous system*, chapter Hippocampal formation, pages 635–704. Elsevier.

Witter, M. P. and Moser, E. I. (2006). Spatial representation and the architecture of the entorhinal cortex. *TRENDS in Neurosciences*, 29(12):671–678.

Xie, X., Hahnloser, R. H. R., and Seung, H. S. (2002). Double-ring network model of the head-direction system. *Physical review. E, Statistical, nonlinear, and soft matter physics*, 66(4 Pt 1):041902.

Yartsev, M. M., Witter, M. P., and Ulanovsky, N. (2011). Grid cells without theta oscillations in the entorhinal cortex of bats. *Nature*, 479(7371):103–107.

Yoon, K., Buice, M. A., Barry, C., Hayman, R., Burgess, N., and Fiete, I. R. (2013). Specific evidence of low-dimensional continuous attractor dynamics in grid cells. *Nature Neuroscience*, 16(8):1077–1084.

Zhang, K. (1996). Representation of spatial orientation by the intrinsic dynamics of the head-direction cell ensemble: a theory. *Journal of Neuroscience*, 16(6):2112–2126.

Zhang, S.-J., Ye, J., Miao, C., Tsao, A., Cerniauskas, I., Ledergerber, D., Moser, M.-B., and Moser, E. I. (2013). Optogenetic dissection of entorhinal-hippocampal functional connectivity. *Science*, 340(6128):1232627–1232627.

Zilli, E. A. (2012). Models of grid cell spatial firing published 2005-2011. *Frontiers in Neural Circuits*, 6:16.

Zilli, E. A. and Hasselmo, M. E. (2010). Coupled noisy spiking neurons as velocity-controlled oscillators in a model of grid cell spatial firing. *Journal of Neuroscience*, 30(41):13850–13860.